

CAPITAL UNIVERSITY OF SCIENCE AND  
TECHNOLOGY, ISLAMABAD



**On Fluid Transport and  
Compressive Strength Properties  
of Bone Scaffolds Manufactured  
Through PolyJet and  
Micro-Stereolithography**

by

**Shummaila Rasheed**

A dissertation submitted in partial fulfillment for the  
degree of Doctor of Philosophy

in the

**Faculty of Engineering**

**Department of Mechanical Engineering**

2024

**On Fluid Transport and Compressive Strength  
Properties of Bone Scaffolds Manufactured  
Through PolyJet and Micro-Stereolithography**

By

Shummaila Rasheed

(DME171001)

**Dr. Farukh Farukh, Senior Lecturer  
De Montfort University, Leicester, UK  
(Foreign Evaluator 1)**

**Dr. Sergiu-Dan Stan, Associate Professor  
Technical University of Cluj-Napoca, Romania  
(Foreign Evaluator 2)**

**Dr. Muhammad Mahabat Khan  
(Research Supervisor)**

**Dr. Muhammad Mahabat Khan  
(Head, Department of Mechanical Engineering)**

**Dr. Imtiaz Ahmad Taj  
(Dean, Faculty of Engineering)**

**DEPARTMENT OF MECHANICAL ENGINEERING  
CAPITAL UNIVERSITY OF SCIENCE AND TECHNOLOGY  
ISLAMABAD**

**2024**

Copyright © 2024 by Shummaila Rasheed

All rights reserved. No part of this dissertation may be reproduced, distributed, or transmitted in any form or by any means, including photocopying, recording, or other electronic or mechanical methods, by any information storage and retrieval system without the prior written permission of the author.

*This modest endeavor is dedicated to*

***My Father***

*for his belief in my abilities, constant encouragement, and boundless love  
throughout this challenging doctoral journey.*

*“Your support has been the foundation of my success, and I dedicate this  
dissertation to you with deep gratitude and love.”*

***My Mother (Late)***

*In loving memory of her, whose endless love, strength, and inspiration continue  
to guide me every step of the way.*

*“This PhD dissertation is dedicated to her cherished memory, with profound  
gratitude for the immeasurable impact she had on shaping my life and academic  
pursuits.”*

***My Research Supervisor***

*A guiding light in this academic pursuit.*

*“Your invaluable support and expertise made this dissertation possible. With  
deepest gratitude, I dedicate this work to you.”*

***My Husband and Son “Muhammad Izhan”***

*This dissertation is dedicated to both of you with profound gratitude and endless  
love for abiding my ignorance with patience during critical stages of my Ph.D.*



**CAPITAL UNIVERSITY OF SCIENCE & TECHNOLOGY  
ISLAMABAD**

Expressway, Kahuta Road, Zone-V, Islamabad  
Phone: +92-51-111-555-666 Fax: +92-51-4486705  
Email: [info@cust.edu.pk](mailto:info@cust.edu.pk) Website: <https://www.cust.edu.pk>

**CERTIFICATE OF APPROVAL**

This is to certify that the research work presented in the dissertation, entitled “**On Fluid Transport and Compressive Strength Properties of Bone Scaffolds Manufactured Through Polyjet and Micro-Stereolithography**” was conducted under the supervision of **Dr. Muhammad Mahabat Khan**. No part of this dissertation has been submitted anywhere else for any other degree. This dissertation is submitted to the **Department of Mechanical Engineering, Capital University of Science and Technology** in partial fulfillment of the requirements for the degree of Doctor in Philosophy in the field of **Mechanical Engineering**. The open defence of the dissertation was conducted on **February 29, 2024**.

**Student Name :** Shummaila Rasheed (DME171001) \_\_\_\_\_

The Examining Committee unanimously agrees to award PhD degree in the mentioned field.

**Examination Committee :**

- (a) External Examiner 1: Dr. Sohail Malik  
Associate Professor  
Pak-AF IAS&T, Haripur
- (b) External Examiner 2: Dr. Owais ur Rehman Shah  
Associate Professor  
IST, Islamabad
- (c) Internal Examiner : Dr. Ghulam Asghar  
Assistant Professor  
CUST, Islamabad

**Supervisor Name :** Dr. Muhammad Mahabat Khan  
Associate Professor  
CUST, Islamabad

**Name of HoD :** Dr. Muhammad Mahabat Khan  
Associate Professor  
CUST, Islamabad

**Name of Dean :** Dr. Imtiaz Ahmed Taj  
Professor  
CUST, Islamabad

\_\_\_\_\_

\_\_\_\_\_

\_\_\_\_\_

\_\_\_\_\_

\_\_\_\_\_

\_\_\_\_\_

## AUTHOR'S DECLARATION

I, **Shummaila Rasheed** (Registration No. **DME171001**), hereby state that my dissertation entitled, '**On Fluid Transport and Compressive Strength Properties of Bone Scaffolds Manufactured Through PolyJet and Micro-Stereolithography**' is my own work and has not been submitted previously by me for taking any degree from Capital University of Science and Technology, Islamabad or anywhere else in the country/ world.

At any time, if my statement is found to be incorrect even after my graduation, the University has the right to withdraw my PhD Degree.



**(Shummaila Rasheed)**

Dated: 29<sup>th</sup> February, 2024

Registration No : DME171001

## PLAGIARISM UNDERTAKING

I solemnly declare that research work presented in the dissertation titled “**On Fluid Transport and Compressive Strength Properties of Bone Scaffolds Manufactured Through PolyJet and Micro-Stereolithography**” is solely my research work with no significant contribution from any other person. Small contribution/ help wherever taken has been duly acknowledged and that complete dissertation has been written by me.

I understand the zero-tolerance policy of the HEC and Capital University of Science and Technology towards plagiarism. Therefore, I as an author of the above titled dissertation declare that no portion of my dissertation has been plagiarized and any material used as reference is properly referred/ cited.

I undertake that if I am found guilty of any formal plagiarism in the above titled dissertation even after award of PhD Degree, the University reserves the right to withdraw/ revoke my PhD degree and that HEC and the University have the right to publish my name on the HEC/ University Website on which names of students are placed who submitted plagiarized dissertation.



(Shummaila Rasheed)

Dated: 29<sup>th</sup> February, 2024

Registration No : DME171001

## *List of Publications*

It is certified that following publication(s) have been made out of the research work that has been carried out for this dissertation:-

1. **S. Rasheed**, W. A. Lughmani, M. M. Khan, D. Brabazon, M. A. Obeidi, and I. U. Ahad, “The porosity design and deformation behavior analysis of additively manufactured bone scaffolds through finite element modelling and mechanical property investigations,” *Journal of Functional Biomaterials*, vol. 14, no. 10, p. 496, 2023.
2. **S. Rasheed**, W. A. Lughmani, M. A. Obeidi, D. Brabazon and I. U. Ahad, “Additive manufacturing of bone scaffolds using polyjet and stereolithography techniques,” *Applied Sciences (Switzerland)*, vol. 11, no. 16, Aug. 2021.

**(Shummaila Rasheed)**

Registration No:DME171001

---

## *Acknowledgement*

“In the name of Allah, the Most Gracious and the Most Merciful! All praises are for Almighty Allah, the Creator of everything, with Whose grace I am here, as one can’t even wish without His will. And all the respect for the Holy Prophet Muhammad (Peace be upon Him).” I extend my heartfelt appreciation to my former research supervisor, Dr. Waqas Akbar Lughmani, whose exceptional mentorship and expertise have shaped me into a diligent researcher. I am also deeply appreciative of my new PhD research supervisor, Dr. M. Mahabat Khan, who has graciously taken me under his wing as I continue my academic voyage. With his support, I am confident that I will be able to navigate the challenges ahead and complete my degree on time. I would like to extend my heartfelt gratitude to the worthy Professor / Vice Chancellor Dr. M. Mansoor Ahmed of Capital University of Science and Technology for the invaluable opportunity for experimental activities in the School of Mechanical and Manufacturing Engineering in Dublin City University Ireland. Additionally, I am immensely thankful for the invaluable insights and global perspectives provided by my international research collaborators Prof. Dermot Brabazon, Dr. Inam ul Ahad and Dr. Muhannad Ahmed Obeidi. Their diverse expertise, innovative ideas, collaborative spirit, acquired from different academic backgrounds and cultural perspectives, has significantly enriched the depth and breadth of this research. I am indebted to the Dean Faculty of Engineering Dr. Imtiaz Ahmad Taj and all other respected faculty members for providing a conducive research environment and invaluable resources, facilitating the pursuit of knowledge. My sincere thanks go to Sadia Bashir and Madeeha Khan for their camaraderie, stimulating discussions, and belief in my capabilities. I cannot express enough gratitude to my beloved family and my students M. Norman Shahid and M. Usman Shahid for their boundless love, encouragement, and constant motivation throughout this challenging journey.

**(Shummaila Rasheed)**

Registration No: DME171001

## *Abstract*

The study of manufacturability, fluid transport characteristics, and mechanical properties of additively manufactured bone scaffolds is of paramount importance in the field of bone tissue engineering. Understanding the manufacturability ensures that these complex structures can be produced efficiently and reproducibly, which is crucial for large-scale adoption. Evaluating fluid transport properties helps assess the scaffold's ability to facilitate nutrient diffusion and waste removal, vital for cell growth and tissue regeneration. Additionally, examining mechanical properties ensures that these scaffolds can bear the physiological loads encountered in the human body, guaranteeing structural integrity and long-term functionality. This interdisciplinary research not only advances the development of effective bone scaffolds but also contributes to the broader application of additive manufacturing in biomedical and clinical settings, potentially revolutionizing the treatment of bone injuries and diseases. The current dissertation is focused on utilizing two distinct additive manufacturing techniques: PolyJet and micro-stereolithography ( $\mu$ SLA). These techniques were explored for their potential to fabricate complex bone scaffold structures designed to aid in the repair and replacement of damaged or fractured bone tissue. The primary objective is to create scaffold structures that mimic the mechanical properties of natural human bone while allowing for adjustability in structural parameters of bone scaffolds. Various combinations of structural parameters such as pore size, porosity and pore shape were employed in the design of these 3D scaffold structures. This dissertation rigorously examines and compares the dimensional accuracy, permeability, and mechanical properties of the 3D-printed scaffold structures produced through these two distinct techniques. It investigates fluid flow rates through these scaffolds, utilizing both experimental measurements and numerical calculations using Darcy's Law and Kozeny Karman equation, respectively. Additionally, compression tests were carried out to assess the mechanical response as well as the impact of the printing techniques on the mechanical properties of the printed scaffold structures. The findings of this investigation reveal that the  $\mu$ SLA printing technique outperformed

the PolyJet printing technique, exhibiting superior permeability and mechanical properties in the fabricated scaffold structures.

Furthermore, the study extends its scope to finite element modeling, specifically analyzing the deformation characteristics of 3D bone scaffolds generated through micro-stereolithography ( $\mu$ SLA) and PolyJet (PJ) 3D printing methods. The scaffolds mechanical response to quasi-static compression was methodically evaluated, employing a crushable foam plasticity model. The experimental validation of the finite element outcomes demonstrated a favorable agreement, with an average percentage error of 12.27%. Furthermore, the yield strength and elastic modulus of the scaffolds were evaluated and compared, revealing noteworthy disparities between cubic and hexagonal closed packed designs. Specifically, cubic pore-shaped bone scaffolds with porosities of 30%, 50%, and 70% exhibited significantly higher yield strengths of 46.89%, 58.29%, and 66.09%, when contrasted with the hexagonal closed packed bone scaffolds at percentage strains of 5%, 6%, and 7% respectively. Similarly, the elastic modulus of the cubic pore-shaped bone scaffolds with porosities of 30%, 50%, and 70% was 42.68%, 59.70%, and 58.18% higher, respectively, compared to the hexagonal closed packed bone scaffolds at the same percentage strain levels. Furthermore, the  $\mu$ SLA-printed bone scaffolds demonstrated elastic moduli and yield strengths that were 1.5 times higher than those of the PJ-printed bone scaffolds.

# Contents

<b>Author's Declaration</b>	<b>v</b>
<b>Plagiarism Undertaking</b>	<b>vi</b>
<b>List of Publications</b>	<b>vii</b>
<b>Acknowledgement</b>	<b>viii</b>
<b>Abstract</b>	<b>ix</b>
<b>List of Figures</b>	<b>xv</b>
<b>List of Tables</b>	<b>xix</b>
<b>Abbreviations</b>	<b>xx</b>
<b>Symbols</b>	<b>xxii</b>
<b>1 Introduction</b>	<b>1</b>
1.1 Background . . . . .	2
1.2 Limitations of Conventional Technologies . . . . .	8
1.3 Limitations of 3D Printing Technologies . . . . .	9
1.4 Problem Statement . . . . .	10
1.5 Objectives . . . . .	11
1.6 Methodology . . . . .	12
1.7 Thesis Layout . . . . .	13
<b>2 Overview of Bone Scaffolds</b>	<b>18</b>
2.1 Introduction . . . . .	18
2.2 The Role of Scaffolds in Bone Tissue Engineering . . . . .	19
2.2.1 Overview of Bone Tissue Structure . . . . .	19
2.2.2 Mechanisms of Bone Regeneration . . . . .	22
2.3 Materials for Bone Scaffolds . . . . .	26
2.3.1 Ceramic Bone Scaffolds . . . . .	29
2.3.2 Polymeric Bone Scaffolds . . . . .	31

---

2.3.3	Metal and Alloy Based Bone Scaffolds . . . . .	33
2.3.4	Multi-materials Bone Scaffolds . . . . .	36
2.4	Bone Scaffolds Structure . . . . .	37
2.4.1	Porosity . . . . .	39
2.4.2	Bone Scaffolds Geometry . . . . .	40
2.4.2.1	Stochastic Bone Scaffolds . . . . .	40
2.4.2.2	Non-Stochastic Bone Scaffolds . . . . .	42
2.4.3	Triply Periodic Minimal Surface Based Bone Scaffolds . . . . .	44
2.4.4	Bone's Mechanical Properties . . . . .	45
2.5	Synthetic Bone Scaffolds Challenges . . . . .	47
2.6	Limitations and Benefits of Polymer-Based Bone Scaffolds . . . . .	49
2.6.1	Benefits of Polymer-Based Bone Scaffolds . . . . .	49
2.6.2	Limitations of Polymer-based Bone Scaffolds . . . . .	50
2.7	Research Gap . . . . .	52
<b>3</b>	<b>Conventional and Additive Manufacturing Techniques</b>	<b>53</b>
3.1	Introduction . . . . .	53
3.2	Conventional Techniques for the Developme- nt of Bone Scaffolds . . . . .	54
3.2.1	Solvent Casting and Particulate Leaching . . . . .	54
3.2.2	Gas-Foaming Process . . . . .	55
3.2.3	Thermally Induced Phase Separation . . . . .	56
3.2.4	Microsphere Sintering . . . . .	57
3.2.5	Electrospinning . . . . .	57
3.3	Additive Manufacturing Techniques for the Development of Bone Scaffolds . . . . .	59
3.3.1	Selective Laser Sintering (SLS) . . . . .	60
3.3.2	Selective Laser Melting (SLM) . . . . .	62
3.3.3	Fused Deposition Modelling (FDM) . . . . .	64
3.3.4	Electron Beam Melting (EBM) . . . . .	66
3.3.5	$\mu$ Stereolithography ( $\mu$ SLA) . . . . .	68
3.3.6	PolyJet Printing (PJ) . . . . .	71
3.4	Designing Technique for Bone Scaffolds . . . . .	72
3.4.1	CAD-Based Method . . . . .	73
3.4.2	Topology Optimization Top of Form . . . . .	75
3.4.3	Reverse Modelling . . . . .	76
3.4.4	Mathematical Modelling . . . . .	78
3.5	Research Gap . . . . .	80
<b>4</b>	<b>Design, Development and Experimentation</b>	<b>83</b>
4.1	Introduction . . . . .	83
4.2	Design and Development of Bone Scaffolds Through PolyJet Tech- nique . . . . .	84
4.2.1	Specifications of Stratasys Objet260 Connex 1 . . . . .	86
4.2.2	Material Used in PolyJet Technique . . . . .	87

---

4.2.3	PolyJet Printing of Bone Scaffolds . . . . .	89
4.3	Design and Development of Bone Scaffolds Through $\mu$ SLA Technique	91
4.3.1	Specifications of Asiga - Freeform Pico Plus 27 – Specifications	91
4.3.2	Material Used in $\mu$ SLA Technique . . . . .	91
4.3.3	$\mu$ SLA Printing of Bone Scaffolds . . . . .	93
4.4	Experimentation of 3D Printed Bone Scaffolds . . . . .	94
4.4.1	Experimental Setup of Flow Rate Measurement . . . . .	94
4.4.2	Scaffold Holding Clamp and Blind Sample . . . . .	95
4.4.3	Leak Tight Test of Scaffolds Holding Clamp . . . . .	95
4.4.4	Test Fluid Preparation . . . . .	96
4.4.5	Viscosity Measurement . . . . .	96
4.4.6	Calculating Contact Angle and Surface Energy . . . . .	97
4.5	Permeability Analysis of Bone Scaffolds . . . . .	98
4.5.1	Experimental Measurement of Permeability . . . . .	98
4.5.2	Numerical Calculation of Permeability . . . . .	99
4.6	Design and Development of Standard Samples . . . . .	100
4.7	Mechanical Testing of Bone Scaffolds . . . . .	101
4.7.1	Structural Characterization of Bone Scaffolds . . . . .	101
4.7.2	Quasi-Static Compression Testing . . . . .	102
<b>5</b>	<b>Experimental Results</b>	<b>105</b>
5.1	Introduction . . . . .	105
5.2	Effect of Contact Angle and Surface Energy on Permeability . . . . .	106
5.3	Experimental Measurement of Permeability for PolyJet Printed Bone Scaffolds . . . . .	107
5.4	Experimental Measurement of Permeability for $\mu$ SLA Printed Bone Scaffolds . . . . .	110
5.5	Numerical Calculation of Permeability . . . . .	115
5.6	Effect of Surface Area on Permeability . . . . .	116
5.7	Mechanical Properties of Bone Scaffolds . . . . .	119
5.8	Effect of Printing Direction on the Mechanical Properties . . . . .	127
<b>6</b>	<b>Numerical Investigation</b>	<b>130</b>
6.1	Introduction . . . . .	130
6.2	Finite Element Modelling . . . . .	131
6.2.1	CAD Model of Bone Scaffolds . . . . .	131
6.2.2	Meshing of Bone Scaffolds . . . . .	131
6.2.3	Boundary Conditions . . . . .	133
6.2.4	Crushable Foam Plasticity Model . . . . .	134
6.3	Fabrication of Bone Scaffolds and Solid Samples . . . . .	137
6.4	Quasi-Static Compression Testing . . . . .	139
6.5	Experimental Validation of FE Results . . . . .	141
6.6	Deformation in Bone Scaffolds . . . . .	145
6.7	Discussion . . . . .	149

---

<b>7 Conclusion and Future Recommendation</b>	<b>153</b>
7.1 Conclusion . . . . .	153
7.1.1 Hydrophobicity and Surface Energy . . . . .	153
7.1.2 Permeability Analysis . . . . .	154
7.1.3 Comparison between Printing Techniques . . . . .	155
7.1.4 Effect of Surface Area . . . . .	155
7.1.5 Mechanical Properties . . . . .	156
7.1.6 Standard Samples and Printing Direction . . . . .	157
7.1.7 Finite Element Analysis (FEA) . . . . .	157
7.1.8 Potential Applications in Bone Tissue Engineering . . . . .	158
7.2 Future Recommendations . . . . .	158
7.2.1 Advanced Printing Techniques . . . . .	158
7.2.2 Material Selection and Optimization . . . . .	159
7.2.3 Biological Integration . . . . .	160
7.2.4 Functional Gradients . . . . .	161
7.2.5 Patient-Specific Design . . . . .	162
7.2.6 Mechanical Performance under Dynamic Loading . . . . .	163
7.2.7 Long-Term Degradation Studies . . . . .	164
7.2.8 Multi-Material Printing . . . . .	164
7.2.9 Clinical Translation . . . . .	165
7.2.10 Incorporating Bioactive Factors . . . . .	166
<b>Bibliography</b>	<b>168</b>

# List of Figures

1.1	Bone Scaffolds [2]	2
1.2	Natural bone grafts and their limitations	3
1.3	Global bone graft substitutes market share 2022 [5]	4
1.4	Generation of materials used to develop the synthetic scaffolds	5
1.5	Classification of Bone Scaffolds	7
1.6	Stages of adopted methodology	12
1.7	Thesis Layout	14
2.1	The four cell types comprising bone tissue are osteoblasts, osteoclasts, osteocytes, and osteogenic cells (John Wiley and Sons, copyright 2023) [20]	19
2.2	Bone architecture shaped by assembling collagen into microfibrils and fibrils (John Wiley and Sons, copyright 2023) [20]	20
2.3	Bone healing: inflammation, repair, remodeling; stages - hematoma, granular tissue, fibrous tissue, soft hard callus. (John Wiley and Sons, copyright 2023) [20]	22
2.4	Bone maturation: apoptosis, osteoclast mineralization, MSC to osteoblasts with growth factors, matrix shift to osteocytes, surface osteoblasts to bone lining cells.(John Wiley and Sons, copyright 2023) [20]	23
2.5	Growth factors and cytokines trigger monocyte-MSc interaction, differentiating MSCs for bone healing response. (John Wiley and Sons, copyright 2023) [20]	24
2.6	Arrangement of various tissue components in cancellous and cortical bone. (John Wiley and Sons, copyright 2023) [20]	26
2.7	Bioinert repels ECM, bioactives release biomolecules for engagement, biomimetics mimic tissues, enhancing cellular communication. (John Wiley and Sons, copyright 2023) [20]	27
2.8	Bioceramic-ECM aids osteo/angiogenesis; ECM cues prompt MSCs to osteoblasts/osteocytes; osteoclasts remodel, osteoblasts enhance bone formation. (John Wiley and Sons, copyright 2023) [20]	28
2.9	Implant response: Adsorption, inflammation, macrophage cooperation, fibroblast-driven collagen. (John Wiley and Sons, copyright 2023) [20]	29
2.10	PBSLP employs three primary categories of synthetic bioactive ceramic scaffolds for bone repair [53]	31

2.11	Schematic illustration of the method used to fabricate 3D porous PLA/Ti64 composite scaffolds [59] . . . . .	32
2.12	The generated models encompass (a) a structured porous framework, (b) an unstructured porous arrangement, and (c) a gradient unstructured porous configuration [66] . . . . .	34
2.13	Porous structures for Ti6Al4V, formed through EDM, include regular, irregular, and gradient irregular arrangements [66] . . . . .	35
2.14	Structural parameters of the synthetic bone scaffolds [85] . . . . .	37
2.15	Stochastic scaffold design involves: A) Establishing a 3D domain with dispersed seeds; B) Generating subdomains from these seeds; and C) Applying a randomly oriented lattice to each subdomain [94] . . . . .	41
2.16	Functionally gradient stochastic scaffolds with 58 to 70 percent porosity along one axis, two axes, or all three axes [94] . . . . .	41
2.17	Non – stochastic bone scaffolds with pore shapes (a) Triangular (b) Square (c) Hexagonal (d) Hexa honeycomb (e) Re-entrant honeycomb (f) Triangular honeycomb . . . . .	43
2.18	(a) Gyroid type (b) Diamond type (c) Primitive type . . . . .	44
2.19	Advantages and disadvantages of natural and synthetic bone scaffolds	51
3.1	Solvent Casting and Particulate Leaching bone scaffolding technique	54
3.2	Gas foaming technique for bone scaffolding . . . . .	55
3.3	Thermally induced phase separation for bone scaffolding . . . . .	56
3.4	Schematics of microsphere sintering [134] . . . . .	58
3.5	Schematics of Selective Laser Sintering [141] . . . . .	60
3.6	Schematics of Selective Laser Melting [162] . . . . .	63
3.7	Schematic of Fused Deposition Modelling [167] . . . . .	64
3.8	Developments on Electron Beam Melting (EBM) of Ti-6Al-4V: A Review: Electron Beam Melting Schematic [181] . . . . .	67
3.9	Schematics of micro-Stereolithography [193] . . . . .	69
4.1	A 3D printed scaffold pore is shown in (a) an isometric view, (b) a front view, and (c) an optical microscopic image. scaffold structure in 3D CAD with hexagonal pore shapes . . . . .	86
4.2	Optical microscopic image of a scaffold pore taken with a 3D printer in (a) an isometric perspective, (b) a front view, and (c) a 3D CAD model of the scaffold structure with a cubic pore shape . . . . .	86
4.3	Procedure followed for the fabrication of 3D synthetic scaffold structure by using PolyJet Technique . . . . .	89
4.4	3D printing of polymeric bone scaffold using PolyJet Technique . . . . .	90
4.5	Procedure followed for the fabrication of 3D synthetic scaffold structure by using micro-stereolithography . . . . .	94
4.6	An experimental setup for an investigation of the permeability of 3D-printed porous bone scaffolds . . . . .	94
4.7	Clamping device: (a) an isometric view of the lower section (b) a side view of the lower part (c), and (d) an isometric view of the top part (d) Side view of the upper part . . . . .	95

4.8	Viscosity measurement (a) Physica MCR-301 (b) 3ml solution sample (c) measurement setting . . . . .	96
4.9	Measurement of Contact Angle: (a) Utilizing the FTA 200 Dynamic Contact Angle Analyzer (b) Employing the Sessile Drop Test . . . . .	98
4.10	(a) Standard Sample printed along the x, y, and z axes (b) cylindrical as well as rectangular cross sections standard samples . . . . .	101
4.11	Keyence-Digital microscope VHX-2000 . . . . .	102
4.12	Sample preparation for compression testing . . . . .	103
5.1	Permeability experiments were conducted on PolyJet 3D-printed scaffold structures with tap water, 15% glycerol-water solution, and 20% glycerol-water solution. The results are shown for both cubic and hexagonal closed packed configurations (a) and (b), respectively	108
5.2	Permeability measurements for $\mu$ SLA 3D-printed scaffold structures, using tap water, 15% glycerol-water solution, and 20% glycerol-water solution, are displayed for 30% porosity in cubic and hexagonal closed packed configurations. . . . .	111
5.3	For both cubic and hexagonal closed packed configurations at 30% porosity, the experimentally observed permeability of 3D-printed scaffold constructs using tap water, 15% glycerol-water solution, and 20% glycerol-water solution . . . . .	113
5.4	Calculated numerically: permeability (a) Cubic (b) closed-packed hexagonal scaffold structures . . . . .	117
5.5	Correlation of specific surface area with pore size and porosity is shown for (a) cubic structures and (b) hexagonal closed-packed structures . . . . .	118
5.6	Stress-strain curves of cubic-shaped PolyJet 3D-printed scaffold structures at (a) 30%, (b) 50%, and (c) 70% for the following pore sizes: 1.5mm, 2.0mm, 2.5mm, and 3.0mm . . . . .	120
5.7	Stress-strain curves for hexagonal closed-packed PolyJet 3D-printed scaffold structures are shown at various porosities (a) 30%, (b) 50%, and (c) 70%, with pore diameters of 1.5 mm to 3.0 mm . . . . .	122
5.8	Stress-strain curves for 3D-printed scaffold structures, produced using polyjet and micro-stereolithography techniques, feature cubic and hexagonal closed packed pores at 30% porosity. . . . .	126
5.9	Stress-strain profiles of standard samples created within 3D space across the x, y, and z directions . . . . .	128
6.1	(a) to (c) present the 2D views of the 3D CAD models; (d) to (f) present the 3D views of the 3D CAD models. (g) to (h) presents the 2D views of the 3D CAD models; (j) to (l) presents the 3D views of the 3D CAD models . . . . .	132
6.2	Top and bottom plates to mimic machine clamps, frictionless connection between plates and boundary conditions for FE simulations	134
6.3	Crushable foam model: yield surface and flow potential in the p-q stress plane . . . . .	135

---

6.4	Summary of stages involved in the development of additively manufactured polymeric bone scaffolds and standard solid samples . . .	139
6.5	Different levels of compression testing of additively manufactured polymeric bone scaffolds and 3D printed standard solid samples . . .	140
6.6	Crushed Sample . . . . .	140
6.7	Experimental stress-strain curves for 3D printed porous polymeric bone scaffolds and 3D printed standard solid samples . . . . .	142
6.8	Experimental and FE elastic moduli and yield strengths of polymeric bone scaffolds . . . . .	143
6.9	Optically measured architectural parameters of as-built polymeric bone scaffolds using Keyence-Digital microscope VHX-2000 (a) cubic pore shape with 30% porosity (b) hexagonal pore shape with 30% porosity (c) cubic pore shape with 50% porosity (b) hexagonal pore shape with 50% porosity [19] . . . . .	144
6.10	Deformation of polymeric bone scaffold under the compression level of 40%, 60% and 80% . . . . .	146
6.11	FE deformation mechanism through compressive stress contours of cubic pore shape at different level of strains consisted of (a) 30% (b) 50% and (c) 70% porosity in comparison with actual deformation behaviour of polymeric bone scaffolds . . . . .	147
6.12	FE deformation mechanism through compressive stress contours of hexagonal closed packed pore shape at different level of strains consisted of (a) 30% (b) 50% and (c) 70% porosity in comparison with actual deformation behaviour of polymeric bone scaffolds . . . . .	148

# List of Tables

2.1	Mathematical formulas defining structures with TPMS [104, 105]	45
2.2	Bone's mechanical characteristics in humans [110, 111]	46
3.1	Advantages and disadvantages of conventional techniques for bone scaffolding	59
4.1	Selected structural parameters for bone scaffold. (C- cubic structures, H- hexagonal closed packed structures, <b>Bold*</b> - not possible because of the thinner struts)	85
4.2	Test fluid pressure and density for measuring permeability	99
5.1	Contact angle and surface energy of PolyJet (VeroClear) and $\mu$ SLA (PlasWhite) 3D printed scaffold structures	106
5.2	Density and pressure of test fluids used in permeability measurement	114
5.3	Mechanical characteristics of scaffold structures printed in polyJet	125
5.4	Mechanical characteristics of scaffold structures produced via $\mu$ SLA 3D printing	125
5.5	Mechanical characteristics of standard samples	128
6.1	Tetrahedral entities with computational time and yield strength for convergence	133
6.2	Material properties for crushable foam plasticity model used in FE modelling [19]	137
6.3	Deviations in the architectural parameters of CAD-based (actual) polymeric bone scaffolds and additively manufactured polymeric bone scaffolds	144

# Abbreviations

<b>AM</b>	Additive manufacturing
<b>ALP</b>	Alkaline phosphate
<b>BTE</b>	Bone tissue engineering
<b>BMPs</b>	Bone morphogenetic proteins
<b>BGs</b>	Bio-glasses
<b>BG</b>	Bioactive glasses
<b>B-Rep</b>	Boundary representation
<b>CAGR</b>	Compound annual growth rate
<b>CAD</b>	Computer-aided design
<b>CPCs</b>	Calcium phosphate ceramics
<b>CSG</b>	Constructive solid geometry
<b>CT</b>	Computed tomography
<b>DMP1</b>	Dentin matrix protein-1
<b>D-type</b>	Diamond type
<b>ECM</b>	Extracellular matrix
<b>ESO</b>	Evolutionary structural optimization
<b>EBM</b>	Electron beam melting
<b>FDM</b>	Fused deposition modelling
<b>FEA</b>	Finite element analysis
<b>HAp</b>	Hydroxyapatite
<b>IL-1Ra</b>	Interleukin-1 receptor antagonist
<b>IPA</b>	Isopropyl alcohol
<b>LDNs</b>	Low-dimensional nanomaterials

<b>MJ</b>	Material Jetting
<b>MSCs</b>	Mesenchymal stem cells
<b>MRI</b>	Magnetic resonance imaging
<b>PLA</b>	Polylactic acid
<b>PCL</b>	Polycaprolactone
<b>PGA</b>	Polyglycolic acid
<b>PU</b>	Polyurethane
<b>P-type</b>	Primitive type
<b>PHBV</b>	Poly(hydroxybutyrate-co-valerate)
<b>PEG</b>	Poly(ethylene glycol)
<b>PEEK</b>	Polyether ether ketone
<b>PLGA</b>	Polylactic-co-glycolic acid
<b>SLA</b>	Stereolithography
<b>SLS</b>	Selective laser sintering
<b>SBF</b>	Simulated body fluids
<b>SIMP</b>	Solid isotropic material with penalization
<b>SLM</b>	Selective laser melting
<b>SEM</b>	Scanning electron microscope
<b>TPMS</b>	Triply periodic minimum surfaces
<b>TCP</b>	Tricalcium phosphate
<b>TGF-<math>\beta</math></b>	Transforming growth rate factor-beta
<b>VEGF</b>	Vascular endothelial growth factor
<b>ZFPs</b>	Zn finger proteins
<b><math>\beta</math>-TCP</b>	$\beta$ tricalcium phosphate

# Symbols

$k$	Coefficient of Permeability
$\mu$	Fluid dynamics viscosity
$e$	Porosity
$\mu_w$	Dynamic viscosity of water
$\rho_w$	Density of water
$D_r$	Density of solid/Density of fluid
$d$	Total cross-sectional area
$q$	Volumetric flow rate
$p$	Pressure

# Chapter 1

## Introduction

Bone grafting is recorded as the second most performed procedure every year after blood transfusion. It integrates the field of orthopedics and reconstructive surgery for healing and regeneration of bone tissue. The choice and effectiveness of bone scaffolds, which play a crucial role in offering temporary support and promoting the regeneration of new bone tissue, are essential to this endeavour [1]. This chapter serves as an introductory overview of the research conducted in this study, providing a comprehensive understanding of the importance of bone grafts in bone tissue engineering. It delves into the background knowledge, highlighting the need for bone grafts in addressing bone defects and discussing the challenges associated with both natural and synthetic bone scaffolds. Furthermore, it explores the merits and demerits of each scaffold type, emphasizing their respective advantages and limitations in supporting bone regeneration. The chapter also explores various manufacturing techniques employed for bone scaffold fabrication, outlining the pros and cons of each approach. Building upon this background knowledge, the chapter then states the aim and objectives of the research, focusing on addressing specific research gaps and contributing to the field of Bone Tissue Engineering (BTE). By establishing a solid foundation through background knowledge, a clear aim, well-defined objectives, and a robust methodology, this research chapter sets the stage for the subsequent chapters. These subsequent chapters will delve into detailed investigations, analysis, and discussions of the research findings.

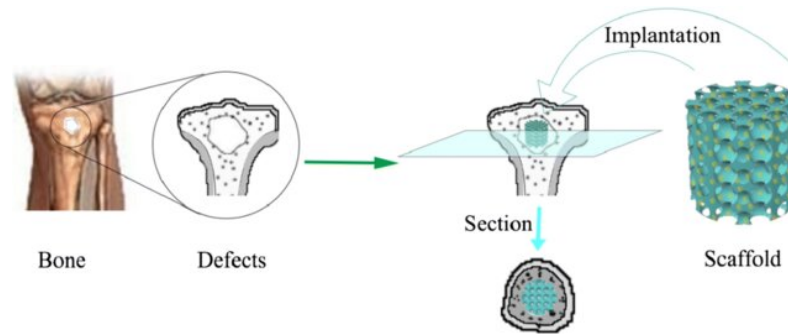


FIGURE 1.1: Bone Scaffolds [2]

## 1.1 Background

Bone has regenerative and healing capabilities through a dynamic biological process. This regenerative capacity is attributed to the presence of specialized cells called osteoblasts and osteoclasts, which work in harmony to remodel and rebuild damaged bone tissue. New bone matrix is created by osteoblasts, whereas old or damaged bone tissue is broken down and removed by osteoclasts. Additionally, the bone healing process is facilitated by the recruitment of mesenchymal stem cells, growth factors, and signaling molecules that orchestrate the regeneration of bone cells and blood vessels. These inherent regenerative properties of bone make it capable of restoring its structure, strength, and functionality over time [3]. However, large bone defects pose significant challenges for bone regeneration. The dimensions of large bone defects can vary, but they typically refer to bone loss or damage exceeding 2-3 centimeters in length and depth. The size and complexity of these defects often exceed the regenerative capacity of the body's natural healing mechanisms. These defects often require immediate mechanical stability for weight-bearing and functional restoration [4]. In such cases, external support and structural guidance are required to facilitate the regeneration process. External support in the form of implants can offer the required stability, allowing the bone to heal without excessive strain or deformity. Implants can provide a scaffold that accelerates the healing process and support functional restoration, allowing for quicker recovery and improved outcomes. The difficulties in bone healing present a notable threat to health and well-being. From \$3.78 billion in 2022 to \$5.71 billion in 2029, the global market for bone graft alternatives is expected to increase

at a compound annual growth rate (CAGR) of 6.1 percent [5]. There are several types of natural bone grafts used in clinical practice, each with its own advantages and limitations. Natural bone grafts come in two main forms: autografts and allografts. Autografts are derived from the patient's body, often from areas like the hip bone or fibula. They're highly regarded for their living cells, growth factors, and structural support crucial for effective bone regeneration. Their main advantage is their high osteogenic potential and excellent integration with the host bone. However, autografts have limitations such as limited availability, increased surgical time, additional donor site morbidity, and the possibility of complications at the donor site [6]. Allografts as an alternative to autografts, are bone grafts obtained

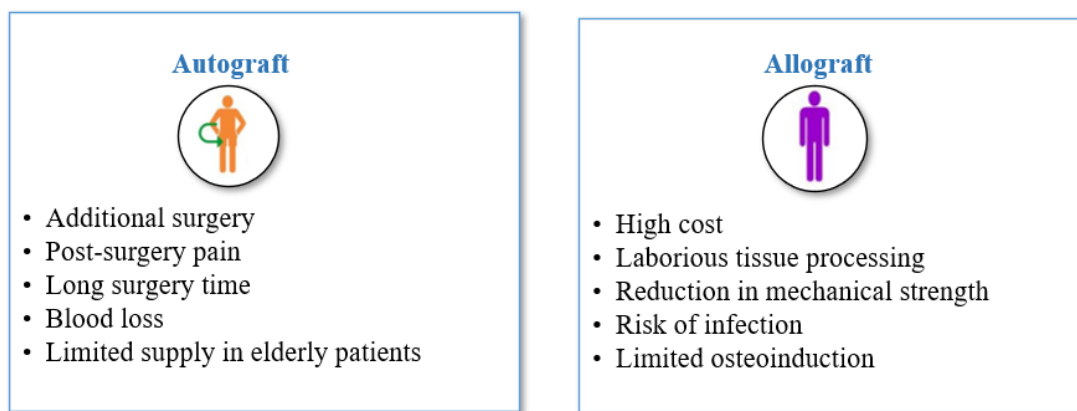


FIGURE 1.2: Natural bone grafts and their limitations

from cadaveric human donors. They are processed and sterilized to remove any potential risk of disease transmission. Allografts provide a structural scaffold and contain growth factors that promote bone regeneration. Their main advantage is their ready availability, avoiding the need for a second surgical site. Allografts have limitations, such as the risk of immune rejection, and they tend to integrate with the host bone more slowly compared to autografts. Additionally, although extensive screening and processing minimize the risk, there is also the potential for disease transmission associated with allografts [7]. Some other limitations of natural bone grafts are also mention in Figure 1.2.

Common limitations among all types of natural bone grafts include limited availability and the potential risk of disease transmission, though rigorous processing and screening help reduce this risk. Variations in graft quality and viability are also

typical issues with natural bone grafts. Additionally, it's challenging to precisely control the characteristics of these grafts. Furthermore, natural bone grafts may not provide immediate mechanical stability. Their potential for osteoinduction and osteogenesis can vary depending on factors like the patient's age, general health, and the presence of underlying medical conditions [8]. These constraints have led

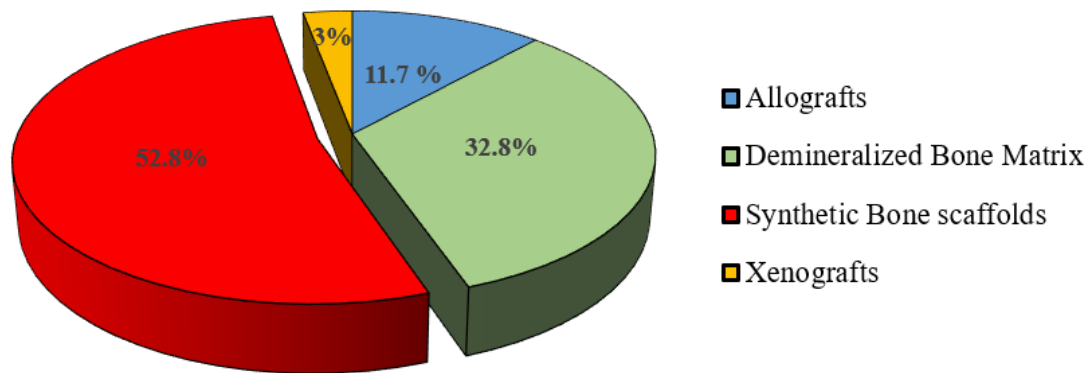


FIGURE 1.3: Global bone graft substitutes market share 2022 [5]

to considerable focus on creating synthetic bone graft substitutes and employing additively manufactured scaffolds. These alternatives provide better manipulation of graft traits, improved bioactivity, and a scalable, customizable method for bone regeneration. However, natural bone grafts remain valuable and widely used in clinical practice, particularly in cases where their unique advantages outweigh their limitations. Figure 1.3 showed the global bone graft substitute market share where synthetic bone scaffolds have major contributions worldwide [5].

Synthetic bone scaffolds, also called engineered bone scaffolds, are biomaterial structures crafted to replicate the form and role of natural bone tissue. These scaffolds are typically made from biocompatible materials that promote cell attachment, proliferation, and tissue ingrowth. Synthetic bone scaffolds offer several advantages over natural bone grafts, including the ability to be precisely engineered, controlled degradation, and the incorporation of bioactive components [9]. There are several forms of synthetic bone scaffolds, such as the composite scaffolds, polymer scaffolds, and ceramic scaffolds shown in Figure 1.4.

Ceramic scaffolds are made from biocompatible materials, typically calcium phosphate ceramics such as hydroxyapatite (HA) and tricalcium phosphate (TCP).

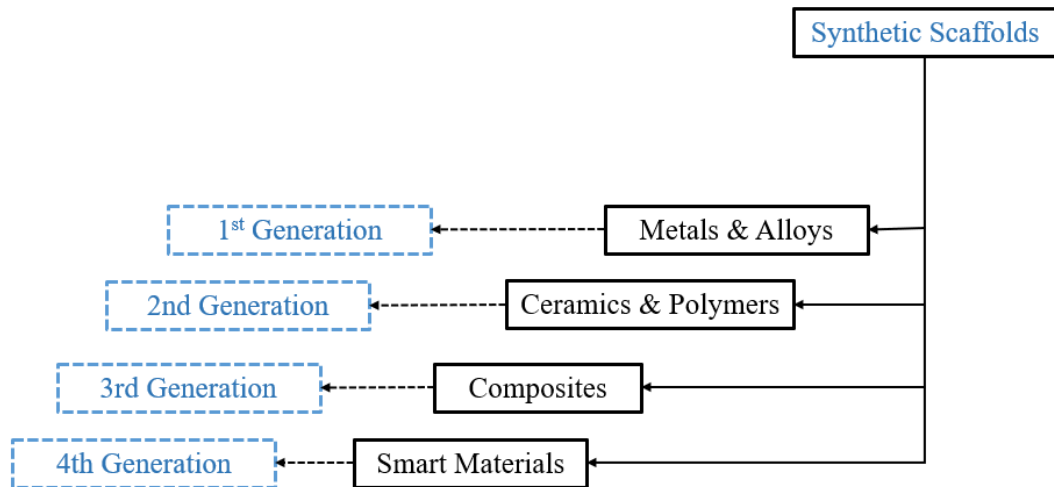


FIGURE 1.4: Generation of materials used to develop the synthetic scaffolds

These materials closely resemble the mineral component of natural bone, providing excellent biocompatibility and osteoconductivity. Ceramic scaffolds offer structural support and serve as a scaffold for new bone formation. They can be manufactured with precise pore sizes, pore interconnectivity, and surface characteristics, allowing for cell infiltration and promoting tissue integration. Ceramic scaffolds possess durable mechanical traits and can be customized to align with the mechanical needs of bone tissue. However, their brittleness and slower degradation rate compared to natural bone are some limitations to consider [10]. Polymer scaffolds are fabricated from biodegradable polymers such as polylactic acid (PLA), polyglycolic acid (PGA), or their copolymers polylactic-co-glycolic acid (PLGA). These scaffolds have a high level of mechanical property, disintegration rate, and porosity tunability. Polymer scaffolds offer a porous structure that facilitates cell infiltration, nutrient diffusion, and extracellular matrix deposition. The degradation products of polymers are generally biocompatible and can be safely metabolized by the body. However, their relatively low stiffness compared to natural bone can be a limitation for load-bearing applications. Surface modifications or incorporation of reinforcing materials can help address this limitation [11]. Composite scaffolds combine different biomaterial components to leverage their advantages. For example, a composite scaffold may consist of a ceramic phase for structural support and a polymer phase for enhanced mechanical properties or controlled drug release. The combination of materials allows for synergistic

effects and tailoring of properties to meet specific requirements. Composite scaffolds can offer improved mechanical strength, stability, and bioactivity compared to individual materials alone. Different combinations of ceramics, polymers, metals, and bio-glasses have been studied to create composite scaffolds with improved properties for applications in bone tissue engineering. Each type of synthetic scaffold offers distinct advantages and limitations, and the selection depends on the specific requirements of the bone defect or implant application. Researchers are actively exploring and optimizing synthetic scaffolds through material innovation and scaffold design optimization. They are also incorporating bioactive cues to further enhance their regenerative potential and clinical efficacy in bone tissue engineering [12]. Classification of synthetic bone scaffolds based on the porosity type, unit cell arrangement and lattice structure is also presented in the Figure 1.5. Synthetic scaffolds can be open pores (bubble in a block) and closed pores (like trabecular). On the basis of unit cell arrangement, they can be stochastic (irregular arrangement of unit cell and non-stochastic (regular arrangement of unit cell) [13].

The manufacturing technique employed to fabricate synthetic bone scaffolds plays a critical role in determining their structural properties, porosity, bioactivity, and overall performance in bone tissue engineering. Numerous techniques, including salt leaching, solvent casting, electrospinning, as well as methods such as 3D printing, have been utilized for the production of these scaffolds [14]. Salt leaching involves mixing a biocompatible polymer with salt particles that act as sacrificial templates. After shaping the polymer-salt mixture into the desired scaffold geometry, the salt particles are leached out using a solvent, leaving behind a porous scaffold structure. The advantages of salt leaching include its simplicity, cost-effectiveness, and ability to generate interconnected porous structures that mimic natural bone. However, limitations include limited control over pore size, difficulty in achieving uniform porosity, and potential for residual salt within the scaffold, which can affect cell behavior and scaffold degradation [15]. Solvent casting entails dissolving a biocompatible polymer in a solvent, pouring it into a mold, and subsequently evaporating the solvent to produce the scaffold. Particulate leaching is

similar, but involves the addition of salt particles that are later removed to create porosity. This technique allows for control over scaffold geometry and porosity. Advantages include simplicity, cost-effectiveness, and the ability to incorporate bioactive agents. However, limitations include the potential for residual solvent, lack of control over pore interconnectivity, and difficulty in achieving high porosity [16]. Electrospinning utilizes an electric field to create ultrafine polymer fibers

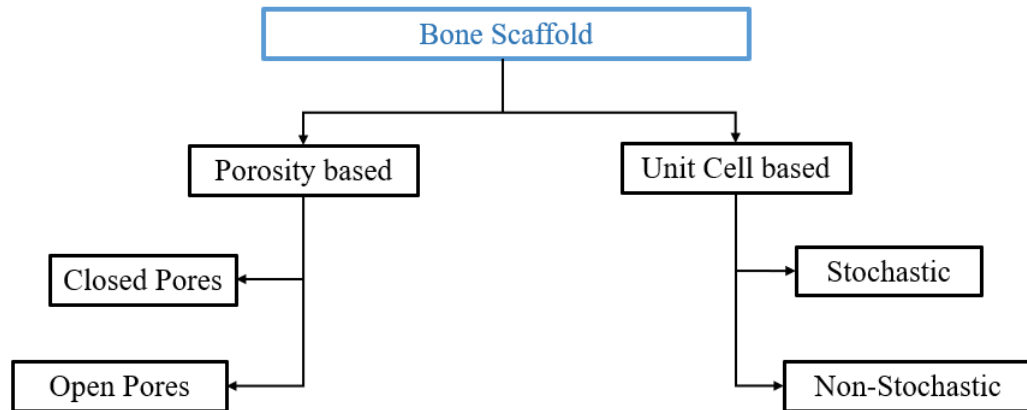


FIGURE 1.5: Classification of Bone Scaffolds

that form a non-woven mesh structure. The resulting scaffold exhibits a substantial surface-to-volume ratio and can replicate the fibrous composition of the extracellular matrix. Advantages of electrospinning include the ability to generate scaffolds with high porosity, tunable fiber diameter, and controlled alignment. Electrospun scaffolds also exhibit good mechanical properties and the potential for controlled drug release [17]. However, challenges include difficulties in achieving large-scale production, limitations in fabricating complex three-dimensional structures, and potential fiber alignment issues. Additive manufacturing also known as 3D printing, is a flexible method enabling meticulous regulation of scaffold design, pore structure, and integration of various materials. This approach entails step-by-step application of biomaterials to construct a three-dimensional scaffold according to computer-aided design (CAD) models. Benefits encompass the capability to craft patient-specific scaffolds, intricate geometries, and internal arrangements with a remarkable degree of precision. 3D-printed scaffolds can also incorporate bioactive agents and multiple materials. However, limitations include cost, material availability, defects, and mechanical properties [18].

## 1.2 Limitations of Conventional Technologies

- i. **Limited control over the scaffold structure:** Conventional manufacturing techniques often result in scaffolds with a random or irregular structure, which can lead to poor mechanical properties and uneven distribution of nutrients and growth factors.
- ii. **Inability to mimic the complexity of natural bone tissue:** Conventional methods frequently encounter limitations in reproducing the intricate structure and composition of natural bone tissue. This limitation can lead to scaffolds that exhibit inadequate biological activity and limited compatibility with the host tissue.
- iii. **Poor reproducibility:** Conventional manufacturing techniques often rely on manual labor and are therefore subject to human error, resulting in inconsistencies in the final product. This can lead to issues with reproducibility and quality control.
- iv. **Limited scalability:** Conventional techniques can be time-consuming and labor-intensive, making it difficult to scale up production to meet the growing demand for bone scaffolds.
- v. **High cost:** Conventional techniques often require expensive equipment and materials, resulting in high production costs that can make bone scaffolds prohibitively expensive for many patients.

In conclusion, the inherent limitations in conventional bone scaffold manufacturing significantly impede progress in achieving optimal mechanical strength and efficient nutrient transport for bone tissue engineering. The challenges arising from limited control over scaffold structure contribute to compromised mechanical properties, fostering irregularities that can impede the scaffold's ability to provide the necessary structural support. Simultaneously, the inability to faithfully mimic the intricate architecture of natural bone tissue hampers nutrient transport within the scaffold, by hindering the delivery of essential elements crucial for cell proliferation and tissue regeneration.

### 1.3 Limitations of 3D Printing Technologies

Emerging techniques, such as 3D printing, offer potential solutions to some of the issues associated with conventional technique discussed previously. Additive manufacturing methods hold significant potential in generating bone scaffolds. However, there are still some challenges and limitations that need to be addressed such as;

- i. **Material limitations:** Not all materials can be effectively used in 3D printing. The available range of printable materials is still limited compared to the wide variety of materials found in nature. Additionally, certain materials may have specific requirements or limitations during the printing process, which can restrict their use in certain applications. The mechanical, chemical, and biological properties of 3D-printed materials may not fully match those of the natural tissues they aim to replicate. This can affect the functionality, integration, and long-term performance of the printed structures. Finding or developing suitable materials that closely resemble the properties of the target tissues remains an ongoing challenge. Ensuring the biocompatibility and bioactivity of 3D-printed materials is crucial for their successful application in medical fields. Some materials used in 3D printing may not exhibit optimal biocompatibility or bioactivity, potentially leading to adverse reactions, inflammation, or poor tissue integration.
- ii. **Architectural limitations:** Attaining accurate management of pore size and porosity in 3D-printed constructs can pose difficulties. The printing resolution and the size of the printing nozzle can limit the achievable range of pore sizes. This limitation can be problematic when it comes to mimicking the intricate and hierarchical nature of bone, which have specific pore sizes and porosity crucial for their function.
- iii. **Manufacturability limitations:** One of the key limitations of 3D printers in terms of manufacturability is dimensional accuracy. Dimensional accuracy for Fused Deposition Modeling (FDM), Micro Stereolithography ( $\mu$ SLA), and

Selective Laser Sintering (SLS) is 0.16 percent, 0.15 percent, and 0.11 percent, with lower limits of  $\pm 0.2$  mm,  $\pm 0.01$  mm, and  $\pm 0.3$  mm respectively [19]. With a lower limit of  $\pm 0.05$  mm and a dimensional accuracy of 0.5 percent, Micro Jetting (MJ) stands out as the approach with the highest level of precision. Moreover, achieving precise dimensional accuracy can be challenging due to various factors involved in the 3D printing process. These factors include thermal expansion and shrinkage of the material, inaccuracies in the positioning and movement of the print head or build platform, and the inherent limitations of the printing technology itself. As a result, there can be slight variations or deviations from the intended dimensions of the printed object. This limitation can impact the fit, function, and overall quality of the printed parts, particularly in applications that require tight tolerances or precise assemblies. Ongoing research aims to improve 3D printing's dimensional accuracy through advancements in techniques, control systems, and materials, expanding its application possibilities. The additively manufactured scaffolds had a maximum acceptable dimensional error of 0.54 mm, which is an acceptable dimensional error for the 3D printing of scaffolds.

## 1.4 Problem Statement

Severe bone defects compromise their inherent ability to regenerate for functional recovery, necessitating immediate external support for load-bearing and regeneration. In response to the limitations of natural bone scaffolds, such as limited availability and the potential for disease transmission and site infections, synthetic bone scaffolds are being developed. Traditional manufacturing techniques offer limited control over the structural aspects of synthetic scaffolds, leading to subpar mechanical properties and an uneven distribution of nutrients and growth factors. In contrast, additive manufacturing techniques present promising solutions to the challenges associated with conventional methods. Materials like ceramics, due to their brittleness, metals, due to ion release, and polymers, owing to their inadequate mechanical strength, hinder their suitability for load-bearing applications.

Considering these limitations, the focus of this study is to investigate the possibility of creating acrylate-based polymer bone scaffolds with improved transport and mechanical properties through the application of PolyJet printing technology while maintaining high precision.

## 1.5 Objectives

The objectives encompass crucial stages in bone scaffold development. Firstly, the focus lies on designing and developing the scaffolds, ensuring they meet the necessary specifications for biomedical applications. Following this, the feasibility of various manufacturing techniques is assessed to determine the most suitable approach in terms of quality and scalability. Subsequently, fluid transport analysis is conducted to understand how fluids interact within the scaffold structure, influencing nutrient distribution and waste removal crucial for tissue regeneration. Meanwhile, finite element analysis evaluates mechanical behavior to optimize scaffold design for withstanding physiological loads and promoting tissue integration.

**Objective 1** - To review the challenges in bone scaffolding in term of architectural design, mechanical response and manufacturing technique.

**Objective 2** - To design and develop polymeric bone scaffolds using CAD software and 3D printing techniques.

**Objective 3** – To investigate the manufacturability of the selected 3D printed techniques.

**Objective 4** - To measure the fluid transport properties of the polymeric bone scaffolds.

**Objective 5** - To investigate the compressive strength of polymeric bone scaffolds through mechanical testing.

**Objective 6** - To perform Finite element analysis for investigating the deformation patterns of polymeric bone scaffolds under quasi-static compression.

## 1.6 Methodology

The methodology section of this study elucidates the systematic approach and research techniques employed to investigate and analyze the objectives of the study in order to derive meaningful and rigorous conclusions. Four stages of adopted methodology is presented in the Figure 1.6.

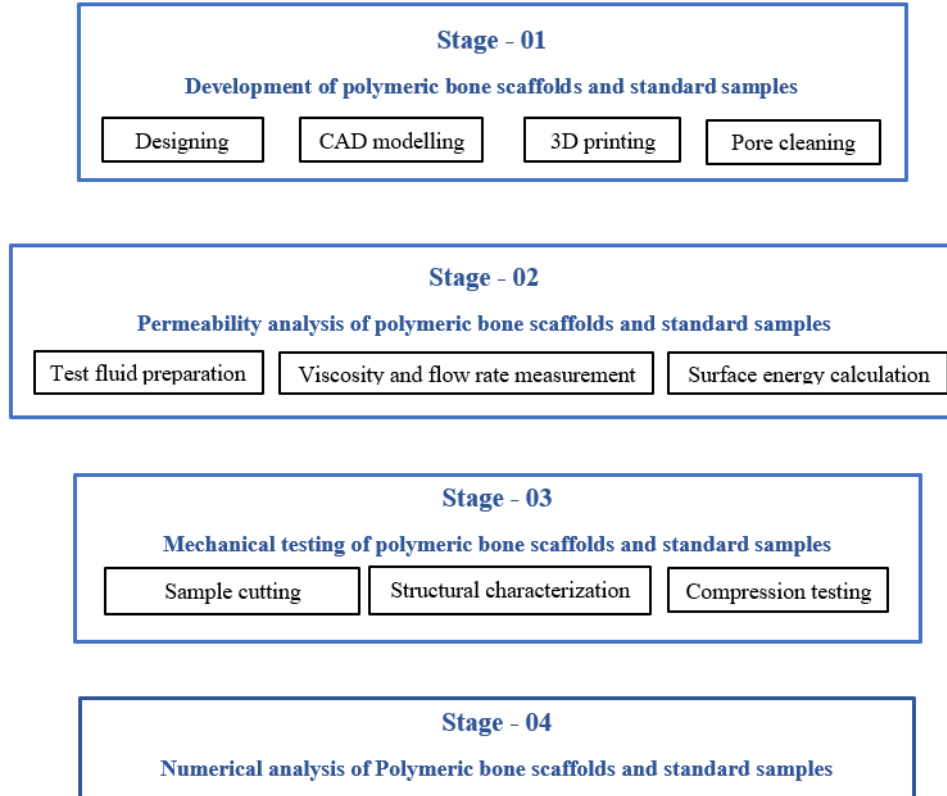


FIGURE 1.6: Stages of adopted methodology

It is comprising of four key stages. In the first stage, the design and development of 3D printed bone scaffolds were undertaken. The second stage involved the experimentation of 3D printed bone scaffolds, exploring their physical characteristics. Moving on to the third stage, the bone scaffolds underwent mechanical testing to assess their structural integrity. In the fourth and final stage, a numerical analysis of the deformation pattern of the bone scaffold was conducted. These stages were meticulously executed to contribute to a comprehensive understanding of the dynamic interplay between design, experimentation, mechanics, and numerical intricacies within the realm of 3D printed bone scaffolds.

## 1.7 Thesis Layout

The subsequent section outlines the structure and organization of this study, presenting a comprehensive overview of the chapters and their respective contributions in addressing the research problem and achieving the stated objectives. It consists of total seven chapters and organized according to the layout shown in Figure 1.7.

**Chapter 1** - In the introduction chapter of the thesis titled "Experimental and Numerical Analysis of Bone Scaffolds," the groundwork is laid for a comprehensive investigation into bone scaffold development and evaluation. This chapter commences with a broad introduction to the research topic, elucidating the central objectives, research methodology, and providing an outline of the thesis structure. Subsequently, the background section explores the pivotal role of bone scaffolds in orthopedic applications, emphasizing the importance of scaffold materials and mechanical properties. The discussion then shifts to the limitations of conventional bone scaffold fabrication technologies, highlighting deficiencies in design flexibility and mechanical properties customization. It further addresses the constraints of 3D printing technologies, particularly in terms of material selection and process optimization. The problem statement identifies the research gap concerning scaffold properties and mechanical behavior, setting the stage for the study's objectives, which aim to bridge this gap by integrating experimental and numerical analyses. The methodology section outlines the research methods, data collection, and analysis techniques, while the thesis layout provides a roadmap for readers to navigate the subsequent chapters. This introductory chapter thus establishes the context, motivations, and framework for the comprehensive exploration that follows in the thesis.

**Chapter 2** - This chapter offers a comprehensive exploration of the crucial role played by bone scaffolds in the domain of bone tissue engineering. It begins with an introduction that sets the stage for the ensuing discussion by framing the significance of bone scaffolds in orthopedic applications. Subsequently, the chapter includes an in-depth analysis of materials commonly employed in bone scaffold

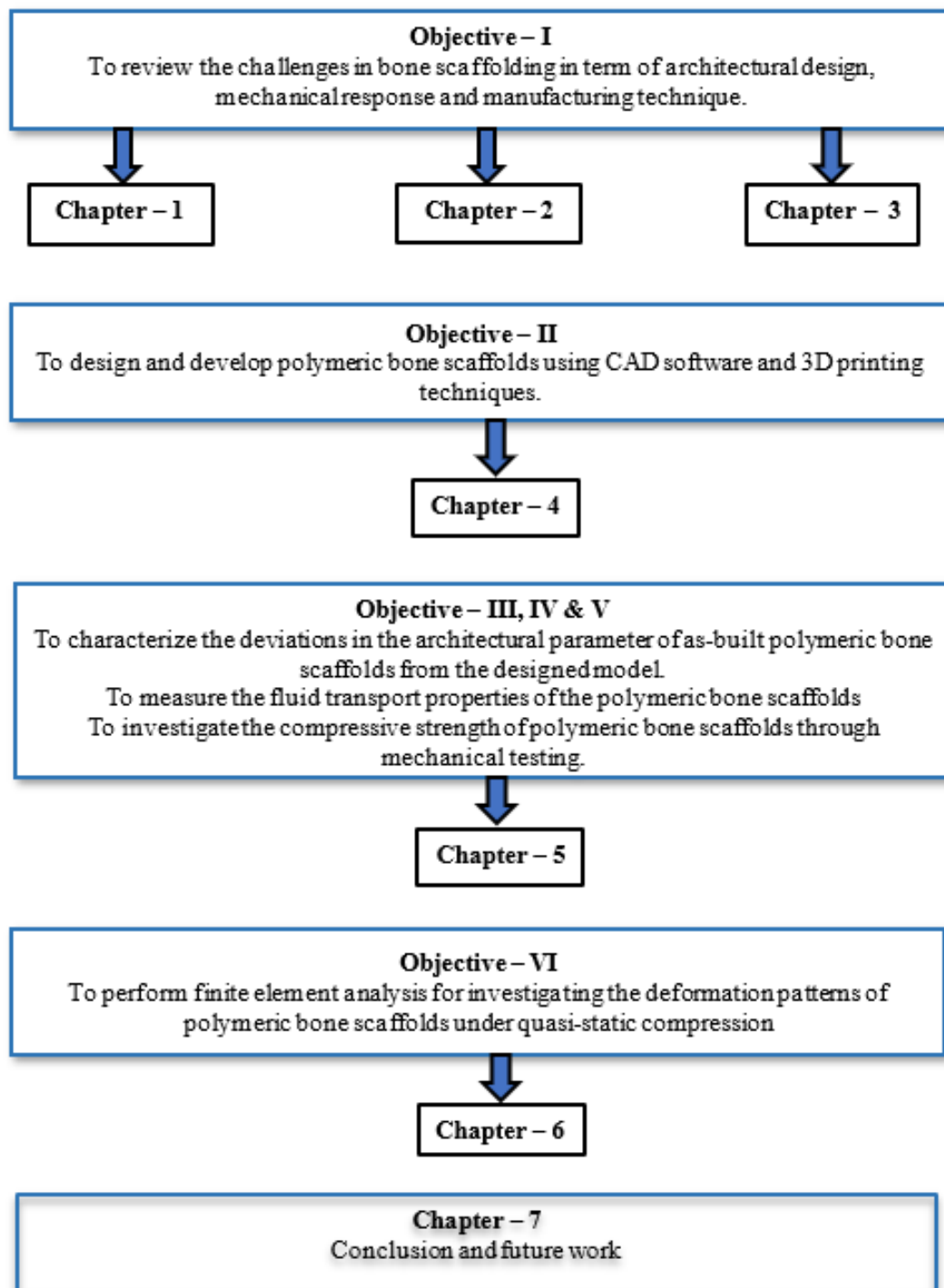


FIGURE 1.7: Thesis Layout

fabrication, elucidating their properties and suitability for the task. The synthetic bone scaffold challenges section discusses designing and making effective synthetic scaffolds. It talks about limitations and advantages of polymer-based bone scaffolds too. It sheds light on their benefits and drawbacks in bone tissue engineering. As a concluding note, the chapter provides a summary that synthesizes the key

insights and prepares the reader for the subsequent chapters, offering a solid foundation for understanding the complexities and potential of bone scaffolds in the field of Bone Tissue Engineering.

**Chapter 3** - This chapter serves as a comprehensive exploration of the methodologies employed in the fabrication of bone scaffolds. The introduction lays the foundation by providing context for the subsequent discussions, highlighting the critical importance of scaffold manufacturing techniques in the field of bone tissue engineering. The chapter then delves into an examination of conventional techniques used for scaffold production, elucidating their historical significance and limitations. It subsequently explores additive manufacturing techniques, such as 3D printing, as innovative approaches to scaffold fabrication, showcasing their advantages and capabilities. Moreover, the chapter addresses the various design techniques employed specifically for bone scaffolds, offering insights into the intricate design considerations necessary to achieve optimal functionality. As a concluding note, the chapter provides a summary that synthesizes key findings and insights, offering a comprehensive overview of the diverse methodologies used in the manufacturing of bone scaffolds, which play a pivotal role in advancing the field of Bone Tissue Engineering.

**Chapter 4** - This chapter includes an intricate exploration of the various stages and facets involved in the fabrication and assessment of bone scaffolds. The introduction provides a contextual framework for the ensuing discussions, emphasizing the paramount importance of scaffold design and experimentation in the realm of bone tissue engineering. Subsequently, the chapter delves into the design and development of bone scaffolds using advanced techniques such as PolyJet and micro-stereolithography, elucidating the specific methodologies and considerations unique to each approach. It further details the experimentation process for 3D-printed bone scaffolds, offering insights into the intricacies of data collection and analysis. The chapter also encompasses a thorough investigation of permeability analysis for bone scaffolds, shedding light on the fluid flow characteristics within these structures. Additionally, it covers the design and development of standard samples and the mechanical testing of bone scaffolds, providing a comprehensive

understanding of the structural and mechanical properties critical for scaffold performance evaluation. In essence, this chapter serves as a holistic journey through the design, development, and experimental phases of bone scaffold research, illuminating the complexities and advancements in the field of Bone Tissue Engineering.

**Chapter 5** - This chapter presents a comprehensive examination of experimental findings pertaining to bone scaffold properties and performance. The introduction provides a context for the ensuing discussions by framing the importance of these experiments in understanding bone scaffold behavior. The chapter goes on to explore various aspects, including the impact of contact angle and surface energy on bone scaffolds, elucidating how these factors influence scaffold performance. It further delves into experimental measurements of permeability for both PolyJet and micro-stereolithography printed bone scaffolds, shedding light on the fluid flow characteristics within these structures. Numerical calculations of permeability are presented, providing valuable insights into the predictive capabilities of computational models in this context. The discussion also touches upon the relationship between surface area and permeability, revealing the role of geometry in scaffold behavior. Moreover, the chapter explores the mechanical properties of bone scaffolds, examining how different printing directions can affect their structural integrity. Overall, this chapter offers a detailed overview of the experimental results that contribute significantly in understanding of bone scaffold performance and properties in the context of Bone Tissue Engineering.

**Chapter 6** - This chapter presents a comprehensive exploration of the numerical aspects in understanding bone scaffold behavior. The introduction sets the stage by providing context for the ensuing discussions, emphasizing the significance of numerical simulations in elucidating the mechanical response of bone scaffolds. The chapter then delves into the material and methods employed in conducting these simulations, detailing the computational techniques and parameters crucial for accurate numerical investigations. It explores the fabrication of bone scaffolds through numerical models, offering insights into the virtual creation and analysis of scaffold structures. The chapter further investigates different levels of compression within bone scaffolds, simulating the mechanical loads they may

experience in practical applications. It examines the experimental validation of finite element (FE) results, highlighting the convergence of numerical predictions with real-world experimental data. Lastly, the chapter delves into the deformation behaviors exhibited by bone scaffolds under varying conditions, shedding light on how numerical simulations contribute in understanding of their mechanical responses. In summary, this chapter serves as a pivotal exploration of the numerical dimension in bone scaffold analysis, unveiling the intricacies and insights offered by computational models in the field of bone tissue engineering.

**Chapter 7** - The chapter titled "Numerical Investigation of Bone Scaffolds" within the thesis "Experimental and Numerical Analysis of Bone Scaffolds" draws to a close with a concluding segment that synthesizes the key findings and insights garnered from the numerical exploration of bone scaffolds. In this concluding section, the chapter encapsulates the cumulative results and implications of the numerical investigations, shedding light on their significance in advancing the understanding of bone scaffold behavior. Additionally, the chapter extends into the territory of future recommendations, offering valuable insights and directions for further research endeavors. It outlines potential avenues for enhancing numerical simulations, refining models, and expanding the scope of analysis in pursuit of more comprehensive and precise assessments of bone scaffold performance. This concluding chapter, therefore, serves as a crucial reflection on the numerical dimension of bone scaffold analysis, paving the way for future research and innovations in the field of Bone Tissue Engineering.

# Chapter 2

## Overview of Bone Scaffolds

### 2.1 Introduction

Over the past decade, the realm of Bone Tissue Engineering (BTE) has gained increasing attention, witnessing notable advancements in materials, manufacturing techniques, and bone healing pathways. These strides have paved the way for promising avenues in research. However, creating synthetic bone scaffolds for BTE that can both withstand mechanical loads and effectively engage with the nearby extracellular matrix to promote the initiation of bone regeneration presents challenges. This chapter delves into the utilization and manipulation of diverse materials and hierarchical architectures, aimed at emulating the intricate arrangement of natural bone tissue. The aim is to produce a synthetic bone scaffold that matches the load-bearing capacity and fluid transport attributes of native tissue.

The chapter begins by discussing the physiological aspects of bone healing and the interplay during different recovery phases. It then examines previous research on biomaterials in Bone Tissue Engineering (BTE) scaffolds. The chapter also investigates multi-material integration strategies and highlights the importance of studying scaffold structure's impact on bone healing. A detailed analysis of the pivotal role of hierarchical architecture within the scaffold is emphasized. Lastly, the review outlines emerging trends in BTE scaffold development. These trends

hold the promise of inspiring novel approaches in tissue engineering and setting the stage for the next generation of synthetic scaffold advancements.

## 2.2 The Role of Scaffolds in Bone Tissue Engineering

### 2.2.1 Overview of Bone Tissue Structure

The musculoskeletal system's skeleton is made up mostly of bone, an evolving material that is constantly changing. Besides providing structural support, it serves as a reservoir for calcium and houses the bone marrow. The intricate hierarchical arrangement spans scales from nanometers to micrometers, as depicted in Figure 2.1.

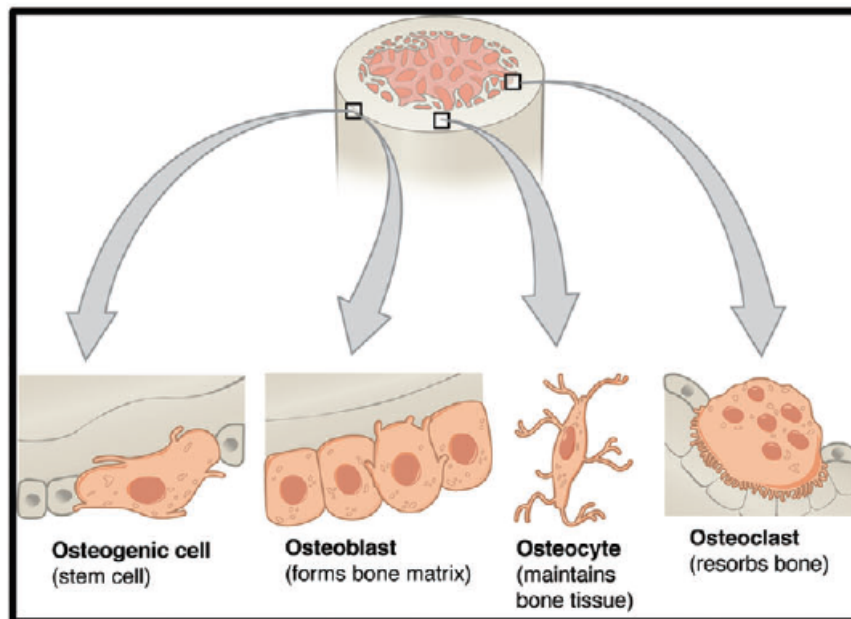


FIGURE 2.1: The four cell types comprising bone tissue are osteoblasts, osteoclasts, osteocytes, and osteogenic cells (John Wiley and Sons, copyright 2023) [20]

The extracellular matrix (ECM) of these bone tissues contains various specialized cell types that enable continuous repair and remodeling. Osteoblasts, osteoclasts, bone lining cells, and osteocytes—each present at the site of injury—fulfill unique

functions in instigating and maintaining the process of bone healing. Osteoblasts, responsible for bone tissue formation, actively synthesize crucial components of the bone extracellular matrix (ECM). These components include glycoproteins with attached glycosaminoglycan chains. Additionally, proteins distinct from type I collagen within extracellular matrices play a significant role in cell adhesion and interaction. They also release matrix vesicles into the ECM, fostering an environment conducive to the initiation of calcium phosphate nucleation [21]. The mineralization process of these vesicles begins with the emergence of crystalline calcium phosphates within them, overseen by transporter membranes and enzymes [22]. Osteoclasts, originating from monocytes and existing as multi-nucleated cells, hold a vital function in bone resorption, activated by local stimuli [23]. This resorption process is essential for maintaining blood calcium levels [24]. Osteocytes,

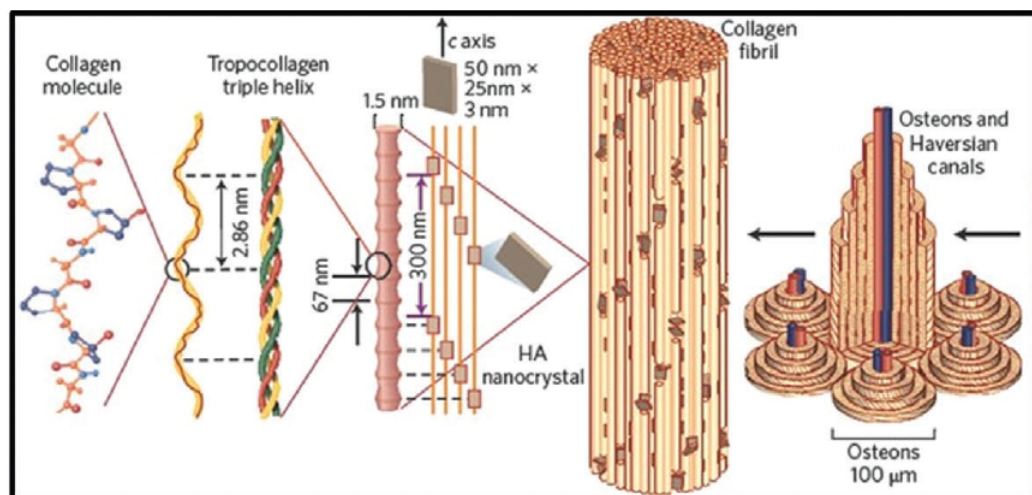


FIGURE 2.2: Bone architecture shaped by assembling collagen into microfibrils and fibrils (John Wiley and Sons, copyright 2023) [20]

enveloped by mineralized bone tissue, are strategically located osteoblast cells with interconnectedness that enables them to perceive and translate mechanical strains into physiological reactions [24]. Functioning as a safeguard against ongoing osteoclast activity, osteogenic cells (also known as bone lining cells) generate a delicate layer that envelops bone surfaces. Nevertheless, given suitable stimuli, these cells can transition into osteoblasts [24]. These osteogenic cell varieties, varying based on location, typically have sizes in the range of a few microns, constituting fundamental units for the establishment and upkeep of bone tissue. The well-being

and recuperation of bone tissue hinge on a variety of cell types, encompassing osteoblasts, osteoclasts, bone lining cells, and osteocytes. For these cells to survive, it is essential to provide them with enough oxygen and nutrition. Oxygen diffusion within tissues is generally limited to about 100–200  $\mu\text{m}$ , indicating that tissues located beyond 200  $\mu\text{m}$  from an oxygen source might face reduced oxygen availability. [25]. Capillaries within the circulatory system play a crucial role in distributing oxygen and nutrients to bone tissues.

As a result of the inflammatory wound healing response, cells at the injured location commonly experience a condition of hypoxia after an injury. In response, vascular endothelial growth factor (VEGF) is released [26]. Vasculogenesis, often known as the conversion of angioblasts into primitive blood vessels, is started by VEGF. Prior to angiogenesis, this vasculogenesis stage is essential. Then, via a process known as angiogenesis, endothelial cells in the tissue join the spaces between these first blood vessels to become capillary buds and sprouts [26]. The structural elements of bone tissues can be categorised into numerous categories based on their relative sizes, such as osteons, lamellae, collagen fibres, and collagen fibrils [27]. Collagen fibrils are made up of plate-like crystals of hydroxyapatite (HAp), as well as other impurities including  $HPO_4$ , Na, Mg, and K, and sub-nanometer-sized type I collagen molecules [28]. These collagen fibrils are capable of forming collagen fibres with sizes ranging from 3 to 7  $\mu\text{SLA}$  by self-organizing into bundles and aligning in certain orientations [29]. The concentric alignment of these fibers results in the formation of osteons, commonly ranging in size from 10 to 500  $\mu\text{SLA}$  [29, 30]. When these collagen fibers are arranged in concentric fashion around Haversian canals, they give rise to Haversian systems, characterized by a thickness of 150–300  $\mu\text{SLA}$ , as illustrated in the Figure 2.2. In the field of BTE, synthetic scaffolds function as a structure that directs tissue development and stimulates the regeneration of bone tissue by interacting with the extracellular matrix (ECM). A key goal of these scaffolds is to emulate the particular surroundings of the regenerating tissue. To ensure the functional effectiveness of the synthetic scaffold, it is crucial to promote angiogenesis within the scaffold. Angiogenesis facilitates the transfer of essential nutrients, waste products, and biomolecules [31]. The progress

of osteogenesis is enhanced through the successful vascularization of the synthetic scaffold, occurring concurrently with the previously mentioned steps. Vital physical attributes of the scaffold, including pore size, porosity, pore structure, and interconnectivity, are pivotal in mimicking the precise microenvironments of the nearby tissue. Recent advancements in BTE scaffold design are significant as they enhance in vivo interactions with surrounding tissue. To fulfil the chemical and physical requirements of a good BTE structure, a variety of materials may be used.

## 2.2.2 Mechanisms of Bone Regeneration

The body's intricate mechanisms for regeneration in response to damage play a vital role in the intricate process of bone repair. The processes leading to bone formation can be divided into distinct phases: an initial inflammatory stage, followed by a reparative phase, and finally, a remodeling stage, as illustrated in the accompanying visual representation in Figure 2.3 [32]. Osteoblasts and osteo-

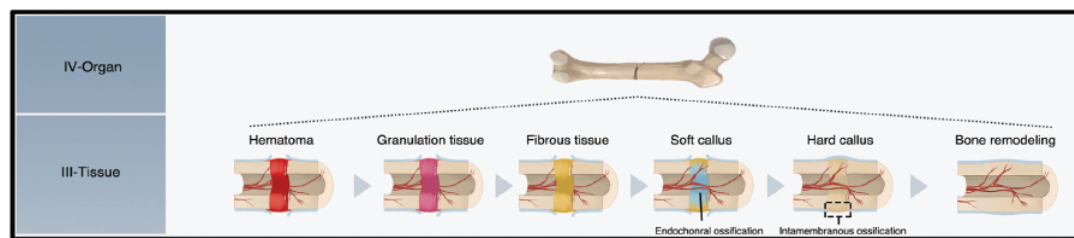


FIGURE 2.3: Bone healing: inflammation, repair, remodeling; stages - hematoma, granular tissue, fibrous tissue, soft hard callus. (John Wiley and Sons, copyright 2023) [20]

clasts are assumed to play crucial roles in instigating and concluding the bone healing process in reaction to the injury. Following the trauma, an immediate inflammatory response is set in motion. This response contributes to the attraction of inflammatory cells and pivotal proinflammatory cytokines that include interleukin-1 (IL-1), interleukin-6 (IL-6), tumor necrosis factor-alpha (TNF- $\alpha$ ), Chemokine ligand 2 (CCL2), among others. These signaling molecules are indispensable for facilitating effective intercellular communication, a critical step that marks the commencement of the bone healing process [31, 33]. Past research has shown the notable engagement of macrophages (both M1 and M2 phenotypes)

during this stage of bone healing. These macrophages are essential for mobilising inflammatory cells and enhancing osteopontin and osteocalcin levels in mesenchymal stem cells (MSCs) [34]. Subsequently, the MSCs undergo differentiation into osteoblasts, with osteocytes contributing to the substitution of impaired tissue, as illustrated in the provided Figure 2.4.

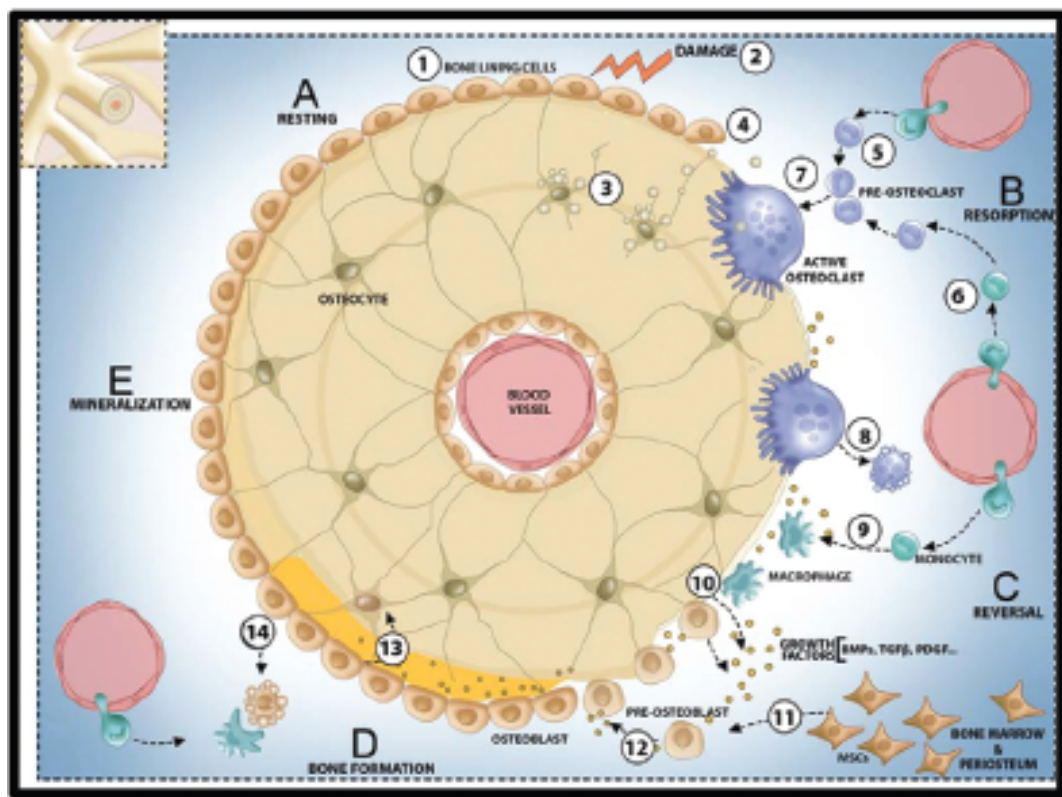


FIGURE 2.4: Bone maturation: apoptosis, osteoclast mineralization, MSC to osteoblasts with growth factors, matrix shift to osteocytes, surface osteoblasts to bone lining cells. (John Wiley and Sons, copyright 2023) [20]

M1 macrophages, representing the pro-inflammatory phenotype, remain at the site of damage for about four days before undergoing a significant transition to the anti-inflammatory M2 morphologies. This transition aids in diminishing inflammation at the site of injury [35]. As illustrated in the preceding Figure 2.4(B), osteoclasts at the fracture site are crucial in absorbing bone fragments and successfully conserving the total amount of bone mass. The precise mechanisms governing the interactions between macrophages and osteoclasts remain undisclosed. Consequently, the question of whether macrophages exert direct or indirect control over this critical phase of bone resorption remains unresolved.

The inflammation at the wounded region starts to decrease, signalling an increased presence of M2 phenotype macrophages, and the repair or regeneration phase occurs. As shown in the accompanying Figure 2.5, These M2 macrophages trigger the bone healing response by inducing the production of development factors such IL-10, TGF- $\beta$ , and interleukin-1 receptor antagonist (IL-1Ra), which in turn activates the response [36].

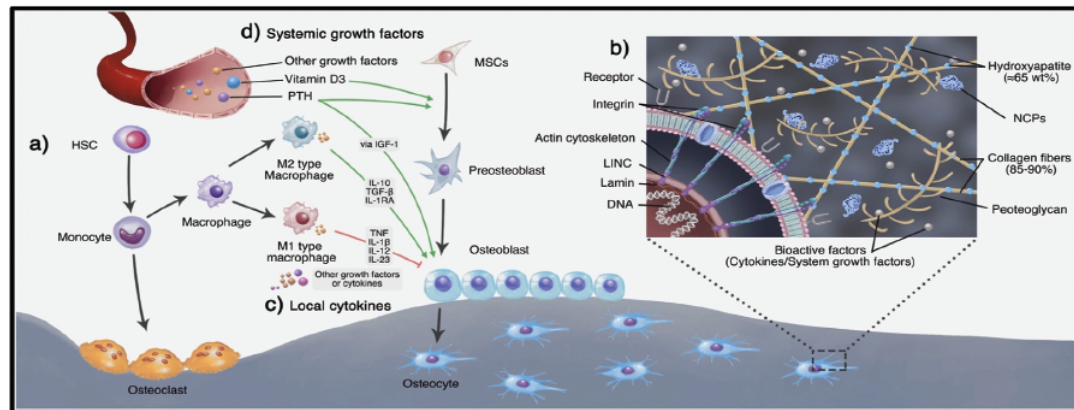


FIGURE 2.5: Growth factors and cytokines trigger monocyte-MSc interaction, differentiating MSCs for bone healing response. (John Wiley and Sons, copyright 2023) [20]

In this stage, intramembranous ossification and endochondral ossification, two processes that promote bone production, are actively being promoted by osteoblasts [37]. During endochondral ossification, collagen fibres that are secreted become a flexible, braided callus. Over time, this soft callus goes through mineralization via hypertrophic differentiation, culminating in the transformation from cartilage to bone [37].

Conversely, in intramembranous ossification, secreted collagen fibers are directly converted into a solid callus. The shattered ends must, however, osseointegrate with the scaffold that has been implanted for the healing phase to be effective. In order to avoid fracture non-unions, which can cause further fractures, proper alignment is essential. As seen in the supplied Figure 2.6, the mineralized matrix eventually completely envelops the osteoblasts and are then referred to as osteocytes [37, 38]. These osteocytes are crucial to the long-term process of remodelling or functionally adjusting bone tissue, which occurs in response to various mechanical stimuli [39]. An intricate balance between osteoblastic and osteoclastic activity

characterises the regrowth phase of bone repair. The aforementioned osteocytes serve as mechanical transmitters, translating mechanical cues from bone loading into the initiation of remodeling procedures [39]. The beginning of the bone healing process causes osteoclasts to go to particular areas, starting the bone resorption process. Usually, this stage of bone resorption lasts for two to four weeks until the osteoclasts undergo apoptosis, which ends the activity of bone resorption [37, 40]. The voids created by resorption subsequently become sites for fresh bone generation. Osteoblasts, monocytes, and pre-osteoblasts within these voids collaborate to establish a new bone matrix, following a process akin to the one outlined in the recovery stage [40, 41].

The remodeling phase is a natural occurrence linked to age and influenced by metabolic activity. Cortical and trabecular bone both have the same healing mechanism, but there are differences in each type's bone balance, which represents the balance between bone creation and bone resorption [40]. Cortical bones usually display a slightly positive bone balance, while trabecular bone exhibits a negative balance. Therefore, the gradual loss of trabecular bone brought on by ageing, metabolic processes, and mechanical factors might result in different structural results in different people. The above processes, including the inflammatory response, repair, and remodelling, depend on the extracellular matrix's (ECM) existence.

The composition of the ECM varies by tissue type. In bone tissues, it typically consists of 40% to 60% inorganic materials, including calcium-deficient apatite and other trace minerals, and 40% to 60% organic materials, such as type 1 collagen and non-collagenous proteins [42]. However, other elements including sex, gender, and health issues may also have an impact on this makeup. Osteoblast cells are the primary producers of extracellular matrix (ECM) in bone tissues prior to mineralization. To facilitate processes like bone remodeling, mesenchymal stem cell (MSC) differentiation, and the maintenance of bone mass, bone cells embedded in the extracellular matrix (ECM) utilize specific glycoproteins including osteonectin, thrombospondins, Rspndins, small integrin-binding ligand N-linked glycoproteins (SIBLINGS), and transforming growth factor-beta (TGF- $\beta$ ) [42]. Osteoblast cells

are positioned in the ECM using the collagen as a scaffolding, which leads to the development of well-organized bone structures [43]. Apart from bone formation, another vital task carried out by osteoclasts within bone tissue is bone remodeling. Changes in the rigidity of the extracellular matrix (ECM) surrounding osteoclast cells regulate dentin matrix protein-1 (DMP1) production, which in turn impacts osteoclast attachment and initiates the remodelling process [44]. Hence, osteocytes perceive mechanical stimuli via glycoproteins like DMP1, found within the extracellular matrix (ECM).

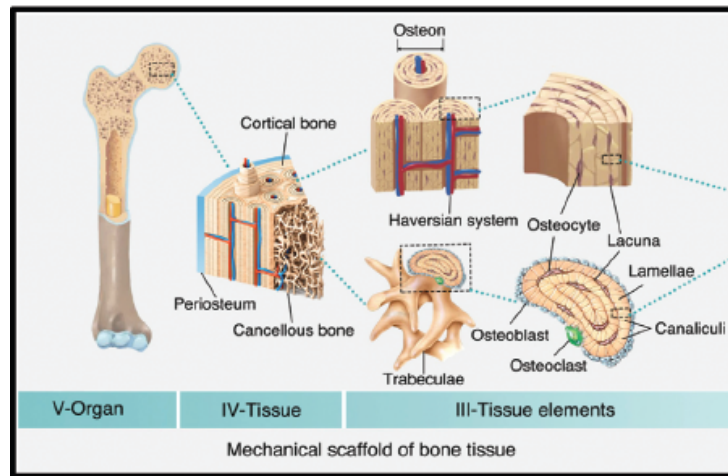


FIGURE 2.6: Arrangement of various tissue components in cancellous and cortical bone. (John Wiley and Sons, copyright 2023) [20]

## 2.3 Materials for Bone Scaffolds

Different qualities offered by metals, ceramics, and polymers are necessary for starting and maintaining bone healing processes [20]. But for bones to repair properly, materials must be able to bind to particular proteins, interact with the surrounding extracellular matrix (ECM) through ion exchange, and draw particular biomolecules or growth hormones. According to the kind of interaction, materials used to make scaffolds may be categorised into three groups: bioinert, bioactive, and biomimetic, as indicated in the provided Figure 2.7. When evaluated from the perspective of the materials, differences in their interactions can be attributed to elements including surface chemistry, roughness, solubility,

and crystallinity. Protein adsorption is often followed by interactions with the extracellular matrix (ECM), and the specific proteins that bind to the surface of the substance will decide the physiological reaction that the body starts [45]. As

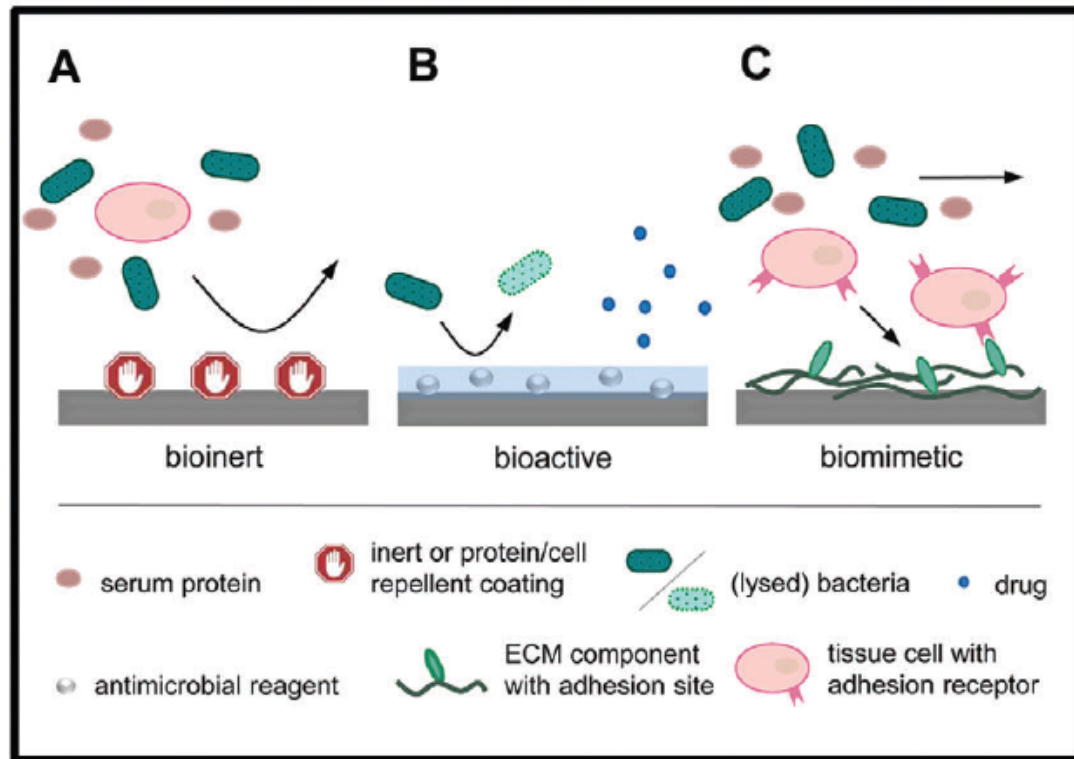


FIGURE 2.7: Bioinert repels ECM, bioactives release biomolecules for engagement, biomimetics mimic tissues, enhancing cellular communication. (John Wiley and Sons, copyright 2023) [20]

shown in the accompanying Figure 2.8, the release of growth factors like Vascular Endothelial Growth Factor (VEGF) and Bone Morphogenetic Proteins (BMPs) can be triggered by the liberation of ions from the substance. Inappropriate materials, on the other hand, may result in a foreign body reaction in which fibrin is preferentially adhered to the implant's surface. Only a few examples of the factors that may affect the selectivity in adsorption include surface charge, wettability, chemical content, and protein structure [45]. Neutrophils around the implant, as previously mentioned, attract monocytes to the fibrin-rich implant surface. These activated monocytes develop into type M1 pro-inflammatory macrophages, which release substances including TNF-alpha, IL-6, and IL-8. As seen in the given Figure 2.9, these macrophage clusters near the damage site cover the surface with fibrous tissue [46]. In this segment, we will delve deeper into the fascinating world

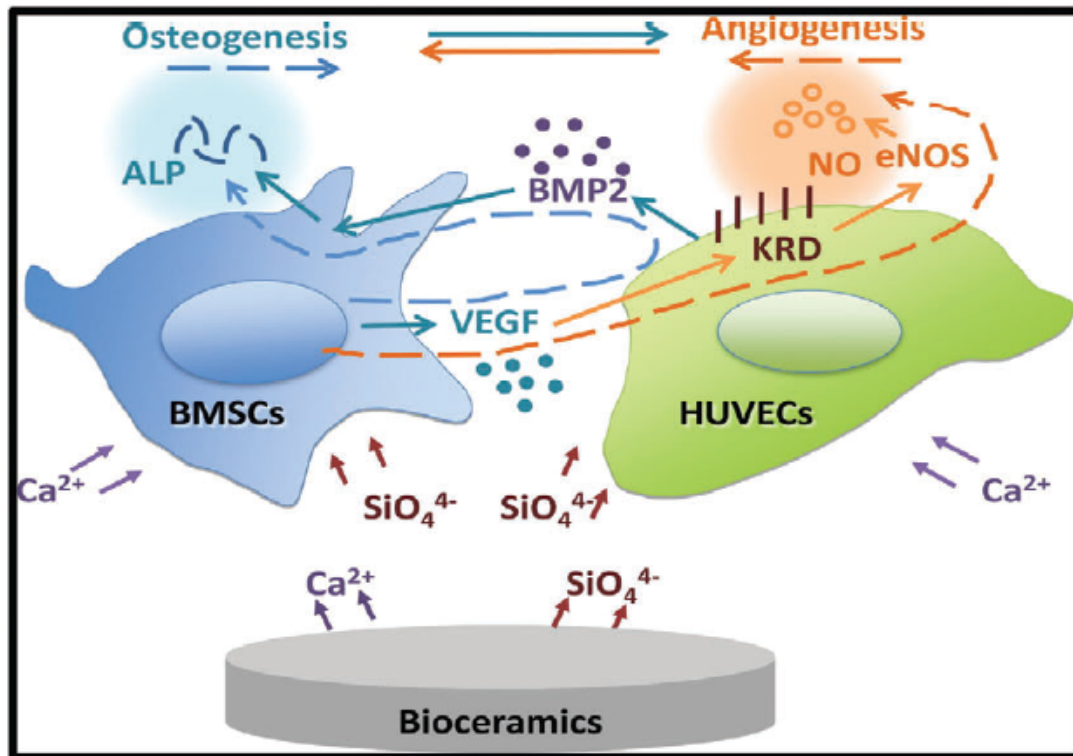


FIGURE 2.8: Bioceramic-ECM aids osteo/angiogenesis; ECM cues prompt MSCs to osteoblasts/osteocytes; osteoclasts remodel, osteoblasts enhance bone formation. (John Wiley and Sons, copyright 2023) [20]

of cellular interactions that occur when materials interface with the nearby extracellular matrix (ECM). The ECM is not merely a passive scaffold but a dynamic and intricate network that plays a pivotal role in various physiological processes, tissue regeneration, and even pathological conditions. Central to these interactions lie the cells themselves, acting as the biological artisans responsible for the construction and upkeep of the ECM. Through a sophisticated dance of molecular signals, adhesion molecules, and mechanical forces, cells engage in intricate communication with their surroundings. This dynamic interplay between cells and the ECM forms the bedrock of tissue homeostasis and repair mechanisms, orchestrating the delicate balance required for optimal physiological function and regenerative processes. This intricate dialogue not only sustains tissue integrity but also underpins the adaptability of living organisms to ever-changing environmental cues. Understanding these nuanced cellular interactions holds the key to unlocking novel strategies for therapeutic interventions and regenerative medicine, paving the way for transformative advancements in healthcare.

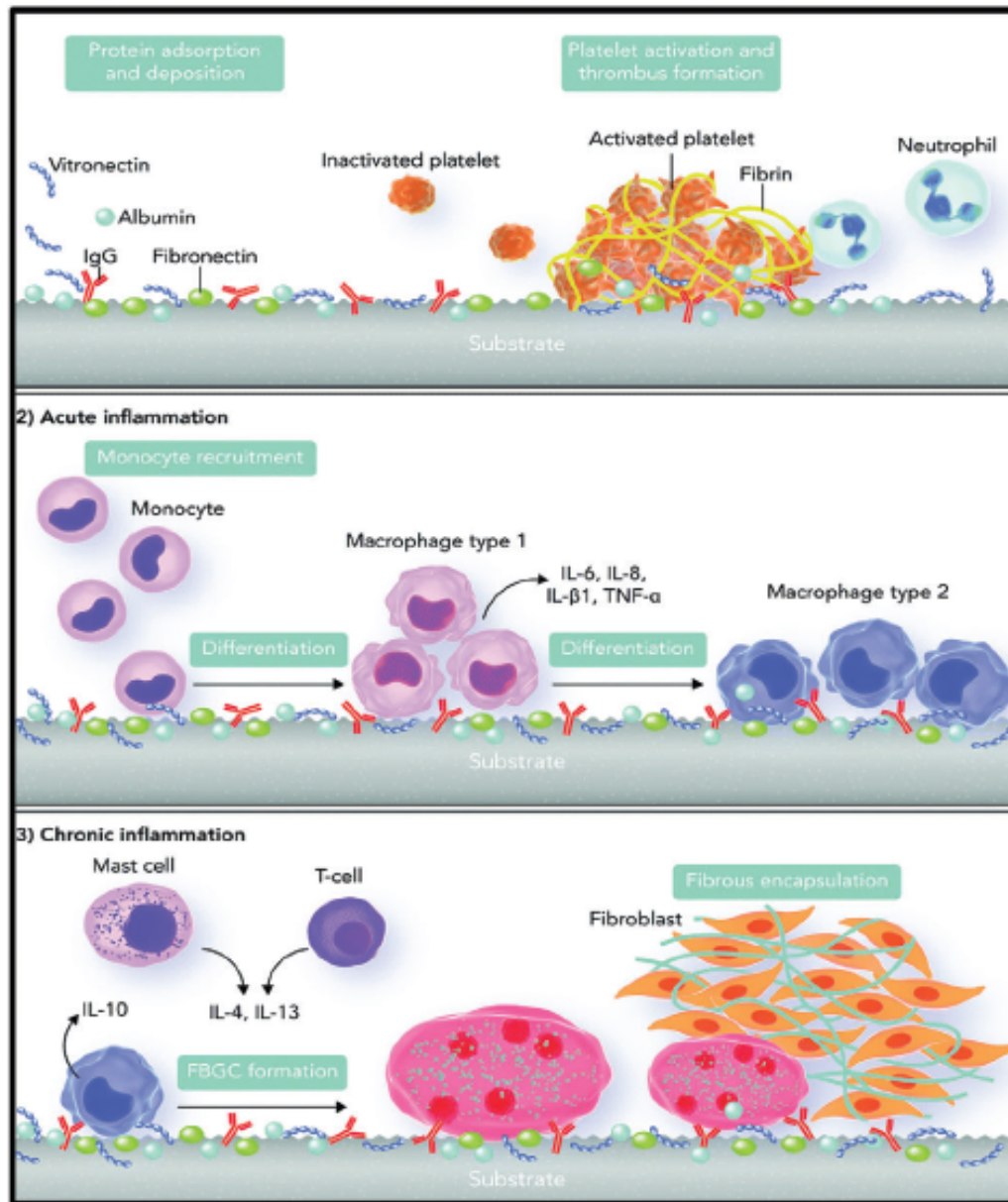


FIGURE 2.9: Implant response: Adsorption, inflammation, macrophage cooperation, fibroblast-driven collagen. (John Wiley and Sons, copyright 2023) [20]

### 2.3.1 Ceramic Bone Scaffolds

Due to its inertness, hardness, and resistance to abrasion, ceramics have found widespread acceptance in biomedical uses [47]. For instance,  $3Y\text{-ZrO}_2$ 's inert properties, mechanical toughness, and tribological performance have led to its broad application in dental crowns and bridges [48]. Ceramics like alumina, zirconia, zirconia toughened alumina, or silicon nitride are replacing the traditionally used metal femoral heads in hip replacement joints due to their enhanced tribological

properties and wear resistance [49]. While these ceramics fulfill the mechanical demands of the mentioned applications, they lack interaction with the body due to their inert characteristics.

Bio-glasses (BGs) and calcium phosphates stand out among ceramics that can interact with the body. Bio-glasses are artificial vitreous materials that have chemical properties with the minerals found in bone. They are easily broken down and produce hydroxyapatite (HAp) on their surface, which makes biological fixation easier [50]. Latest research has devised methods to modulate their degradation rates to align with tissue growth [51]. They function better when it comes to interacting with the body than phosphate-based ceramics, but they still lack the necessary mechanical qualities to operate as a stand-alone support [51]. Calcium phosphate ceramics (CPCs) utilized in Bone Tissue Engineering (BTE) scaffolds are renowned for their osteoinductive and osteoconductive properties. The effectiveness of CPCs in promoting bone healing is significantly affected by factors such as Ca/P ratios, crystallinity, and composition. CPCs with a Ca/P ratio of 1.5 have higher solubility in aqueous environments, releasing  $Ca^{2+}$  and  $PO_4^{3-}$  ions, which catalyze a carbonated apatite layer formation. In contrast, hydroxyapatite, with a 1.67 stoichiometric ratio, is more stable and less soluble within the body's aqueous environment [20]. Through mechanisms driven by liquids and controlled by cells, bioceramics enhance protein adsorption and interaction with the local extracellular matrix (ECM). Although the exact mechanism of this interaction with the ECM is not fully understood, it is significantly affected by the specific proteins adhering to the ceramic surface [46]. In order to change this property, cationic or anionic impurities are added to CPCs in order to alter their rate of dissolution, increase their stability, or improve their biological performance. However, due to their limited mechanical strength and brittleness, CPCs are unsuitable for load-bearing regions [52]. To enhance their structural robustness, they are combined with polymers, metals, or alternative ceramics, yielding multi-material scaffolds. Various methods, such as homogeneous mixtures, polymer matrix composites, coatings, ceramic matrix composites, and layering, are employed to integrate diverse materials into the scaffold. The Figure 2.10 shows an illustration of Synthetic Bioactive Ceramic

Structures for Critical Size Bone Inconsistencies by Powder Bed Selective Laser Processing (PBSLP).

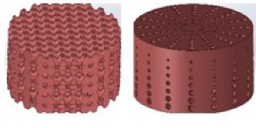
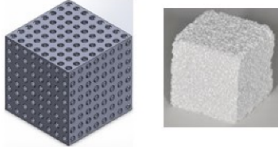
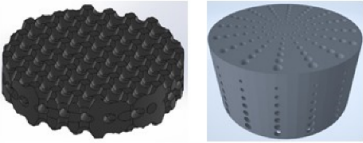
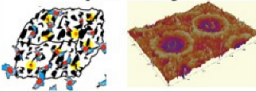
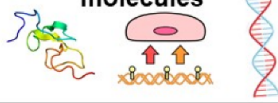
	<b>Ceramic scaffolds</b>	<b>Ceramic scaffolds + bioactive molecules</b>	<b>Ceramic scaffolds + stem cells</b>
<b>Selective laser processing scaffolds</b>			
<b>Functionality</b>	<b>Surface roughness, pore size, and porosity</b> 	<b>Growth factors, drugs, genes, and small molecules</b> 	<b>Stem cells, MSCs, and PDSCs</b> 
<b>Fracture site length</b>	<b>Fracture sites &lt; 2 cm</b> 	<b>Fracture sites 2–4 cm</b> 	<b>Fracture sites &gt; 4 cm</b> 

FIGURE 2.10: PBSLP employs three primary categories of synthetic bioactive ceramic scaffolds for bone repair [53]

### 2.3.2 Polymeric Bone Scaffolds

Based on where they come from, the polymers used in Bone Tissue Engineering (BTE) can be categorised as natural or synthetic. In BTE applications, natural polymers including alginate, chitosan, and collagen are used. Due to their ease of protein binding to their surfaces and resemblance to the body’s original tissues, natural polymers frequently evoke a favourable reaction in ECM interactions [54]. However, its poor structural strength, difficult processing, and possible danger of disease transfer limit its use in BTE [55]. The limitations of natural polymers can be overcome by synthetic polymers, such as polylactic acid (PLA), polycaprolactone (PCL), polyglycolic acid (PGA), and polyurethane (PU). However, the hydrophobic properties of these synthetic polymers prohibit proteins from attaching to them, necessitating direct contact with the ECM to

stimulate a bone repair response [56]. To bolster cell adhesion and proliferation, polymers are frequently augmented with bioactive molecules like Arginine-Glycine-Aspartic (RGD), Tyrosine-Isoleucine-Glycine-Serine-Arginine (YIGSR), and Isoleucine-Lysine-Valine-Alanine-Valine (IKVAV) [57]. Ester linkage hydrolysis is used to break down polymers including PLA, PGA, and PCL, with degradation rates ranging from months to years. These rates depend on factors like polymer crystallinity, composition, and hydrophilicity. Common degradation durations are approximately 3-6 years for PLA, 1-2 years for PCL, and 3-4 months for PGA [58]. The scaffold interacts with the ECM, which leads to the breakdown

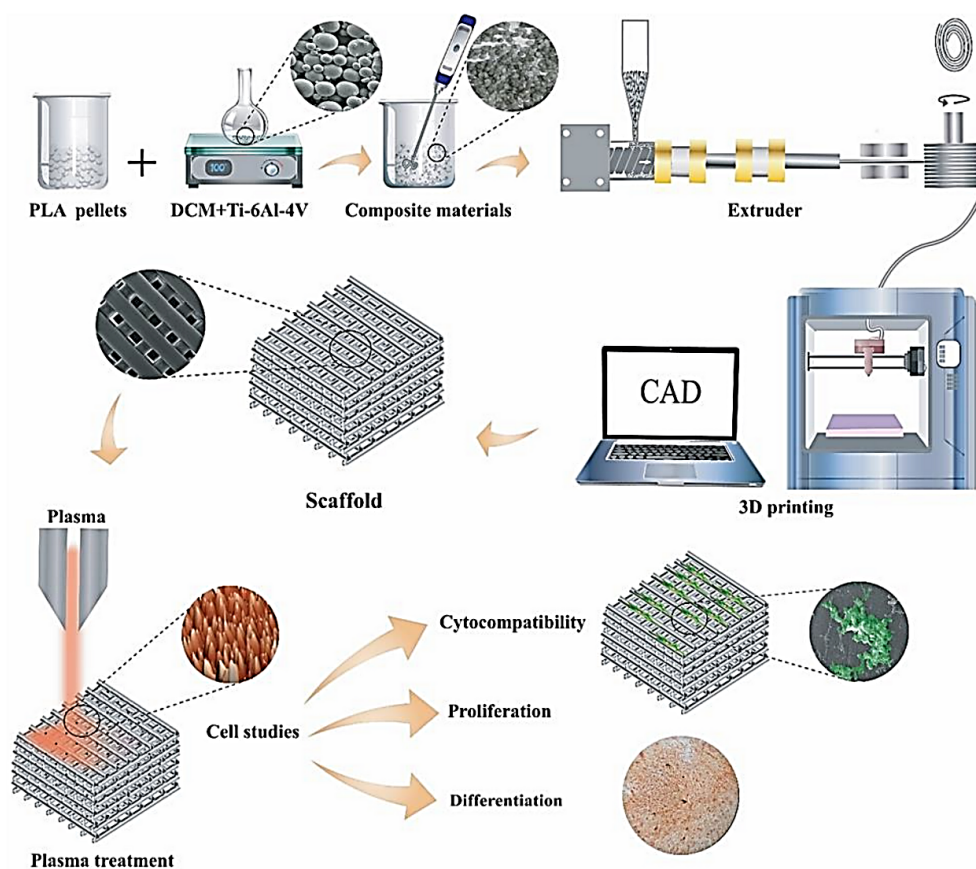


FIGURE 2.11: Schematic illustration of the method used to fabricate 3D porous PLA/Ti64 composite scaffolds [59]

of the polymer and changes in the mechanical and physiological properties of the implanted scaffold. As an illustration, the hydrolysis of PGA may result in an increase in the local pH, which may impede the development of osteogenesis [60]. Proteins, biomolecules, growth factors, and peptides bound to the polymer surface also initiate a series of bone healing activities, which enhances the scaffold's

ability to encourage tissue regeneration [61]. These bioactive polymers may also transport growth factors and other biomolecules, which is crucial for easing the complex process of bone healing. By providing a controlled release mechanism, they contribute to orchestrating the cellular responses necessary for successful tissue regeneration and bone formation. This capability enhances their therapeutic potential in Bone Tissue Engineering (BTE) applications, where precise delivery of bioactive agents is essential for optimal healing outcomes [62].

Polymer scaffolds exhibit significant potential in Bone Tissue Engineering (BTE) due to their favorable biological interactions. However, their limited mechanical strength and propensity to increase in porosity over time hinder their suitability for load-bearing applications. While these scaffolds promote cellular activities, their inability to withstand substantial mechanical loads poses challenges. The gradual rise in porosity further compromises their structural integrity. Addressing these concerns necessitates innovative approaches. These approaches may involve incorporating reinforcing agents and utilizing advanced fabrication techniques to enhance the mechanical properties and overall performance of polymer scaffolds in load-bearing BTE scenarios. However, these enhancements can compromise the scaffolds' ability to provide robust structural support for load-bearing scenarios [20]. A schematic depiction of the process employed to create 3D porous PLA/Ti64 composite scaffolds is presented in the Figure 2.11.

### 2.3.3 Metal and Alloy Based Bone Scaffolds

The word "bioinert" refers to metals often utilised in bone tissue engineering (BTE), which implies they do not trigger a foreign body reaction when implanted [20]. There are titanium and tantalum alloys among these metals, as well as magnesium alloys and zinc used in BTE applications. These materials can be applied as bulk forms, nanoparticles, or a hybrid combination of both [20, 63]. The observed functionalities exhibit significant variations depending on the form of utilization. However, a significant issue arises because of the mechanical mismatch between metal alloys and natural bone when using them as bulk materials. This difference

in load-bearing capacity may cause bone resorption near the implant, which might result in attachment failure or loosening [20, 64]. Additionally, whether in bulk or nanoparticle forms, the bioinert nature of several metals and alloys restricts their capacity to interact positively with the local extracellular matrix (ECM) and foster a good bone healing response [63, 65].

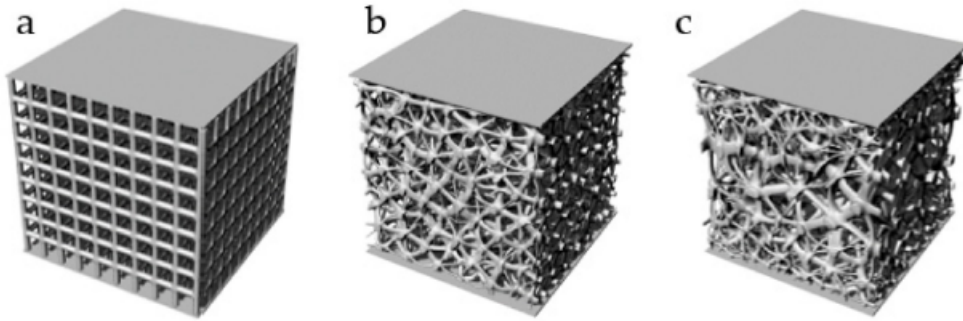


FIGURE 2.12: The generated models encompass (a) a structured porous framework, (b) an unstructured porous arrangement, and (c) a gradient unstructured porous configuration [66]

The main reason titanium alloys are widely used for orthopaedic purposes is because they are bioinert [65]. These metal alloys are introduced with alloying elements including Zr, Nb, Al, and V to increase their usefulness in BTE applications. These alloying elements enhance interactions with the local environment and bolster corrosion resistance [67]. Research has demonstrated heightened alkaline phosphatase (ALP) activity and reduced cytotoxicity through the incorporation of Nb and Zr into Ti alloys [67, 68]. Zn, Fe, and Mg are three bioresorbable metals that are gaining popularity due to their potential for use in Bone Tissue Engineering (BTE) procedures. Due to its slow rate of degradation and the importance of Zn finger proteins (ZFPs) in the human body, Zn is being used increasingly frequently in BTE. ZFPs have a role in regulating a variety of biological activities as DNA-binding transcription factors [69]. Upon implantation, Zn undergoes degradation through galvanic coupling, resulting in the release of Zn ions. These ions interact with  $Ca^{2+}$  and  $PO_4^{3-}$  ions present in simulated body fluids (SBF) [69]. But only about 15 to 40 mg of zinc ions may be absorbed daily by the body [69, 70]. Hence, it is vital to regulate the scaffold's degradation rate to remain within this physiological threshold. Similarly, magnesium is also bioresorbable like Zn, but

a notable distinction lies in its degradation rate. Magnesium degrades swiftly within the body, resulting in the release of hydrogen gas  $H_2$  [71]. Regrettably, the discharge of  $H_2$  gas has been observed to disturb the bone healing cascade, as it leads to an elevation in the local pH of the nearby region [72]. Despite these challenges, magnesium is regarded as a potential substitute for bone. This is because it exhibits mechanical strength similar to that of bone and plays a crucial role in numerous physiological processes within the body through its ions [71]. When combined with other bioactive materials, nanoparticles can provide osteogenic or other essential qualities needed to start and maintain the bone repair cascade [63].

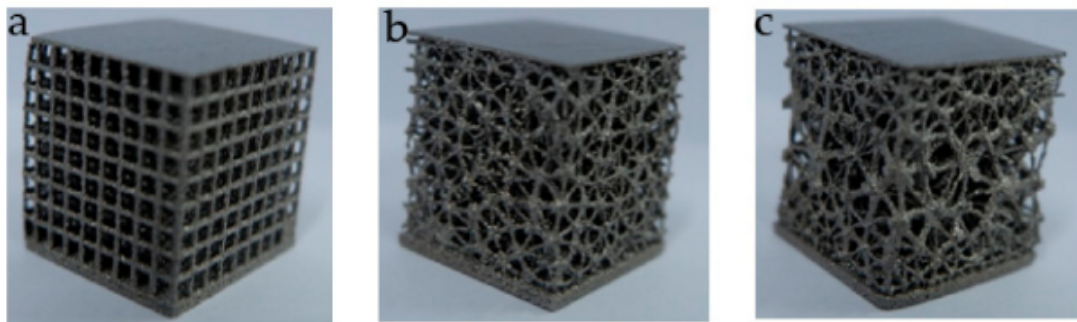


FIGURE 2.13: Porous structures for Ti6Al4V, formed through EDM, include regular, irregular, and gradient irregular arrangements [66]

Gold (AuNP), silver (AgNP), iron, aluminium, copper, zirconium, and hydroxyapatite nanoparticles are examples of commonly used nanoparticles [63]. At low doses, AuNP has been found to act as synthetic alternatives to bone morphogenetic proteins (BMP), crucial for bone mass regulation through the Wnt/ $\beta$ -Catenin signaling pathways [73]. The ability of silver nanoparticles to penetrate bacterial cell walls and cause DNA damage makes them well known for their bactericidal effects [63]. Polymer scaffolds are frequently combined with titanium oxide nanoparticles for use in bone tissue engineering (BTE). It has been shown that including them improves the wettability and mechanical properties of the resultant polymer scaffold [74]. In Figure 2.12, the generated models showcase various porous frameworks, including a structured framework (a), an unstructured arrangement (b), and a gradient unstructured configuration (c). Additionally, Figure 2.13 illustrates porous structures for Ti6Al4V, produced via EDM, featuring regular, irregular, and gradient irregular arrangements.

### 2.3.4 Multi-materials Bone Scaffolds

The use of two or more materials combined in a variety of ways, such as homogeneous mixes, different structures, doping agents, or surface coatings, is referred to as the use of multi-material scaffolds. Depending on the type of combination, the qualities of the composite might significantly alter. For instance, a bioactive site is created when zirconia-based scaffolds are mixed uniformly with nano-HAp, and this combination also increases mechanical strength by preventing fracture propagation [75]. On the other hand, scaffolds made of Ti alloys with nano-HAp coatings improve osseointegration by interacting with the ECM. However, due to their poor surface adherence, these coatings do not greatly increase the material's strength [76]. Bioactive glasses (BG) demonstrate considerable bioactivity and can speed up the process of osteointegration, as was previously mentioned. This leads to the use of BG coatings on materials including stainless steel, Ti-6Al-7Nb, nitinol, and other biocompatible alloys [77]. Multi-material scaffolds have extended their utility as drug delivery systems by combining organic and inorganic biomaterials. An instance of this is seen in chitosan-HAp-based scaffolds, functioning as carriers for therapeutic metal ions. These scaffolds emit strontium ions, which have been found to promote bone formation and affect the expression of the osteoclast gene. Additionally, the first burst release of copper ions from the chitosan polysaccharide, which serves as a transporter for copper ions, prevents bacterial proliferation [78, 79].

Because higher post-processing temperatures are required to increase the strength of ceramic materials, integrating natural polymers into bioceramic scaffolds present challenges. However, the combination of HAp-PCL-based composites with starch-based natural polymers provides a solution by acting as a binding agent to improve mechanical characteristics. Additionally, the addition of starch prolongs the time until these scaffolds degrade, which is important for promoting cellular development and adhesion in Bone Tissue Engineering (BTE) scaffolds [80].

Due to their inherent limitations, the use of particular materials alone may not be optimal for Bone Tissue Engineering (BTE) applications. Consequently, the

amalgamation of materials into composites offers a solution to surpass these limitations. Recent studies have focused on examining multi-material scaffolds designed for BTE applications [81]. Incorporating a secondary phase significantly alters the composite's chemical properties, whether in the form of nanoparticles, doping agents, or uniform blends. It requires careful procedure selection to achieve desired outcomes. For instance, processing magnesium alloys incorporating nano-bioactive glass (BG) particles via powder metallurgy results in intermetallic  $Mg_2Si$  and MgO phases, which accelerate the in vitro breakdown of the magnesium composite [82]. However, a different result is obtained when the same composite is processed using spark plasma sintering (SPS). In this case, the BG remains integrated within the matrix of the magnesium alloy and the production of intermetallic phases is inhibited. Cell viability is enhanced and in vitro degradation is decreased as a result. This underscores the significance of processing methods in attaining the intended characteristics of the composite [83]. Therefore, the simultaneous processing of these materials poses challenges when aiming to create multi-material scaffolds with specific properties and desired interactions.

## 2.4 Bone Scaffolds Structure

There are four crucial factors that may be used to determine the porosity structure of BTE scaffolds: Figure 2.14 illustrates porosity (%), pore size, surface area, and interconnectivity [84]. Porosity reflects open space within the scaffold. Pore

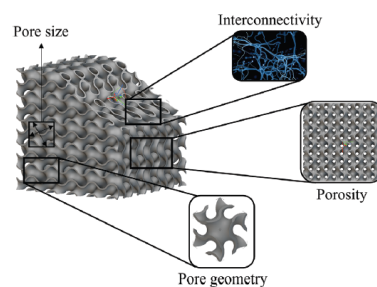


FIGURE 2.14: Structural parameters of the synthetic bone scaffolds [85]

size defines pore dimensions. Surface area combines surface pore sizes and overall porosity. Interconnectivity, determined by pore arrangement and sizes, affects

cell infiltration and nutrient diffusion post-implantation. The scaffold's pore size plays a critical role in defining both its mechanical strength and infiltration capability. Figure 2.14 demonstrates that increasing pore size reduces scaffold compression strength, highlighting the need for a balanced pore size for fluid ingress and strength. Pore diameters in common BTE scaffolds range from 100 to 900  $\mu\text{m}$ . Pore diameters greater than 300  $\mu\text{m}$  are preferred by osteoblast cells (10–50  $\mu\text{m}$ ), which facilitates nutrition exchange and biomolecule infiltration [86]. Reduced water contact angles are another benefit of larger pores for fluid penetration. For the scaffold to integrate with native bone and transmit loads, bone must continue to develop inside it. Smaller pore sizes (200–300  $\mu\text{SLA}$ ) that limit infiltration tend to induce chondrogenesis in MSCs, resulting in cartilaginous tissue formation instead of bone. Optimal in-growth pore sizes are typically within the 250–500  $\mu\text{SLA}$  range. While larger pores can enhance functionalization, they may compromise scaffold strength and structural integrity [87].

Smaller holes ( $\leq 100 \mu\text{m}$ ) on the other hand cause the production of fibrous tissue, which reduces the interaction between the scaffold and angiogenesis. Micropores (within 10  $\mu\text{m}$ ) enhance surface area, facilitating ion exchange and protein adsorption.

These varied effects of pore sizes highlight their distinct contributions to the physiological and structural aspects of BTE scaffolds. Thus, incorporating heterogeneous pore sizes can provide multifaceted benefits crucial for effective bone healing. Additionally, the scaffold's capacity to accommodate diverse stages of tissue development, including osteogenesis, angiogenesis, and cell migration, is influenced by the hierarchical arrangement of hole diameters. This arrangement mimics the native bone's complex structure, providing cues for the orchestrated healing process. Notably, the interplay between pore sizes within the scaffold can significantly influence nutrient diffusion, waste removal, and overall mechanical stability, all of which are fundamental for successful bone tissue engineering applications [88]. Notably, the interplay between pore sizes within the scaffold can significantly influence nutrient diffusion, waste removal, and overall mechanical stability, all of which are fundamental for successful bone tissue engineering applications.

### 2.4.1 Porosity

The pore size and overall geometry of a BTE scaffold influence its porosity. After being implanted, the scaffold's porous volume offers a surface for osteoblast cells to live on and promote cellular connections. Porosities of BTE scaffolds commonly fall within the range of 50% to 80%, which varies based on desired mechanical characteristics [89]. Elevated porosities (above 65%) facilitate improved infiltration of the extracellular matrix (ECM), yet they might compromise the scaffold's overall structural strength.

Increasing the scaffold's porosity creates more surface area, which improves interaction with the ECM, speeds up bone ingrowth, and encourages vascularization. However, sustained ECM contact can lead to eventual pore occlusion. Thus, higher porosities ensure ample permeability for nutrient and biomolecule transport. Conversely, porosities under 65% offer superior mechanical strength but may limit ECM interaction, potentially reducing cellular Alkaline Phosphatase (ALP) activity [90]. Permeability, a critical need, hinges on both porosity and interconnectivity. The required permeability varies based on defect size, with larger defects demanding greater oxygen and nutrient supply for effective bone healing. For example, when comparing 3D-printed stainless-steel scaffolds with porosities of 60 and 70 percent, those with a porosity of 58 percent exhibited stronger cell proliferation and growth. This could be attributed to their superior retention of cell media over longer periods of time [91].

Balancing scaffold porosity also influences the scaffold's mechanical properties, as excessive porosity can compromise its structural integrity. Therefore, it's crucial to design scaffolds with a porosity level that aligns with the specific requirements of the bone regeneration site. Achieving this balance requires a deep understanding of the tissue's natural healing processes and the biocompatibility of the scaffold materials [92]. Moreover, the interconnectedness of pores within the scaffold plays a pivotal role in nutrient diffusion and waste removal, directly impacting the cellular responses. An optimized scaffold design should address both porosity and pore interconnectivity to maximize its therapeutic potential in bone healing.

In this study, the formula used to calculate the porosity of CAD-based lattice structures, such as bone scaffolds, is expressed as

$$\text{Porosity (\%)} = 1 - \left( \frac{V_{\text{solid}}}{V_{\text{total}}} \right) \times 100 \quad (2.1)$$

Porosity distribution in synthetic bone scaffolds varies through techniques like gradient control, random patterns, ordered designs, and hybrid methods. Gradient porosity aids nutrient diffusion, randomness ensures uniform cell seeding, ordered structures offer mechanical strength, while hybrid approaches balance structure and cell function. Tailoring porosity distribution optimizes scaffold performance in bone tissue engineering.

## 2.4.2 Bone Scaffolds Geometry

In Bone Tissue Engineering (BTE), scaffold geometry refers to the spatial arrangement of pores within the scaffold matrix, a critical factor influencing its performance. This aspect can be broadly classified into two main types: stochastic and non-stochastic. Stochastic geometry exhibits a random distribution of pores throughout the scaffold, while non-stochastic geometry involves a more ordered arrangement of pores. Each type offers distinct advantages and challenges, shaping the scaffold's ability to support cell infiltration, nutrient diffusion, and ultimately, tissue regeneration.

### 2.4.2.1 Stochastic Bone Scaffolds

Stochastic scaffold orientation refers to structures lacking repeating patterns. Despite the fact that they resemble normal bone architecture, their erratic orientations cause variances in scaffold compression strength and make replication difficult. Stochastic bone scaffolds are three-dimensional structures employed in regenerative medicine and tissue engineering to facilitate bone tissue regeneration [93].

Unlike non-stochastic scaffolds, which have a regular and predetermined pattern, stochastic scaffolds feature a random arrangement of pores throughout the

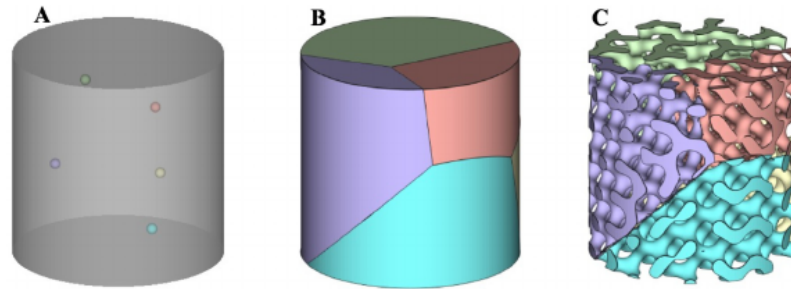


FIGURE 2.15: Stochastic scaffold design involves: A) Establishing a 3D domain with dispersed seeds; B) Generating subdomains from these seeds; and C) Applying a randomly oriented lattice to each subdomain [94]

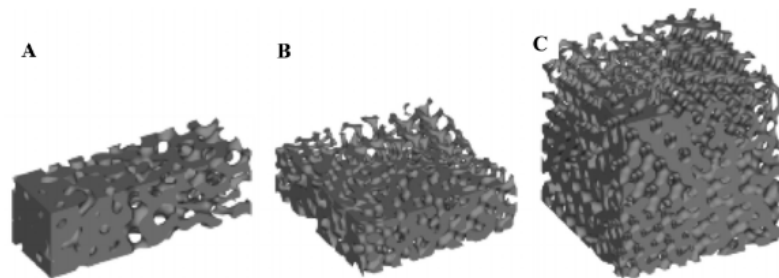


FIGURE 2.16: Functionally gradient stochastic scaffolds with 58 to 70 percent porosity along one axis, two axes, or all three axes [94]

structure. This randomness provides unique advantages and characteristics that make them valuable in various applications within the field of BTE. The random pore arrangement allows for easier modification and customization, making them suitable for different anatomical shapes and defect sizes. Moreover, stochastic scaffolds enhance cell interactions, as bone-forming cells can attach to the scaffold at multiple points due to the scattered pores. This characteristic encourages cell proliferation and the generation of new bone tissue, ultimately resulting in enhanced bone regeneration outcomes. Additionally, the irregular configuration of holes makes it easier for nutrients and oxygen to diffuse to more cells inside the scaffold, better enabling the development of new bone tissue [95]. However, the stochastic nature of these structures presents difficulties in precisely manipulating the scaffold's mechanical properties, potentially leading to less consistent outcomes compared to non-stochastic scaffolds. Nonetheless, stochastic bone scaffolds remain valuable tools in bone tissue engineering, offering promising approaches to promoting bone regeneration and addressing various bone-related challenges in regenerative medicine [96]. As research and technology advance, both stochastic

and non-stochastic scaffolds hold great potential in improving patient outcomes and advancing the field further. Figure 2.15 and Figure 2.16 show the stochastic bone scaffolds and change in porosity in three different axes respectively.

#### 2.4.2.2 Non-Stochastic Bone Scaffolds

Non-stochastic scaffolds with regular orientations contain a variety of forms, including cubic, hexagonal, triply periodic minimum surfaces (TPMS), spherical, and honeycomb structures. The figure 2.17 displays them. Scaffold geometry itself does not directly influence bone healing, regular structures offer advantages in terms of ensuring vascular growth, nutrient diffusion, and load-bearing capacity [97]. The regular and ordered pore architecture of non-stochastic scaffolds enhances cell interaction. The scaffold allows for effective cell attachment, migration, and proliferation, which is essential for tissue ingrowth and the development of new bone. Non-stochastic scaffolds can be designed to incorporate channels or interconnected pores, promoting vascularization within the scaffold structure. As a result, blood vessels may develop more easily, supplying the nutrients and oxygen vital for tissue growth and cell survival. Another significant benefit is the reduced risk of foreign body reactions. Controlled pore arrangement in non-stochastic scaffolds reduces the likelihood of causing inflammation or adverse reactions in the host tissue [98]. This, in turn, enhances the scaffold's biocompatibility and integration with the surrounding bone. In practical applications, non-stochastic bone scaffolds find use in various clinical scenarios. They are employed to facilitate the healing of bone defects caused by trauma, tumor resection, or congenital abnormalities. In orthopedic implants, non-stochastic scaffolds can serve as bioactive coatings or porous components to enhance their integration with the host bone. In dentistry, these scaffolds are valuable for guided bone regeneration to augment bone volume, enabling the successful placement of dental implants. Non-stochastic scaffolds can be fabricated using various biomaterials with tunable degradation rates [99]. This makes it possible for the scaffold to deteriorate in step with the growth of new bone tissue. A seamless transition from the scaffold to the regenerated bone tissue is ensured as the scaffold deteriorates and the newly produced bone progressively

takes on the load-bearing function. The capacity to modify the mechanical prop-

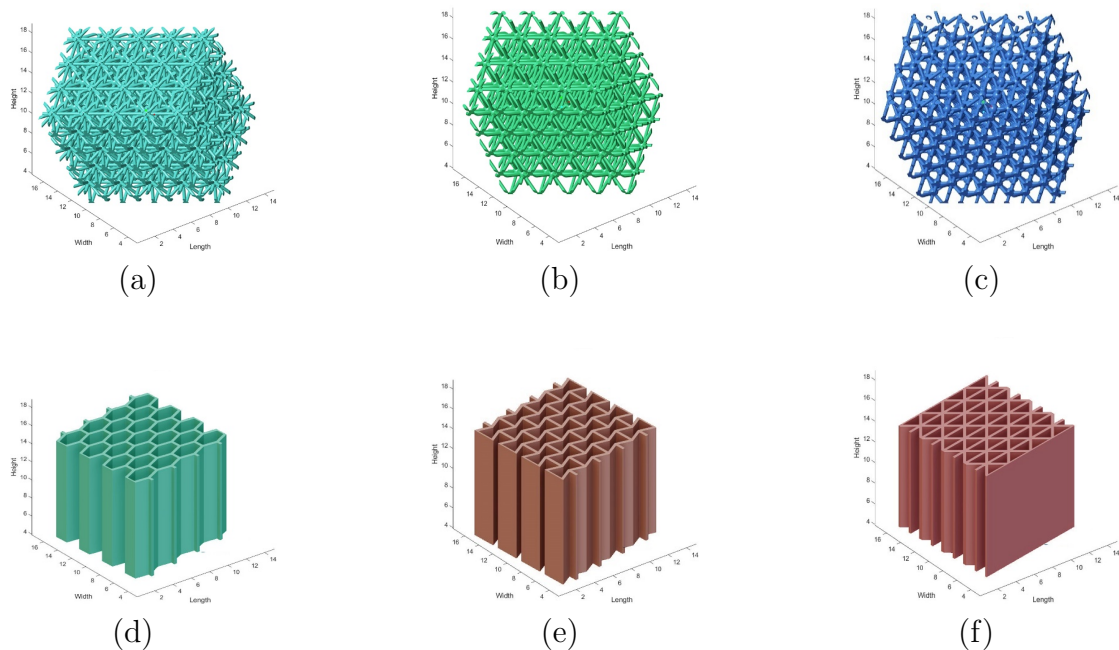


FIGURE 2.17: Non – stochastic bone scaffolds with pore shapes (a) Triangular (b) Square (c) Hexagonal (d) Hexa honeycomb (e) Re-entrant honeycomb (f) Triangular honeycomb

erties of non-stochastic scaffolds such that they mimic real bone is one of their key benefits. This includes adjusting parameters like porosity, pore size, and stiffness. By fine-tuning these properties, the scaffold can offer optimal support to bone cells during the healing process, leading to more successful outcomes in bone tissue regeneration [100].

The ability of TPMS structures to create an ideal balance between stiffness and permeability has recently led to an increase in their usage in BTE scaffolds. According to research, gyroid-based scaffolds for bone defect restoration have compressive strengths between 1.5 and 45 MPa that are comparable to human trabecular bone at porosities of 75 and 90 percent [101]. These scaffolds collapse in layers, and the orientation of the elliptical struts in the load direction gives the scaffold a substantial amount of stiffness and strength. Importantly, the scaffold responds to stresses quite differently at  $45^\circ$  angles than it does under axial loading, highlighting the need of taking load direction into account when choosing scaffold geometry. Pore geometry affects bone healing in a way that interacts with other elements

such as porosity, pore diameters, interconnectivity, and surface area, although its effects on mechanical characteristics may be studied independently. Therefore, a common strategy involves evaluating mechanical properties by isolating the study of pore geometry, as demonstrated in previous research. Additionally, bone healing behavior is analyzed based on specific scaffold features, such as pore size, porosity, and interconnectivity. This comprehensive understanding guides the design and fabrication of scaffolds that holistically address the multifaceted requirements of effective bone tissue engineering [102]. Moreover, researchers continue to explore innovative methods for assessing the *in vivo* performance of these intricate scaffold designs. This encompasses the utilization of cutting-edge imaging modalities and continuous monitoring techniques to glean invaluable insights into the intricate interplay between scaffolds and the host tissue environment. By leveraging these tools, researchers can adopt a more responsive and flexible strategy in optimizing and refining scaffolds tailored to specific clinical contexts. Such comprehensive understanding not only enhances the efficacy of tissue engineering interventions but also paves the way for personalized therapeutic solutions and improved patient outcomes.

### 2.4.3 Triply Periodic Minimal Surface Based Bone Scaffolds

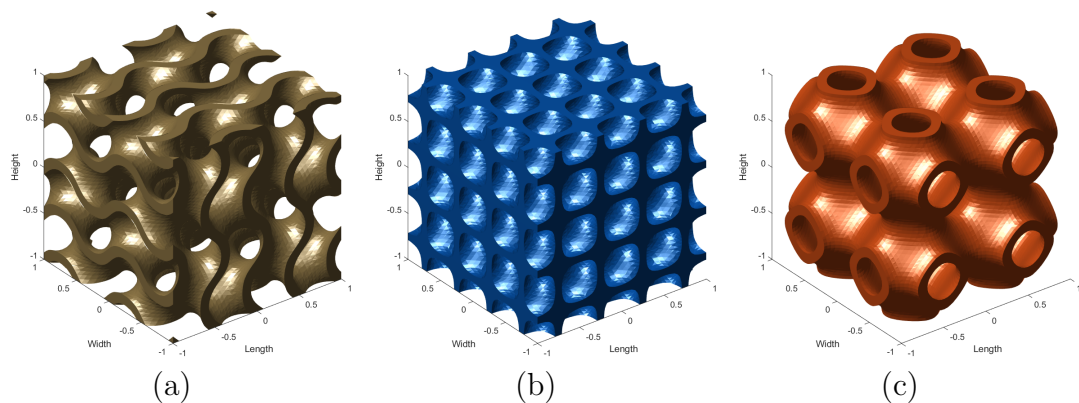


FIGURE 2.18: (a) Gyroid type (b) Diamond type (c) Primitive type

The smallest surface area feasible inside a restricted zone and zero mean curvature are the two characteristics of minimal surfaces. Triply periodic minimum

surfaces (TPMS) are such surfaces that are regularly replicated along three axes. Trigonometric operations, unit cell length, and unit cell type may all be used to mathematically represent these structures [103]. Customization of this mathematical framework is possible by changing the variables listed in Table 2.1.

TABLE 2.1: Mathematical formulas defining structures with TPMS [104, 105]

TPMS Structures	Equation
Gyroid	$\cos(wx) + \cos(wy) + \cos(wz) = c$ $\sin(wx) \sin(wy) \sin(wz) +$
Diamond	$\cos(wx) \sin(wy) \sin(wz) +$ $\sin(wx) \cos(wy) \sin(wz) +$ $\sin(wx) \sin(wy) \cos(wz) = c$
Primitive	$(wx) + \cos(wy) + \cos(wz) = c$

TPMS structures have three fundamental types: primitive type, gyroid type, and diamond type shown in Figure 2.18. The structural type of TPMS structures has a greater impact on their mechanical strength and energy absorption than does the material itself. During the plateau stage, P-type structures show localised buckling of curved walls, which causes stress variations. In contrast, Gyroid-type structures, characterized by unconnected porous formations, demonstrate superior structural strength by preventing microcrack propagation. Diamond-based TPMS structures offer the highest mechanical strength, with variations in plateau stress between sheet and skeletal diamond structures affecting energy absorption and toughness [106].

#### 2.4.4 Bone's Mechanical Properties

The mechanical strength parameters in the context of bone implants and tissue engineering related to the required amount of strength and stability that the implant must have to successfully perform its load-bearing job. Load-bearing applications involve implants that are expected to support the mechanical stresses and loads that natural bone typically experiences in the body. These specifications are crucial because inadequate mechanical strength could lead to implant failure, compromising the healing process and patient outcomes [107]. One key consideration

in designing bone substitutes for load-bearing applications is the level of porosity or porousness. Porosity refers to the presence of void spaces or pores within the implant's structure. Porous bone substitutes are desirable as they facilitate cell infiltration, nutrient diffusion, and tissue integration, promoting bone regeneration. However, an excessive level of porosity could compromise the mechanical strength of the implant, making it less capable of withstanding the necessary mechanical loads. Therefore, it is important to strike a compromise between mechanical strength and porosity. Starting with in vitro seeding process, the bone substitute is typically pre-seeded with bone-forming cells, such as osteoblasts, before implantation. This seeding process aims to encourage cell attachment and proliferation within the scaffold's pores, promoting tissue formation and integration [108]. Throughout the in vitro phase and after implantation in vivo, the bone substitute should offer physical support to the surrounding tissue. The chosen scaffold should possess appropriate mechanical properties, including compressive and tensile strength, within the context of in vitro cell culture for bone tissue engineering. These properties are crucial for facilitating cell adhesion, migration, and proliferation. This ensures that the scaffold can withstand the forces exerted by cells during tissue formation, contributing to a successful environment for cell growth and tissue regeneration. In tandem with suitable mechanical properties, the scaffold should also exhibit stability to uphold its structural integrity throughout the duration of cell culture. This stability ensures that the scaffold can provide a consistent and supportive substrate for cellular processes, fostering optimal cell attachment, proliferation, and ultimately, successful tissue development [109].

TABLE 2.2: Bone's mechanical characteristics in humans [110, 111]

Type of bone	Compressive strength (MPa)	Tensile strength (MPa)	Elastic Modulus (GPa)
Cortical bone	130-225	60-160	3-30
Trabecular bone	4-12	N. A	0.01-0.5

After implantation in vivo, the bone substitute continues to serve as a support structure for the developing tissue. As the surrounding tissue remodels and regenerates, the mechanical strength of the implant is essential in maintaining its structural integrity and resisting the loads imposed on it by daily activities or

movements. A well-designed bone substitute with adequate mechanical strength ensures that the implant can support the surrounding tissue during the healing process and eventually integrate seamlessly with the host bone [112]. In summary, when developing bone substitutes for load-bearing applications, careful consideration must be given to the mechanical strength specifications. The porosity level should be optimized to strike a balance between tissue integration and mechanical strength. This optimization ensures that the implant can effectively support the surrounding tissue during the *in vitro* seeding process and maintain its support throughout *in vivo* modification. Ultimately, a bone substitute with the appropriate mechanical properties will contribute to successful bone regeneration and a positive clinical outcome for the patient [113]. Table 2.2 lists the mechanical properties of human cancellous and cortical bone.

## 2.5 Synthetic Bone Scaffolds Challenges

Production of best and optimized porous bone substitutes in terms of their mechanical and structural characteristics is extremely difficult due to a number of variables. With respect to the architectural perspective, the bone substitute supports both mechanical and biological activities, which may compete with one another [114]. For instance, a denser material is required to increase the material's load-bearing capacity, which clashes with the necessity for a permeable structure to promote bone penetration and liquid porosity [115]. The adjusting of a single variable with little thought to how additional scaffold qualities are changed is probably what is typically referred to as an enhancement of scaffold characteristics. In addition to this, it is challenging to characterize, digitize, and manufacture the scaffold architecture. Digitizing information to interpret production methods can be challenging, particularly when examining structural parameters and interconnectivity in bone tissues through continuous or discrete approaches [114]. The interconnected macro-porosity should typically be greater than 50  $\mu\text{m}$  with a particular direction to fit the nutrient transport mechanics. Fluid and stress loading constraints and conditions [111, 114, 116]. The biological response of scaffolds has

been demonstrated to be influenced by what is known as micro-porosity, which has a diameter range between 0.1 and 10  $\mu$ SLA. As a result, the pores at this particular scale need to be identified, described and incorporated into the final design [115, 117]. The advancement and development of effective software design strategies are essential to translate the desired porous architecture and mechanical properties of the bone to be replaced into appropriate voxel units. These units can then be manufactured using various manufacturing platforms [118, 119]. Another concern regarding the production of a suitable bone substitute architecture. Such voxels can be analytically calculated through the use of topological optimization techniques or numerical simulation [113, 118, 119].

Developing architectures that are capable of undergoing *in vivo* bio-resorption at a specific pace acceptable for bone remodeling presents challenges from a material perspective. The terms "materials with biodegradable, bioresorbable, bio-erodible, and bioabsorbable properties" are frequently used in the context of regenerative medicine [120]. The mechanical, structural, and biochemical features of the scaffold will be impacted by the biodegradation pathway, which necessitates a thorough understanding [114]. Furthermore, factors such as pore size, pore interconnectivity, porosity, scaffold shape and volume, and the position of implantation within the musculoskeletal system all play pivotal roles in determining the degradation rate of the scaffold. Additionally, it is imperative to take into account the long-term response of native tissue to the degradation products of the scaffold.

This includes considering the biochemical, structural, and mechanical characteristics of the bone substitute to ensure they align with the unique requirements of each patient. Such comprehensive considerations are essential for optimizing the effectiveness and safety of tissue engineering implants in clinical practice. These multifaceted factors collectively influence not only the degradation kinetics of the scaffold but also its ability to support tissue regeneration and integration within the host environment. These requirements encompass factors like age, gender, overall health, metabolic rate, implant location, and loading conditions, which contribute to the complexity of achieving an ideal implant [114]. This underscores the multifaceted nature of achieving optimal outcomes in bone tissue engineering.

## 2.6 Limitations and Benefits of Polymer-Based Bone Scaffolds

Polymer-based bone scaffolds have garnered attention in the field of regenerative medicine and tissue engineering due to their adaptability, customizability, high biocompatibility, and ability to mimic the natural extracellular matrix. While these scaffolds offer notable advantages, they also come with inherent limitations. Here, we delve into the pros and cons of utilizing polymer-based bone scaffolds.

### 2.6.1 Benefits of Polymer-Based Bone Scaffolds

- i. **Biocompatibility:** Polymers chosen for bone scaffolds are frequently biocompatible, signifying their compatibility with the body and their ability to avoid triggering harmful immune reactions. This characteristic facilitates seamless integration between the scaffold and the host tissue, thereby fostering effective tissue regeneration.
- ii. **Tunable Mechanical Properties:** Polymers offer the advantage of tunable mechanical properties, allowing researchers to adjust the scaffold's stiffness and strength to match those of natural bone. This tailoring is crucial for load-bearing applications and ensures proper support during the healing process.
- iii. **Porosity and Interconnectivity:** Polymer-based scaffolds can be designed with controlled porosity and interconnectivity, providing pathways for cell infiltration, nutrient diffusion, and waste removal. These features enhance cell attachment, proliferation, and tissue formation within the scaffold.
- iv. **Degradability:** Some polymers used in bone scaffolds are biodegradable, meaning they can gradually degrade over time as the new bone tissue forms. The biocompatibility of these polymers eliminates the necessity for a secondary surgical procedure to remove the scaffold, effectively minimizing the potential for complications.

- v. **Versatility:** Polymers offer a wide range of choices, allowing researchers to select the most suitable material for specific applications. Furthermore, these scaffolds can be produced using diverse methods such as 3D printing, electrospinning, or solvent casting, providing versatility in scaffold design.
- vi. **Drug Delivery Capability:** Polymers can be engineered to incorporate drug delivery systems within the scaffold. This feature enables the controlled release of bioactive molecules, growth factors, or antibiotics, further promoting tissue regeneration and preventing infections.

### 2.6.2 Limitations of Polymer-based Bone Scaffolds

- i. **Mechanical Strength:** While polymer-based scaffolds offer tunable mechanical properties, they may not always match the strength of natural bone. In load-bearing applications, the scaffold's mechanical strength may be a limitation, potentially leading to premature failure or inadequate support.
- ii. **Degradation Rate:** Matching the rate of scaffold degradation with the formation of new bone tissue is crucial. If the polymer degrades too rapidly, it might not offer adequate support during the healing process. On the other hand, slow degradation could hinder bone regeneration and lead to long-term foreign body reactions.
- iii. **Lack of Osteoinductivity:** While polymers can serve as a framework for tissue growth, they may lack inherent osteoinductivity, meaning they do not actively stimulate bone-forming cells. Additional modifications, such as the incorporation of growth factors, may be required to enhance osteoinductivity.
- iv. **Inflammatory Response:** Some polymer-based scaffolds may trigger a mild inflammatory response during the degradation process. Although biocompatible, the scaffold's degradation products could cause local inflammation in the surrounding tissue.
- v. **Limited Vascularization:** Achieving efficient vascularization within polymer based scaffolds can be challenging. The lack of a well-developed vascular

network may impede the delivery of nutrients and oxygen to cells within the scaffold, limiting its overall effectiveness in larger or more complex defects. Therefore, strategies to promote vascular growth and integration are pivotal for enhancing the functionality and success of these scaffolds.

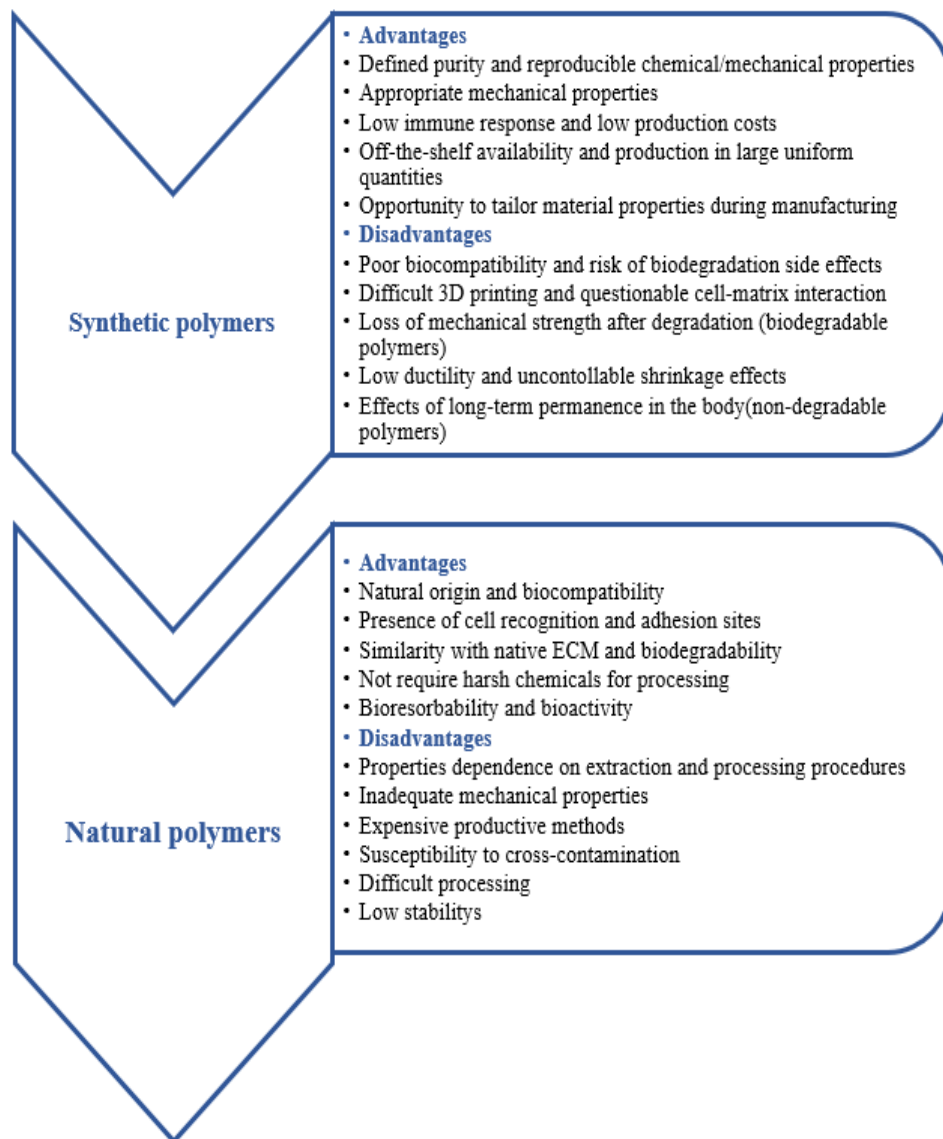


FIGURE 2.19: Advantages and disadvantages of natural and synthetic bone scaffolds

The graphic representation in Figure 2.19 concisely presents the pros and cons related to the application of natural and synthetic polymers. This visualization serves as a comprehensive guide for assessing the advantages and disadvantages of both types of polymers in various contexts, offering invaluable insights for researchers and industry professionals alike [121–124].

## 2.7 Research Gap

In order to create efficient bone scaffolds for tissue engineering applications, it is essential to understand the physical and mechanical characteristics of bone. These properties depend on its hierarchical structure, which consists of nanoscale collagen fibrils and hydroxyapatite crystals. Creating an ideal bone scaffold poses several challenges. First, mimicking the complex hierarchical structure of natural bone at different length scales is difficult. Achieving proper mechanical strength, porosity, and biocompatibility while maintaining a suitable degradation rate is also challenging. Moreover, ensuring adequate nutrient and oxygen supply to cells within the scaffold can be problematic. Polymeric bone scaffolds have gained attention due to their tunable properties and versatility. However, they have limitations. For instance, matching the mechanical properties of natural bone is challenging, as polymers may not possess the same strength or toughness. Degradation rates must be carefully controlled to avoid premature breakdown or excessive persistence. In order to facilitate cell proliferation and tissue ingrowth, it's also critical to have ideal pore size and interconnectivity.

Polymeric bone scaffolds, despite limitations, offer tailored customization and diverse fabrication methods like 3D printing. They also provide biocompatibility for cell functions, along with osteoinductive and osteoconductive traits. Furthermore, these scaffolds present reduced immunogenicity and lower risks of disease transmission when compared to natural bone grafts. These advantages position polymeric bone scaffolds as promising solutions in bone tissue engineering.

In conclusion, polymer-based bone scaffolds offer significant benefits in tissue engineering and regenerative medicine due to their biocompatibility, tunable properties, and controlled degradation. However, they also have limitations related to mechanical strength, degradation rate, osteoinductivity, and vascularization. To tackle these challenges, current research focuses on to explore the potential for enhancing the transport and mechanical characteristics of acrylate-based polymer bone scaffolds using PolyJet printing technology, all while upholding a high level of precision as stated in problem statement.

# Chapter 3

## Conventional and Additive Manufacturing Techniques

### 3.1 Introduction

Conventional and additive manufacturing techniques offer diverse approaches to fabricate synthetic bone scaffolds, while CAD-based and formula-based models contribute valuable designing techniques. Traditional fabrication methods like gas foaming and particulate leaching are employed to craft scaffolds possessing interconnected porosity and customized mechanical attributes. Electrospinning, on the other hand, produces fine fibers that mimic the bone's extracellular matrix. Additive manufacturing, particularly 3D printing, enables precise layer-by-layer construction of scaffolds with complex geometries. CAD-based models aid in designing patient-specific scaffolds, utilizing medical imaging to customize the structure according to individual anatomies. On the other hand, formula-based models help optimize material composition, porosity, and mechanical strength based on specific formulas and requirements. The fusion of these manufacturing and design methodologies presents compelling prospects for the development of highly sophisticated synthetic bone scaffolds. These breakthroughs hold immense potential to transform the landscape of bone tissue engineering and regenerative medicine, offering

unprecedented avenues for addressing complex clinical challenges and advancing patient care. With continued innovation and collaboration across disciplines, the future holds exciting possibilities for enhancing skeletal repair and regeneration.

## 3.2 Conventional Techniques for the Development of Bone Scaffolds

### 3.2.1 Solvent Casting and Particulate Leaching

Conventional fabrication methods like solvent casting/particulate leaching offer control over porosity and pore size based on polymer and salt selection. These techniques provide control over porosity and pore size, depending on the choice of polymer and salt used [125]. In this technique polymers are dissolved with organic solvent, mixed with porogen that are water soluble such as sodium chloride, sodium nitrate, gelatin particle and waxy hydrocarbons. The solution is then poured into the mold, solvent evaporated and a porous structure is achieved. Steps involved in the solvent casting and particulate leaching technique are summarized in Figure 3.1. Porosity and pore size depend upon the porogen amount and crystal

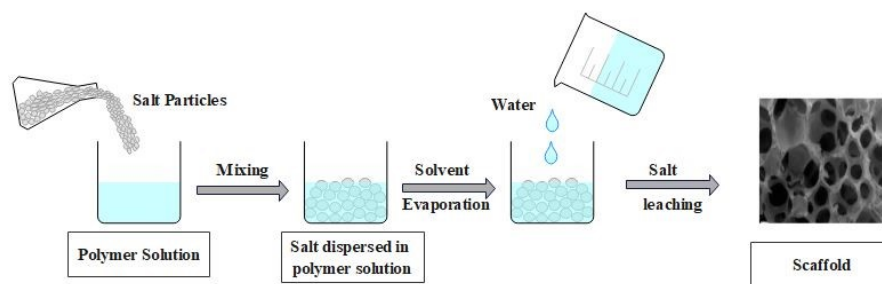


FIGURE 3.1: Solvent Casting and Particulate Leaching bone scaffolding technique

size respectively. It was observed that 70 wt.% of porogen exhibits higher pores interconnectivity. No special equipment is required for solvent casting technique. The disadvantage of this technique is the use of toxic solvents that can reduce

bioactivity of molecules, and cause denaturation of incorporated molecules. Feature controlled porosity and pores interconnectivity can be obtained in case of polymer-ceramics fabricated synthetic scaffolds [126]. The main drawbacks of solvent casting are: (i) the potential for hazardous solvent to remain in the polymer; and (ii) the shape restrictions (mostly flat sheets and tubes). Moreover, organic solvents can induce protein denaturation in the polymer. Porosity can be controlled by altering the salt/polymer ratio and salt particle size. However, there is relatively little control on the interconnectivity and morphology of the pores [127].

### 3.2.2 Gas-Foaming Process

Efficient fabrication of synthetic porous scaffolds for tissue engineering can be achieved through gas foaming, a process that involves generating pores using gas expansion. This technique uses a gas with high pressure instead of toxic solvent to fabricate porous structure [128]. Steps involved in the gas-foaming process are summarized in Figure 3.2. In this technique, polymer is placed in the chamber with

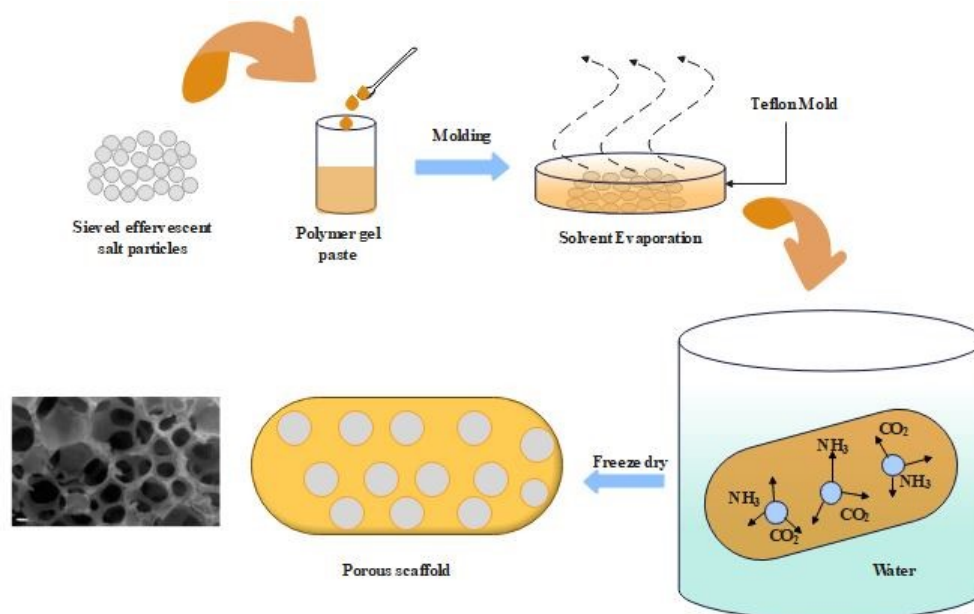


FIGURE 3.2: Gas foaming technique for bone scaffolding

a gas such as  $CO_2$  and increase the pressure to that extent where gas sufficiently become soluble in the polymer. After that lower the pressure to the atmospheric

pressure that will induce thermodynamic instability in gaseous phase, that results in porous structure. Scaffolds fabricated through this technique offers a maximum porosity of 90% and pore size around 100  $\mu\text{m}$  but poor pore interconnectivity specifically on the surface of scaffold just between 10 % - 30 % [129]. Trabecular structure-based scaffold can be fabricated through gas foaming process. Porous structure with pore sizes of 100  $\mu\text{m}$  to 500  $\mu\text{m}$  can be created with high cell viability and higher cell seeding efficiency. Gas foaming is relatively easy and cheap method for scaffold fabrication. The disadvantages of gas foaming techniques are that it cannot use glassy and hydrophobic polymers such as chitosan that has less solubility in  $\text{CO}_2$ . The solubility problem can be resolved by using the solvent such as diluted acid and ethanol [130].

### 3.2.3 Thermally Induced Phase Separation

Porous scaffold structure conventionally fabricated through thermally induced phase separation method (TIPS) can be controlled easily and exhibits low defect probability for both soft and hard tissues [131]. Steps involved in the thermally induced phase separation are summarized in Figure 3.3. In this process, polymer

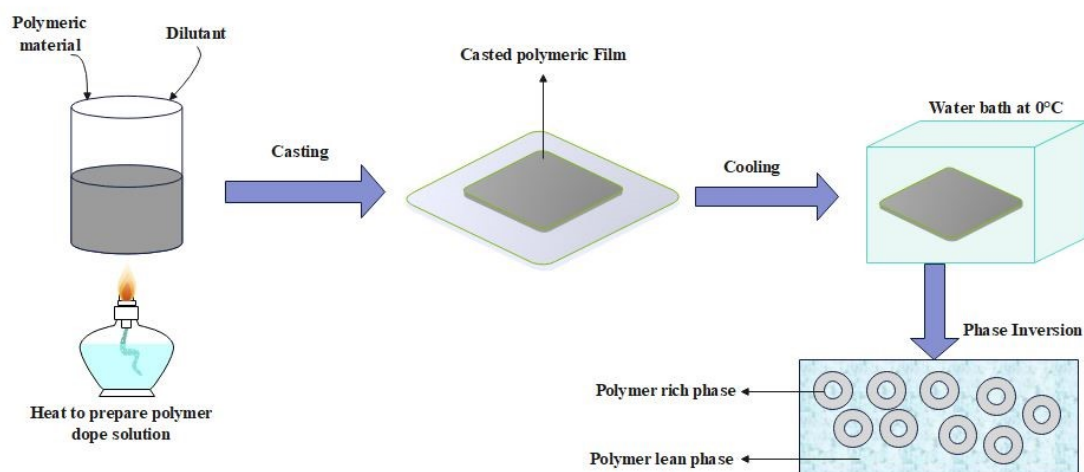


FIGURE 3.3: Thermally induced phase separation for bone scaffolding

is generally dissolved in the solvent at higher temperature. Homogenous mixture is cooled to remove the solvent from the mixture, which develops microstructure

porous structure scaffold. Degradation rate, bioactivity, mechanics and pore morphology properties of porous scaffold structures depend on the volume and the concentration of secondary phase fraction and polymers respectively. However, it is not suitable for cell seeding and bone growth because of pore size range i.e., 10  $\mu\text{m}$  – 100  $\mu\text{m}$ . To overcome this issue, pore size of scaffold is increased (greater than 100  $\mu\text{m}$ ) by using a coarsening process [132]. TIPS manufactured scaffold's properties depend upon the temperature gradient, solvent type and polymer concentration. The drawback of this process is the use of organic process which takes long time to sublime. Universal crystallizable solvent DMSO<sub>2</sub> (Dimethyl sulfone) is recommended for polymers due to which it is called a green method because solvent can be recovered by sublimation and recrystallization. Another biodegradable, water soluble and environment friendly solvent, PolarClean, is recommended to use in TIPS as a solvent [133].

### 3.2.4 Microsphere Sintering

This technique involves sintering polymer microspheres that were previously produced using an emulsion/solvent evaporation technique, shown in Figure 3.4. Based on the technique utilized to combine and blend the microspheres into a cohesive structure, the sintering process might be chemically or thermally activated, i.e. heat or vapor from a solvent [135]. In the case of composites, the microspheres have been filled with inorganic particles. Three-dimensional biodegradable and bioactive scaffolds offer mechanical qualities that are more similar to cancellous bone than solvent casting or TIPS, but with lesser porosity.

### 3.2.5 Electrospinning

Recently, electrospinning has received a great deal of consideration in the scaffold fabrication field, especially for use in reconstructive surgery. Making fibrous mats out of biodegradable polymers is an easy and diverse method. In an effort to artificially replicate the extracellular matrix of biological tissues, the size of the

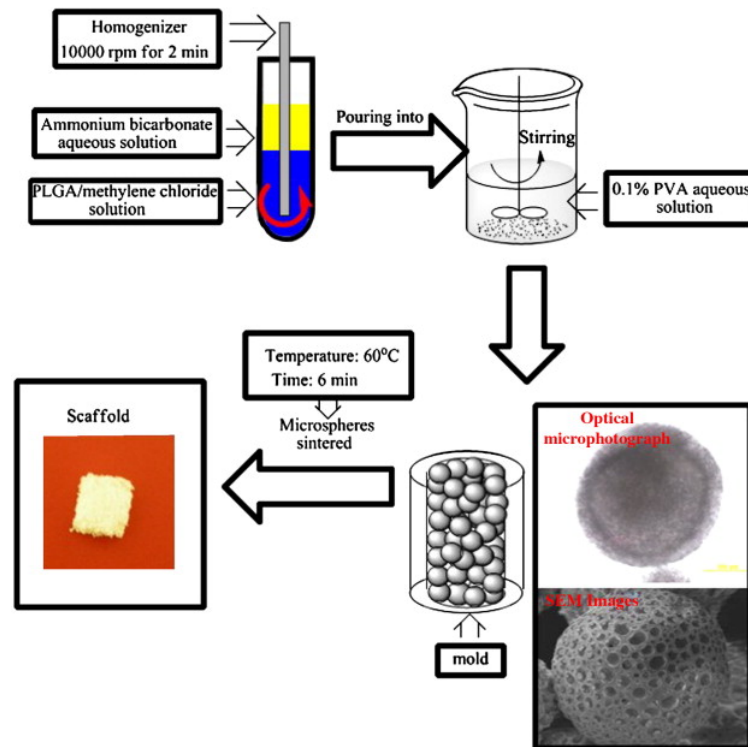


FIGURE 3.4: Schematics of microsphere sintering [134]

fibers at the micro-nanoscale is of special relevance [108]. During the procedure, a capillary is pressed to contain a polymer solution, which creates a jet of solution at the tip. A high voltage is used to deposit the thin fibre mat between the tip and the collector after a volatile solvent has evaporated.

This approach is particularly attractive for tissue engineering applications because of the ease with which biological signals, such as drugs, growth factors, or enzymes, can be incorporated. Nonetheless, this approach has notable drawbacks, including: (i) limited use of synthetic (PLGA, PCL, PLA) and natural (fibrinogen, collagen) polymers for random fiber scaffold creation; (ii) the production of only thin layers, posing challenges for crafting 3D support structures with controlled pore morphology and intricate geometry [136]. Finally, fibre diameter can occasionally be in the range of micrometer, which is incorrect for the extracellular matrix seen naturally.

In conclude, Table 3.1 provides a concise overview of the primary benefits and constraints associated with conventional fabrication techniques. This snapshot offers valuable insights into the strengths and weaknesses of established methods, aiding

TABLE 3.1: Advantages and disadvantages of conventional techniques for bone scaffolding

Technique	Advantages	Disadvantages
Solvent casting/particulate leaching	Easy, quick and highly porous scaffolds	Organic solvents
Thermally induced phase separation	Easily combined with other techniques and high porous scaffolds	Shrinkage of scaffolds, use of organic solvent and anisotropic pores
Microsphere sintering	Pore size gradient and complex shapes are possible to achieve	Lack of interconnectivity
Gas Foaming	High temperature and organic solvents are not required	Low control on structural parameters
Electrospinning	Structure similar to ECM with high surface area and aspect ratio	Use of organic solvent and low control on structural parameters

researchers and practitioners in navigating the intricacies of scaffold production and guiding future advancements in the field.

### 3.3 Additive Manufacturing Techniques for the Development of Bone Scaffolds

Additive manufacturing (AM), which emerged in the 1980s, has revolutionized scaffold production. It allows for the rapid construction of structures with intricate external profiles and internal porosity configurations. Rapid customisation of implants is made possible by combining AM with Computed Tomography (CT) data from damage locations, which is helpful for orthopaedic applications. Various established additive manufacturing (AM) processes, such as selective laser sintering (SLS), selective laser melting (SLM), fused deposition modeling (FDM), electron beam melting (EBM) and micro-stereolithography ( $\mu$ SLA) have been successfully employed to produce intricate bone implants. In addition to established AM methods, novel techniques like continuous liquid interface polymerization hold promise for scaffold fabrication [137]. Two-photon polymerization (TPP) has also

shown significant potential in advancing scaffold fabrication [138]. This chapter concentrates on the pertinent additive manufacturing (AM) techniques tailored for creating bone scaffolds. Additive manufacturing (AM) methods for scaffold fabrication can accommodate a wide range of biomaterials, including metals, polymers, and ceramics. This versatility results in scaffolds that create favorable biomechanical and biochemical environments, promoting cell proliferation and tissue development. Conversely, the scaffold-free AM approach employs multicellular bio-inks for crafting 3D tissues and organs, with a primary emphasis on generating soft tissue structures [139, 140].

### 3.3.1 Selective Laser Sintering (SLS)

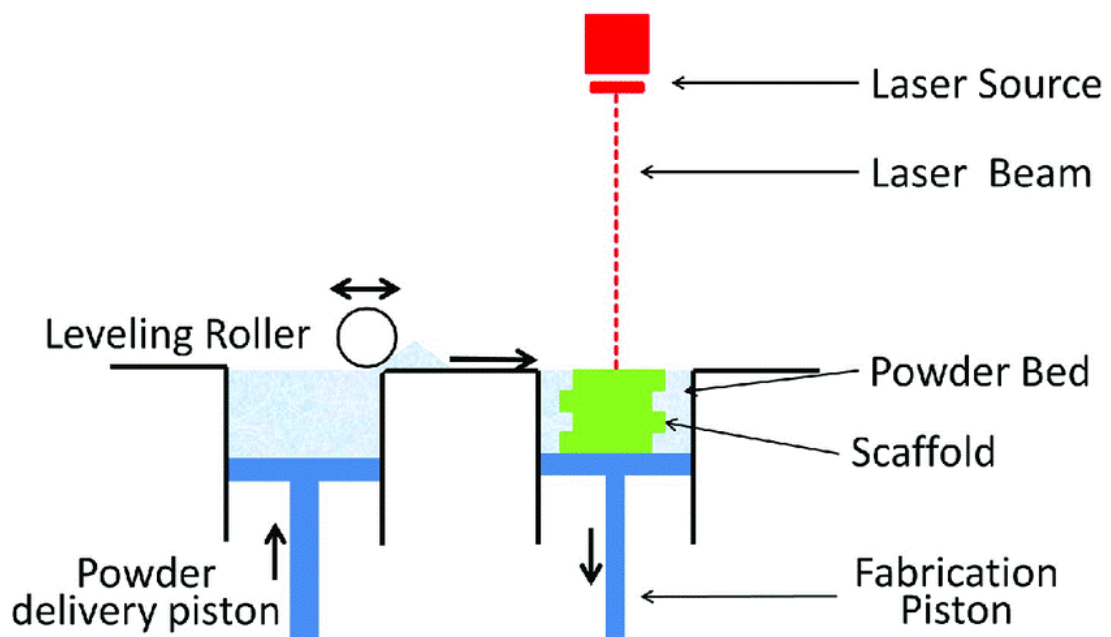


FIGURE 3.5: Schematics of Selective Laser Sintering [141]

Selective laser sintering (SLS) was initially proposed as an idea in 1986 [142]. A laser, a powder bed, a piston that moves vertically, and a roller for applying fresh layers of powder make up the fundamental building blocks of an SLS (Selective Laser Sintering) system. The powder is sinterized by a laser beam that is controlled by a computer, and the untreated powder serves as structural support for the scaffold that is being constructed. Figure 3.5 shows a schematic of the SLS procedure. Consolidation happens through solid or semisolid processes during the

SLS process at a sintering temperature below the material's melting point [143]. During semisolid sintering, powder particles undergo partial melting, resulting in a small liquid phase that binds adjacent solid particles together, forming solid parts. Processing of low melting point polymers like polylactic acid (PLA) [144], polyglycolide [145], poly(L-lactide) (PLLA) [146], and poly( $\epsilon$ -caprolactone) (PCL)[147] is well suited to the use of semisolid consolidation processes in SLS.

SLS has also been used by researchers to treat polymer and ceramic composites. For example, Du et al. utilized SLS to create composite scaffolds based on microsphere-based hydroxyapatite (HA)/PCL composites [148, 149]. The successful connectivity of microspheres created by laser sintering in the composite scaffolds was confirmed by scanning electron microscope (SEM) pictures. These scaffolds promoted cell adhesion, proliferation, and differentiation, according to *in vitro* tests. Moreover, *in vivo* assays revealed remarkable histocompatibility and the stimulation of new vascularized tissue. Another notable application of SLS was showcased in the creation of polyamide/HA composite scaffolds, as demonstrated by Kumaresan et al [150]. The porosities of these composite scaffolds ranged from 40% to 70%. The scaffolds achieved favourable mechanical properties, including a peak tensile strength of 21.4 MPa and a compression stress of 25.2 MPa, by meticulous optimisation and the addition of 15 wt% of HA.

SLS processes bioceramic scaffolds like Hydroxyapatite (HA) [151],  $\beta$ -tricalcium phosphate ( $\beta$ -TCP) [152], and Bioglass [153] effectively. Due to their higher melting points compared to polymers, the SLS process for bioceramics primarily relies on the solid consolidation mechanism [154]. This method involves shining a powerful laser beam at the ceramic particles, which raises their surface temperature and causes them to sinter together. Additionally, material along the grain boundary diffuses into the pores, facilitating densification. SLS has the ability to effectively limit the diffusion of grain boundaries, resulting in the creation of ceramic scaffolds with nanoscale grains. This procedure is characterised by a short sintering duration due to the high heating rate and brief holding time. Additionally, SLS shows great potential in the creation of scaffolds reinforced with low-dimensional nanomaterials (LDNs), such as carbon nanotubes, graphene, and boron nitride

nanotubes [155]. The structure of LDNs is preserved by the short sintering time and low sintering temperature employed in SLS, reducing damage throughout the production [156]. The increased biological qualities and better mechanical properties of these scaffolds supplemented with LDNs have been confirmed by mechanical testing and in vitro cell culture experiments [157, 158]. Addressing the challenge of limited liquid formation in SLS is crucial to prevent inadequate densification and uneven microstructures. Incorporating low melting point infiltration into the SLS procedure is an alternate remedy. This method improves the overall densification process by promoting the formation of a liquid phase and facilitating the rearrangement of crystallites.

Duan et al. [159] introduced a  $CaO - Al_2O_3 - SiO_2$  liquid phase into HA scaffolds using SLS. This led to a significant enhancement in densification during sintering, resulting in improved mechanical properties. The compression strength, fracture toughness, and hardness all witnessed noteworthy increases of 105%, 63%, and 11%, respectively. These improvements were particularly noticeable in the main mechanical parameters. Likewise, in Liu et al.'s study [160], incorporating Poly-L-Lactic Acid (PLLA) as a liquid phase into  $\beta$ -TCP scaffolds during SLS led to a notable 18.18% rise in fracture toughness.

### 3.3.2 Selective Laser Melting (SLM)

SLM was first developed to make it possible to fabricate metals in three dimensions with freeform shapes [154]. When compared to SLS, SLM uses a laser with a higher energy density to fully melt and solidify the metal material [161]. As a result, items created by SLM often have better surface quality, density, and mechanical strength. Selective Laser Melting (SLM) is predominantly favored for the fabrication of metal scaffolds owing to its exceptional energy density. This characteristic enables precise control over the melting and solidification process, facilitating the creation of intricately designed structures with enhanced mechanical properties and structural integrity. Figure 3.6 illustrates the SLM process. For instance, Čapek et al. [163] used SLM to create a joint replacement scaffold

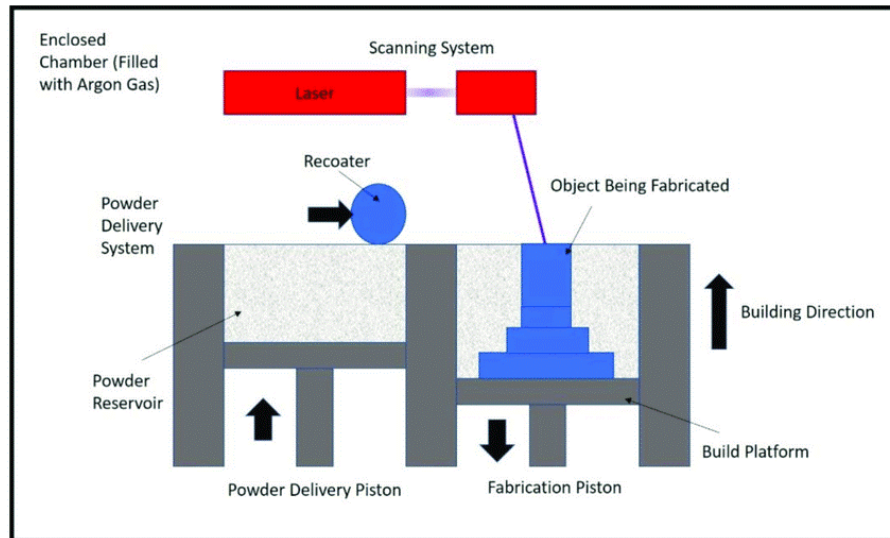


FIGURE 3.6: Schematics of Selective Laser Melting [162]

out of 316 L stainless steel, which is very porous (87 vol.%). The generated scaffolds had a compressive modulus of elasticity of 0.15 GPa and a compressive yield strength of 3 MPa, which were similar to those of trabecular bone in terms of their mechanical characteristics.

Weißmann et al. [164] employed Selective Laser Melting (SLM) to fabricate porous scaffolds using Ti-6Al-4V alloy. Their study demonstrated a wide range of elastic modulus values, ranging from 3.4 to 26.3 GPa, along with porosities falling within the 54% to 60% range. Notably, their findings highlighted the significant impact of unit cell orientation on the elastic modulus, compressive strength, and strain characteristics of the scaffolds. This underscores the importance of meticulous design considerations in optimizing scaffold properties for specific biomedical applications. Wang et al. [165] performed a study to determine how different factors affected the mechanical properties of scaffolds made using SLM. Their findings demonstrated that the porous architecture design led to a reduction of approximately 75–80% in the effective modulus of the resulting scaffolds. Furthermore, Shah et al. [166] produced Ti-6Al-4V scaffolds for load-bearing orthopaedic applications using SLM. Following a 6-month implantation period in adult sheep, an examination of the bone/scaffold interface was conducted. The compressive strength was observed to vary between 35 and 120 MPa, corresponding to the porosity levels ranging from 55% to 75%.

### 3.3.3 Fused Deposition Modelling (FDM)

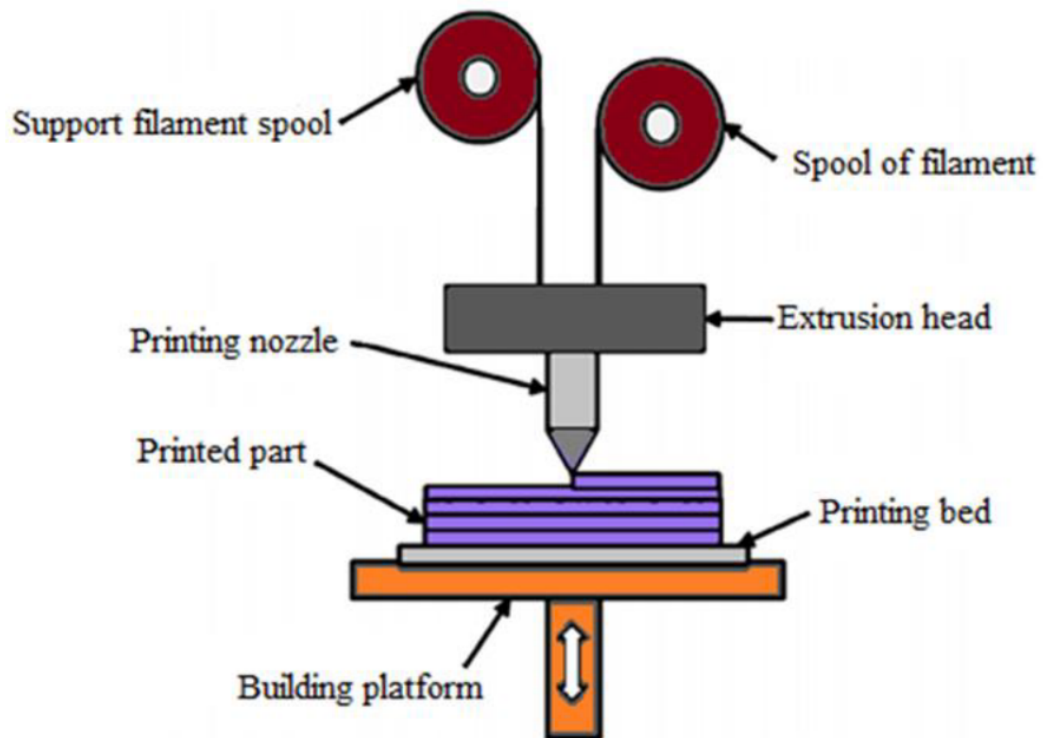


FIGURE 3.7: Schematic of Fused Deposition Modelling [167]

Crump originally proposed FDM, commonly referred to as extrusion-based methods, in 1988. Materials are heated to a molten state and then extruded or pushed out of a nozzle when using the FDM process. Following layer-by-layer deposition of the extruded material onto a substrate, a 3D scaffold is finally created. The FDM procedure is demonstrated in Figure 3.7. The characteristics of the printing nozzle have a significant impact on the precision and accuracy of the extruded scaffolds. FDM technology is mainly employed for processing polymers with low melting temperatures. With PCL and orientation patterns of  $0^\circ$ ,  $60^\circ$ , and  $120^\circ$ , Hutmacher et al. [168] used FDM to create porous scaffolds, reaching a porosity of more than 56% with pore diameters ranging from 380 to 590  $\mu\text{m}$ . Zhou et al. [169] used FDM to effectively create hierarchical polymer scaffolds with macropore sizes ranging from 100 to 800  $\mu\text{m}$ . The study demonstrated that FDM is a useful technique for producing scaffolds with a relatively high precision of pore structure by highlighting that the porosity printing errors between the manufactured scaffolds and the intended design were below 5 percent. Tellis et al. [170]

used micro-CT imaging together with FDM to create scaffolds out of polybutylene terephthalate. These scaffolds were designed for applications involving the repair of trabecular bone. Kosorn et al. [171] carried out a study on the fabrication of porous scaffolds by FDM utilising a mixture of poly(caprolactone) and poly(hydroxybutyrate-co-valerate) (PHBV). Their results showed that the compressive strength of the scaffolds increased with the addition of a greater quantity of PHBV. Furthermore, the researchers successfully created composite scaffolds using FDM by combining PCL with poly(ethylene glycol) (PEG) [172].

Certainly, in recent advancements, even polymers with higher melting points have become valuable for FDM applications. An illustration of this is seen with polyether ether ketone (PEEK), which boasts a notably elevated melting point within the range of 330°C to 340°C. This distinctive attribute has paved the way for scaffold fabrication through a dedicated FDM system, precisely engineered to accommodate the properties of PEEK material [173]. The designed FDM system included a syringe with two different metal tubes: an accompanying stainless steel tube and a brass tube with an internal diameter of 17 mm and a 500 µm nozzle. The employment of the thermally conductive brass tube facilitated the efficient absorption of energy by the PEEK material, resulting in its complete melting. The effective production of PEEK scaffolds with a 38 percent porosity was accomplished by carefully controlling the nozzle temperature within the range of 400°C to 430°C and an extrusion rate set at 2.2 mg/s. Interestingly, these scaffold specimens showed a compressive yield strength of 29.34 MPa and a compressive yield strain of 4.4%.

Additionally, Rinaldi et al. [174] delved into the utilization of FDM for the production of PEEK scaffolds. Nevertheless, the utilization of high melting point polymers in Fused Deposition Modeling (FDM) poses several challenges. The notably high extrusion temperature creates a significant temperature gradient, leading to noticeable issues such as shrinkage, warping, and delamination. Consequently, meticulous regulation of the cooling process within the FDM framework is imperative to address these concerns. Notably, FDM techniques have been harnessed for the creation of composite scaffolds that incorporate a blend of both

polymers and ceramics, showcasing the versatility of this method in scaffold fabrication [175, 176]. Xu et al. [177] harnessed CT-guided FDM to craft bone scaffolds that combined PCL and HA, resulting in structures with attributes reminiscent of cortical bone. Interestingly, the structural characteristics and chemical makeup of these scaffolds were very similar to those of native bone. In compared to pure PCL scaffolds, in vivo evaluations demonstrated significantly enhanced biodegradability and greater capacity to promote new bone growth. Likewise, Kim et al. [178] used FDM to create a scaffold from a mixture of  $\beta$ -TCP and polylactic-co-glycolic acid (PLGA). Impressively, these scaffolds showed strong integration with the surrounding bone tissue after a 12-week implantation period, confirming their exceptional biocompatibility.

Poh et al. [179] built composite scaffolds out of PCL and bioglass using FDM. Intriguingly, in vitro research showed that the composite scaffold increased the expression of osteogenic genes. Furthermore, host tissue was observed to infiltrate the scaffolds effectively after an 8-week implantation period in nude rats. Although adding bioactive ceramics can improve the biological qualities of polymer scaffolds, doing so also presents unique difficulties. The addition of bioceramics with higher melting temperatures to the FDM process of composites causes the slurry to become more viscous and less fluid, which affects the precision and effectiveness of moulding. Additionally, many holes develop between the ceramic particles and matrix as a result of the various shrinkage characteristics, greatly reducing the mechanical properties of the scaffold. Therefore, supplementary processing steps play a crucial role in ensuring the scaffold's structural integrity and augmenting its mechanical properties.

### 3.3.4 Electron Beam Melting (EBM)

Arcam, a Swedish business, invented and first patented EBM technology [180]. Figure 3.8 illustrates the division of the EBM equipment into two main compartments: one housing the electron beam cannon and the other designated for specimen fabrication. Both compartments are maintained within a high vacuum

environment. EBM technique uses a high-energy electron beam to melt metal

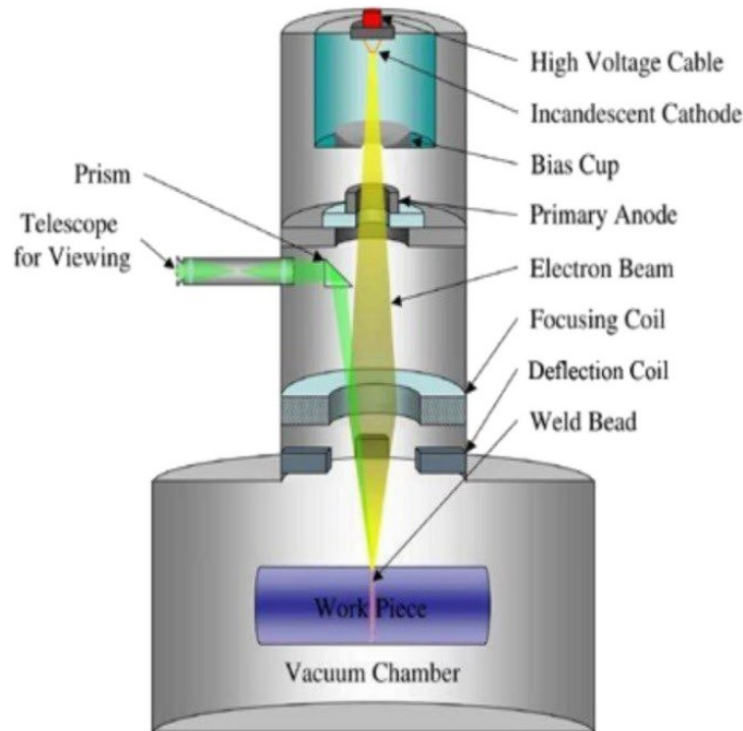


FIGURE 3.8: Developments on Electron Beam Melting (EBM) of Ti-6Al-4V: A Review: Electron Beam Melting Schematic [181]

powder as opposed to SLS or SLM. The powder layer is quickly scanned by the electron beam before to the EBM process, slightly heating it. The warmed powder is then selectively scanned by the electron beam using 3D hierarchical data, melting and solidifying it. High beam-material coupling efficiency of EBM, which enables processing of metals with extraordinarily high melting points, is a key benefit over SLS/SLM [182]. As a result, much study has been focused on using EBM for the creation of porous metal scaffolds. Certainly, Yan et al. [183] discussed a notable instance in which a 3D titanium scaffold was created utilising EBM after being modelled for a patient with a full mandibular deformity. The subsequent mandible graft exhibited successful integration, underscoring EBM's potential in bone grafting applications. Moreover, EBM was used by Ataei et al. [184] to create titanium alloy (Ti-6Al-4V) gyroid scaffolds with unusually high porosities between 82 and 85%. The resulting scaffolds demonstrated yield strengths of 13.1–15.0 MPa and elastic moduli of 637–1084 MPa, falling within the range of trabecular bone properties. Surmeneva et al. [185] demonstrated the fabrication of

triple- and double-layered titanium-based scaffolds through EBM, featuring gradient porosities spanning 21% to 65%. Comprehensive mechanical studies revealed that these scaffolds have compressive strengths between 31 MPa and 212 MPa and elastic moduli between 0.9 GPa and 3.6 GPa. Additionally, by adjusting the cellular shape, the mechanical properties of EBM-produced Ti-6Al-4V scaffolds, including their compressive strength, elastic modulus, and deformation behaviour, could be fine-tuned [186].

By utilizing Electron Beam Melting (EBM), Shah et al. [187] effectively produced Ti-6Al-4V and CoCr scaffolds that exhibited similar architectural characteristics. Later in vivo tests intended to investigate their impact on bone tissue growth. Nevertheless, both scaffold types exhibited similar patterns of bone formation within their porous structures. However, the CoCr scaffolds displayed a higher osteocyte density at their outer boundaries, which was attributed to their superior biomechanical properties. These results highlight the promising future of CoCr scaffolds in load-bearing applications requiring successful osseointegration. It is important to recognise that the limited resolution of the electron beam used in EBM, caused by focusing issues, causes a significant amount of surface roughness in the created scaffolds [188]. Additionally, the precision of EBM is limited to 0.3–0.4 mm, which presents difficulties when making scaffolds with small pore diameters. Eldesoukya et al. [189] looked into this restriction by measuring the geometric differences between the scaffolds made by EBM and the original CAD model under a digital optical microscope. According to the study, struts made with thinner walls produced more than they needed to, which reduced pore size and increased relative density. Furthermore, it was shown that strut thicknesses of less than 0.5 mm are insufficient for effective EBM processing.

### 3.3.5 $\mu$ Stereolithography ( $\mu$ SLA)

Vat polymerization, generally known as  $\mu$ SLA, is a manufacturing process that creates products by selectively curing photoreactive resin [190]. It starts with creating a liquid photopolymer inside of a container. Then, the surface of the liquid

is exposed to ultraviolet light in a preset pattern, which causes the photoreactive liquid to begin polymerizing. After each fresh layer has dried, the platform gradually lowers the partially completed components. This process is repeated until the entire item is constructed. The completed product has the desired structure once the extra resin has been drained. Free-radical polymerization and cationic polymerization are the two types of polymerization processes that  $\mu$ SLA often uses [191, 192].

The vector scan approach and the mask projection approach are the two subcategories of  $\mu$ SLA's irradiation types. In the vector scan method, a single UV beam acts as the radiation source and is focused using optics and a scanning galvanometer onto the liquid surface for polymerization. The mask projection method, on the other hand, uses a radiation source to create a broad pattern with a digital micromirror device, allowing one layer to harden at a time. In contrast, the vector scan technique often offers superior accuracy while the mask projection approach can yield improved construction efficiency. Figure 3.9 is an illustration of the  $\mu$ SLA technique.  $\mu$ SLA leverages specific synthetic polymers with photoreac-

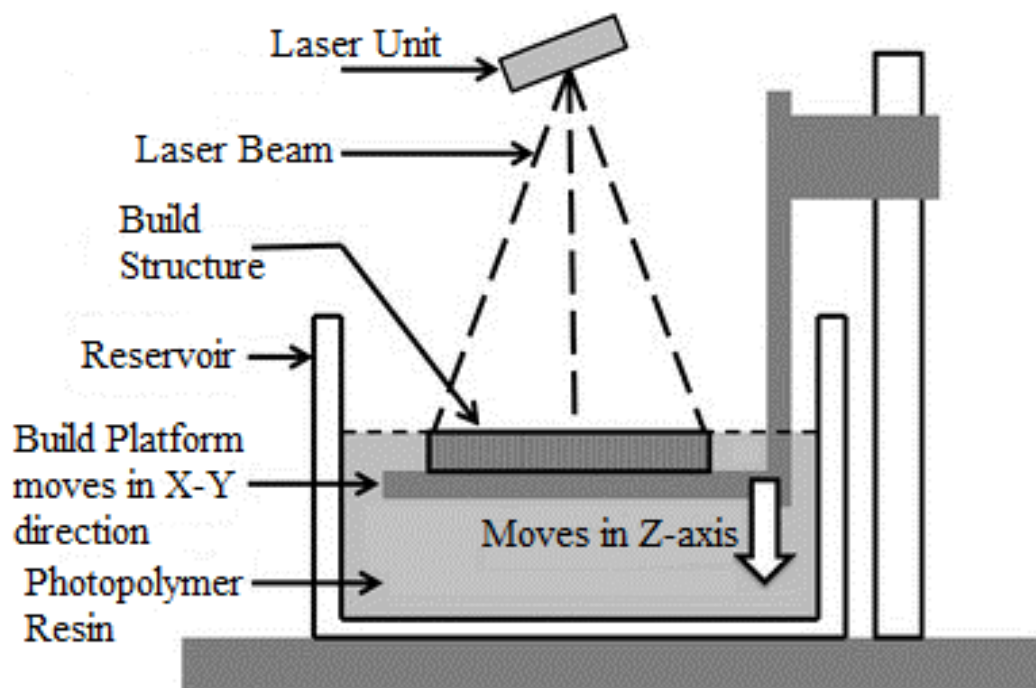


FIGURE 3.9: Schematics of micro-Stereolithography [193]

tive properties, high biocompatibility, and suitable mechanical characteristics. For

example, PCL has been employed in the  $\mu$ SLA process to create scaffolds [194]. The elastic characteristics of the  $\mu$ SLA-fabricated PCL scaffolds, demonstrated by a Young's modulus ranging from 6.7 to 15.4 MPa, were highlighted by mechanical assessments. Additionally, tests using cell culture verified their favourable biocompatibility. Poly(tetrahydrofuran), a different polymer with a Young's modulus range of 5.7 to 27.5 MPa and a bending strength range of 1.1 to 3.5 MPa, was also utilised in the creation of printed scaffolds [195]. This material exhibited no cytotoxic effects [196]. Additionally, Polyethylene glycol (PEG) was used in conjunction with  $\mu$ SLA procedures to create scaffolds with a wide elastic modulus range ( $5.3 \pm 0.9 - 74.6 \pm 1.5$  kPa).  $\mu$ SLA has furthermore been used to make composite scaffolds for bone tissue engineering.

In an instance,  $\mu$ SLA was successfully used by Guillaume et al. [197] to create composite scaffolds made of poly(trimethylene carbonate) (PTMC) and HA. A microscale structure was created on the scaffold's surface as a result of the addition of HA. Experiments in both the lab and on animals showed that the microscale-structured PTMC/HA scaffolds expedited bone repair kinetics and improved differentiation of marrow stem cells.  $\mu$ SLA has also demonstrated its applicability for crafting ceramic scaffolds. In this method, ceramic particles are typically evenly suspended within a resin and subsequently subjected to photopolymerization during the  $\mu$ SLA process.

Following this, the resin is incinerated, leaving the ceramic particles to sinter and fuse together. Thavornytikarn et al. [198] created bioceramic scaffolds by mixing 41 volume percent bioglass, 49 volume percent acrylate-based photopolymer resin, and 10 volume percent dispersion agent. The scaffolds were heated to 550°C for three hours to remove the binder, after which they underwent two hours of 950°C sintering. Similarly, Du et al. [199] used  $\mu$ SLA to successfully create customised ceramic scaffolds based on a model of a rabbit femoral segment. The cells consistently attached and multiplied over the scaffolds after a 5-day culture in oscillatory perfusion. Moreover, Levy et al. [200] successfully used  $\mu$ SLA methods to create HA ceramic scaffolds for orbital floor prostheses. It's noteworthy that employing  $\mu$ SLA to produce composite resins incorporating ceramics can present significant

challenges due to the substantial increase in viscosity. Furthermore, it's crucial that the particle size of the added ceramics is smaller than the curing thickness to prevent compromising processing accuracy. An alternative approach to scaffold production through  $\mu$ SLA has also been explored. For instance, Sabree et al. [201] used  $\mu$ SLA to make an epoxy mould from distorted pictures of implants. The mould was then filled with a very concentrated HA-acrylate suspension. Following that, pyrolysis was used to get rid of the mould and the acrylic binder. To speed up the densification procedure, sintering was applied to the remaining HA scaffolds. These resultant scaffolds had pores that ranged in size from 300 to 600  $\mu$ m and had a porosity of around 42%. In comparison to previous ceramic scaffolds with equivalent porosity produced utilising various fabrication techniques, their average crushing strength ranged from 10 to 25 MPa. Similarly, Kim et al. [202] used a similar deceptive method to create HA scaffolds.

$\mu$ SLA is distinguished from other additive manufacturing (AM) methods by its remarkable precision and resolution.  $\mu$ SLA has the capacity to create components with an accuracy as fine as 200 nm using the two-photon curing technique [203].  $\mu$ SLA has been used to create vascular scaffolds with complex and smaller pore architectures thanks to its special property. However, limitations in material selection and time-consuming post-processing steps continue to prevent  $\mu$ SLA from being used more widely in a range of biological settings.

### 3.3.6 PolyJet Printing (PJ)

PolyJet, an additive manufacturing technique, uses inkjet technology to fabricate a high-resolution physical model with a layer thickness of 16 micro -m. PolyJet technique uses a UV cured a photopolymer, inkjet head travel along x and y-axis to fabricate a final 3D product. Water soluble support material is used in this technique that can be removed with pressurized water. PolyJet technology boasts the unique capability to concurrently print multiple materials within a single product, which can result in enhanced material strength [204]. PolyJet 3D printing is a cutting-edge additive manufacturing method that relies on a photopolymer resin

to construct objects layer by layer. This technique holds substantial potential for producing bone scaffolds due to its capacity to craft intricate geometries with exceptional precision and accuracy.

One advantage of PolyJet 3D printing is that it can produce scaffolds with high resolution and smooth surfaces. This is because the technique uses inkjet print heads to deposit droplets of the photopolymer resin, which can be as small as 16 microns. This makes it possible to create scaffolds with complicated geometries and minute features that can imitate the intricate structure of real bone tissue. Another advantage of PolyJet 3D printing is that it can use a range of different materials to produce scaffolds with varying mechanical properties and biological activity. For example, researchers have harnessed PolyJet 3D printing to produce bone scaffolds by combining biocompatible polymers with hydroxyapatite nanoparticles. This combination enhances the scaffold's mechanical strength and biological activity. PolyJet 3D printing also offers the potential for mass customization of bone scaffolds, as the technique can produce multiple designs simultaneously, each with a different shape or porosity. This allows for the creation of scaffolds that are tailored to the specific needs of individual patients, improving their efficacy and reducing the risk of rejection or implant failure.

In summary, PolyJet 3D printing offers a promising approach to bone scaffold manufacturing. Its advantages include superior resolution, customizable designs, and the flexibility to employ various materials, resulting in scaffolds with a wide range of mechanical and biological characteristics. Nevertheless, continued research is essential to fine-tune the technique and comprehensively assess its performance in real-life scenarios, particularly in vivo applications.

### **3.4 Designing Technique for Bone Scaffolds**

The design of scaffolds holds a pivotal role in the advancement of bone scaffold development through additive manufacturing (AM). Porosity, pore size, and interconnectivity are fundamental characteristics of the porous structure that have a

significant impact on both their biological effectiveness and mechanical properties [205–207].

In particular, an ideal pore size in combination with increased porosity promotes the intake of nutrients and the ejection of metabolic waste, producing a setting favourable to the growth of bone formation [208].

Furthermore, the interior pore structure and material distribution within the scaffold exert a nuanced impact on its flexibility and stiffness. These factors play a crucial role in determining the stress dynamics experienced by the adjacent bone tissue following implantation [209]. Equally vital is the assessment of how the scaffold's mechanical performance evolves after implantation, a critical aspect woven into the fabric of the design process. Furthermore, the external geometry of the scaffold must align harmoniously with the unique morphological characteristics of the injury site, ensuring a seamless integration. Importantly, the design considerations should also cater to the specific requirements of additive manufacturing (AM) techniques, guaranteeing a smooth and efficient fabrication process. This holistic approach ensures not only the initial success of the implant but also its long-term functionality and compatibility with the surrounding tissue environment. For instance, accounting for overhanging structures devoid of corresponding support during the construction phase can avert undesired flaws [210].

### **3.4.1 CAD-Based Method**

The common technique for designing scaffolds relies heavily on computer-aided design (CAD) approaches and a variety of CAD programmes, including UG, CATIA, and Pro/E [211, 212].

These tools make it easier to build models based on the ideas of boundary representation (B-Rep) or constructive solid geometry (CSG). Through a series of Boolean operations utilising common solid primitives including cubes, cylinders, spheres, and prisms, CSG involves creating models. In contrast, B-Rep encapsulates solid models by delineating their borders, which are made up of vertices, edges, and

loops, without any direct relationship between these parts [213]. Models emerging from the B-Rep paradigm necessitate more storage space than CSG-generated models.

Consequently, when model complexity escalates or intricate internal structures are involved, B-Rep-derived models exhibit significantly larger file sizes, posing challenges for subsequent operations. Leveraging these modeling principles, CAD tools formulate an array of porous unit cells that amalgamate to construct comprehensive scaffolds. Researchers have crafted a diverse assortment of unit cells to typify bone scaffold architectures [214, 215]. For instance, Melchels et al. [216] developed three complex unit cells, the cube, diamond, and gyroid, which combined to create computer models that filled space and had different architectures. In comparison to the cube construction, gyroid architecture enabled a more equal distribution of stress and strain, according to finite element simulations of compression behaviour. Consequently, scaffolds adopting the gyroid architecture hold potential for affording adherent cells relatively uniform mechanical stimuli, potentially enhancing bone regeneration.

In a separate investigation, Sercombe et al. [217] created a unit cell with octahedral geometry. This structure's ability to withstand high tensile stress was demonstrated via finite element analysis. Specialised software has been created as a result of the need to streamline the CAD-based design process. Notably, the Belgian business Materialise unveiled Magics, a pre-processing tool for 3D printing that enables designers to easily combine a variety of connected unit cells. In a specific case, Murr et al. [218] used cross 1, G6, G7, and code thin components from the MATERIALISE programme to quickly build scaffolds. Researchers have developed the Computer-Aided System for Tissue Scaffolds (CASTS). This system incorporates a parametric library of scaffold architectures and an algorithm to regulate parameters such as pore size, porosity, and surface-to-volume ratio [214, 219]. By adjusting a number of factors, CASTS gives designers the ability to create scaffold models that are suited for porosity and pore size. Although CAD-based methods provide strong design skills, they do have certain drawbacks. The limited ability to influence the mechanical properties and structural performance

of the developed scaffolds is a key limitation. However, the utilization of Boolean operations introduces an inherent "staircase effect" on the external contours of models, which contributes to geometric distortions and potential mechanical instability [220]. The investigation of more complex and irregular designs is further hindered by the CAD-based methodology's restriction to developing scaffolds with periodic and regular structures.

### 3.4.2 Topology Optimization Top of Form

The optimal design of bone scaffolds requires a delicate balance between highly porous structures for cell infiltration and nutrient transport, and adequate mechanical properties for stable structural support [221–224]. This balance becomes even more challenging since increasing porosity to enhance material transport can often lead to compromised mechanical performance. Striking this equilibrium demands careful consideration of both aspects to achieve a comprehensive and optimal scaffold design. To address this challenge, topology optimization emerges as a valuable approach. This technique optimizes material distribution within a defined space, taking into account loading conditions, constraints, and performance criteria [225]. By applying topology optimization to scaffold design, it becomes possible to achieve an overall optimized performance while adhering to specific requirements. This could involve maximizing mechanical properties while maintaining a desired porosity level or achieving the highest permeability within defined constraints. In scaffold topology optimization, the problem is usually approached indirectly by optimizing a fundamental unit cell using specialized algorithms.

Once this optimized unit cell architecture is determined, it is replicated throughout the scaffold. The Solid Isotropic Material with Penalization (SIMP) technique and the Evolutionary Structural Optimization (ESO) method are recognized optimization algorithms for scaffold topology. They both analyze the structure point-by-point to achieve desired outcomes [226]. For instance, researchers have employed the SIMP algorithm to tailor competing properties, such as modulus and permeability, through a unified objective function [227, 228]. This approach has also

been used to optimize elastic properties, leading to scaffolds with bone-like remodeling rates [229]. The ESO-based topology optimization has resulted in unit cells with specific stiffness ratios and functionally graded structures [230]. The bidirectional evolutionary ESO method has been applied to optimize scaffold bulk and shear moduli under various volume fractions [231].

Another widely used technique in topology optimization is the level-set algorithm, which traces phase boundaries to describe smooth transitions between different materials [232]. This approach has been applied to scaffold design to maximize permeability [233], addressing fluid dynamics in porous structures [234]. Additionally, topology optimization has been utilized to tailor the thermal expansion properties of multimaterial porous structures [235]. Indeed, while topology optimization offers valuable insights into scaffold design, it's important to acknowledge its limitations. The conventional approach of optimizing unit cells and then arranging them periodically restricts the achievable architectures to regular and repetitive patterns. This stands in contrast to the intricate and irregular structures found in natural bone. Consequently, while topology optimization is a powerful tool, it may not fully capture the complexity of natural bone's architecture. Further research and innovation are needed to develop approaches that can mimic the irregular and hierarchical structures seen in real bone tissue.

### 3.4.3 Reverse Modelling

The process of directly reconstructing bone tissue microstructures involves using imaging modalities such as computed tomography (CT) or magnetic resonance imaging (MRI) scans of the item of interest. This approach is referred to as reverse modeling design, also known as image-based design [236]. In this approach, key elements for the reconstruction process are extracted from the CT/MRI slice images through a series of analysis. The slice data is often analysed using a binary value technique, where "1" denotes the solid region and "0" denotes the emptiness [237]. The information extracted from the slices is then utilized to map a predefined unit cell, generating a 2D model. The 3D model is then built layer by

layer using an additive manufacturing (AM) method using this 2D representation that has been turned into STL files. Reverse modelling details using pictorial illustrations are given in [238]. To provide a more precise architecture for bone tissue creation, this reverse modelling technology combines cutting-edge medical imaging tools, powerful image processing software, and quick AM techniques. Researchers are very interested in reverse modelling since it makes it possible to make customised scaffolds.

Sun et al. [239] used a unit library technique while methodically investigating modelling concepts to biomimetic construct porous structures. Similar methodologies were investigated by Hollister et al. [240, 241], wherein internal architectures were generated by modifying density in voxel datasets. Podshivalov et al. [242] created microscale structural scaffolds based on genuine micro-CT scans, building on these ground-breaking findings to produce geometrically exact models that closely resemble natural trabecular bone structures. Corroborating research has shown that the porous structures achieved through reverse modeling are highly favorable for cell growth. This further validates the benefits of irregular porous architectures [243, 244]. It's important to note, however, that the accuracy of reverse modeling is intricately tied to the resolution of the image acquisition apparatus. Additionally, this method calls for a significant amount of processing power and storage space, which presents difficulties for both consumers and software developers.

The process of directly reconstructing bone tissue microstructures involves using imaging modalities such as computed tomography (CT) or magnetic resonance imaging (MRI) scans of the item of interest. This approach is referred to as reverse modeling design, also known as image-based design [236]. In this approach, key elements for the reconstruction process are extracted from the CT/MRI slice images through a series of analysis. The slice data is often analysed using a binary value technique, where "1" denotes the solid region and "0" denotes the emptiness [237]. The information extracted from the slices is then utilized to map a predefined unit cell, generating a 2D model. The 3D model is then built layer by layer using an additive manufacturing (AM) method using this 2D representation that has been turned into STL files. To provide a more precise architecture for bone

tissue creation, this reverse modelling technology combines cutting-edge medical imaging tools, powerful image processing software, and quick AM techniques. Researchers are very interested in reverse modelling since it makes it possible to make customised scaffolds. Sun et al. [239] used a unit library technique while methodically investigating modelling concepts to biomimetic construct porous structures. Similar methodologies were investigated by Hollister et al. [240, 241], wherein internal architectures were generated by modifying density in voxel datasets.

Podshivalov et al. [242] created microscale structural scaffolds based on genuine micro-CT scans, building on these ground-breaking findings to produce geometrically exact models that closely resemble natural trabecular bone structures. Corroborating research has shown that the porous structures achieved through reverse modeling are highly favorable for cell growth. This further validates the benefits of irregular porous architectures [243, 244]. It's important to note, however, that the accuracy of reverse modeling is intricately tied to the resolution of the image acquisition apparatus. Additionally, this method calls for a significant amount of processing power and storage space, which presents difficulties for both consumers and software developers.

### 3.4.4 Mathematical Modelling

When designing scaffolds, mathematical modelling is essential because it makes it possible to use irregular polygonal models or implicit function surfaces to create porous structures with improved qualities. The triply periodic minimum surface (TPMS) method, a well-established technique in this strategy, employs trigonometric functions to craft intricate porous structures. These structures exhibit minimal surfaces, with zero curvature at every point [237]. Due to the periodic nature of trigonometric functions, TPMS structures also display periodicity in three distinct directions, guaranteeing that there are no sealed cavities in the geometry [245]. Surprisingly, natural objects like beetle shells, butterfly wings, and crab bones have limited surface geometries [246]. Rajagopalan et al. [247] invented a TPMS-based method for creating tissue scaffolds that makes use of a

straightforward primitive (P-type) unit. For the design of bone scaffolds, other TPMS unit types, such as diamond (D-type) and gyroid (G-type), have also been proposed [248].

Research on the impact of TPMS-based morphologies on cell migration showed that, in comparison to salt-leached scaffolds with random-pore architectures, scaffolds with minimum surfaces had increased permeability. They also exhibited improved wetting qualities and a more uniform dispersion of cells [249]. Kapfer et al. [248] investigated network solids and sheet solids as two different TPMS-based structural types. In sheet solids, porous structures are generated by extending the minimal surfaces into sheets with a predefined thickness. In network solids, the minimal surface forms the solid/void interface. With comparable volume fractions and Poisson's ratios, sheet solids showed much better mechanical stiffness than network solids, according to a finite element analysis.

Sheet solids also demonstrated superior material utilisation, providing more pore space and surface area for cell activity. The development of gradient, heterogeneous, hybrid, and irregular porous structures using TPMS has received substantial research. For instance, Melchels et al. [216] used a linear function to illustrate gradient porous structures based on TPMS. Feng et al. [250] used TPMS with solid T-splines to create heterogeneous porous scaffolds with irregular thresholds, periods, and units. Yang et al. [251] introduced CAD techniques for hybrid porous structures with various TPMS-based substructures and specified transition borders. These techniques allow TPMS-based substructures to be positioned fluidly inside the scaffold domain [252–255]. Similarly, Yoo et al. [256–258] combined distance fields with TPMS-based functions to create pseudorandom porous scaffolds with specific goals. Yang et al. [259] created gradient and completely irregular porous structures using coordinate transformation based on TPMS, extending the use of TPMS to irregular design fields. The stochastic porous structures made using this technique, however, had porosities lower than 74 percent, the threshold at which the solid phase detached. The Voronoi-Tessellation method, which creates porous models using Voronoi diagrams, is another widely used mathematical modelling technique. In this method, the design volume is divided into regions by a

series of points (called seeds). To build a porous scaffold, the partitioned sections' edges are given a thickness [260, 261]. With a focus on 2D pore structures, Kou and Tan introduced the idea of building porous structures based on the Voronoi diagram. They did this by utilising the vertices of the Voronoi diagram as control points for a closed B-spline curve to produce convex-shaped cells [262, 263].

Chow et al. [264] arranged the Voronoi seeds into concentric circles to create a 2D shape area. By adding a time dimension to the dynamic pattern in the third dimension of the 2D shape region, chow extended it to create 3D porous structures. Significant improvements in Voronoi-Tessellation-based scaffold design have been made recently. Fantini et al. [265] combined the Grasshopper Plug-in with Rhinoceros CAD 3D software to create bone scaffolds using the Voronoi-Tessellation approach, creating relationships between input variables and scaffold structures. [266].

Gómez et al. [267] offered a concept for a trabecular structure that resembles a bone utilising the Voronoi-Tessellation method and seeds taken from micro-CT images of trabecular bone. The primary histomorphometric indices of the isotropic porous scaffolds matched those of normal bone. Wang et al. [268] introduced a probability sphere method for random seed generation based on Voronoi-Tessellation, achieving a balance between irregularity and controllability. The method enabled precise design of highly mimic scaffolds with adjustable porosities, pore sizes, and porosity gradients. The Voronoi-Tessellation method combines the benefits of reverse modeling and topology optimization. This approach allows for the creation of bionic structures while improving their porosity, permeability, and mechanical strength.

### 3.5 Research Gap

Additive manufacturing techniques have revolutionized the field of bone scaffold development by providing distinct advantages along with their own set of challenges. Among these techniques, Selective Laser Sintering (SLS) stands out as a

powerful method capable of processing a diverse range of biomaterials, including polymers, ceramics, and metals. Selective laser sintering (SLS) boasts remarkable beam-material coupling efficiency, making it highly effective for processing metals with high melting points. Furthermore, it has the potential to manufacture ceramic scaffolds with nanoscale grains, which can enhance their mechanical properties. However, SLS's inherent limitation in resolution can lead to surface roughness, and its relatively brief sintering duration may hinder complete densification and efficient grain boundary diffusion.

Selective Laser Melting (SLM) distinguishes itself through its comprehensive melting and solidification process, yielding fabricated parts with remarkable surface quality, density, and mechanical strength. This technique is particularly well-suited for crafting metal scaffolds featuring intricate geometries. Nonetheless, SLM's applicability is confined to conductive metal materials. The elevated extrusion temperature it employs can give rise to challenges such as shrinkage, warpage, and delamination during the manufacturing process. Furthermore, the prolonged cooling period inherent in SLM can have a detrimental effect on efficiency. This emphasizes the importance of thorough material selection and the careful consideration of design parameters.

Fused Deposition Modeling (FDM) stands out as a versatile and cost-effective approach, particularly adept at handling polymers with lower fusing temperatures. This method excels at creating scaffolds with an admirable degree of pore structural precision, making it a desirable option for applications in bone tissue creation. FDM also makes it possible to build scaffolds that are strengthened with nanomaterials with small dimensions. Nonetheless, its utility is governed by the selection of polymers with lower fusing temperatures, which can potentially constrain the range of available materials. Moreover, the potential for shrinkage and warpage exists due to the pronounced temperature gradients during the fabrication process. Achieving smaller pore sizes can also be a challenging task.

Electron Beam Melting (EBM) is distinguished by its remarkable efficiency in coupling the electron beam with materials, thereby enabling the processing of metals

boasting exceedingly high melting points. This technique showcases impressive mechanical strength and offers porosities that align well with the requirements of bone tissue engineering. Furthermore, EBM's promise extends to the creation of Osseointegrated scaffolds designed for load-bearing scenarios. However, EBM does encounter resolution limitations due to the difficulties in precisely focusing the electron beam. This complexity can arise when attempting to fabricate scaffolds with smaller pore sizes. Moreover, the extended periods required for sintering and cooling can impact overall efficiency, necessitating meticulous process control measures. In summary, each additive manufacturing technique brings distinct advantages and limitations to the realm of bone scaffold fabrication. Researchers and practitioners must meticulously assess the particular requirements of their intended applications and consider the properties of the biomaterials involved. This thoughtful assessment will guide the selection of the most fitting technique, ensuring optimal scaffold design and performance outcomes. This study aims to overcome challenges related to material constraints, manufacturing techniques, and fluid transport properties. In light of these limitations, this study aims to examine the feasibility of enhancing the transport and mechanical properties of acrylate-based polymer bone scaffolds by leveraging PolyJet printing technology, all the while ensuring the maintenance of a high degree of precision. The investigation will encompass not only experimental assessments but also numerical analyses to scrutinize the deformation behaviors exhibited by these 3D-printed scaffolds as stated in problem statement.

# Chapter 4

## Design, Development and Experimentation

### 4.1 Introduction

This chapter is primarily concerned with the design and development of all the elements employed in the experimental examination of the synthetic bone scaffolds. CAD- based technique is used to create bone scaffolds for 3D printing, as it allows for precise and accurate design specifications for tailoring the scaffold's geometry to match specific patient needs. An experimental setup for flow rate measurement along with scaffold holding clamp is developed for permeability analysis. The experimentation included test fluid preparation and viscosity measurement of bone scaffolds. To ensure the reliability and safety of the scaffold holding clamp, a leak tightness test is performed using a blind sample. The blind sample is specially designed and 3D printed to assess the leak-proof characteristics and its capability to securely hold the scaffolds during permeability analysis. The mechanical testing of synthetic bone scaffolds for compressive response is an integral part of this chapter. Alongside this, standard samples are designed and developed to examine the compressive properties under various printing orientations. Through these

investigations, we gain invaluable insights into how the structural arrangement of the scaffold impact its overall mechanical behavior and performance.

## **4.2 Design and Development of Bone Scaffolds Through PolyJet Technique**

Scaffolds inherently differ from the intricate and variable structure of natural bone tissue. Hence, there is a need for research into simpler scaffold designs that can effectively mimic the mechanical and functional aspects of the target tissue. This includes aspects like pore size, porosity, pore shape, and other characteristics. Careful consideration is given to the scaffolds' pore size, porosity, and pore shape in order to address this. The choice of pore sizes was guided by cellular responses, aiming to emulate the natural bone environment for optimal tissue regeneration. Furthermore, the study incorporated three distinct porosity levels to minimize the stiffness discrepancy between the scaffold and native tissue, thereby alleviating the stress shielding phenomenon. Specific pore shapes were also identified to optimize mechanical properties, enhancing scaffold efficacy. In healthy human bones, pores typically fall within the range of 300 to 600  $\mu\text{m}$ . However, in cases of osteoporosis, this range can expand to 3000  $\mu\text{m}$ , accompanied by porosity levels that span from 30% to 90%. By harmonizing scaffold parameters with these characteristic ranges, the study endeavors to forge more efficient load-bearing bone scaffolds.

Creo Parametric 4.0 and SolidWorks modelling software were employed to carefully select and generate 3D CAD models of bone scaffold constructs after carefully assessing all relevant factors. The chosen structures were hexagonal and cubic closed-packed pore geometries, selected for their simplicity. In these structures, all of their struts are arranged perpendicularly at angles of either  $90^\circ$  or  $60^\circ$  to one another. Referring to Figures 4.1 & 4.2, The CAD models depicted the enclosed cylindrical structure as having dimensions of 15 millimetres in height and 30 millimetres in diameter. The closed-packed cubic and hexagonal formations in Table 4.1, CAD models of 3D scaffolds were developed to show the capabilities of the

selected additive manufacturing technologies. The inner length of the cube's sides and the smallest diameter of the inscribed circle in the hexagonal closed-packed structure geometries were measured to determine the pore diameters. With the use of these particular pore geometries, a thorough design process for CAD-based scaffolds is being undertaken in an effort to maximise mechanical performance and appropriateness for bone tissue regeneration.

TABLE 4.1: Selected structural parameters for bone scaffold. (C- cubic structures, H- hexagonal closed packed structures, **Bold\*** - not possible because of the thinner struts)

Pore Size	Porosity Level					
	mm	30%		50%		70%
<b>0.2</b>	<b>C*</b>	<b>H*</b>	<b>C*</b>	<b>H*</b>	<b>C*</b>	<b>H*</b>
<b>0.34</b>	C	<b>H*</b>	<b>C*</b>	<b>H*</b>	<b>C*</b>	<b>H*</b>
<b>0.6</b>	C	H	C	<b>H*</b>	<b>C*</b>	<b>H*</b>
<b>1.5</b>	C	H	C	H	C	H
<b>2</b>	C	H	C	H	C	H
<b>2.5</b>	C	H	C	H	C	H
<b>3</b>	C	H	C	H	C	H

Figures 4.1 depicts front and isometric views of the 3D CAD models of the scaffolds with cubic and hexagonal closed-packed pore geometries (a) and (b), as well as Figures 4.2 (a) and (b). Figures 4.1 (c) and 4.2(c) exhibit optical pictures of the 3D-printed scaffold structures taken with a Keyence-Digital microscope model VHX-2000. The cylindrical structures that contained the cubic and hexagonal closed-packed structures were made to lock them in place within a particular rig for performing permeability tests. The 3D printing process commenced by exporting and saving the CAD models in the  $\mu$ STL (micro-stereolithography) format. This format is widely used in additive manufacturing because of its simplicity, lightweight nature, and ease of handling. The cubic and hexagonal closed-packed scaffolds were produced using the PolyJet and micro-stereolithography ( $\mu$ SLA) printers. STRATASYS and ASIGA provide several alternatives for 3D printing materials. For this project, it was decided to print the scaffold structures using

commercially available VeroClear material from STRATASYS and PlasWhite material from ASIGA. These materials were selected based on their suitability for the intended purpose of the study.

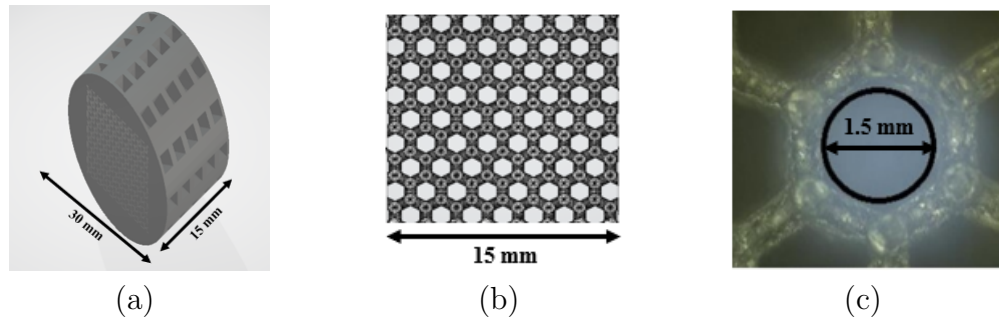


FIGURE 4.1: A 3D printed scaffold pore is shown in (a) an isometric view, (b) a front view, and (c) an optical microscopic image. scaffold structure in 3D CAD with hexagonal pore shapes

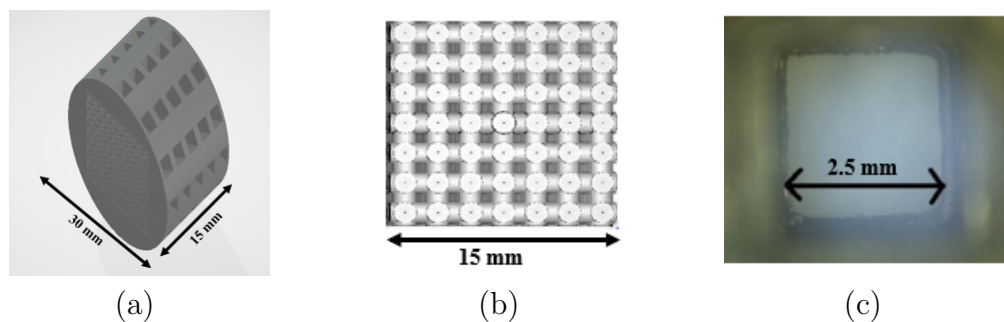


FIGURE 4.2: Optical microscopic image of a scaffold pore taken with a 3D printer in (a) an isometric perspective, (b) a front view, and (c) a 3D CAD model of the scaffold structure with a cubic pore shape

#### 4.2.1 Specifications of Stratasys Objet260 Connex 1

The 3D printer is equipped with a high-capacity material cabinet capable of holding up to eight sealed 3.6 kg cartridges. This enables the loading of three different model materials simultaneously and facilitates hot-swapping when necessary. The printer's net build size is 255 x 252 x 200 mm (10.0 x 9.9 x 7.9 in.), allowing for the construction of rather big sculptures. Impressively, the printer provides exceptionally accurate printing by providing horizontal build layers with a maximum thickness of 16 microns (0.0006 in.). The build resolution is equally impressive with a 600 dpi resolution for both the X and Y axes and an outstanding 1600 dpi

resolution for the Z-axis. The printer delivers enhanced precision, with features smaller than 50  $\mu\text{m}$  falling within a range of 20-85  $\mu\text{m}$  and full model sizes up to 200  $\mu\text{m}$  (relevant to rigid materials only). The outcome is influenced by factors such as geometry, build settings, and model orientation.

In terms of its physical dimensions, the printer measures 870  $\times$  735  $\times$  1200 mm (34.25  $\times$  28.9  $\times$  47.25 inches) and weighs 410 kg. Additionally, it has a material cabinet with enough storage for the different printing-related supplies, measuring 330  $\times$  1170  $\times$  640 mm (13  $\times$  46.1  $\times$  26.2 in.) and weighing 76 kg. Overall, the printer is a fantastic tool for a variety of 3D printing applications due to its remarkable capabilities and exact output.

## 4.2.2 Material Used in PolyJet Technique

VeroClear (acrylic monomer < 30%, acrylic oligomer < 15%, isobornyl acrylate < 25%, photoinitiator < 2%, and acrylic acid ester < 0.3%) is a type of 3D printing material that offers high clarity and transparency, making it well-suited for creating objects with a glass-like appearance. It is often used in various industries, including product design, prototyping, architecture, and medical modeling. Here's a detailed explanation of VeroClear material:

- i. **Material Composition:** VeroClear is typically a photopolymer resin used in a specific type of 3D printing called PolyJet technology. PolyJet printers use a UV-curable liquid resin that is jetted onto a build platform layer by layer and then cured with UV light. The resulting object is built up from these cured layers.
- ii. **Transparency and Clarity:** VeroClear is specifically formulated to achieve a high level of optical clarity and transparency, similar to glass or clear plastic. This unique property allows for the creation of objects that are see-through, allowing light to pass through the material and giving it a visually appealing, glass-like appearance.

- iii. **Applications:** Due to its clarity, VeroClear is often used in applications where visual representation, aesthetics, and transparency are important. It's commonly employed in product design and prototyping to create realistic, transparent prototypes that accurately mimic the look of the final product.
- iv. **Prototyping and Visualization:** Engineers, designers, and manufacturers utilize VeroClear for prototyping purposes. This allows them to visualize internal structures, mechanisms, and other design features that may not be easily observable when using opaque materials. This is particularly useful for testing fit, form, and function before proceeding to production.
- v. **Medical and Scientific Models:** VeroClear is also used in medical and scientific fields to create anatomical models, medical devices, and research prototypes. Its transparency is advantageous for creating accurate models that can be examined, studied, and even used for surgical planning.
- vi. **Multi-Material Printing:** Some PolyJet 3D printers allow for multi-material printing, where different materials can be jetted simultaneously to create objects with varying properties. VeroClear can be used in conjunction with other materials to achieve specific effects, such as combining transparent and opaque components within the same model.
- vii. **Post-Processing and Finishing:** Although VeroClear produces objects with impressive transparency, post-processing steps, such as sanding and polishing, can further improve the clarity and smoothness of the final printed piece. This can result in an even more glass-like appearance.
- viii. **Limitations:** Despite its optical clarity, VeroClear may not have the same level of impact resistance or mechanical strength as some other 3D printing materials like ABS or nylon. Care must be taken when designing functional parts that require durability.

In summary, VeroClear stands out as a specialized material tailored for 3D printing, renowned for its remarkable transparency and clarity. This particular material

finds application across diverse industries, serving purposes such as prototyping, visualization, and crafting objects with a striking glass-like finish.

VeroClear's exceptional characteristics make it an invaluable tool for a wide range of professionals, including designers, engineers, and researchers. It enables them to create models and prototypes that not only have visual appeal but also demonstrate functional precision and accuracy. This distinctive material choice empowers the creation of aesthetically appealing yet fully functional models across various fields of endeavor.

### 4.2.3 PolyJet Printing of Bone Scaffolds

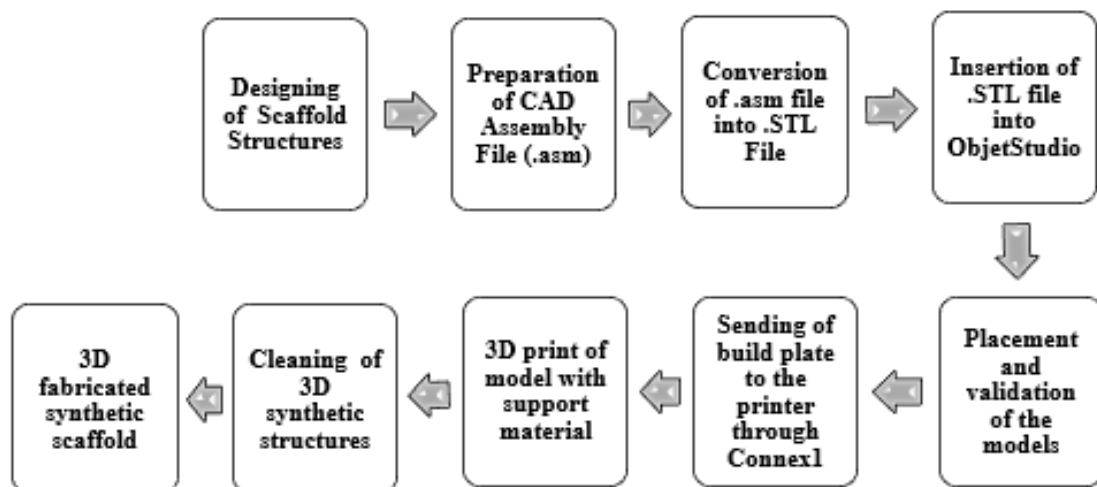


FIGURE 4.3: Procedure followed for the fabrication of 3D synthetic scaffold structure by using PolyJet Technique

PolyJet 3D printing (3DP) involved a series of steps to fabricate the scaffold structures. The scaffold structure is designed before the CAD assembly file is prepared. The assembly file is then converted into an .STL file, which is subsequently inserted into ObjetStudio. In ObjetStudio, the models are placed and validated, ensuring the correct positioning and avoidance of any potential issues during the printing process. The build plate is sent to the printer through Connex1, and the 3D printing is carried out. Upon completion of the printing process, the printed

object is cleaned, with support structures being removed, and any necessary post-processing steps being performed to enhance structural integrity and surface finish. Six scaffold samples were successfully produced on the PolyJet printer in around 90 minutes, and all 28 samples were printed successfully in a total of 7 hours.

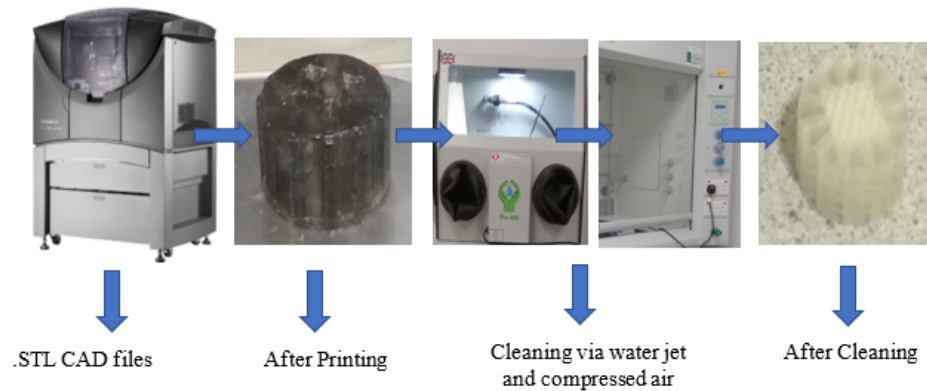


FIGURE 4.4: 3D printing of polymeric bone scaffold using PolyJet Technique

It is important to note that the scaffold samples with hexagonal pore geometry took somewhat longer to print than those with cubic pore geometry. The longer printing time can be ascribed to the hexagonal pore shape's higher complexity. The support material (SUP706) that was employed during printing was taken out of the structures thereafter. After being treated to a water jet at a pressure of 30 bars, the structures were cleaned using compressed air at 4 bars. The full elimination of any lingering support material residues was guaranteed by this comprehensive cleaning procedure. However, it's important to mention that the successful printing of scaffold structures can sometimes be influenced by specific design parameters. In the case of certain scaffold structures marked with an asterisk (\*) in Table 4.1, their smaller strut thickness presented challenges during the PolyJet printing process. It was challenging to replicate these structures precisely due to the complexity of these designs and the constraints of the printing technology. This highlights the sensitivity of additive manufacturing to design intricacies and emphasizes the need for careful consideration of design parameters to ensure successful fabrication. Such insights are valuable for researchers and practitioners aiming to optimize the additive manufacturing process for intricate scaffold designs.

## **4.3 Design and Development of Bone Scaffolds Through $\mu$ SLA Technique**

### **4.3.1 Specifications of Asiga - Freeform Pico Plus 27 – Specifications**

The "Asiga - Freeform Pico Plus 27" printer boasts compact dimensions of 35 x 21.8 x 76mm\*, offering precise printing with a layer thickness of 27 microns. The printer's high-resolution capabilities are enhanced by a pixel density of 0.5 pixels per centimetre, adjustable in 1-micron increments. This versatile printer features a UV LED light source and supports both STL and SLC file formats. It is compatible with various operating systems, including PC, Linux, and Mac. Additionally, it comes with Composer software included. With a built-in 10/100 Ethernet connection, it ensures seamless communication.

The Freeform Pico Plus 27 finds applications in both medical and general settings. Despite its powerful performance, the printer maintains a relatively small footprint, measuring 220 x 225 x 505mm and weighing only 10Kg. For transportation or storage, the dimensions with packaging are 320 x 320 x 700mm, with a total weight of 15.5Kg. The printer supports a wide range of power inputs, ranging from 100V to 240V at 50 to 60Hz, with a maximum current of 2A. Its exceptional features and capabilities make it an ideal choice for precision 3D printing tasks across various industries.

### **4.3.2 Material Used in $\mu$ SLA Technique**

PlasWHITE is a durable and versatile 3D printing material designed to replicate the properties of tough materials like ABS (Acrylonitrile Butadiene Styrene) and Polypropylene (PP). It offers a combination of high strength and intricate detailing, making it well-suited for a variety of prototyping applications. Here's a breakdown of the key features and characteristics of PlasWHITE material:

- i. **Material Composition:** PlasWHITE is a specialized polymer-based material that shares similarities with ABS and Polypropylene. These materials are known for their toughness, impact resistance, and versatility.
- ii. **Strength and Durability:** PlasWHITE is engineered to provide elevated levels of strength, making it capable of withstanding mechanical stress and impact. This property is crucial for creating functional prototypes, jigs, fixtures, and other components that need to endure real-world conditions.
- iii. **Prototyping Applications:** PlasWHITE is particularly well-suited for general prototyping purposes. It can be used to create functional prototypes that closely resemble the properties of the final product, allowing for testing and evaluation before committing to mass production.
- iv. **Versatility in Applications:** In addition to prototyping, PlasWHITE can be utilized for crafting jigs and fixtures. These tools are used to assist in manufacturing and assembly processes. The material's durability and strength make it suitable for creating custom tools that withstand repetitive use.
- v. **Printer Compatibility:** PlasWHITE is designed to be used with 3D printers that operate at wavelengths of 385nm and 405nm. This compatibility ensures that the material can be effectively used with specific types of 3D printing equipment. The material is formulated to retain fine details and intricate features during the 3D printing process. This characteristic ensures that the printed objects have a high level of precision and accuracy, suitable for creating prototypes with complex geometries.
- vi. **Quality Assurance:** PlasWHITE, manufactured by Asiga, embodies the pinnacle of quality and reliability in additive manufacturing. Asiga's unwavering commitment to excellence is evident in every aspect of PlasWHITE's production, meticulously adhering to internationally recognized quality standards. With certifications such as ISO 13485:2016 and EN ISO 13485:2016, specifically tailored for medical devices, PlasWHITE is meticulously crafted to meet and exceed the stringent requirements of the medical industry.

In summary, PlasWHITE is a robust 3D printing material that combines the toughness of ABS and Polypropylene with the precision and detail definition required for various prototyping and functional applications. Its properties make it a valuable choice for industries that require durable and accurately detailed prototypes, tools, enclosures, and more.

### 4.3.3 $\mu$ SLA Printing of Bone Scaffolds

When utilizing microstereolithography ( $\mu$ SLA) 3D printing, the process involved sending the scaffold's .STL files to the  $\mu$ SLA printer through the associated software are shown in Figure 4.5 The scaffold structure is designed before the CAD assembly file is prepared. The assembly file is then converted into an .STL file, which is subsequently inserted into Composer software. In Composer, the models are placed and validated, ensuring the correct positioning and avoidance of any potential issues during the printing process. The build plate is sent to the printer through Connex1, and the 3D printing is carried out. Upon completion of the printing process, the printed object is cleaned, with support structures being removed, and any necessary post-processing steps being performed to enhance structural integrity and surface finish. The printing process was subsequently completed by the  $\mu$ SLA printer, which produced one scaffold at a time in around three hours and twelve minutes. To get precise details, a slice thickness of 0.025 mm was used. After printing, the printed scaffold structures underwent a post-processing step. Initially, the structures were subjected to sonication in Isopropyl Alcohol (IPA) for a duration of 20 minutes. This step aided in the removal of any residual resin material that might have remained on the scaffold surfaces. Subsequently, the solid support structures that were used during printing were manually removed from the scaffold structures. This multi-step post-processing procedure ensured the cleanliness and integrity of the final printed scaffold products. This study was more focused on investigating the effect of the different pore geometry on the compression performance of AM parts; hence the input processing parameters were unified and kept constant so that a direct comparison can be carried out.

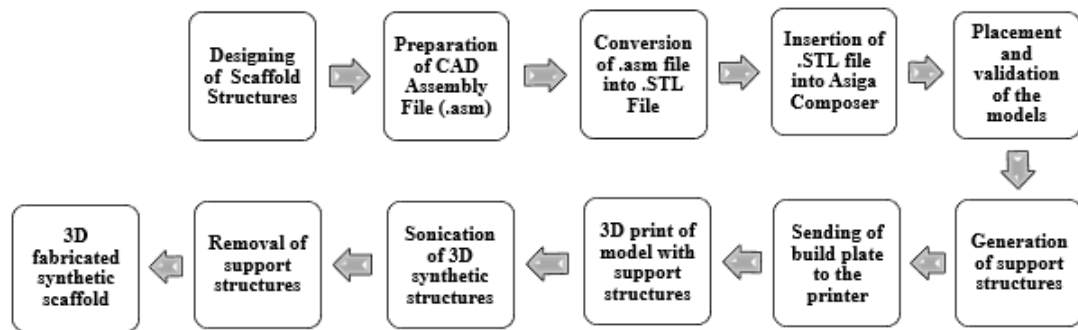


FIGURE 4.5: Procedure followed for the fabrication of 3D synthetic scaffold structure by using micro-stereolithography

## 4.4 Experimentation of 3D Printed Bone Scaffolds

### 4.4.1 Experimental Setup of Flow Rate Measurement

In order to assess the inherent permeability of the scaffold structures, a constant head permeability testing setup was carefully designed and conducted, as illustrated in Figure 4.6. The fluid storage tank for the device had a substantial

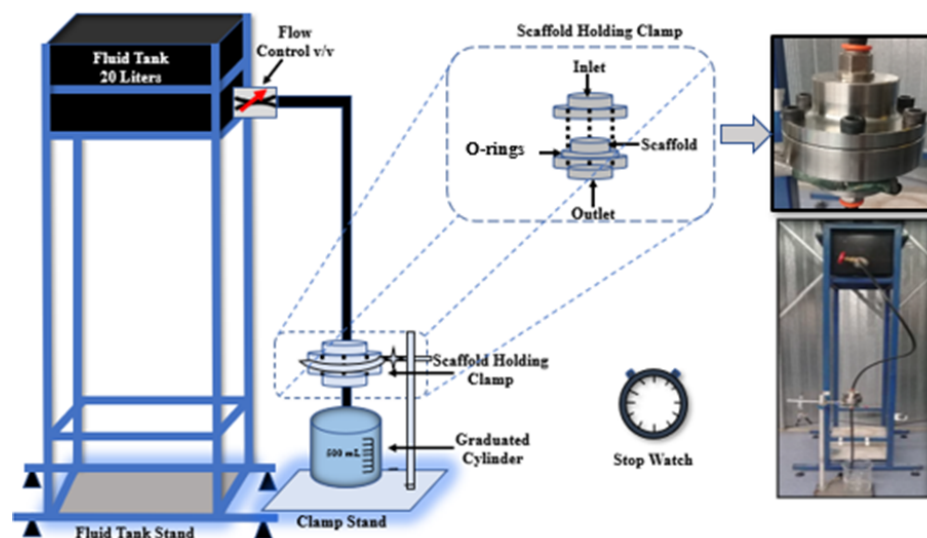


FIGURE 4.6: An experimental setup for an investigation of the permeability of 3D-printed porous bone scaffolds

20-liter capacity and was positioned 800 millimetres above the scaffold's surface.

This arrangement was devised to apply a hydrostatic pressure to the scaffold, ensuring a consistent head of fluid above the structure during testing. This hydrostatic pressure was essential for generating a controlled flow through the scaffold, enabling accurate measurements of its intrinsic permeability characteristics.

#### 4.4.2 Scaffold Holding Clamp and Blind Sample

Stainless-steel holding clamps were precision-machined with a high-precision CNC machine and created using Creo Parametric 4.0 software to anchor the scaffold structures during flow rate measurements. This made sure that the scaffold was placed correctly and consistently for the flow rate measurements.

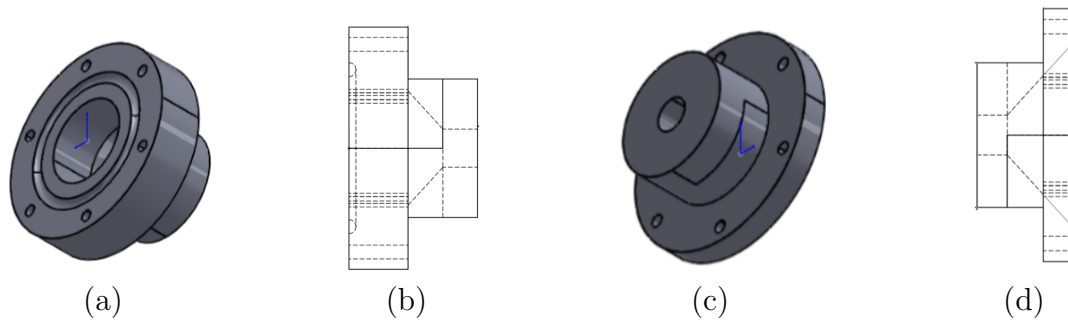


FIGURE 4.7: Clamping device: (a) an isometric view of the lower section (b) a side view of the lower part (c), and (d) an isometric view of the top part (d) Side view of the upper part

#### 4.4.3 Leak Tight Test of Scaffolds Holding Clamp

To validate the effectiveness and sealing performance of the clamp, a leak-tight test was conducted. Three copies of a dummy sample that had dimensions similar to those of the scaffold were created using the PolyJet printer. These samples were then subjected to a three-hour leak-tight test using tap water, mimicking the conditions of the subsequent permeability tests. The clamping process was repeated periodically to ensure the integrity of the O-rings and their resistance to wear or flattening. The laboratory temperature was maintained at 22°C to avoid any potential impact on the samples, test fluids, and seals, in consideration of the ambient conditions.

#### 4.4.4 Test Fluid Preparation

Tap water, a 15% glycerol-water mixture, and a 20% glycerol-water mixture were carefully chosen as the three test fluids to carefully assess the permeability of the 3D printed scaffolds samples. Previous studies have used these specific test fluids in permeability assessments of different scaffold topologies [269]. A variety of test fluids have also been used in other research, including raw seed oil [270], olive oil [271], acrylic cement [272], silicone oil [273], and corn oil [274].

The inclusion of these three distinct test fluids aimed to examine how fluid viscosity affects permeability. The compositions of the water-glycerol solutions were meticulously adjusted to mimic human blood viscosity in the absence of cells, covering a viscosity range from  $1 \times 10^{-3}$  Pa·s to  $1.3 \times 10^{-3}$  Pa·s [275]. The glycerol used in the test fluids was sourced from Alfa Aesar in England.

#### 4.4.5 Viscosity Measurement

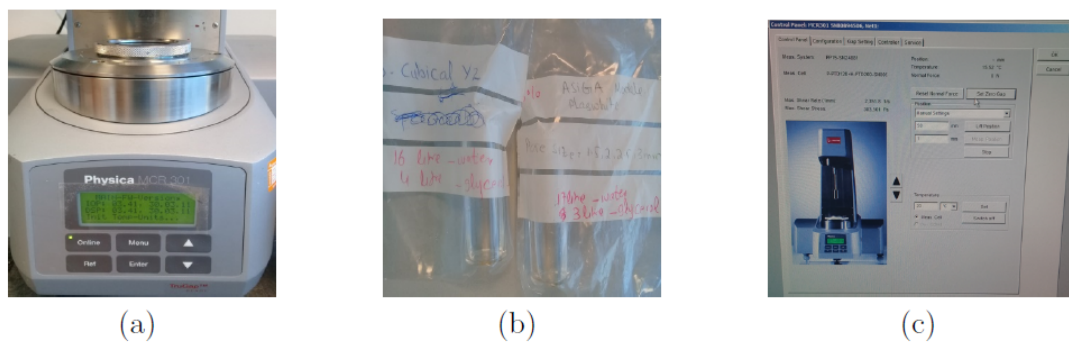


FIGURE 4.8: Viscosity measurement (a) Physica MCR-301 (b) 3ml solution sample (c) measurement setting

The viscosity of the prepared test fluids was measured using the Anton Paar Physica MCR-301 Rheometer. To ensure accuracy, three 3 ml samples were used for each test fluid.

Viscosity measurements were taken at the 100th iteration, yielding average viscosities of approximately 1.1 mPa·s, 2.35 mPa·s, and 2.87 mPa·s at 22°C for tap water, a 15% glycerol-water solution, and a 20% glycerol-water solution, respectively.

#### 4.4.6 Calculating Contact Angle and Surface Energy

The surface energy and contact angle of a material have a significant impact on and result in increased permeability. It's important to remember that experimentally measured permeability may be affected by higher contact angles caused by the surface energy of the material used to construct the 3D scaffold structures. To investigate the effect of contact angle and the surface energy of the printed scaffolds on fluid penetration through the pores, the FTA 200 Dynamic contact angle analyzer was employed. Using test liquids such tap water, a 15 percent glycerol-water solution, and a 20 percent glycerol-water solution, this equipment made it possible to determine contact angles. This approach provided new understanding of how permeability, surface energy, and contact angle interact.

In this work, the contact angle was determined using the sessile drop technique. Scaffold constructions with a height of 5 mm were created and 3D printed utilising the PolyJet and  $\mu$ SLA printing technologies to enable precise measurements. It's critical to keep in mind that the original scaffold designs were 15 millimetres tall. To match the maximum working height of the FTA 200 Dynamic contact angle analyzer, which also measured 15 millimetres, special scaffold designs with a height of 5 mm were created. The intention was to guarantee correct angle measurement and the entire creation of a hanging drop.

The scaffold constructions were set up for testing on a horizontal stage in the direction they were built. Using a micro syringe, 3  $\mu$ L of the probe liquid were then injected at a regulated flow rate of 1  $\mu$ L/s onto the scaffold surface. In order to provide accurate results, each reported contact angle value is the average of at least three measurements taken at various points on the 3D printed sample surface. This method ensures accurate data collection and a precise representation of the scaffold's wetting behaviour. This methodical testing procedure, in general, enables correct perceptions of the interactions between the probe liquid and the scaffold surface. To calculate surface energy, we considered the measured contact angle along with the surface tension, including polar and dispersive components, as well as surface tension alone. A number of models, including the Girifalco,

Owens, Wendt geometric mean, Wu harmonic mean, and Lewis acid/base theory, can be used to study surface energy.

However, there are certain limitations on the number of test liquids that may be used and the allowed angles for each model. For this inquiry, the Zisman critical wetting tension model was used since it only calls for two test liquids and has the capacity to offer a precise assessment of surface energy.

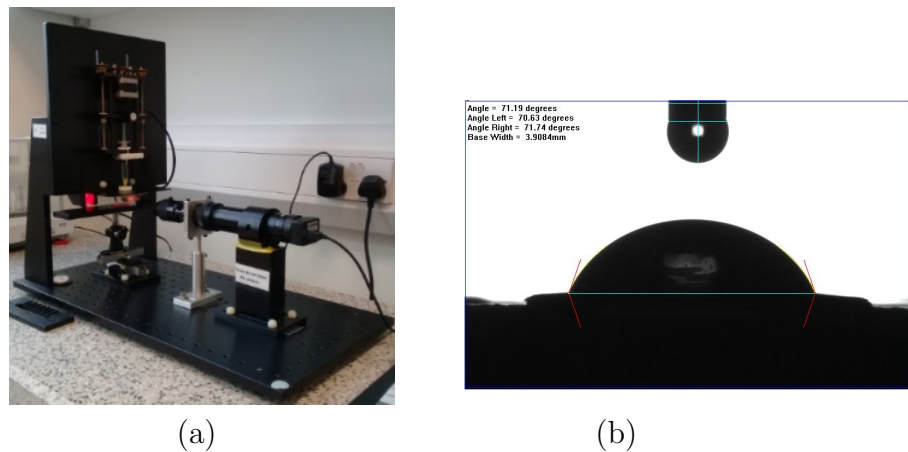


FIGURE 4.9: Measurement of Contact Angle: (a) Utilizing the FTA 200 Dynamic Contact Angle Analyzer (b) Employing the Sessile Drop Test

## 4.5 Permeability Analysis of Bone Scaffolds

### 4.5.1 Experimental Measurement of Permeability

By timing the flow of 500 millilitres of fluid through scaffolding erected in the direction of the sample, flow rate was calculated. Despite having omnidirectional characteristics, cubic scaffold layouts were only explored in one direction. In contrast, hexagonal closed packed constructions with a primary axis having minimal blockage were employed in this specific direction.

Three time readings per scaffold sample were averaged to determine the time for 500 ml fluid traversal, repeated for all test fluids. Using Darcy's Law and the collected data, experimental permeability was calculated.

$$k = \frac{q \cdot l \cdot \mu}{p \cdot d} \quad (4.1)$$

where "p" is defined as:

$$p = \rho g \Delta h \quad (4.2)$$

Within this context, the computation of permeability ( $k$ ) in  $m^2$  involves the application of Darcy's Law. Here,  $d$  refers to the entire cross-sectional area in  $m^2$ ,  $q$  denotes the volumetric flow rate in  $m^3/s$ ,  $t$  signifies the duration in seconds required for the traversal of 500 milliliter through a sample,  $l$  corresponds to the length of the sample in meters,  $h$  represents the fluid head,  $\mu$  stands for the fluid's dynamic viscosity in Pa·s, and  $p$  represents the pressure in Pa, which is evaluated utilizing Equation 4.2. The accompanying Table 4.2 shows test fluids' appropriate pressure and density levels.

TABLE 4.2: Test fluid pressure and density for measuring permeability

Test Fluids	Tap Water	15 % glycerol-water	20 % glycerol-water
Density (Kg/m <sup>3</sup> )	998	1045	1060
Pressure (Pa)	7833	8192	8318

#### 4.5.2 Numerical Calculation of Permeability

The Kozeny-Carman equation, initially introduced by Kozeny and subsequently refined by Carman, serves as a widely adopted tool for predicting intrinsic permeability [270]. This equation has been employed in the current study to numerically calculate permeability. In the equation, permeability is influenced by structural characteristics such as porosity, surface area, and density. The specific form utilized in this research to ascertain the permeability factor, denoted as  $k$  and expressed in units of  $m^2$ , is outlined as follows:

$$k = C \cdot \frac{g}{\mu_w \rho_w} \cdot \frac{e^3}{S^2 D_r^2 (1 + e)} \quad (4.3)$$

In the provided equation,  $k$  represents the coefficient of permeability in  $m^2$ ,  $C$  is a constant (with a value of 0.2) that considers the morphology of flow-through

channels within a spongy medium [57],  $e$  stands for porosity,  $S$  signifies specific surface area in  $m^2/kg$ ,  $D_r$  denotes the ratio of solid density to fluid density,  $\mu_w$  represents the dynamic viscosity of water in Pa·s,  $g$  represents the gravitational acceleration in  $m/s^2$ , and  $\rho_w$  corresponds to the density of water in  $kg/m^3$ .

This equation can also be utilized to determine the intrinsic permeability  $K$  as follows:

$$k = K^* \cdot \frac{\rho_w g}{\mu_w} \quad (4.4)$$

The Kozeny-Carman equation can be reformulated to express it in terms of permeability using equations 4.3 and 4.4:

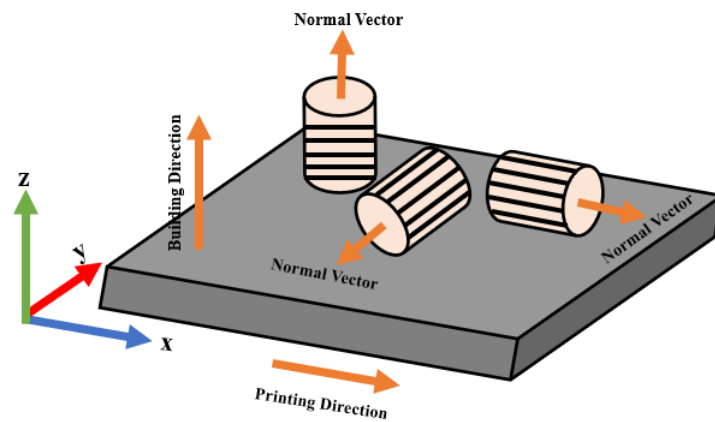
$$k = \frac{C}{\rho^2} \cdot \frac{e^3}{S^2 D_r^2 (1 + e)} \quad (4.5)$$

The density of PolyJet material varies from 1182 to 1920  $kg/m^3$ , while the density of  $\mu$ SLA material is 1182  $kg/m^3$ . Equation 4.5 shows that the fluid densities cancel each other out, proving that the results of the calculated permeability are not affected by the fluid type.

## 4.6 Design and Development of Standard Samples

To analyze the influence of printing direction on mechanical characteristics, standard circular and rectangular samples were designed following ASTM D-695 (ISO 604) norms [276]. These were 3D-printed and cleaned in a manner similar to bone scaffolds. Replicas were meticulously crafted in three-dimensional space, spanning across the x, y, and z directions, resulting in a comprehensive set of eighteen samples. The intricate printing process ensured the faithful reproduction of each specimen with precision and accuracy. In Figure 4.10(a), the intricate details of their printing orientation are vividly depicted, showcasing the deliberate arrangement necessary for optimal fabrication. Meanwhile, Figure 4.10(b) offers an insightful

glimpse into the samples' diverse geometric forms, presenting cross-sectional views of both cylindrical and rectangular shapes. This deliberate variation in shapes adds richness to the dataset, allowing for comprehensive analysis and comparison across different structural configurations.



(a)



(b)

FIGURE 4.10: (a) Standard Sample printed along the x, y, and z axes (b) cylindrical as well as rectangular cross sections standard samples

## 4.7 Mechanical Testing of Bone Scaffolds

### 4.7.1 Structural Characterization of Bone Scaffolds

After 3D printing, optical microscopic images of the as-built polymeric bone scaffolds were captured using the Keyence-Digital microscope VHX-2000. This was

done to identify any discrepancies in the measurements of architectural parameters between the as-built scaffolds and the CAD-based models. These discrep-

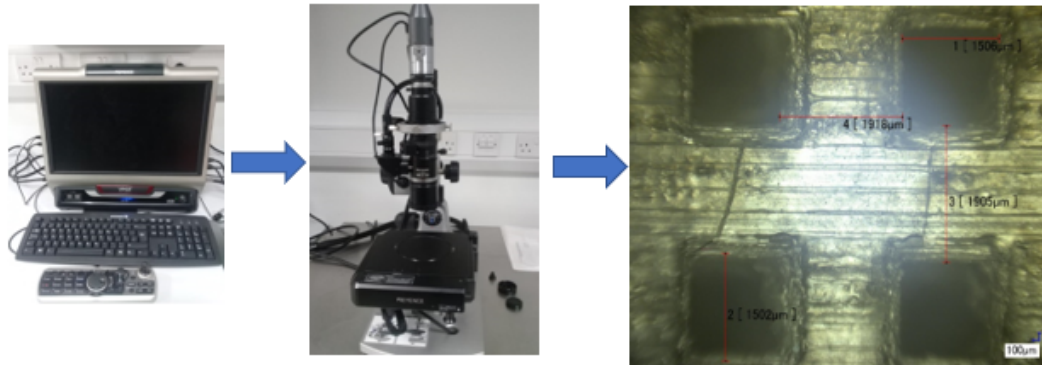


FIGURE 4.11: Keyence-Digital microscope VHX-2000

ancies could potentially explain variations in the experimental and finite element (FE) mechanical responses of the bone scaffolds. Progressive scanning method was used by the Keyence-Digital microscope VHX-2000 to capture 28 frames/sec with a resolution of 8 million pixels.

Before imaging, initialization of the x-y motorized stage was made following the color and brightness adjustment. After that, the x-y motorized stage was moved and tilted for angle adjustment to capture high quality images of the polymeric bone scaffolds.

#### 4.7.2 Quasi-Static Compression Testing

Compression testing that complies with the ASTM D-695 (ISO 604) standard is carried out to evaluate the compressive qualities of rigid polymers. The universal testing machine utilised was a Zwick/Roel Z50 with a 50 kN maximum load capacity and Zwick TestXpert simulation software. Preparatory activities were carried out prior to starting the compression testing on the scaffold constructions. Using a Startrite-20RWF machine, the 3D-printed scaffolding was carefully removed from its circular packaging. Any surplus material was meticulously removed with a grinder, ensuring the samples were well-prepared for compression tests. The actual compression process involved inserting the prepared samples into the testing

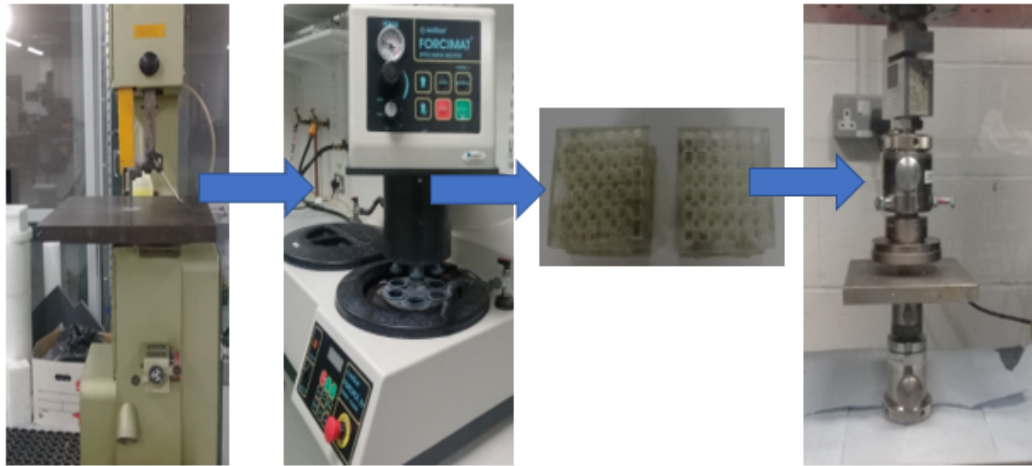


FIGURE 4.12: Sample preparation for compression testing

machine. An incremental application of controlled force was made at a 2 mm/min compression rate. As the force was applied, the vertical deformation that resulted was measured. The compression continued until the samples experienced failure, reaching a point where they could no longer withstand the applied force and underwent more pronounced deformation. During the compression test, the testing machine generated data that included the relationship between the force applied (measured in Newtons, N) and the displacement (measured in millimeters, mm) of the samples. This data was recorded in the Zwick TestXpert simulation software. From this data, key parameters were derived:

- i. **Stress ( $\sigma$ ) Calculation:** The stress experienced by the samples was calculated using the formula  $\sigma = \frac{F}{A}$ , where  $\sigma$  stands for stress,  $F$  for applied force, and  $A$  for the sample's cross-sectional area. This calculation quantified how the samples reacted to the applied force in relation to their surface area.
- ii. **Strain ( $\varepsilon$ ) Calculation:** Strain, which measures the amount of deformation, was calculated using the formula  $\varepsilon = \frac{\delta}{L}$ , where  $\varepsilon$  represents strain,  $\delta$  is the change in length of the sample due to deformation, and  $L$  is the original length of the sample. This calculation indicated how much the samples deformed in response to the applied force.

Utilizing the acquired stress and strain data, a stress-strain diagram was formulated. This visual representation provided insight into the behavior of the samples under the compression force. Important compressive parameters, including yield strength (the stress at which plastic deformation begins), elastic moduli (a measure of stiffness), and compressive strength (the greatest stress the sample can sustain), were extracted using the stress-strain diagram. The surface finish is mainly affecting the fatigue performance. Since this study is focused on the compression strength, it was decided to carry out this test directly after removing the support structure (as-built).

# Chapter 5

## Experimental Results

### 5.1 Introduction

In this chapter, the comprehensive presentation of experimental results on the permeability and mechanical properties of 3D printed bone scaffolds serves as a critical cornerstone in the field of tissue engineering. By precisely examining the influence of contact angle and surface energy on scaffold permeability using both PolyJet and micro-stereolithography techniques, invaluable insights are gained into the optimization of scaffold designs for enhanced biocompatibility. Moreover, the numerical permeability assessments delve into the complex interplay between fluids and solids within the scaffold's porous structure, providing a quantitative comprehension of its transport properties. This in-depth analysis sheds light on the intricate mechanisms governing fluid flow through the scaffold, offering valuable insights into its performance characteristics. The investigation of structural parameters not only explains their impact on permeability but also unveils new avenues for tailoring scaffolds to specific tissue engineering applications. The thorough analysis of mechanical properties serves a dual purpose, safeguarding both the immediate structural integrity and the long-term viability of the bone scaffolds. These comprehensive findings represent a significant stride forward in

the fields of tissue engineering and regenerative medicine, offering valuable insights that pave the way for further research and eventual clinical application.

## 5.2 Effect of Contact Angle and Surface Energy on Permeability

The tendency of a surface to repelled or resist water is known as hydrophobicity. A hydrophobic surface is one that does not easily interact with water molecules, causing water to bead up and roll off the surface. This property is typically measured by the contact angle formed between a liquid droplet and the surface. A higher contact angle indicates greater hydrophobicity, while a lower angle suggests a more hydrophilic (water-attracting) surface. Permeability refers to how easily a substance can pass through a material or surface. In this case, it frequently refers to how quickly liquids may travel through a certain substance. The angle that is created when a liquid droplet collides with a solid surface is known as the contact angle. It shows how thoroughly the liquid has wettened the surface. A greater contact angle signifies more hydrophobicity since the liquid is less likely to spread out on the surface. The energy needed to expand a material's surface area is referred to as surface energy. In general, materials with lower surface energies are more hydrophobic because water molecules stick to them. Contact angles and surface energies of 3D-printed scaffold structures using PolyJet (VeroClear) and  $\mu$ SLA (PlasWhite) are outlined in Table 5.1.

TABLE 5.1: Contact angle and surface energy of PolyJet (VeroClear) and  $\mu$ SLA (PlasWhite) 3D printed scaffold structures

Test Liquids	Contact Angle		Surface Energy (mN/m)	
	VeroClear	PlasWhite	VeroClear	PlasWhite
Tap Water	67	69.1	41.7	38.5
15% Glycerol – Water	70	72.6	40	37.9
20% Glycerol – Water	72.9	73.7	39.8	37.1

For both materials, VeroClear and PlasWhite, tap water shows contact angles of around  $67.0^\circ$  and  $69.1^\circ$ , respectively. These angles are moderate, indicating that the surfaces have a certain level of hydrophobicity but are not strongly water-repellent. The surface energy values are around  $41.7 \text{ mN/m}$  and  $38.5 \text{ mN/m}$ , which implies moderate water-attracting characteristics.

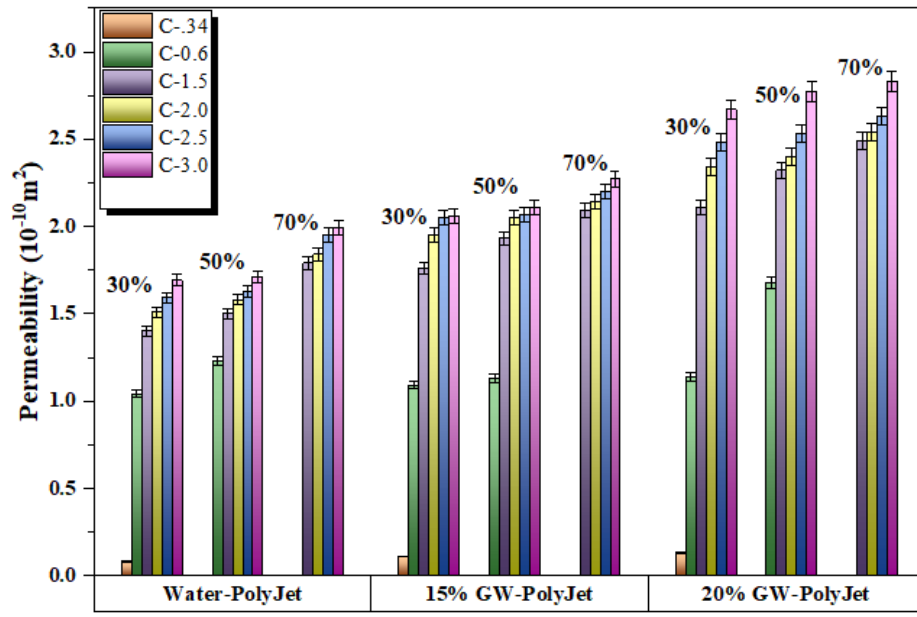
In the case of 15% Glycerol - Water solution the contact angles increase to around  $70.0^\circ$  and  $72.6^\circ$  for VeroClear and PlasWhite, respectively. This suggests an increase in hydrophobicity compared to tap water, as the droplets are less likely to spread out. The surface energy values decrease to around  $40.0 \text{ mN/m}$  and  $37.9 \text{ mN/m}$ , indicating a reduction in water-attracting tendencies. In the case of 20% Glycerol - Water solution the contact angles increase further to approximately  $72.9^\circ$  and  $73.7^\circ$  for VeroClear and PlasWhite, respectively. This indicates even higher hydrophobicity compared to the previous liquids. The surface energy values decrease again to around  $39.8 \text{ mN/m}$  and  $37.1 \text{ mN/m}$ , suggesting that the surfaces are becoming more water-repellent.

Overall, the trend in the data shows that as the glycerol concentration in water increases, the contact angles increase and the surface energy values decrease. This suggests that the surfaces of both VeroClear and PlasWhite become more hydrophobic and less permeable to these liquid mixtures. This information could be important when selecting materials for applications where water resistance and permeability are important factors.

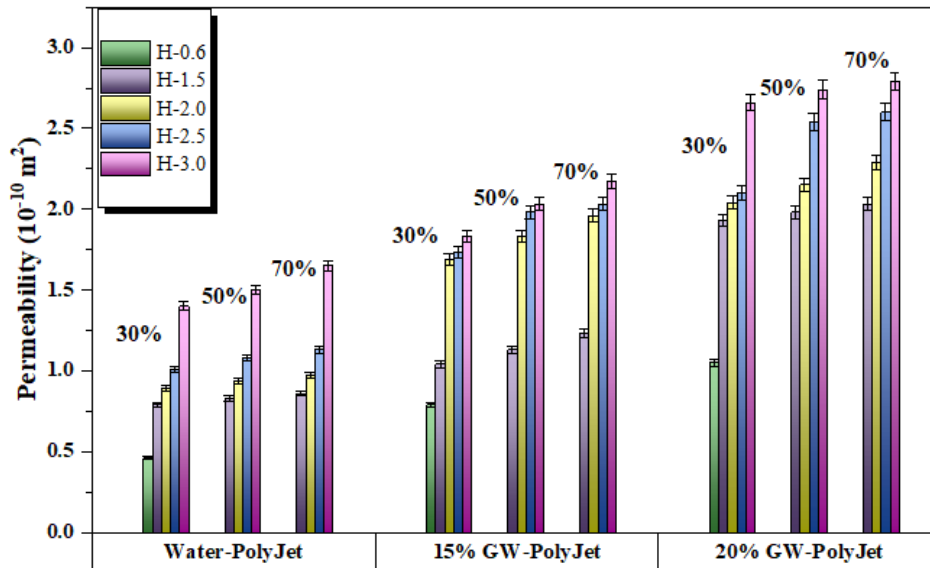
### **5.3 Experimental Measurement of Permeability for PolyJet Printed Bone Scaffolds**

In Figure 5.1, The data shows the findings of an experimentally measured permeability of bone scaffolds fabricated permeability of scaffold structures made with a 3D printer called PolyJet. Cubic and closed packed hexagonal shapes were analyzed. The permeability was evaluated using three distinct liquids: tap water, a

15% glycerol-water solution, and a 20% glycerol-water solution. It is important to assess how well change in viscosity allow the flow of fluids with properties similar to blood. This ensures that the materials will function effectively within the human body body.



(a)



(b)

FIGURE 5.1: Permeability experiments were conducted on PolyJet 3D-printed scaffold structures with tap water, 15% glycerol-water solution, and 20% glycerol-water solution. The results are shown for both cubic and hexagonal closed packed configurations (a) and (b), respectively

The following are the main conclusions from the data:

- i. **Effect of Pore Size, Porosity, and Viscosity:** The gathered information reveals a distinct correlation between the observed permeability of scaffold structures and pore size, porosity, and fluid viscosity. Larger pores, higher porosity, and thicker fluid viscosity all contribute to increased permeability, unveiling a multifaceted interplay between these factors. This understanding has significant implications for scaffold design and applications. It provides the potential to finely adjust scaffold properties to attain the desired permeability tailored to specific functional requirements in tissue engineering. By harnessing these relationships, researchers can create tailored scaffold architectures. These architectures facilitate optimal nutrient transport, waste removal, and cellular communication within engineered tissues. Beyond immediate practical applications, this study contributes to our fundamental understanding of scaffold-fluid interactions. This knowledge aids in designing biomimetic systems that closely mimic natural tissue functions, thereby advancing the fields of regenerative medicine and biomedical engineering.
- ii. **Dominance of Pore Size:** Within the realm of factors influencing permeability, including pore size, porosity, and viscosity, this study unveiled the preeminence of pore size in driving notable effects. This observation suggests that modifications in pore size carry a more significant weight in influencing permeability than adjustments in porosity or viscosity.
- iii. **Permeability Range:** The predicted permeability values of the 3D-printed scaffold constructs with cubic pore shapes varied from  $1.05 \times 10^{-10} \text{ m}^2$  to  $2.83 \times 10^{-10} \text{ m}^2$ , indicating a considerable 69% disparity between the lowest and highest values. The materials with hexagonal closed packed pore shapes also showed a permeability range of  $0.46 \times 10^{-10} \text{ m}^2$  and  $2.75 \times 10^{-10} \text{ m}^2$ , with a substantial 78% difference between the lowest and highest values.
- iv. **Comparison between Pore Shapes:** Furthermore, the data supports the idea that 3D printed scaffold structures, characterized by cubic pores,

generally demonstrate higher permeability values. This is in contrast to structures that utilize a hexagonal closed-packed pore arrangement. This result underscores the pivotal role that the precise geometric arrangement of pores plays. Whether cubic or hexagonally closed-packed, it significantly influences the permeability properties of scaffold architectures.

The results of this work highlight the complex interactions between fluid viscosity, permeability, pore size, and porosity in 3D printed scaffold architectures. Notably, larger pores, higher porosity levels, and the presence of more viscous fluids tend to correlate with increased permeability. Among the variables examined, pore size emerges as the dominant factor influencing permeability. Additionally, the geometric arrangement of pores also exerts its influence. Such insights hold the potential to inform the design of scaffold structures tailored for precise applications that necessitate well-regulated fluid flow and permeability characteristics. These findings contribute to advancing our comprehension of the intricate mechanisms governing fluid transport through engineered biomaterials. They can also assist in optimizing scaffold design for various tissue engineering and regenerative medicine applications.

## 5.4 Experimental Measurement of Permeability for $\mu$ SLA Printed Bone Scaffolds

The influence of micro-stereolithography ( $\mu$ SLA) printing techniques on the ability of bone scaffolds to facilitate fluid flow is rigorously investigated and quantified. These permeability characteristics are being analyzed through a series of experiments, setting the stage for a comprehensive understanding of how  $\mu$ SLA printed bone scaffolds impact fluid transport properties in the context of cutting-edge scaffold design and fabrication. The permeability of 3D scaffold structures created by micro-stereolithography ( $\mu$ SLA) printing is shown in the Figure 5.2. This data is comparable to the results obtained from PolyJet printing, as both techniques involve creating scaffold structures and assessing their permeability characteristics.

The results of permeability tests performed on  $\mu$ SLA 3D-printed scaffold structures with two different pore arrangements—cubic and hexagonal closed packed—are shown in Figure 5.2. Tap water, a 15 % glycerol-water solution, and a 20 % glycerol-water solution were used as test fluids in the tests.

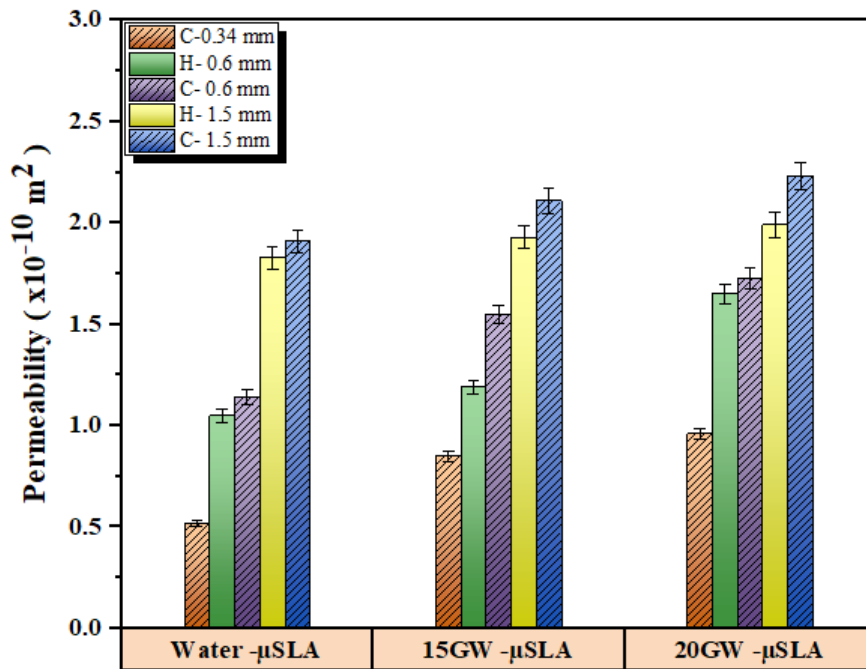


FIGURE 5.2: Permeability measurements for  $\mu$ SLA 3D-printed scaffold structures, using tap water, 15% glycerol-water solution, and 20% glycerol-water solution, are displayed for 30% porosity in cubic and hexagonal closed packed configurations.

The following are the main findings from the data:

- i. **Effects of Porosity, Viscosity, and Pore Size:** Similar to the previous case of PolyJet printing, the data demonstrates that higher values of pore size, porosity, and viscosity lead to higher permeability values. This suggests that in scaffold structures created via  $\mu$ SLA printing, larger pore sizes, higher porosity, and more viscous test fluids collectively contribute to increased permeability.
- ii. **Dominance of Pore Size:** Just like in the previous findings, the data highlights that among the factors affecting permeability—pore size, porosity,

and viscosity—pore size has a more pronounced effect. Changes in pore size exert a stronger influence on permeability compared to variations in porosity or viscosity.

- iii. **Permeability Range:** The permeability of  $\mu$ SLA 3D-printed scaffold structures with cubic pore shape varied from  $0.52 \times 10^{-10} \text{ m}^2$  to  $2.23 \times 10^{-10} \text{ m}^2$ , exhibiting a 76% difference between the lowest and highest readings. Similarly, for hexagonal closed packed pore shape structures, the permeability ranged from  $1.05 \times 10^{-10} \text{ m}^2$  to  $1.99 \times 10^{-10} \text{ m}^2$ , with a 47% difference between the lowest and highest values. These ranges provide insight into the variation in permeability for different pore shapes.
- iv. **Comparison between Pore Shapes:** The study revealed that, at 30% porosity,  $\mu$ SLA 3D printed scaffold structures with cubic pore shapes frequently exhibited superior permeability values. This was in contrast to those with hexagonal closed-packed pore forms. This emphasises the impact of pore configuration on the scaffold structures' permeability properties.

In conclusion, the findings imply that the permeability behaviour of  $\mu$ SLA printed 3D scaffold structures and PolyJet printed samples is similar. The relationships between pore size, porosity, viscosity, and permeability are consistent between the two printing techniques. Larger pore sizes and higher porosity levels enhance permeability, with pore size exerting a stronger impact. The comparison between cubic and hexagonal closed packed pore shapes indicates that geometric arrangement plays a role in determining permeability. These findings can aid in designing scaffold structures to meet specific requirements for controlled fluid flow and permeability in various applications.

The information in Figure 5.3 compares the experimentally determined permeability of scaffold structure made using two different 3D printing processes: Microstereolithography ( $\mu$ SLA) and PolyJet. The data aims to understand how these printing techniques influence the permeability characteristics of the resulting scaffold structures.

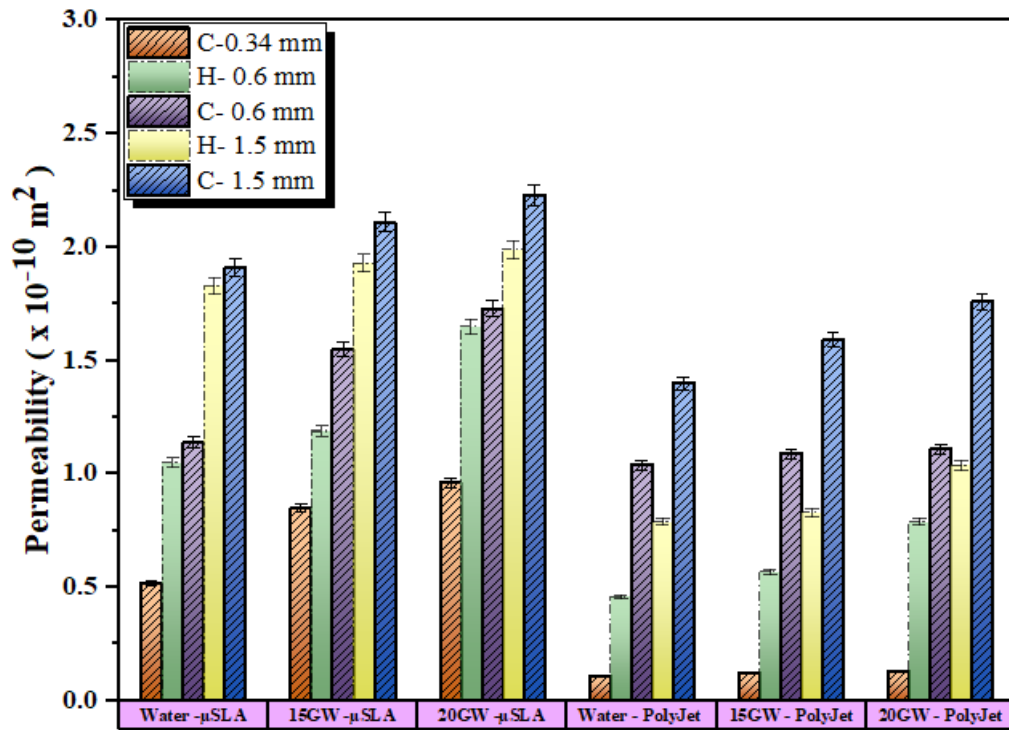


FIGURE 5.3: For both cubic and hexagonal closed packed configurations at 30% porosity, the experimentally observed permeability of 3D-printed scaffold constructs using tap water, 15% glycerol-water solution, and 20% glycerol-water solution

The key points from the data are as follows:

- i. **Precision and Permeability:** The data draws attention to an aspect highlighted earlier in the development section:  $\mu$ SLA printing is known for its higher precision in creating fine and detailed structures. This accuracy appears to play a role in the tendency that scaffold structures produced using  $\mu$ SLA exhibit greater permeability values than structures printed using PolyJet, especially when dealing with smaller pore sizes.
- ii. **Impact of Pore Sizes:** It is hypothesised that samples produced using  $\mu$ SLA have greater permeability values at smaller pore sizes than those printed using PolyJet. This observation indicates that the  $\mu$ SLA technique's precision allows for the creation of finer pores, which can influence fluid flow and permeability within the scaffold structures.

In summary, the data from Figure 5.3 emphasizes the comparison between the permeability of scaffold structures produced using PolyJet and  $\mu$ SLA 3D printing methods. The difference between these structures and those produced by PolyJet printing is in the accuracy of  $\mu$ SLA printing, which produces smaller pore sizes and, as a result, greater permeability values for these structures. This research emphasises the importance of choosing the right printing technique when trying to obtain specified permeability properties in 3D printed scaffold structures, especially where accuracy and pore size are important aspects. In the presented Table 5.2, the permeability values for scaffold structures made with two distinct 3D printing technologies—PolyJet and micro-stereolithography ( $\mu$ SLA)—are thoroughly compared in units of  $10^{-10} \text{ m}^2$ . The values for permeability are shown for two different pore types: cubic (C) and hexagonal (H).

TABLE 5.2: Density and pressure of test fluids used in permeability measurement

Permeability ( $\times 10^{-10} \text{ m}^2$ )	PolyJet		$\mu$ SLA	
	C	H	C	H
Measured	1.05 – 2.83	0.46 - 2.75	0.52 – 2.23	1.05 – 1.99
Theoretical	0.3 – 2.11	0.12 - 2.0	0.3 – 2.11	0.12 - 2.0

The permeability of scaffold structures produced through PolyJet printing with cubic pore shapes ranges from  $1.05 \times 10^{-10} \text{ m}^2$  to  $2.83 \times 10^{-10} \text{ m}^2$ . This represents a difference of  $1.78 \times 10^{-10} \text{ m}^2$  between the highest and lowest measured values. The permeability for PolyJet printed structures with hexagonal pores falls between  $0.46 \times 10^{-10} \text{ m}^2$  and  $2.75 \times 10^{-10} \text{ m}^2$ , showing a range of  $2.29 \times 10^{-10} \text{ m}^2$ . The measured permeability for scaffold structures created through  $\mu$ SLA printing with cubic pores varies from  $0.52 \times 10^{-10} \text{ m}^2$  to  $2.23 \times 10^{-10} \text{ m}^2$ , indicating a range of  $1.71 \times 10^{-10} \text{ m}^2$ . The permeability range for  $\mu$ SLA-printed structures with hexagonal pores is from  $1.05 \times 10^{-10} \text{ m}^2$  to  $1.99 \times 10^{-10} \text{ m}^2$ , indicating a span of  $0.94 \times 10^{-10} \text{ m}^2$ . The Table 5.2 also provides theoretical permeability ranges for both printing methods and pore shapes. These theoretical values serve as references or expectations based on modeling or calculations. They give insight into the potential range of permeability that could be achieved in an ideal scenario. The theoretical permeability ranges are similar for both printing methods

and pore shapes. For cubic pore structures, the theoretical permeability spans from  $0.3 \times 10^{-10} \text{ m}^2$  to  $2.11 \times 10^{-10} \text{ m}^2$ . For hexagonal pore structures, the theoretical permeability range is  $0.12 \times 10^{-10} \text{ m}^2$  to  $2.0 \times 10^{-10} \text{ m}^2$ . In summary, the Table 5.2 provides a comprehensive overview of measured and theoretical permeability values for scaffold structures produced through PolyJet and  $\mu$ SLA 3D printing techniques. The data demonstrates the variations in permeability based on printing method and pore shape, giving valuable insights into the performance and potential of these structures in terms of fluid flow and permeability. The experimentally determined permeability consistently decreased with respect to numerically calculated permeability across all scenarios. The disparity between the measured and estimated permeability could be attributed to several factors. These may include improper cleaning of the 3D-printed scaffold structures or aspects not considered by the Kozeny-Carman equation, such as pressure drop across the sample, fluid viscosity, and surface energy. As a result, a hybrid model that combines the advantages of both computed and experimental techniques could provide a more precise way to measure permeability. Furthermore, future research should focus on refining the cleaning procedures for 3D-printed scaffold structures to minimize potential contaminants that could affect permeability measurements. Additionally, investigating the impact of pressure drop variations, fluid viscosity fluctuations, and surface energy alterations on permeability could help bridge the gap between experimental and numerical results. Developing an improved Kozeny-Carman equation that accounts for these factors may also enhance the accuracy of permeability predictions.

## 5.5 Numerical Calculation of Permeability

Cubic scaffold structures excel due to their well-defined geometry, fostering interconnected porosity that eases fluid flow, reducing resistance, and boosting permeability. The Kozeny-Carman equation reliably predicts permeability across different 3D printing methods, relying on porosity and specific surface area. This

has implications for scaffold design optimization, crucial in fields like tissue engineering, where controlled fluid transport is essential for cell growth and tissue regeneration. In summary, cubic scaffolds outperform counterparts due to geometry, interconnected porosity, and reduced flow resistance, offering tailored design possibilities for diverse scientific and engineering applications.

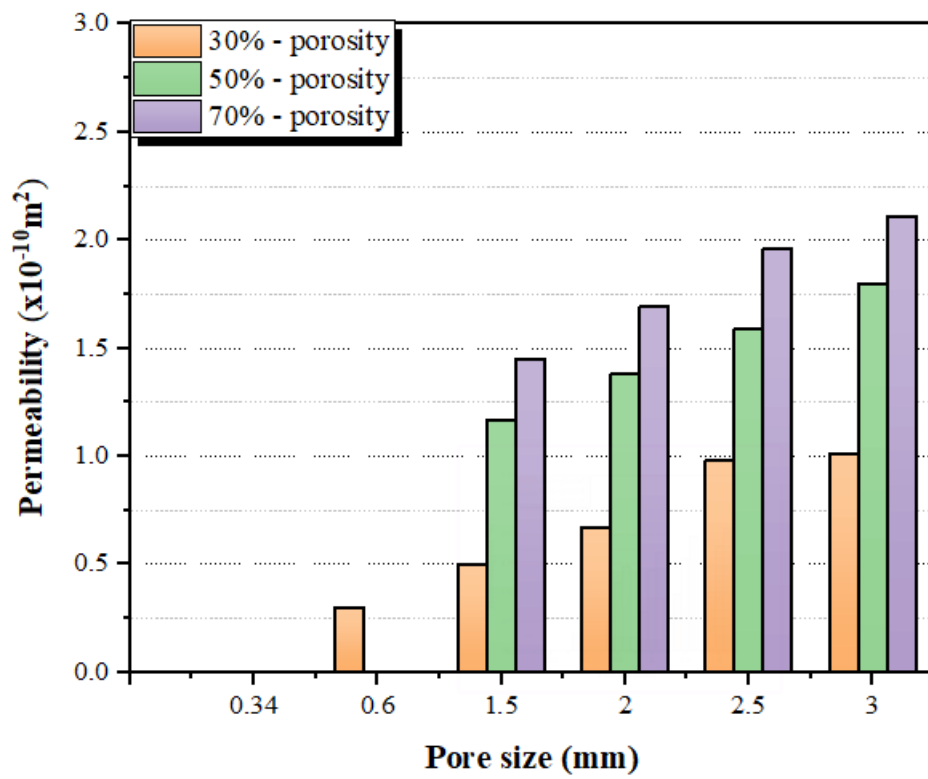
Cubic scaffold structures have greater permeability values than other types of scaffolding, according to calculations, with values ranging from  $0.3 \times 10^{-10} \text{ m}^2$  to  $2.4 \times 10^{-10} \text{ m}^2$ , Compared to scaffolds that were hexagonally closed-packed and varied from  $0.13 \times 10^{-10} \text{ m}^2$  to  $2.0 \times 10^{-10} \text{ m}^2$ .

Interestingly, the calculated permeability was consistent for both PolyJet 3D printed and  $\mu$ SLA 3D printed scaffold structures. This is due to the Kozeny-Carman equation relying solely on structural properties, where porosity and specific surface area played vital roles. These properties were accurately derived from CAD models, remaining consistent across both 3D printing techniques employed in this study. Visual representation in Figure 5.4 revealed that in both cubic and hexagonal closed packed scaffold structures, permeability improved with greater pore size and higher porosity. This underscores the considerable influence of pore characteristics on scaffold permeability.

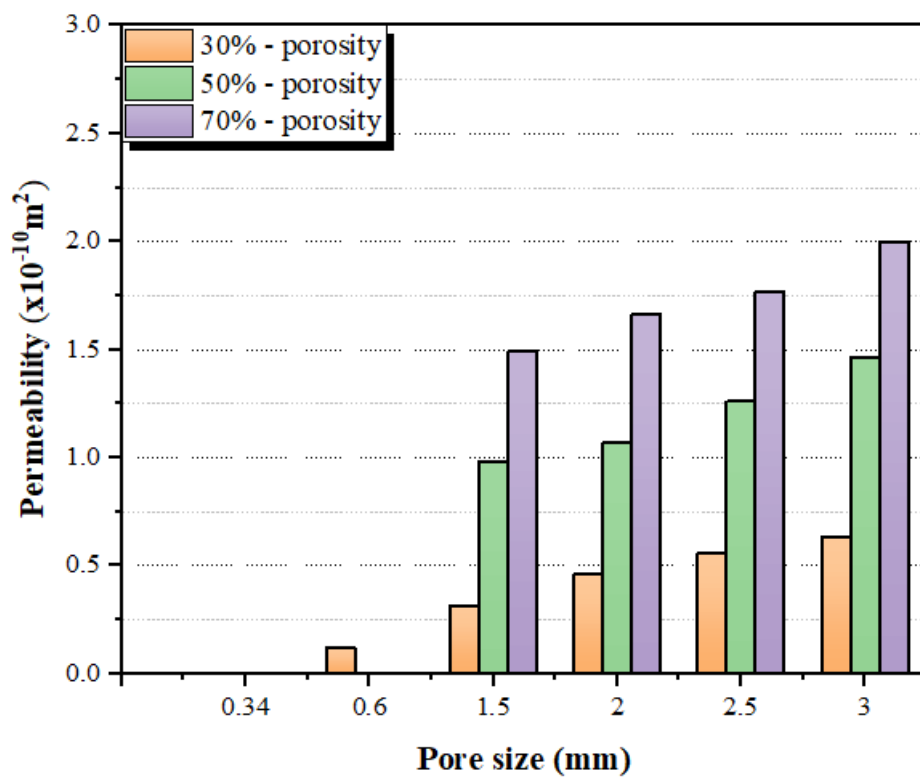
## 5.6 Effect of Surface Area on Permeability

In the context of this research, Equation 4.5 offers a mathematical explanation that emphasises the critical part that the precise surface area plays in determining the permeability of scaffold systems. Each unit volume of the scaffold has a specified surface area that describes how much surface is accessible for fluid interaction. This particular parameter holds immense importance as it dictates how easily fluids can move through the scaffold's matrix.

It's essential to note that the specific surface area isn't a constant value; rather, it varies depending on the unique configuration of each scaffold design. This



(a)



(b)

FIGURE 5.4: Calculated numerically: permeability (a) Cubic (b) closed-packed hexagonal scaffold structures

variation is attributed to differences in the arrangement of pores and the overall structural layout. It is crucial to investigate the complex interaction between pore size, porosity, and the particular surface area in order to fully comprehend the impact of permeability.

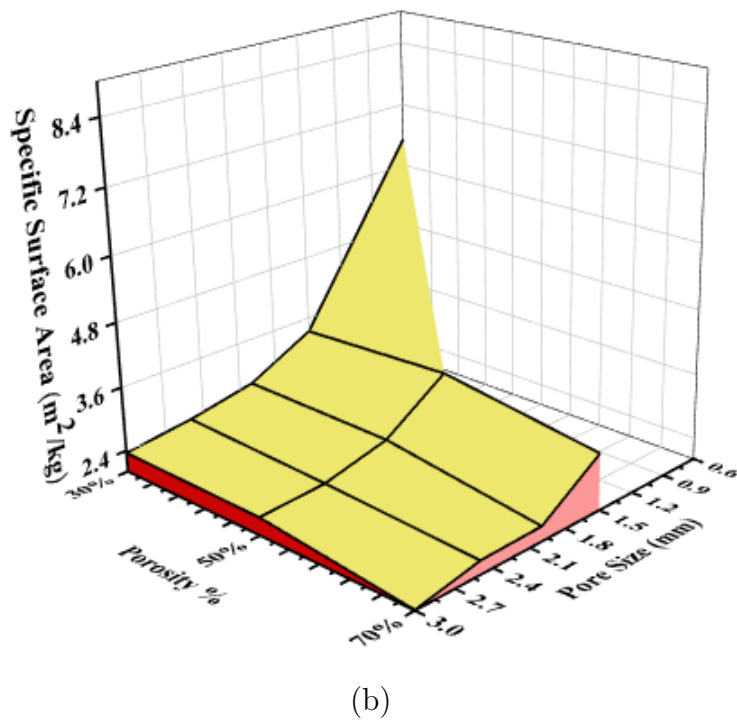
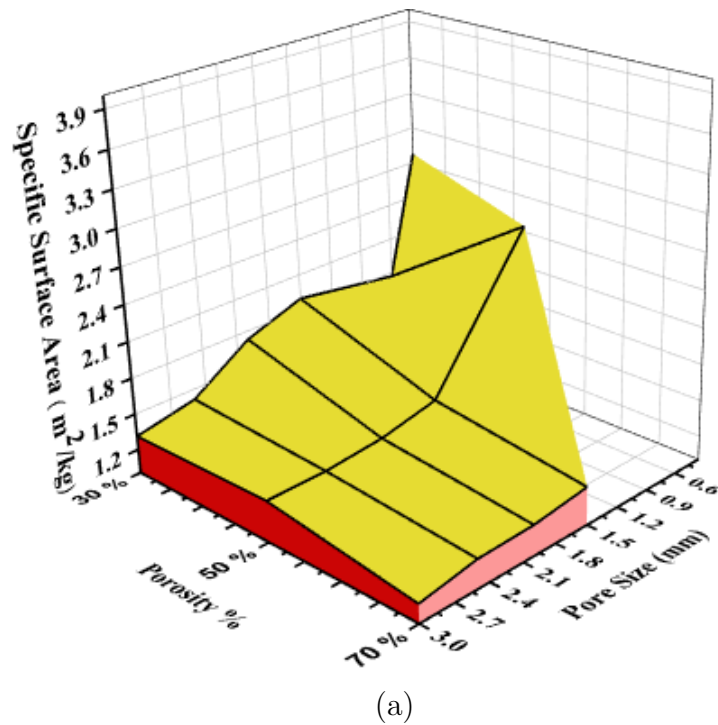


FIGURE 5.5: Correlation of specific surface area with pore size and porosity is shown for (a) cubic structures and (b) hexagonal closed-packed structures

While porosity level quantifies the volume of these voids in relation to the overall volume of the scaffold, pore size measures the size of the empty spaces present inside the scaffold construction. Both these factors play a substantial role in determining the specific surface area inherent in the scaffold's architecture. As a result, the research underscores the importance of comprehending how variations in pore size and porosity interact dynamically. These variations influence the specific surface area and collectively have a significant impact on the overall permeability properties of the scaffold.

This work emphasises the need of understanding the complex interactions between pore size, porosity, and specific surface area. An in-depth examination of these elements can provide a clearer understanding of how variations in pore size and porosity levels can successfully regulate a given surface area. This, in turn, exerts a notable influence on the permeability of the scaffold structure, adding a new layer of understanding to the field of scaffold design and fluid transport within such structures.

This dynamic relationship between specific surface area, pore size, and porosity is vividly elucidated in Figure 5.5. The graphical representation demonstrates how a rise in pore size and porosity corresponds with a decrease in specific surface area. This reduction in specific surface area, in turn, translates into an augmented permeability of the scaffold structures. In essence, the Figure 5.5 visually captures the concept that larger pores and higher porosity configurations result in a more efficient fluid flow through the scaffold, thereby shedding light on optimal design principles for applications such as tissue engineering.

## **5.7 Mechanical Properties of Bone Scaffolds**

The mechanical characteristics of scaffold structures created by 3D printing were experimentally tested in this study. The total samples were twenty-eight and according to the 95% confidence level author should have to perform three repetitions of compression test on each type of sample. Therefore, eighty-four samples

(three copies of each sample) were printed to perform compression test. Figure 5.6 demonstrates the stress-strain curves of the PolyJet printed, uniaxially printed scaffold constructs for a range of pore diameters and porosities. Comparing 3D printed cellular structures to conventional solid materials, the stress-strain relationship shows unique behaviours. In the initial stages of loading a 3D printed cellular structure, the stress-strain curve demonstrates a linear elastic region. As an external force is applied, the cellular lattice deforms proportionally to the applied stress within this linear regime. The elastic modulus of the material from which the lattice is manufactured principally controls this deformation. When the imposed stress is removed during this phase, the cellular structure maintains its original shape, demonstrating the ability to experience reversible deformation.

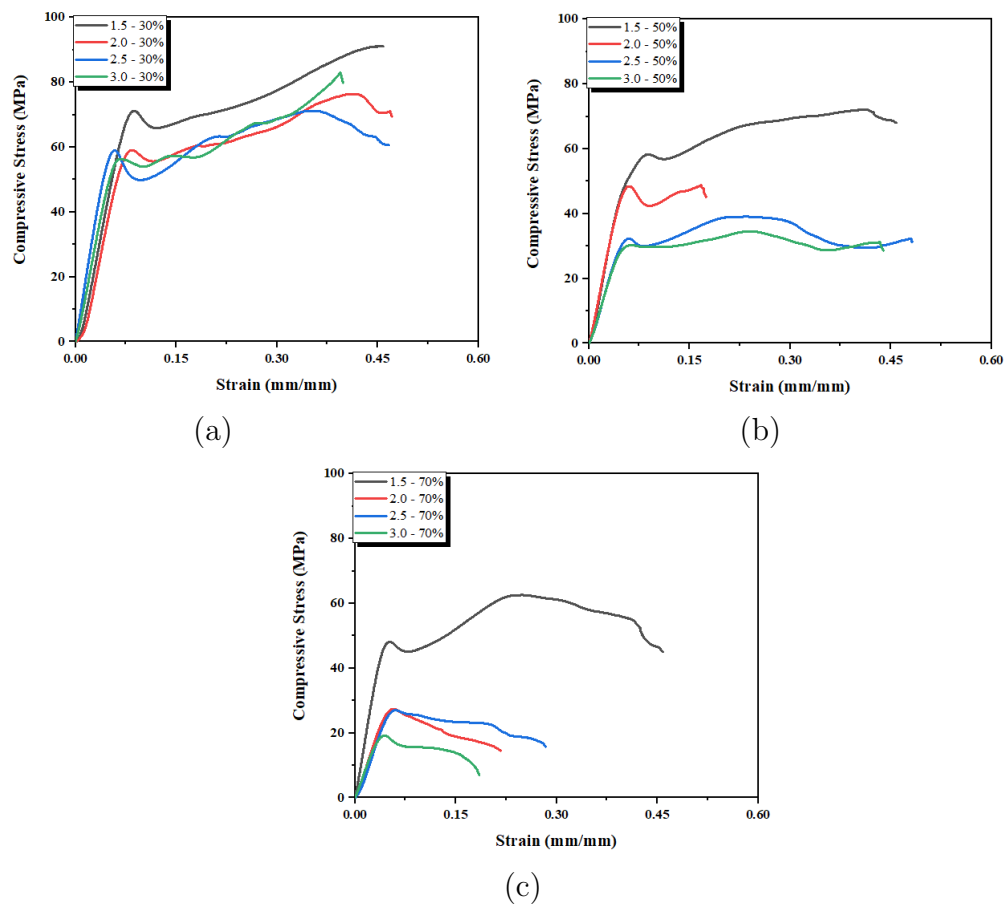


FIGURE 5.6: Stress-strain curves of cubic-shaped PolyJet 3D-printed scaffold structures at (a) 30%, (b) 50%, and (c) 70% for the following pore sizes: 1.5mm, 2.0mm, 2.5mm, and 3.0mm

The stress-strain curve for the cellular structure gradually shifts into a nonlinear

zone as the applied stress rises. This nonlinear phase is characterized by plastic deformation within the lattice elements. Unlike traditional solid materials, 3D printed cellular structures often exhibit a gradual yielding behavior without a distinct yield point. The interconnected lattice geometry allows for energy absorption and dissipation through the redistribution of stresses along multiple load paths. Consequently, the cellular structure can sustain significant deformation without undergoing catastrophic failure.

In the later stages of loading, the stress-strain curve may exhibit a plateau, indicating a relatively constant stress level while the deformation continues. This behavior is attributed to the intricate geometry of the cellular lattice, which facilitates a complex redistribution of stresses and strains. This plateau phase contributes to the unique energy-absorbing capabilities of 3D printed cellular structures, making them suitable for applications requiring impact resistance and damping. In the end, the post-plateau zone, where the structure gets close to its maximal load-carrying capacity, is where the stress-strain curve of 3D printed cellular structures reaches its peak. Fracture or failure of the lattice elements may occur as the stress continues to increase, leading to a steep decline in load-carrying capacity and the eventual collapse of the structure.

In summary, the stress-strain trend for 3D printed cellular structures reflects their intricate geometry and unique mechanical behavior. These structures exhibit linear elastic deformation, gradual yielding, a stress plateau, and ultimately fracture. Their ability to withstand substantial deformation while maintaining load-carrying capacity makes them valuable for applications ranging from lightweight structural components to impact-absorbing elements in engineering and design. The results in Figure 5.6 show that, with the exception of pore widths 2.0 mm, 2.5 mm, and 3.0 mm at 70% porosity, the 3D printed scaffold structures bent like a ductile material. The massive reduction in mechanical properties of scaffolds H- 0.6 mm is due to its very small strut thickness which was 0.12 mm. Similar patterns were seen in the polyjet 3D scaffolds with hexagonal closed packed pore shapes in Figure 5.7. Table 5.3 display the numerical value of stress-strain curves used to calculate

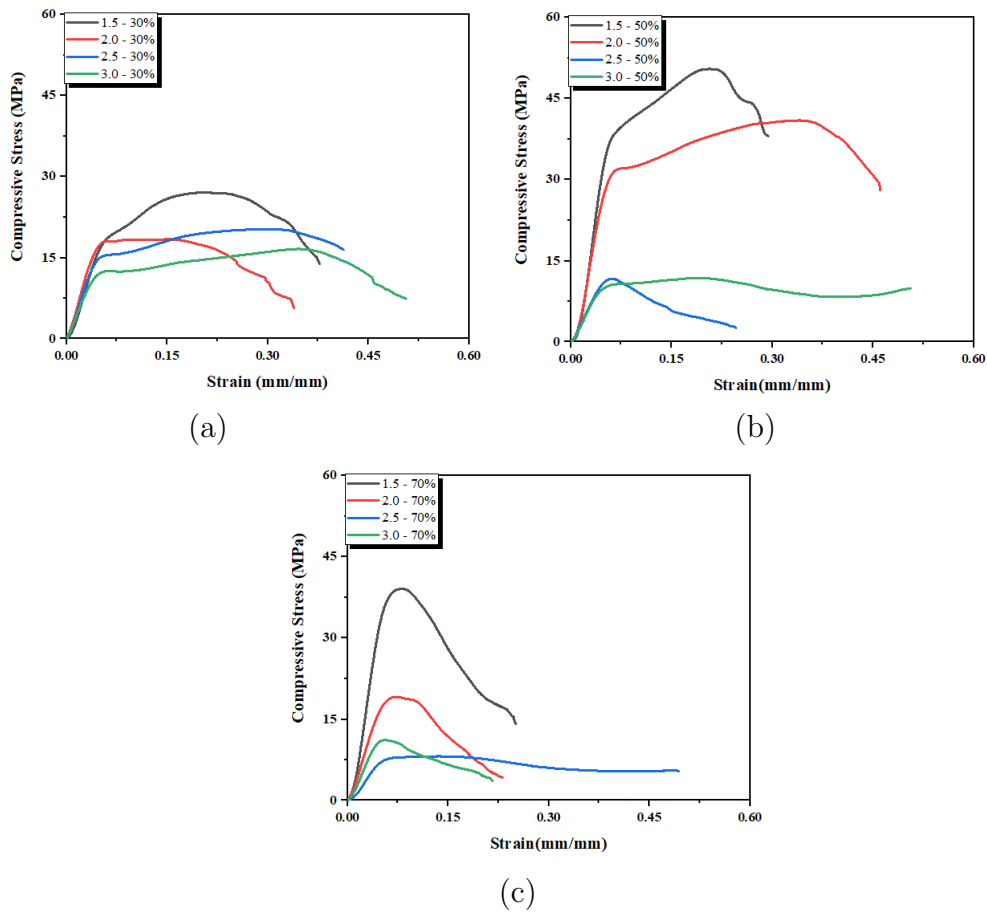


FIGURE 5.7: Stress-strain curves for hexagonal closed-packed PolyJet 3D-printed scaffold structures are shown at various porosities (a) 30%, (b) 50%, and (c) 70%, with pore diameters of 1.5 mm to 3.0 mm

the elastic moduli and yield strengths of the scaffold constructs created by PolyJet 3D printing.

- i. **Pore Size and Elastic Modulus:** As the pore size increases, the elastic modulus tends to decrease. For instance, while comparing the same porosity level (such as 30%), we find that the elastic modulus falls from 1.3 GPa to 0.7 GPa when the pore size grows from 1.5 mm to 3.0 mm. This suggests that larger pore sizes are associated with reduced material stiffness, leading to a more compliant structure.
- ii. **Porosity and Elastic Modulus:** At a given pore size, increasing porosity generally results in a lower elastic modulus. For example, at a pore size of 1.5, as porosity increases from 30% to 70%, the elastic modulus decreases from

1.3 GPa to 1.0 GPa. This indicates that higher levels of porosity contribute to decreased material rigidity.

- iii. **Pore Size and Yield Strength:** In general, larger pore sizes are associated with lower yield strengths. For instance, at a porosity of 30%, as the pore size increases from 0.34 to 3.0, the yield strength decreases from 72 MPa to 56 MPa. This trend suggests that materials with larger pores are more susceptible to plastic deformation at lower stress levels.
- iv. **Porosity and Yield Strength:** The relationship between porosity and yield strength is somewhat complex. For certain pore sizes, increasing porosity results in lower yield strength, while for others, it leads to higher yield strength. For example, at a pore size of 1.5, the yield strength increases from 42 MPa (50% porosity) to 60 MPa (70% porosity), indicating that the material becomes stronger as porosity increases. However, at a pore size of 3.0, the yield strength decreases from 25 MPa (50% porosity) to 30 MPa (70% porosity), suggesting a decrease in strength with higher porosity.

The tabulated numerical data encapsulates intricate relationships among pore size, porosity, elastic modulus, and yield strength within 3D printed cellular structures. These connections illuminate how adjustments in pore size and porosity significantly influence mechanical properties, encompassing stiffness and resistance to deformation. This information holds paramount importance for fine-tuning the design and engineering of cellular structures in applications where specific mechanical behaviors are crucially required.

The data presented in Table 5.3 demonstrates a clear correlation between the porosity and pore size of PolyJet 3D printed scaffold constructs and their mechanical properties. Both elastic moduli and yield strength significantly decrease as porosity and pore size rise. The relationship between material density and mechanical resilience is highlighted as being critically important. The results highlight the importance of careful pore size and porosity optimisation to obtain desirable mechanical characteristics while fulfilling functional requirements. These findings

underscore the intricate interplay between pore characteristics and mechanical properties in scaffold materials. Notably, as pore size increases, the scaffold's stiffness and resistance to deformation decrease significantly. This correlation is of paramount importance in applications where precise control over mechanical behavior is essential, such as orthopedic implants and tissue engineering scaffolds.

The relationship between porosity and mechanical properties is evident from the data in Table 5.3. As porosity and pore size increase, both the elastic modulus and yield strength decrease. This behavior can be attributed to the reduction in material density, as higher porosity leads to a larger volume of void spaces within the scaffold, resulting in decreased structural integrity.

These insights have far-reaching implications for scaffold design and engineering. They emphasize the need for meticulous optimization of pore size and porosity to achieve desired mechanical characteristics while meeting functional requirements. Tailoring these parameters according to specific application needs can result in scaffolds that provide the necessary support and biomechanical compatibility for tissue regeneration, implantation, or other uses.

Furthermore, this research paves the way for the development of advanced materials with tunable mechanical properties. By systematically adjusting pore characteristics, researchers and engineers can create scaffolds that mimic the mechanical behavior of natural tissues and organs, enhancing their functionality and biocompatibility in biomedical applications.

In conclusion, the correlation between pore size, porosity, and mechanical properties in PolyJet 3D printed scaffold constructs reveals the critical importance of precise control over these parameters in scaffold design. This knowledge empowers scientists and engineers to craft tailored materials with optimal mechanical characteristics for various applications, ultimately advancing the field of tissue engineering and biomaterials science.

Comparing cubic pores to hexagonal closed packed pore shapes in scaffold structures also reveals that the former exhibits higher elastic moduli and yield strengths.

TABLE 5.3: Mechanical characteristics of scaffold structures printed in polyJet

Pore Size	Elastic Modulus (GPa)						Yield Strength (MPa)					
	30 %		50%		70%		30 %		50 %		70 %	
	C	H	C	H	C	H	C	H	C	H	C	H
0.34	0.4	-	-	-	-	-	28	-	-	-	-	-
0.6	0.5	0.4	0.5	-	-	-	30	25	29	-	-	-
1.5	1.3	0.6	1.1	0.7	1.0	0.9	72	42	60	40	48	38
2.0	0.9	0.5	0.8	0.6	0.7	0.5	60	37	50	33	28	19
2.5	0.7	0.4	0.6	0.2	0.5	0.2	58	30	34	13	26	8
3.0	0.7	0.3	0.5	0.2	0.4	0.2	56	25	30	10	18	7.5

TABLE 5.4: Mechanical characteristics of scaffold structures produced via  $\mu$ SLA 3D printing

Mechanical Properties (MPa)	Pore Shape	Pore Size (mm)		
		0.34	0.6	1.5
Elastic Modulus	C	600	800	1900
	H	-	600	900
Yield Strength	C	42	45	108
	H	-	38	63

This indicates the important role that pore shape plays in influencing mechanical behaviour, maybe as a result of improved stress distribution. These findings have significant ramifications for improving the engineering and design of 3D-printed scaffold structures, particularly for uses needing certain mechanical properties. Figure 5.8 shows the stress-strain curves of  $\mu$ SLA printed scaffold structures. With increased porosity, such as in scaffolding made with PolyJet 3D printing, mechanical characteristics declined. Figure 5.8 provides an additional perspective by comparing scaffold structures generated through the PolyJet and  $\mu$ SLA 3D printing methods. Notably, the scaffold structures produced using  $\mu$ SLA have mechanical qualities that are 1.5 times better than their PolyJet 3D printed equivalents. Similarly, Table 5.4 shows how, as porosity and pore size increase, the elastic moduli and yield strength of  $\mu$ SLA 3D printed scaffold structures decrease. Comparing scaffold structures with hexagonal closed packed pore configurations to those with cubic pore geometries reveals better elastic moduli and yield strength.

The insights gained from these findings have profound implications for the enhancement of 3D-printed scaffold structures, especially in applications demanding specific mechanical properties. As depicted in Figure 5.8, the stress-strain curves of  $\mu$ SLA printed scaffold structures exhibit a clear relationship between porosity and mechanical behavior, mirroring the trends observed in PolyJet 3D printed scaffolds. Comparing the mechanical properties of scaffold structures produced

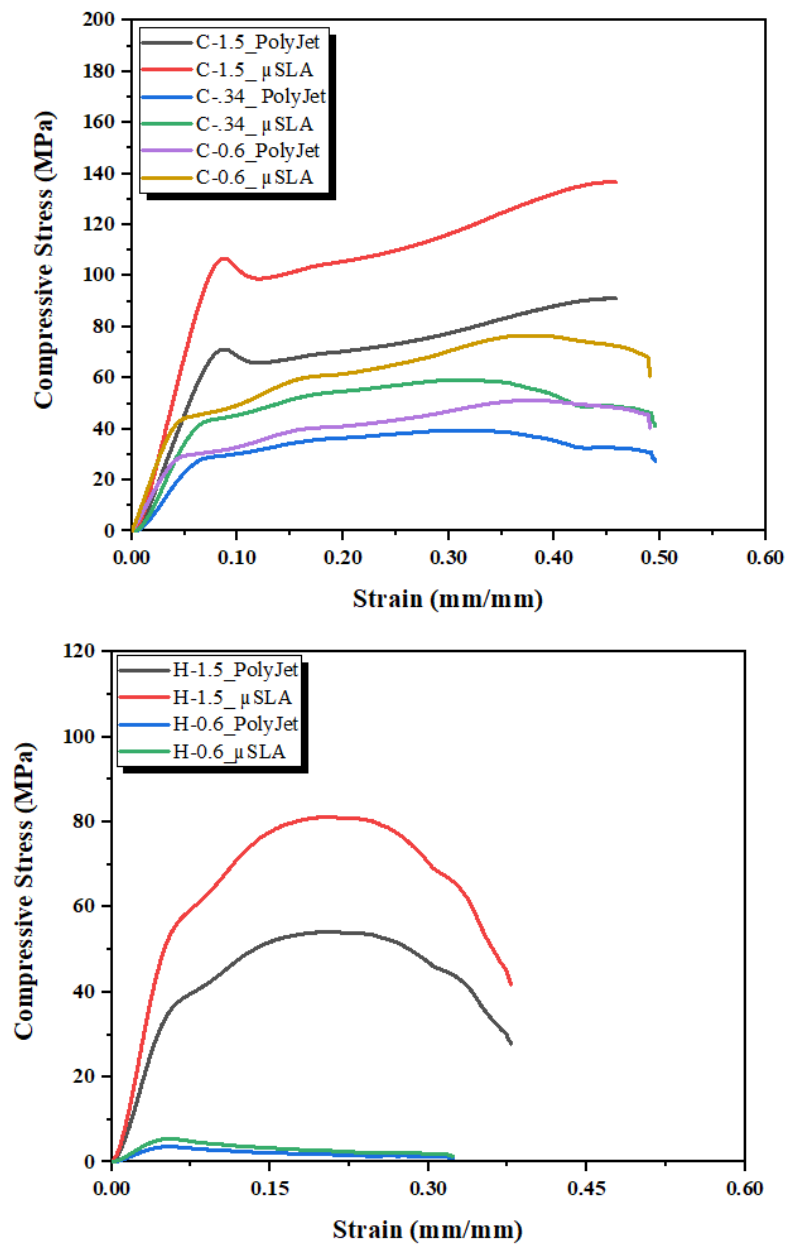


FIGURE 5.8: Stress-strain curves for 3D-printed scaffold structures, produced using polyjet and micro-stereolithography techniques, feature cubic and hexagonal closed packed pores at 30% porosity.

through PolyJet and  $\mu$ SLA 3D printing methods offers valuable insights. Notably,  $\mu$ SLA-printed scaffold structures display mechanical characteristics that outperform their PolyJet 3D printed counterparts by a factor of 1.5. This substantial difference underscores the importance of selecting the appropriate 3D printing method to achieve desired mechanical outcomes in scaffold design.

The data presented in Table 5.4 further emphasizes the impact of porosity and pore size on the mechanical properties of  $\mu$ SLA 3D printed scaffold structures. As porosity and pore size increase, both the elastic moduli and yield strength decrease, aligning with the observed trends in PolyJet scaffolds. This consistency in behavior across different 3D printing methods highlights the universal importance of pore characteristics in dictating scaffold mechanical performance.

## 5.8 Effect of Printing Direction on the Mechanical Properties

In order to comprehensively investigate how printing direction and method impact the mechanical characteristics of 3D printed scaffold structures, the study employed standardised samples as a starting point for investigation. Figure 5.9 displays how samples generated using a traditional PolyJet 3D printer in the x, y, and z axes responded to stress-strain analysis. These curves collectively illustrate the ductile deformation behavior observed across all standard samples printed using the PolyJet 3D printing method. Notably, printing the standard samples in the z-direction notably enhances their mechanical characteristics, underscoring the pivotal role that directionality plays in shaping structural integrity and behavior. Understanding the influence of printing orientation on mechanical properties provides valuable insights for tailored scaffold design. Table 5.5 shows the elastic moduli and yield strength of test samples manufactured in the x, y, and z directions. A noteworthy finding was that PolyJet samples printed in the z-direction exhibited superior mechanical properties to those printed in the y and x directions.

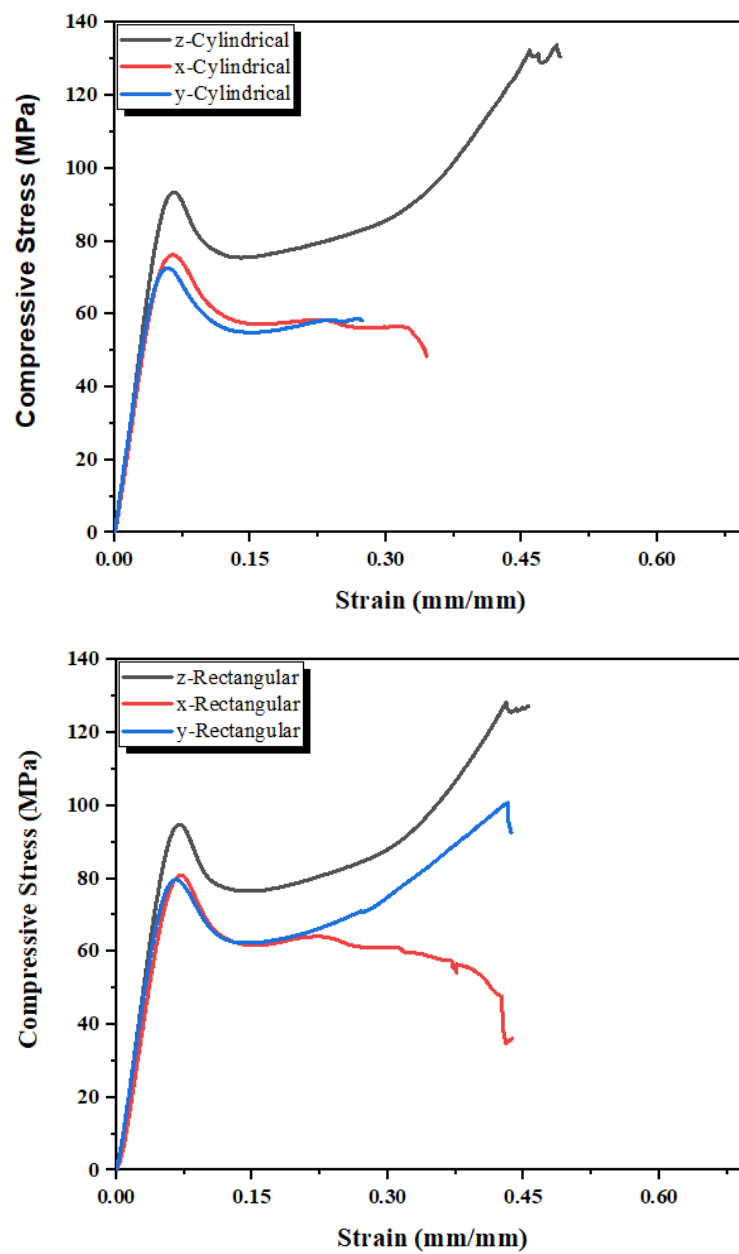


FIGURE 5.9: Stress-strain profiles of standard samples created within 3D space across the x, y, and z directions

TABLE 5.5: Mechanical characteristics of standard samples

Mechanical Properties (MPa)	Rectangular Direction			Cylindrical Direction		
	x	y	z	x	y	z
Elastic Modulus	1400	1300	1600	1300	1200	1600
Yield Strength	82	80	96	78	74	100

The standard sample could only be printed in the z-direction due to the limitations on the build area imposed by  $\mu$ SLA. The compression test results indicated that the yield strength and Young's modulus values of the standard  $\mu$ SLA-produced samples were 1.3 times higher compared to the same standard samples printed using PolyJet 3D technology.

# Chapter 6

## Numerical Investigation

### 6.1 Introduction

This chapter presents a comprehensive investigation of the deformation patterns exhibited by polymeric bone scaffolds. Within this pursuit, cubic and hexagonal closed-packed uniform scaffolds, distinguished by porosities of 30%, 50%, and 70%, serve as pivotal subjects in finite element (FE) models. The design of polymeric bone scaffolds is a critical stage where the process of creating scaffold structures is explained that closely mimic the properties and architecture of natural bone. Boundary conditions, a crucial aspect of numerical simulations, will be discussed in detail, shedding light on the parameters that influence the interactions between bone scaffolds and external loads. Crushable foam plasticity model, a fundamental tool for analyzing the deformation pattern of these scaffolds is utilized in this study under compression loading conditions. The development and structural characterization of the polymeric bone scaffold is another focal point, allowing to gain a deeper understanding of the scaffold's properties, composition, and architecture. Experimental validation of finite element (FE) results serves as a crucial link between numerical and experimental predictions, demonstrating the dependability and precision of the numerical simulations. This process not only verifies the accuracy of the computational models but also reinforces confidence in their

real-world applicability by confirming their alignment with empirical observations. In summary, this chapter serves as a foundational introduction to the numerical investigation of deformation pattern of bone scaffolds in the field of bone tissue engineering.

## 6.2 Finite Element Modelling

### 6.2.1 CAD Model of Bone Scaffolds

In this study, the 30%, 50% and 70% porous 3D finite element models of bone scaffolds with overall dimensions of 15 mm x 15 mm x 15 mm having pore size of 2.5 mm are designed using PTC Creo 7.0. The cubic and hexagonal unit cells with 2.5 mm pore size and struts at an angle of 90° and 60° are tessellated in 3D space to get an overall cubic structure of bone scaffolds. This study was focused on the testing of materials and the characterization of its properties both experimentally and by modelling. For this reason, the current dimensions were applied in order to obtain higher resolution and more loading capacity to prove and the validation of the mathematical model on wide range of data.

Strut diameters of 3D finite element models are mutated to introduce a required porosity of 30%, 50% and 70% of porosity. The pore sizes of hexagonal closed packed and cubic finite element models are defined as an inscribed circle and length of sides respectively. The detailed 3D finite element models of polymeric bone scaffolds with different views are presented in Figure 6.1.

### 6.2.2 Meshing of Bone Scaffolds

In finite element analysis, mesh size has great influence on the computational results. Therefore, the effect of mesh size on the mechanical response of polymeric bone scaffolds and ultimately on the damage was investigated at first. Different sizes of tetrahedral mesh on 70% porous polymeric bone scaffold were generated

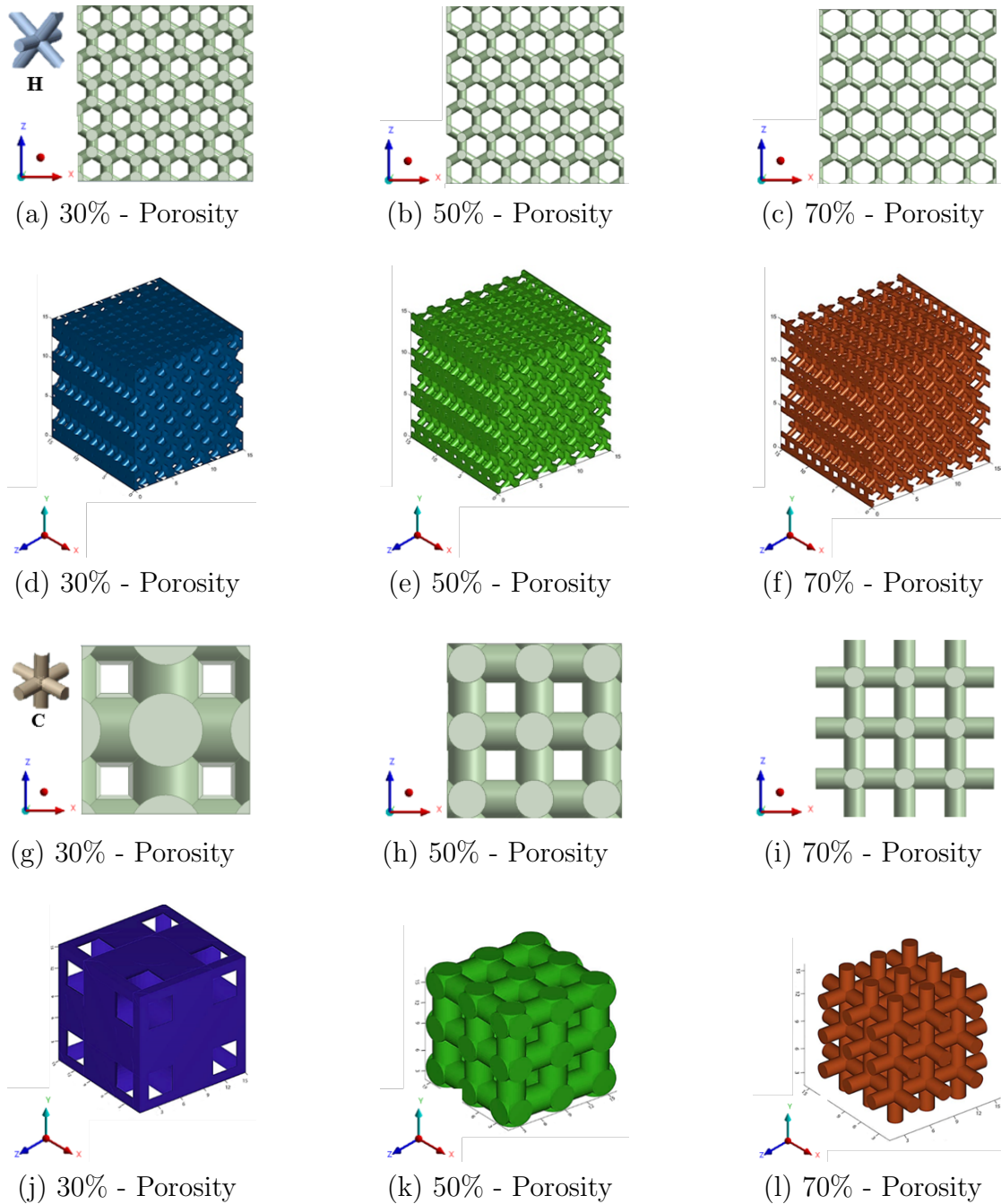
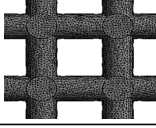
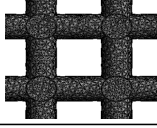
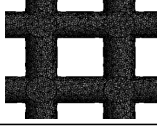
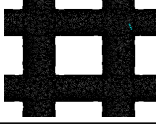
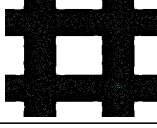


FIGURE 6.1: (a) to (c) present the 2D views of the 3D CAD models; (d) to (f) present the 3D views of the 3D CAD models. (g) to (h) presents the 2D views of the 3D CAD models; (j) to (l) presents the 3D views of the 3D CAD models

by keeping all other parameters same. The yield strength against every decreasing mesh size was calculated as an output parameter to measure the convergence. The element size, number of tetrahedral elements, computational time and yield strength are presented in Table 6.1. The Table 6.1 shows that the yield strength changed by 7.04% if the element size was reduced from 5.0 mm to 0.8 mm. whereas,

TABLE 6.1: Tetrahedral entities with computational time and yield strength for convergence

	Mesh 1	Mesh 2	Mesh 3
Bone Scaffold			
Element size (mm)	5	3	2
No. of tetrahedral elements	333945	656999	1121900
Computational time (min)	15	20	28
Yield strength (MPA)	26.57	25.54	25.47
	Mesh 3	Mesh 4	Mesh 5
Bone Scaffold			
Element size (mm)	1	0.8	0.6
No. of tetrahedral elements	3198744	4550711	7472326
Computational time (min)	41	47	72
Yield strength (MPA)	25.38	24.9	24.7

it only changed by 0.80% if the mesh size was further reduced to 0.6 mm. However, utilizing the element size of 0.6mm required more computational power as compared to the 0.8 mm element size. Hence, 0.6 mm tetrahedral mesh size was generated on each polymeric bone scaffold and produced computational results with good accuracy and reasonable computational time.

### 6.2.3 Boundary Conditions

For the FE simulations, 3D CAD models of the polymeric bone scaffolds with cubic and hexagonal closed packed unit cells were saved into the .STEP files and imported into the explicit dynamics ANSYS. The plates were added at the top and

bottom of the polymeric bone scaffolds to imitate clamps of compression testing machine. Frictionless connections were developed between the polymeric bone scaffolds and loading plates to mimic the real connection between the compression machine clamps and as-built polymeric bone scaffolds. The top and bottom plates were defined as rigid bodies and polymeric bone scaffolds were defined as a flexible body. Remote displacement-controlled boundary conditions were applied on the plates to simulate compression testing. The polymeric bone scaffolds were quasi-

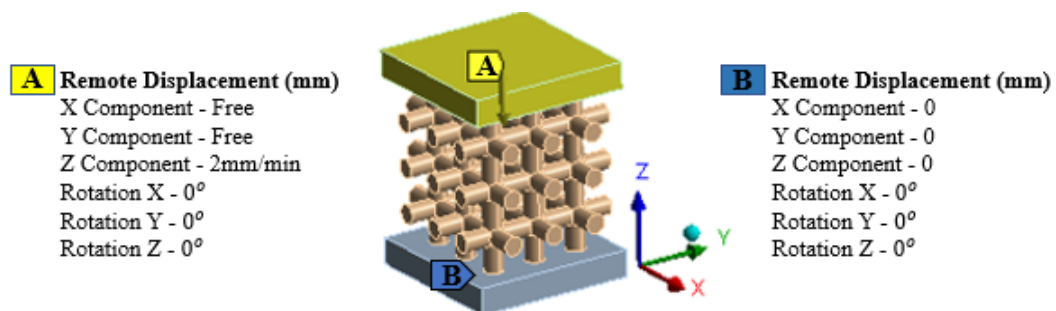


FIGURE 6.2: Top and bottom plates to mimic machine clamps, frictionless connection between plates and boundary conditions for FE simulations

statically compressed with a displacement rate of 2 mm/min. Bottom plate was fixed to the ground by using the remote displacement with all the translation and rotations values set to zero and compressive displacement was applied in -z direction on the top plate of each polymeric bone scaffolds to solve the FEM problems. FE simulation setup with loading plates, connections and boundary conditions is presented in Figure 6.2.

## 6.2.4 Crushable Foam Plasticity Model

To analyze the deformation of the polymeric bone scaffolds, the research utilized the crushable foam plasticity model. The governing factors for the Crushable Foam model, which incorporates an isotropic hardening rule, are the von Mises equivalent stress (referred to as 'q') and the hydrostatic pressure (denoted as 'p') [277]. Within the stress plane of 'p-q,' the yield surface is portrayed as a centered ellipse, as illustrated in Figure 6.3. In the condition of hydrostatic equilibrium, the

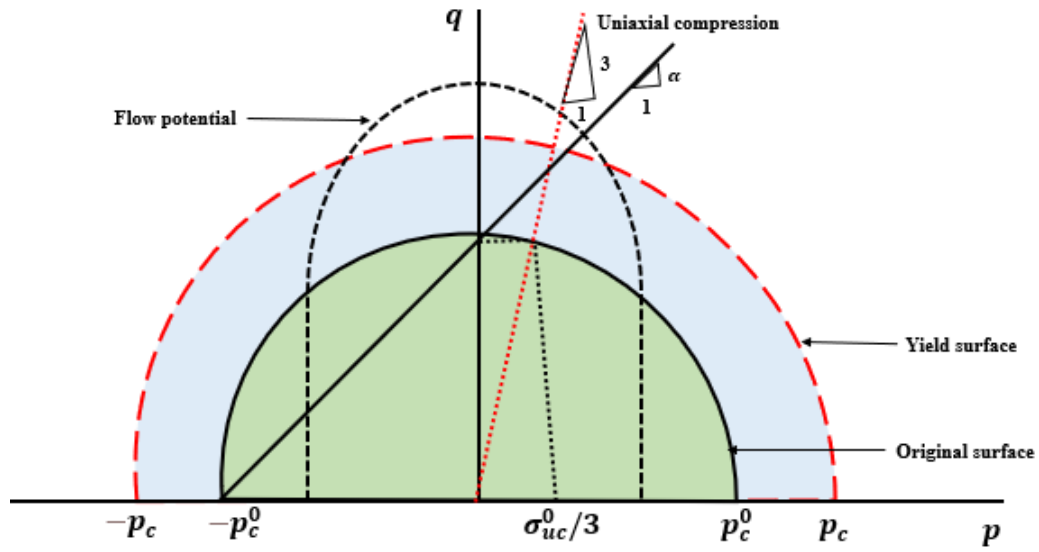


FIGURE 6.3: Crushable foam model: yield surface and flow potential in the p-q stress plane

yield surface extends along the pressure axis. The yield surface of the Crushable Foam model featuring isotropic hardening is defined as follows:

$$F = \sqrt{q^2 + \alpha^2 p^2} - B \tag{6.1}$$

The expression incorporates 'B,' which signifies the q-axis dimension of the yield ellipse. Moreover, ' $\sigma_{uc}$ ' denotes the absolute compressive strength under uniaxial loading, whereas 'a' represents the shape factor of the yield ellipse. Their respective definitions are as follows:

$$B = \alpha \cdot p_c = \sigma_{uc} \cdot \sqrt{1 + \frac{a^2}{3}} \tag{6.2}$$

$$\alpha = \frac{3k}{\sqrt{9 - k^2}} \tag{6.3}$$

The parameters in the aforementioned equations carry specific meanings. ' $\alpha$ ' characterizes the shape of the yield ellipse in the 'p-q' stress plane, while 'B' represents the size of the yield ellipse. Additionally, ' $p_c$ ' indicates the yield strength under hydrostatic compression, 'k' signifies the compression yield stress ratio, ' $\sigma_{uc}^0$ ' stands for the initial yield strength under uniaxial compression, and ' $p_c^0$ ' represents the

initial yield strength when exposed to hydrostatic compression. It is important to note that, due to the inherent challenges associated with directly measuring hydrostatic compressive and tensile strength, several researchers, as cited in [278], often make assumptions about constant ratios 'k' based on experimental data. Therefore, the sole parameter needed to define the yield surface is the value of 'k'. In the case of many low-density foams, the parameter 'α' was found to be close to one, allowing the value of 'k' to be set to unity, as reported in [277], which corresponds to a value of 1. Furthermore, the flow potential is defined as presented in [279]:

$$k = \frac{\sigma_{uc}^0}{p_c^0} \quad (6.4)$$

$$G = \sqrt{q^2 + \beta^2 p^2} \quad (6.5)$$

The parameter 'β' represents the lengths of the principal axes of the flow potential ellipse in the 'p-q' stress plane, and its correlation is established by the plastic Poisson's ratio.

$$\beta = 3\sqrt{2} \sqrt{\frac{1 - 2\nu_p}{1 + \nu_p}} \quad (6.6)$$

The geometry of the isotropic Crushable Foam yield criterion in the 'q-p' plane is determined by these relationships. Additionally, the evolving yield stress's work hardening slope (H) was determined using the following linear equation, as referenced in [279]:

$$H = \left(\frac{\sigma_e}{\hat{\sigma}}\right) \cdot h_\sigma + \left(1 - \frac{\sigma_e}{\hat{\sigma}}\right) \cdot h_p \quad (6.7)$$

'σ<sub>e</sub>' represents the von Mises effective stress, while 'σ̂' denotes the equivalent stress. Additionally, 'h<sub>σ</sub>' and 'h<sub>p</sub>' indicate the slopes of the stress versus logarithmic plastic strain curve during uniaxial and hydrostatic compression, respectively. Numerous finite element (FE) solvers have been integrated with the crushable foam plasticity model, requiring a complete definition that consists of five parameters: modulus of elasticity, Poisson's ratio, density, stress-strain curve, and maximum tensile stress for tension cut-off. The specific values of these parameters, as detailed in Table 6.2, were obtained from the prior study [19]. The previous study primarily focused on investigating the mechanical response of 3D printed standard

solid samples under compression. For the finite element analysis in this current study, the stress-strain curves obtained from the 3D printed standard solid samples in the z-direction were utilized. This choice was made due to the fact that the polymeric bone scaffolds used in this study were also printed in the same z-direction.

TABLE 6.2: Material properties for crushable foam plasticity model used in FE modelling [19]

Parameters	Values
Elastic modulus (GPa)	1.6
Poisson ratio	0.32
Maximum tensile stress (MPa)	50
Density ( $\text{kg}/\text{m}^3$ )	1190

### 6.3 Fabrication of Bone Scaffolds and Solid Samples

The process of fabricating the polymeric bone scaffolds began by converting the 3D CAD models into the widely used .stl format to facilitate manufacturing. Subsequently, a PolyJet printer, the Stratasys Objet260 Connex 1 (located at the Stratasys EMEA Regional Office in Baden-Baden, Germany), was employed for printing these scaffolds. This PolyJet printer is equipped with a high-capacity material cabinet capable of holding up to eight sealed 3.6 kg cartridges, enabling the simultaneous use of three different model materials and facilitating hot-swapping when necessary. The printer's net build size is  $255 \times 252 \times 200 \text{ mm}^3$  ( $10.0 \times 9.9 \times 7.9 \text{ in.}$ ). It provides exceptionally accurate printing with horizontal build layers having a maximum thickness of 16 microns (0.0006 in.). The build resolution is equally impressive, featuring a 600-dpi resolution for both the x and y axes, and a remarkable 1600 dpi resolution for the z-axis. This high precision allows for features smaller than 50  $\mu\text{m}$  to fall within a range of 20–85 microns, and full model sizes can be as small as 200 microns. For the printing process,

the specific material used was VeroClear from STRATASYS. VeroClear was chosen for its transparency, which aids in visualizing porosity and scaffold structure during the design and prototyping phases. Additionally, it is a popular material for 3D printing substrates in biomedical engineering applications [280–282], making it a suitable choice for this study. Its cost-effectiveness in the early stages of the project allowed for a focus on porosity and deformation behavior analysis, with plans for biocompatibility enhancements in future research phases. The PolyJet printer took approximately ninety minutes to print six polymeric bone scaffolds. After printing, the support material (SUP706) was removed using pressurized water, followed by the elimination of residual particles using compressed air. The support material was a non-toxic gel-like photopolymer support manufactured and designed by Stratasys (North America—Stratasys Units). During the PolyJet printing process, SUP 706 was simultaneously deposited alongside the model material in areas where support was needed. These support structures were essential for upholding overhanging features and complex geometries of the model. In contrast, in a previous study [19], conducted using  $\mu$ SLA (located at Krämpferstraße 4, 99084 Erfurt, Germany), each scaffold took approximately three hours and twelve minutes to print individually, with a thickness of 0.025 mm. The support material for these as-built polymeric bone scaffolds was removed through sonication in isopropyl alcohol (IPA) for twenty minutes, and the solid support beams were manually removed, as detailed in the previous study [19]. The IPA used for this process was obtained from Sigma Aldrich, Ireland, and had been previously employed for rinsing 3D-printed parts by the co-authors in other studies [280]. For the visual representation of the stages involved in the development of the polymeric bone scaffolds, are represented in Figure 6.4. These same stages were followed for fabricating the standard solid samples required for the crushable foam plasticity model in finite element modeling. For the solid samples, three replicates were created in the x-, y-, and z-directions and printed in the x-direction using the printer. It's important to note that the crooked appearance of the samples is due to the angular perspective from which the images were captured. The build direction for the polymeric bone scaffolds was in the z-direction, while different

printing directions were utilized to assess the effect of the printing direction on the mechanical properties of the samples and to determine the most relevant results for the crushable foam plasticity model.

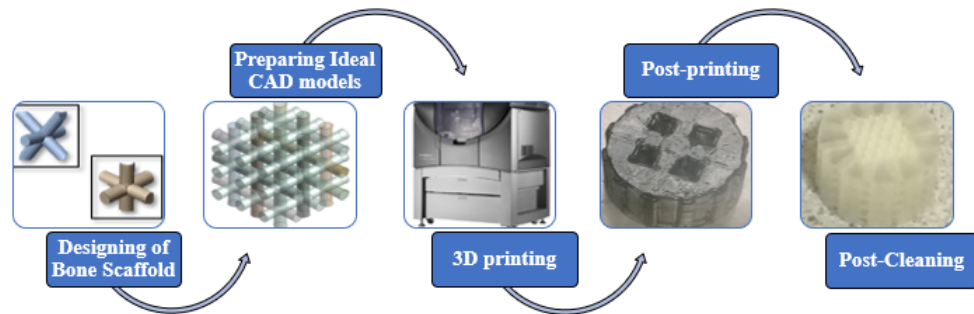


FIGURE 6.4: Summary of stages involved in the development of additively manufactured polymeric bone scaffolds and standard solid samples

## 6.4 Quasi-Static Compression Testing

After capturing optical microscopy images, the as-built polymeric bone scaffolds underwent compression testing using the Zwick/Roel Z50, a universal testing machine produced by Zwick/Roell GmbH Co. KG in Ulm, Germany. The testing apparatus was coupled with the Zwick TestXpert III simulation software. The characterization of the as-built scaffolds followed the ASTM D-695 standard, applying a deformation rate of 2 mm/min and a maximum loading capacity of 50 kN. To ensure proper contact between the mating parts and minimize potential sliding effects, a pre-loading force of 5 N was employed. In this study, the struts of the scaffolds functioned as short columns, given their slenderness ratio of less than 9. Short columns typically fail due to compression rather than buckling, which eliminated the need for additional buckling supports during the compression testing. There were a total of twenty-eight samples. To establish a 95% confidence level, three repetitions of the compression test were performed on each sample, resulting in a total of eighty-four samples (three copies of each sample) that were fabricated for the compression tests. The compression test was conducted three times for each of the three replicates of the as-built polymeric bone scaffolds.

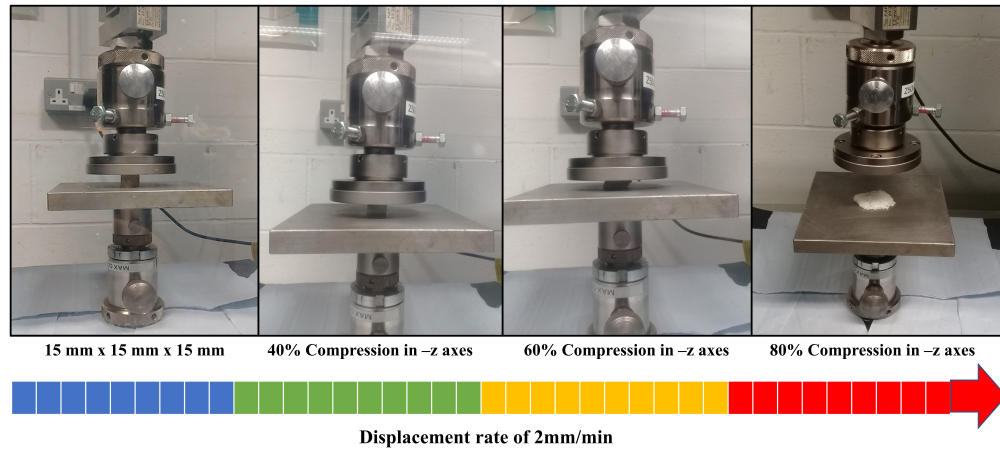


FIGURE 6.5: Different levels of compression testing of additively manufactured polymeric bone scaffolds and 3D printed standard solid samples

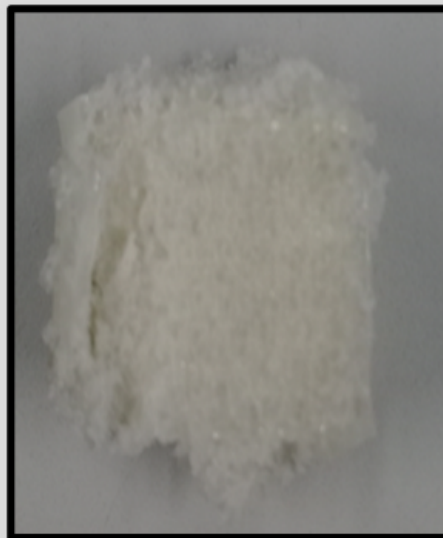


FIGURE 6.6: Crushed Sample

Figure 6.5 visually illustrates the different stages of the compression process. The force versus displacement data obtained from Zwick TestXpert III were utilized to construct stress-strain diagrams for the as-built polymeric bone scaffolds. A similar procedure, as outlined in a prior study [19], was employed to characterize the mechanical behavior of the 3D printed standard solid samples. The mechanical

properties derived from the compression testing of the 3D printed solid samples were subsequently integrated into the finite element analysis conducted in this study. Figure 6.6 shows the crushed sample.

## 6.5 Experimental Validation of FE Results

Figure 6.7 depicts the mechanical response of polymeric bone scaffolds featuring porosities of 30%, 50%, and 70%, with a consistent pore size of 2.5 mm. The stress-strain curve presented in Figure 6.7 represents the averaged performance derived from three separate replicates of polymeric bone scaffolds, and this average exhibits an impressively low average percentage error of under 1% (specifically 0.32). Additionally, the inclusion of the solid sample curve within Figure 6.7 serves as a valuable reference point when evaluating the behavior of the porous samples (30%, 50%, and 70%). This strategic use of the solid sample curve provides a clear means of assessing how varying porosities (30%, 50%, and 70%) influence the material's characteristics.

The stress-strain curves for all the bone scaffolds exhibit a pattern similar to that of cellular materials. After the elastic region, energy absorption occurs during the plateau phase until the onset of densification. In cellular materials, the plateau region can be marked by either strain hardening or strain softening. In our study, we observed a stress decrease at the end of the initial peak in the stress-strain curve for the 30% and 50% porous polymeric bone scaffolds with a cubic unit cell, indicating strain softening leading up to the onset of densification. However, for the 70% porous polymeric bone scaffolds with a cubic unit cell, no densification region was observed. Among the hexagonal closed-packed unit cell types, only the 30% porous bone scaffolds exhibited a plateau and densification region. No other bone scaffolds displayed densification. The presence of a densification region is contingent on the deformation and failure mechanisms, particularly at higher strain values during the crushing stage. The absence of a densification region and the subsequent terminal hardening were anticipated in cases involving highly

brittle failure of thin struts and delamination of the material. Additionally, the

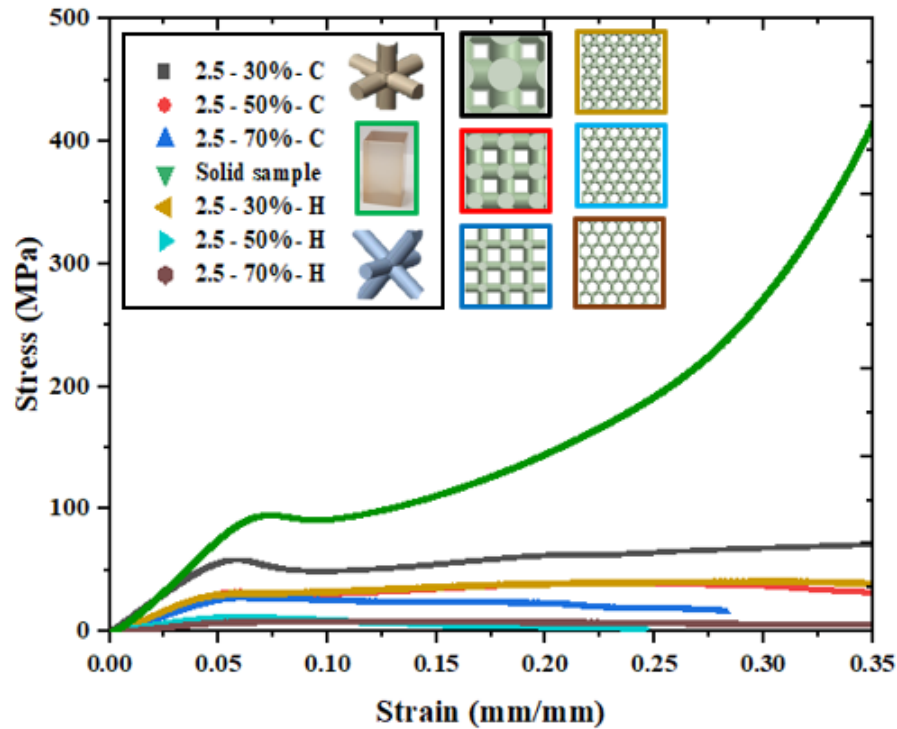


FIGURE 6.7: Experimental stress-strain curves for 3D printed porous polymeric bone scaffolds and 3D printed standard solid samples

stress-strain curves revealed that the 50% porous bone scaffolds with a hexagonal pore shape and the 70% porous bone scaffolds with a cubic pore shape did not reach the densification region up to a strain value of 0.35 mm/mm. This behavior aligns with the findings of the prior study [19], which investigated bone scaffolds fabricated using the  $\mu$ SLA technique. Figure 6.7 provides a comparison between the mechanical responses of the 3D printed standard solid samples, cubic polymeric bone scaffolds, and hexagonal polymeric bone scaffolds. It is evident that the elastic moduli and yield strength values are higher for the cubic pore shape compared to the hexagonal pore shape. Additionally, the mechanical response of denser or less porous polymeric bone scaffolds closely resembles that of the solid sample, while it deviates for higher porosity polymeric bone scaffolds.

The mechanical properties of the polymeric bone scaffolds, as assessed using the crushable foam plasticity model, exhibited strong agreement with the experimental data, with an average percentage error of 12.27% (standard deviation = 3.05). This

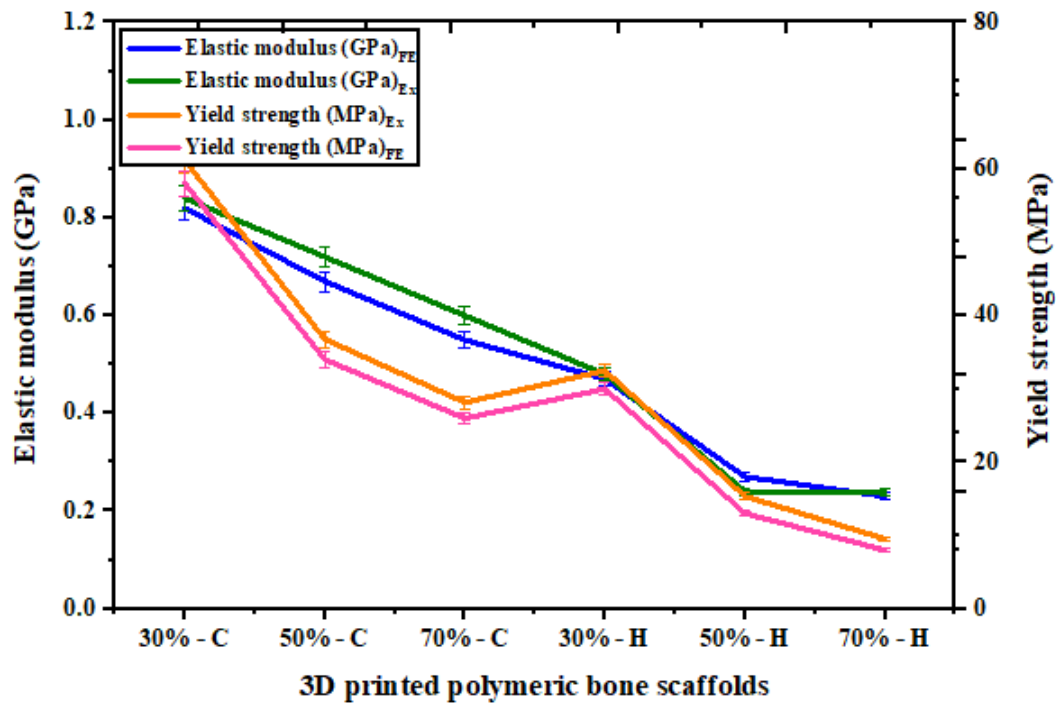


FIGURE 6.8: Experimental and FE elastic moduli and yield strengths of polymeric bone scaffolds

percentage error is calculated as ( $\% \text{ error} = (\text{measured value} - \text{numerical value}) / \text{measured value}$ ). Figures 6.7 and 6.8 provide a comprehensive comparison between different regions of the experimental and finite element (FE) stress-strain behavior. In the elastic regions of the experimental and FE stress-strain curves, there is a commendable alignment between the two. In the plastic region, while the FE stress magnitude was slightly higher than the experimental stress, the trend of the plateau stress closely matched the numerical results. Additionally, the Young's moduli and yield strengths of the polymeric bone scaffolds, as presented in Figure 6.10, affirm the accuracy of the crushable foam plasticity model in predicting the maximum and plateau stress, with an overall percentage error of 12.27% when compared to the experimental values. A similar pattern was observed for bone scaffolds created through  $\mu$ SLA, with a percentage error of less than 3% [19].

The differences between the experimental and finite element (FE) mechanical properties of the polymeric bone scaffolds can be attributed to significant variations in strut diameters and deviations of the struts from the intended building direction. Figure 6.9 displays microscopic images of the as-built polymeric bone scaffolds,

which were acquired using the Keyence-Digital microscope VHX-2000. These images were instrumental in studying these geometric discrepancies.

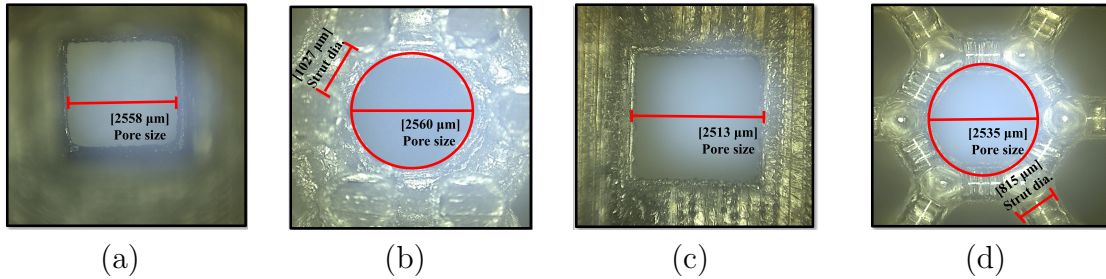


FIGURE 6.9: Optically measured architectural parameters of as-built polymeric bone scaffolds using Keyence-Digital microscope VHX-2000 (a) cubic pore shape with 30% porosity (b) hexagonal pore shape with 30% porosity (c) cubic pore shape with 50% porosity (d) hexagonal pore shape with 50% porosity [19]

TABLE 6.3: Deviations in the architectural parameters of CAD-based (actual) polymeric bone scaffolds and additively manufactured polymeric bone scaffolds

Pore shapes	Porosities (%)		Diff. (%)	Pore sizes (mm)		Diff. (%)	Strut diameters (mm)		Diff. (%)
	Actual	As-built		Actual	As-built		Actual	As-built	
H	30	29.29 ± 4.05%	2.37	2.5	2.56 ± 5.75%	2.34	1.004	1.027 ± 1.08%	2.34
H	50	49.22 ± 3.42%	1.56	2.5	2.54 ± 4.05%	1.57	0.802	0.815 ± 0.09%	1.57
H	70	69.45 ± 3.15%	0.78	2.5	2.52 ± 4.05%	0.79	0.59	0.595 ± 0.08%	0.78
C	30	29.29 ± 1.33%	2.37	2.5	2.56 ± 4.05%	2.34	6.6	6.754 ± 0.13%	2.35
C	50	49.41 ± 1.05%	1.18	2.5	2.53 ± 4.05%	1.18	3.28	3.319 ± 0.11%	1.18
C	70	69.72 ± 0.08%	0.4	2.5	2.51 ± 4.05%	0.4	1.75	1.757 ± 0.09%	0.41

The variations in architectural parameters between the as-built polymeric bone scaffolds and the CAD-based models (the actual) are summarized in Table 6.3. Following a detailed geometric characterization, it was noted that the strut diameter of the as-built polymeric bone scaffolds exhibited a consistent trend of gradual increase with decreasing porosity. This phenomenon was observed across all samples, with an average difference of approximately 2.53% and 2.54%. The observed augmentation in strut diameters within each as-built polymeric bone scaffold can be attributed to the overcuring of the printed layers during the fabrication process. This finding underscores the importance of meticulous control over the printing parameters to achieve the desired structural characteristics and porosity levels in additive manufacturing processes. Moreover, in the case of SLA, there was a slight discrepancy of approximately 2.5% observed in the architectural parameters between the as-built polymeric bone scaffold and the CAD-based polymeric bone scaffolds. This underscores the importance of meticulous calibration and

optimization of printing parameters to ensure precise replication of the intended scaffold design [19].

## 6.6 Deformation in Bone Scaffolds

The numerical analysis of the deformation of polymeric bone scaffolds under compression levels of 40%, 60%, and 80% is illustrated in Figure 6.10. It's evident that the 30% porous polymeric bone scaffolds with a hexagonal pore shape exhibit deformations approximately 4% higher than those of the polymeric bone scaffolds with a cubic pore shape. This percentage error decreases to 1% as the porosity increases from 50% to 70%. Overall, the polymeric bone scaffolds consistently displayed outward bulging during compression, progressing from 40% to 80%.

Similarly, compressive stress contours were generated to examine the stress distribution in polymeric bone scaffolds with a cubic pore shape following the finite element analysis, as depicted in Figure 6.11. Figure 6.11(a) illustrates the uniform deformation of vertical struts in the elastic region for the 30% porous polymeric bone scaffolds. After reaching the maximum stress in the elastic region, post-yield softening initiated, leading to the breakage of struts.

Subsequently, deformation was accompanied by pore blockage due to extensive strut failure in the plateau region, which continued until the start of the densification region. Ultimately, the entire structure was crushed and transformed into a disc-like shape at the end of densification. A similar failure pattern was observed for the 50% porous polymeric bone scaffolds, as depicted in Figure 6.11(b).

However, for the 70% porous polymeric bone scaffolds shown in Figure 6.11(c), post-yield softening was absent, and the collapse of the structure occurred before reaching a strain of 0.35 (mm/mm) due to continuous buckling and breakage of micro-struts. During the failure process, minor stress fluctuations were also observed, which corresponded to the failure and buckling of micro-struts within both the plateau and densification regions of the scaffold structure. These fluctuations,

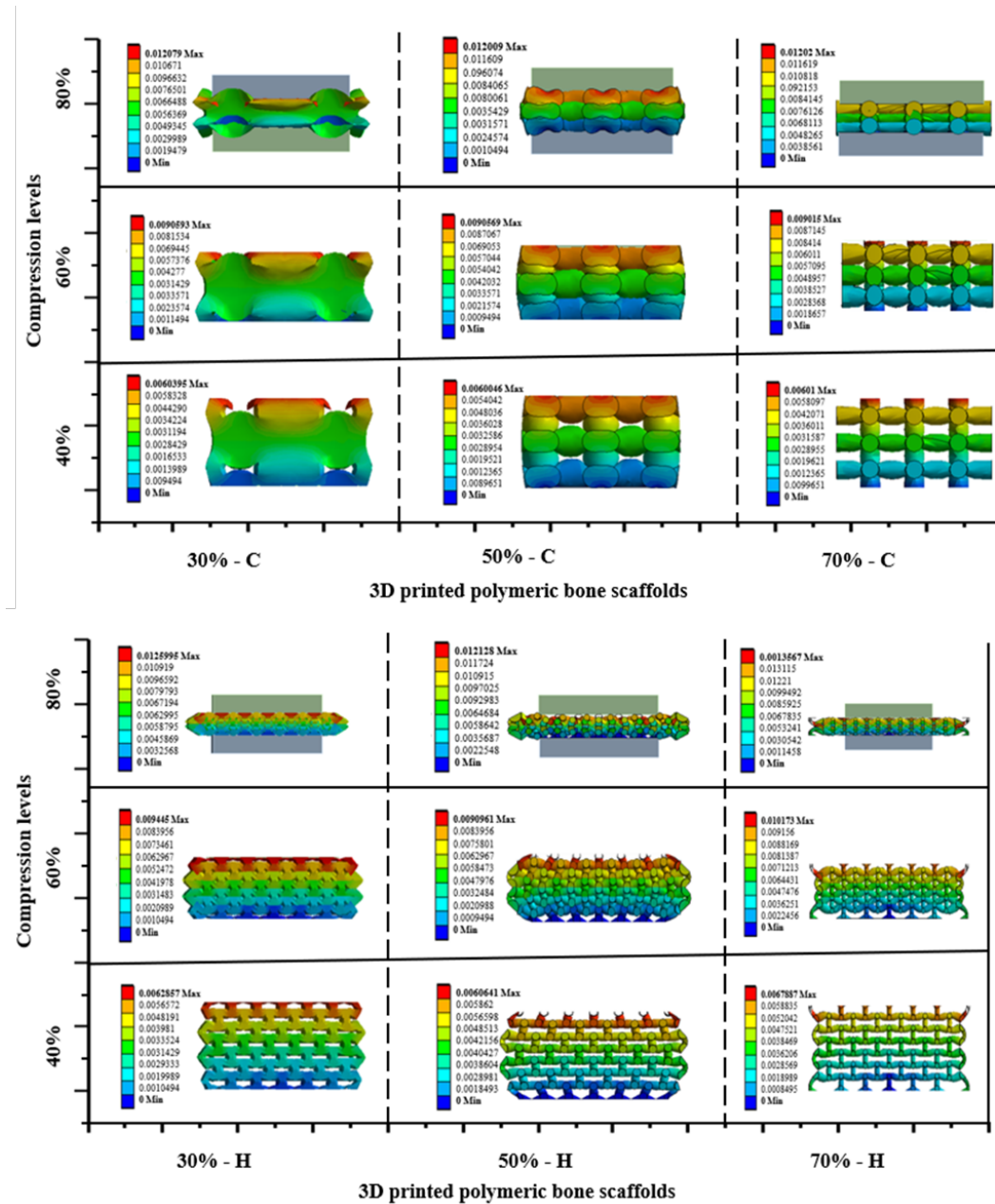


FIGURE 6.10: Deformation of polymeric bone scaffold under the compression level of 40%, 60% and 80%

although minor in magnitude, played a significant role in the overall failure mechanism, highlighting the complex interplay between structural integrity and mechanical behavior in bone scaffold materials. Understanding these nuanced stress fluctuations provides valuable insights for optimizing scaffold design and fabrication processes to enhance their mechanical performance and long-term durability in biomedical applications. Polymeric bone scaffolds with a hexagonal closed-packed pore shape, characterized by porosities of 30%, 50%, and 70%, displayed

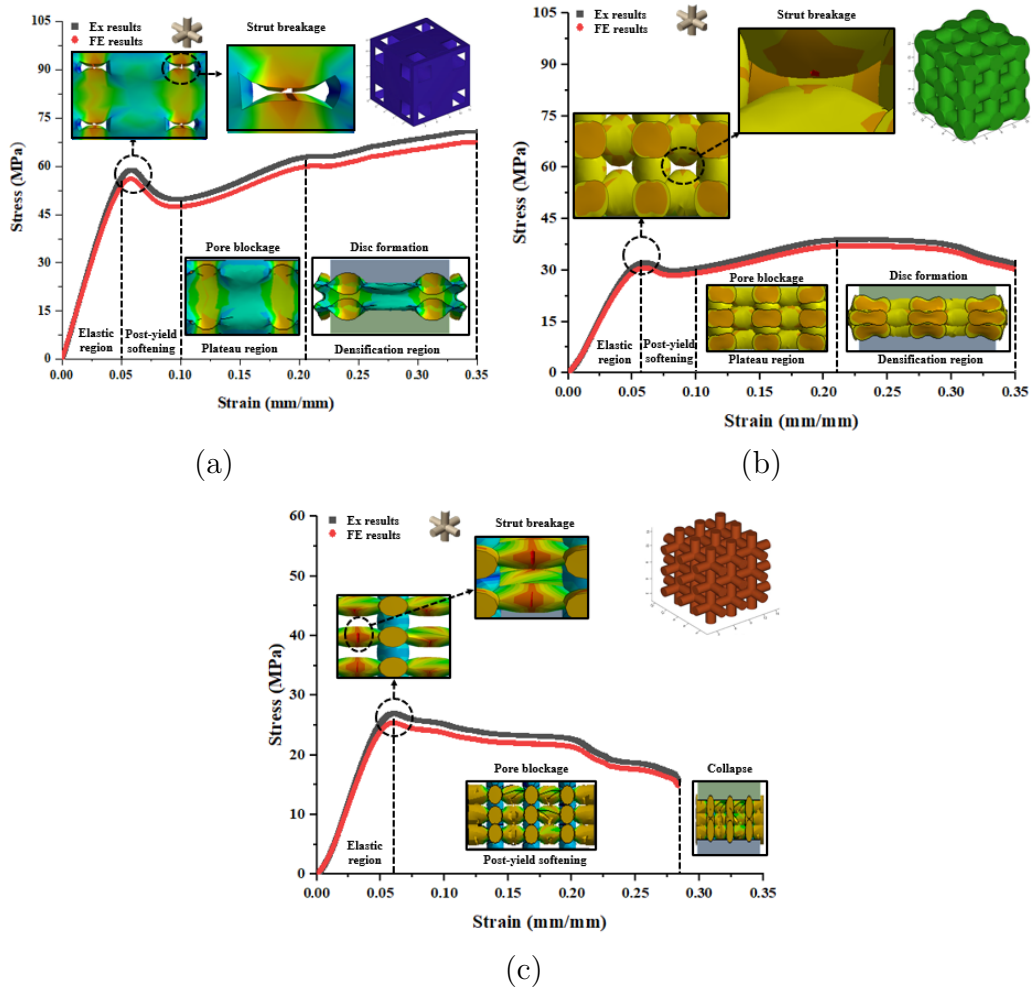


FIGURE 6.11: FE deformation mechanism through compressive stress contours of cubic pore shape at different level of strains consisted of (a) 30% (b) 50% and (c) 70% porosity in comparison with actual deformation behaviour of polymeric bone scaffolds

unique mechanical behaviors. Compressive stress contours obtained from the finite element analysis were categorized into different regions based on their associated strain levels, as illustrated in Figure 6.12. Figure 6.12(a) illustrates the deformation behavior of the 30% porous bone scaffolds, featuring uniform deformation along with strut breakage in the elastic region. Subsequently, the deformation progresses with pore blockage observed in the plateau region until the start of the densification region. Ultimately, the entire structure undergoes crushing and transforms into a disc-like shape at the end of the densification. In Figure 6.12(b), the deformation is characterized by post-yield softening, leading to the collapse

of the structure before reaching a strain of 0.35 (mm/mm). Similarly, the deformation behavior of the 70% porous bone scaffolds, as observed in Figure 6.12(c), follows a pattern akin to that of the 30% porous bone scaffolds. Initially, pore blockage occurs in the plateau region, gradually progressing towards the densification region. During this process, the entire structure undergoes crushing, ulti-

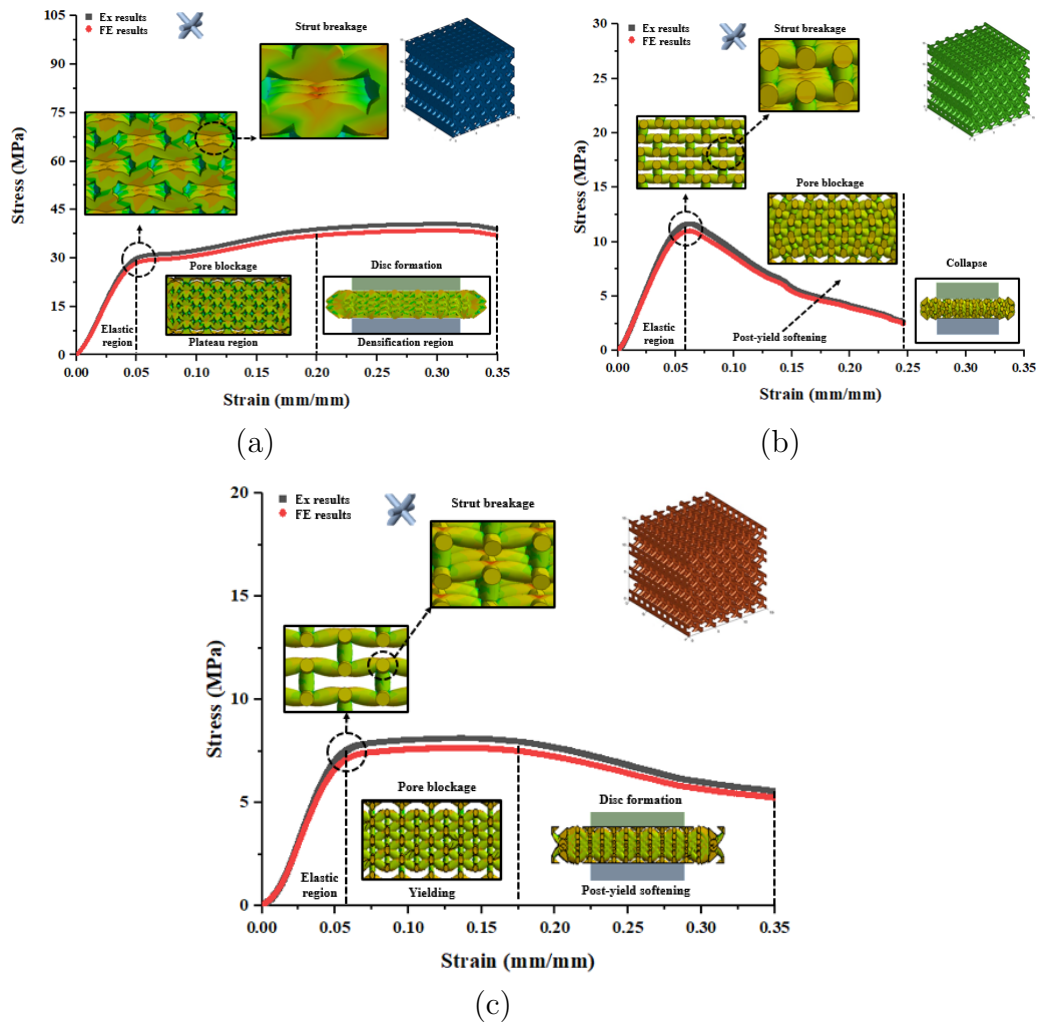


FIGURE 6.12: FE deformation mechanism through compressive stress contours of hexagonal closed packed pore shape at different level of strains consisted of (a) 30% (b) 50% and (c) 70% porosity in comparison with actual deformation behaviour of polymeric bone scaffolds

mately transforming into a disc-like shape by the end of the densification phase. This deformation mechanism highlights the complex interplay between pore structure, material properties, and external loading conditions, underscoring the need for comprehensive computational modeling and experimental validation to elucidate the underlying phenomena. Furthermore, understanding these deformation

mechanisms is crucial for optimizing scaffold design and fabrication processes to achieve desired mechanical properties and structural integrity, thereby enhancing their suitability for biomedical applications.

## 6.7 Discussion

The development of bone scaffolds with complex shapes and controlled architectural parameters is crucial. It is essential when fabricating scaffolds intended to accurately mimic native tissue in bone tissue engineering applications [280]. Additive manufacturing technique permits such control and allows the fabrication of biocompatible and mechanically appropriate bone scaffolds that serve as a bone substitute in orthopaedics [281]. In tissue engineering, finite element (FE) analysis has become increasingly popular, particularly for improving the design of bone scaffolds. According to prior research, this method emphasises the influence of architectural elements on the mechanical characteristics and fluid transport features of such scaffolds [282]. There were very few studies which predict the deformation and failure mechanism of the additively manufactured bone scaffolds. Nevertheless, it remains a significant challenge to develop finite element models capable of accurately predicting the deformation and failure mechanisms of bone scaffolds. Ongoing research is being conducted to propose a material model that can enable precise simulations of the deformation of bone scaffolds. By keeping this in mind, authors focused to investigate the deformation of the polymeric bone scaffolds using finite element analysis. Six CAD-based polymeric bone scaffolds were designed in this study and fabricated through micro-stereolithography ( $\mu$ SLA) and PolyJet (PJ) using two different polymeric materials. Crushable foam plasticity model was utilized in finite element modeling for defining the plastic range of the polymeric bone scaffolds. Compression testing of standard solid samples and polymeric bone scaffolds was conducted to experimentally validate the FE results. The discrepancy of 12.27% between the experimental data and finite element results may be attributed to the assumption of material isotropy. Additionally, deviations of nearly 2.5% in the architectural parameters were observed between

CAD-based polymeric bone scaffolds and the as-built polymeric bone scaffolds. Strut diameters of almost every as-built polymeric bone scaffold were larger than the CAD-based polymeric bone scaffolds could be due to the overcuring of layers during printing. Due to the deviations in architectural parameters the porosity of as-built polymeric bone scaffold was also reduced to 29.29%, 49.41% and 69.72%, very close to the CAD-based polymeric bone scaffolds. This also represents the high fidelity of the CAD-based bone scaffold models used for the additive manufacturing. Consequently, it can be reasonably anticipated that CAD-based finite element models provide a satisfactory approximation of the real porous bone scaffolds. Nonetheless, deviations in the architectural parameters of as-built bone scaffolds from their nominal values were observed, which might have the potential to influence the outcomes of finite element analyses. Hence, it is recommended that the reconstruction of as-built bone scaffolds using optical microscopy images be considered. This approach has the potential to further reduce discrepancies between experimental and finite element results in future studies and enhance the accuracy of finite element analysis.

The CAD-designed polymeric bone scaffolds in this study, featuring various combinations of architectural parameters, exhibited distinct deformation patterns under investigation through finite element analysis coupled with a damage model. Notably, for 30% and 50% porous polymeric bone scaffolds with cubic pore shapes, a stress decline was observed following the initial stress-strain curve peak, indicating a softening region. This was followed by the failure of struts within the polymeric bone scaffolds. Afterwards plateau region showed the pore blockage upto the beginning of densification region. On the other hand, no densification region was observed in case of 70% porous polymeric bone scaffolds with same pore shape. Absence of densification region in case of 70% polymeric bone scaffolds was expected when deformation was followed by the high brittle failure of thin struts. In case polymeric bone scaffolds with hexagonal closed packed pore shape, only of 30% porous bone scaffolds showed the plateau and densification region. 50% and 70% porous bone scaffolds crushed before densification region upto the 0.35mm/mm

strain values. The findings revealed that while cubic pore shapes exhibited superior mechanical responses compared to hexagonal closed packed shapes, the failure mode in the latter was more uniform. Interestingly, 50% porous scaffolds for both pore shapes closely resembled human bone in terms of mechanical properties. Significantly, the crushable foam plasticity model has proven to be a valuable tool for simulating deformations in polymeric bone scaffolds. This model facilitates the redesign of bone scaffolds to mitigate the risk of harming native tissues in bone tissue engineering applications.

This research work focused on evaluating the crushable foam plasticity model. It aimed to assess its effectiveness in predicting the deformation and failure mechanisms of 3D printed polymeric bone scaffolds. These scaffolds were fabricated using micro-stereolithography ( $\mu$ SLA) and PolyJet (PJ) 3D printing techniques. Three distinct porosity levels, such as 30%, 50%, and 70%, were obtained by modifying strut diameters in CAD-based bone scaffolds with cubic and hexagonal closed packed pore forms. These CAD-based models were used in the finite element analysis to investigate the deformation at different strain values. Stress-strain curves of almost all the bone scaffolds showed different region of deformations corresponding to the strain values such as elastic region, post-yield softening region, plateau region and densification region. A comparison between the two different polymeric bone scaffolds was conducted. The results revealed that the bone scaffolds with a cubic pore shape exhibited higher mechanical properties. This makes them a more suitable choice for bone replacement applications in orthopedics. Moreover, discrepancy between the FE results and experimental results showed that crushable foam plasticity model can properly estimate the maximum and plateau stresses of polymeric bone scaffolds with a percentage error of 12.27%. Therefore, developing more detailed numerical methods consisting of failure mode can improve understanding effect of deformation of 3D printed polymeric bone scaffolds. The comparison of finite element (FE) stress-strain curves with experimental results was conducted. This comparison highlighted the robustness of the crushable foam plasticity model in assessing stress at the first peak and plateau regions. However, a comprehensive investigation is still necessary, especially concerning factors such

as architectural parameters and the production process. In essence, the simulation methods provided a more elucidating perspective on the deformation behavior of polymeric bone scaffolds characterized by diverse architectural parameters. Furthermore, based on the mode of failure and deformation observed, new structures can be redesigned. These redesigns aim to create more suitable options for bone replacement in bone tissue engineering applications.

# Chapter 7

## Conclusion and Future Recommendation

### 7.1 Conclusion

This study investigated at the hydrophobicity, permeability, and mechanical characteristics of 3D printed scaffold constructions using two distinct 3D printing technologies: PolyJet and micro-stereolithography ( $\mu$ SLA).

#### 7.1.1 Hydrophobicity and Surface Energy

In the experiment, the contact angle and surface energy of 3D printed scaffold constructs were examined using PolyJet (VeroClear) and  $\mu$ SLA (PlasWhite) techniques with various liquids. The results showed that when glycerol content in water rose, contact angles trended upward and surface energy trended downward. This observation indicated heightened hydrophobicity and reduced permeability of both VeroClear and PlasWhite materials in response to liquid mixtures with elevated glycerol content. For both VeroClear and PlasWhite materials, the contact angles with tap water measure approximately  $67.0^\circ$  and  $69.1^\circ$ , respectively,

indicating a moderate level of hydrophobicity without strong water-repellent properties, as their surface energy values stand at around 41.7 mN/m and 38.5 mN/m, signifying a moderate attraction to water. When a 15% Glycerol-Water solution is introduced, the contact angles rise to approximately 70.0° and 72.6° for VeroClear and PlasWhite, respectively, demonstrating increased hydrophobicity compared to tap water, with decreased surface energy values of around 40.0 mN/m and 37.9 mN/m, indicating reduced water-attracting tendencies. Furthermore, with a 20% Glycerol-Water solution, the contact angles further increase to approximately 72.9° and 73.7° for VeroClear and PlasWhite, signifying even greater hydrophobicity, and the surface energy values decrease once more to around 39.8 mN/m and 37.1 mN/m, suggesting an increasing degree of water repellency.

### **7.1.2 Permeability Analysis**

Using various pore sizes and test fluids, permeability studies were carried out on both PolyJet and  $\mu$ SLA 3D printed scaffold constructions. The data revealed that pore size, porosity, and viscosity had significant impacts on permeability. Larger pore sizes, higher porosity, and more viscous fluids led to greater permeability. Pore size was found to be the most influential factor, and the geometric arrangement of pores also affected permeability. The experimentally determined permeability consistently exceeded the permeability calculated numerically in all scenarios. The difference between the measured and estimated permeability can be attributed to various factors, including inadequate cleaning of the 3D-printed scaffold structures and factors not accounted for by the Kozeny-Carman equation, such as pressure drop across the sample, fluid viscosity, and surface energy. Consequently, a hybrid model that combines the strengths of both computational and experimental techniques could offer a more precise approach to permeability measurement. Furthermore, future research should emphasize the refinement of cleaning procedures for 3D-printed scaffold structures to minimize potential contaminants that could impact permeability measurements. Additionally, exploring the effects of variations in pressure drop, fluctuations in fluid viscosity, and changes

in surface energy on permeability could help bridge the gap between experimental and numerical results. The development of an improved Kozeny-Carman equation that takes these factors into account could also enhance the accuracy of permeability predictions.

### **7.1.3 Comparison between Printing Techniques**

A comparison was made between PolyJet and  $\mu$ SLA printing techniques.  $\mu$ SLA is more precise than PolyJet technique when printing complex shapes while PolyJet is faster than  $\mu$ SLA. The comparison revealed that  $\mu$ SLA printed scaffold structures typically displayed higher permeability values. This outcome can be attributed to  $\mu$ SLA's higher precision in creating fine and detailed structures. The specific geometric arrangement of pores influenced the permeability characteristics of the scaffold structures. Analyzing the mechanical attributes of scaffold structures fabricated using PolyJet and  $\mu$ SLA 3D printing techniques provides valuable insights. Significantly, scaffold structures created through  $\mu$ SLA printing exhibit mechanical properties that surpass those of their PolyJet 3D printed counterparts by a factor of 1.5. This marked contrast emphasizes the critical role of choosing the right 3D printing method to attain the desired mechanical characteristics in scaffold design.

### **7.1.4 Effect of Surface Area**

The study underscored the pivotal role of specific surface area in shaping the permeability of scaffold structures. Through the investigation of the relationship between pore size, porosity, and specific surface area, it became evident that scaffold configurations featuring larger pores and higher porosity values exhibited reduced specific surface area, thereby contributing to heightened permeability. This relationship between the interplay of pore size, porosity, and specific surface area is crucial in understanding and optimizing the permeability of scaffold structures, with implications for various applications in fields such as tissue engineering and filtration systems.

### 7.1.5 Mechanical Properties

Compression testing was used to examine the mechanical properties of scaffold constructions made with 3D printing. The stress-strain curves displayed different patterns that included linear elastic deformation, progressive yielding, a stress plateau, and ultimately fracture. Notably, the elastic modulus and yield strength exhibited a decline with rising porosity and pore size. Comparative research of 3D printed scaffold constructions produced using PolyJet and  $\mu$ SLA revealed that the latter often had higher mechanical properties. The study employed compression testing as a robust method to thoroughly assess the mechanical characteristics of scaffold structures fabricated through 3D printing. The stress-strain curves derived from these tests revealed distinctive patterns, encompassing phases of linear elastic deformation, progressive yielding, a stress plateau, and ultimately fracture, providing a comprehensive view of the scaffold's mechanical behavior. It was particularly noteworthy that as porosity and pore size increased, both the elastic modulus (indicative of material stiffness) and yield strength (point at which permanent deformation occurs) exhibited a consistent decline. This finding underscores the direct influence of pore-related factors on the mechanical properties of 3D-printed scaffolds, implying that designs with larger pores and higher porosity may sacrifice some mechanical strength.

Additionally, when comparing scaffold constructions produced through PolyJet and  $\mu$ SLA 3D printing methods, the latter often displayed superior mechanical qualities. This suggests that the choice of 3D printing technology can significantly impact the mechanical performance of scaffold structures, with  $\mu$ SLA exhibiting a propensity for higher mechanical integrity, potentially due to differences in printing precision, material properties, or layer bonding. These findings are essential in guiding the selection of 3D printing methods for specific applications, where mechanical strength is a critical consideration in scaffold design.

### 7.1.6 Standard Samples and Printing Direction

The impact of printing direction on mechanical properties was assessed using standard samples. When compared to PolyJet samples printed in the x and y directions, those printed in the z-direction had better mechanical properties. In contrast to normal PolyJet samples,  $\mu$ SLA samples were only printed in the z-direction and shown improved mechanical characteristics. The study suggested the potential for a combined model that integrates experimental and calculated methods to measure permeability more accurately. In order to improve permeability calculations, future study may examine the influence of other factors such pressure drop, fluid viscosity, and surface energy. Moreover, the study highlighted the need for further exploration of 3D printing techniques and material designs to optimize scaffold structures for specific applications. The study provided useful knowledge on the hydrophobicity, permeability, and mechanical properties of 3D-printed scaffold structures built of different pore shapes and materials. These findings contribute to the understanding of how these structures can be designed and optimized for various applications, including tissue engineering, fluid flow control, and impact resistance.

### 7.1.7 Finite Element Analysis (FEA)

The CAD-based models were subjected to finite element analysis to investigate the behaviour of deformation under various strain levels. Stress-strain curves exhibited distinct regions: elastic, post-yield softening, plateau, and densification. A discrepancy between finite element (FE) results and experimental data was observed. Despite this, the crushable foam plasticity model accurately estimated maximum and plateau stresses with an average percentage error of 12.27%. Despite the need for refinement, comparing FE stress-strain curves with experimental results demonstrated the crushable foam plasticity model's efficacy in evaluating stress at initial peak and plateau regions.

### **7.1.8 Potential Applications in Bone Tissue Engineering**

Simulation methods offer valuable insights into the deformation behavior of polymeric bone scaffolds with various architectural parameters. This knowledge plays a pivotal role in guiding the redesign of structures that are more aptly tailored for bone replacement within the field of bone tissue engineering. Such redesign takes into account the observed modes of failure and deformation, thus facilitating the creation of more effective and efficient bone tissue engineering solutions.

## **7.2 Future Recommendations**

The current study lays a solid foundation for future research in several promising directions within the field of bone tissue engineering and additive manufacturing. Some potential avenues for future work based on the findings and scope of this study include:

### **7.2.1 Advanced Printing Techniques**

Given the dynamic nature of the 3D printing field, it is prudent to consider the exploration of emerging 3D printing technologies and hybrid approaches in scaffold design. These innovative approaches have the potential to harness the strengths of both PolyJet and  $\mu$ SLA printing techniques to create scaffold structures with improved mechanical properties, precision, and intricate geometries. By blending the advantages of different printing methods, such as the high resolution and material diversity of PolyJet with the superior mechanical performance of  $\mu$ SLA, researchers can achieve a synergy that leads to advanced scaffold designs. This hybridization may enable the production of intricate, patient-specific bone scaffolds that not only mimic the mechanical properties of natural bone but also facilitate more accurate and personalized regenerative treatments.

Moreover, the pursuit of such hybrid approaches aligns with the broader trend in the 3D printing field towards enhancing the biofabrication of scaffolds for various tissue engineering applications. As we delve deeper into the integration of advanced biomaterials and precise printing techniques, the potential for more realistic and functional bone scaffolds becomes increasingly attainable. These innovations promise to drive forward the capabilities of 3D printing in regenerative medicine, and it's essential to continue exploring such avenues to remain at the forefront of scaffold design and manufacturing. This forward-looking approach opens new horizons for the development of scaffold structures that can offer not only mechanical support but also foster effective tissue regeneration and healing.

### **7.2.2 Material Selection and Optimization**

Explore a wider range of biomaterials and composite materials to enhance the mechanical performance, biocompatibility, and overall functionality of the printed bone scaffolds. Optimization of material composition and printing parameters can lead to improved scaffold properties. Diversifying the exploration of biomaterials and composite materials represents another pivotal avenue for advancing the field of 3D-printed bone scaffolds. While existing materials have demonstrated their utility, further research should encompass a broader spectrum of materials to enhance mechanical performance, biocompatibility, and overall functionality. The quest for innovative materials can potentially lead to the development of scaffold structures that more closely replicate the characteristics of natural bone, such as its strength, density, and mineral composition. Optimizing material composition and refining printing parameters are integral steps in this journey, as they can have a profound impact on the final scaffold properties. Through systematic experimentation and material science research, it's possible to achieve a deeper understanding of how different biomaterials and composites interact with printing processes, thereby enabling the production of highly tailored, patient-specific bone scaffolds.

Furthermore, this quest for diverse biomaterials aligns with the overarching goal of expanding the range of applications for 3D-printed bone scaffolds. Beyond traditional regenerative medicine, these innovative materials may find use in drug delivery systems, diagnostic tools, and even as models for studying bone-related diseases. By pushing the boundaries of material exploration and development, researchers can pioneer advancements that enhance the versatility, adaptability, and overall efficacy of 3D-printed bone scaffolds, ultimately benefitting a wide array of healthcare and biomedical applications. The journey towards more advanced and versatile scaffold designs underscores the ever-evolving nature of medical 3D printing and its transformative potential in modern medicine.

### **7.2.3 Biological Integration**

An essential aspect of advancing the field of 3D-printed bone scaffolds is the in-depth study of their biological response and compatibility within the human body. To accomplish this, researchers should conduct comprehensive investigations into how these scaffolds interact with living tissues. Such studies can involve assessing the potential for cell attachment, proliferation, and tissue regeneration, both in controlled laboratory settings (*in vitro*) and within living organisms (*in vivo*).

*In vitro* research provides a controlled environment to evaluate how cells, such as osteoblasts or mesenchymal stem cells, interact with the scaffold materials. This controlled setting allows for meticulous examination of cell attachment and proliferation on the scaffold's surface and within its pores. Researchers can manipulate various factors to optimize conditions for encouraging cell growth and tissue regeneration, such as scaffold surface modifications, growth factors, and biocompatible coatings.

Concurrently, *in vivo* research takes these investigations to the next level by introducing the 3D-printed bone scaffolds into animal models or, eventually, human subjects. This provides a more accurate representation of how the scaffold behaves

within a living organism. Researchers can evaluate how the scaffold influences tissue regeneration and natural bone formation in a dynamic, biological context. The goal here is to closely simulate and understand how the scaffold interacts with the host's own biological processes, aiding not only in the development of improved scaffolds but also in the potential for personalized regenerative treatments.

Ultimately, this dual approach of *in vitro* and *in vivo* research is essential to comprehensively assess the performance of 3D-printed bone scaffolds. By scrutinizing the biological response and compatibility of these scaffolds in varying biological contexts, we move closer to harnessing their full potential in clinical applications, including bone reconstruction, repair, and regenerative medicine.

#### **7.2.4 Functional Gradients**

A promising avenue of research in the development of 3D-printed bone scaffolds is the exploration of functional gradients within the scaffold structure. This innovative approach involves carefully tailoring the scaffold's characteristics, such as porosity or material properties, to create seamless transitions between the scaffold and the adjacent natural tissues, which can be bone or other types of tissues. The primary objective of these modifications is to enhance the integration and healing processes, particularly in the context of tissue engineering applications.

Functional gradients within the scaffold can serve multiple purposes. They can provide a gradual shift in mechanical properties, transitioning from the scaffold's stiffness to the natural tissue's properties, which can be essential for load-bearing regions where a sudden transition might cause stress concentrations and lead to complications. Furthermore, these gradients can facilitate the gradual transfer of biological signals, promoting the recruitment of cells and tissue regeneration at the scaffold-tissue interface. This strategy can significantly improve the long-term stability and functionality of the engineered tissue.

In the context of bone tissue engineering, these functional gradients can be particularly beneficial when dealing with complex structures like the bone-cartilage

interface or bone-tendon junctions, where a gradual shift in mechanical properties and tissue types is a critical design consideration. By meticulously fine-tuning the scaffold's properties to match the surrounding tissues, researchers can pave the way for more successful and efficient regenerative treatments and significantly enhance the patient's quality of life after bone injuries or degenerative diseases.

### **7.2.5 Patient-Specific Design**

An essential advancement in the field of 3D-printed bone scaffolds involves the development of methods for crafting patient-specific scaffolds by harnessing the power of medical imaging data and computer modeling. This approach centers around the idea of tailoring scaffold designs to precisely match the unique needs and anatomical variations of each individual patient. By doing so, the potential emerges for creating highly effective and personalized solutions for bone repair and regeneration.

The process begins with the acquisition of detailed medical imaging data, such as CT scans or MRI images, which provide comprehensive insights into the patient's specific bone structure and any existing defects or injuries. This data is then translated into digital 3D models through computer modeling software, offering a highly accurate representation of the patient's anatomy.

The next step involves using these digital models as a blueprint for 3D printing patient-specific bone scaffolds. By customizing the design to align with the patient's precise requirements, including the size, shape, and unique features of the affected bone or area, the resulting scaffold can provide an exact fit. This level of personalization enhances the scaffold's ability to support bone repair and regeneration while minimizing potential complications associated with ill-fitting, generic solutions.

In essence, the development of patient-specific bone scaffolds represents a significant leap forward in the field of regenerative medicine. It not only addresses the

challenges of anatomical variation but also opens doors to more efficient and successful bone repair treatments, ultimately improving the quality of life for patients facing bone-related injuries and conditions.

### **7.2.6 Mechanical Performance under Dynamic Loading**

Broadening the scope of research to comprehensively evaluate the mechanical performance of 3D-printed bone scaffolds is a recommended approach. This expanded assessment should encompass not only static loading scenarios but also dynamic or cyclic loading conditions. These dynamic loading conditions are designed to mimic the real-world pressures and stresses that bones endure during everyday activities, such as walking, running, or engaging in physical activities.

Static loading tests provide valuable insights into a scaffold's initial response to a constant force, but dynamic or cyclic loading experiments are essential for a more holistic understanding of how these scaffolds perform over time. This dynamic loading replication helps researchers better predict how scaffolds will function in practical scenarios, as bones rarely encounter static loads in real life. By simulating the repetitive stresses associated with dynamic activities, researchers can assess factors like fatigue resistance, long-term durability, and the ability of the scaffold to support healing and regeneration in a more realistic manner.

Incorporating dynamic or cyclic loading tests is particularly important when developing 3D-printed bone scaffolds, as these structures must not only provide mechanical support but also withstand the rigors of daily life. This approach ensures that the scaffolds meet the stringent requirements for long-term stability and effectiveness, ultimately contributing to their potential success in clinical applications, such as bone reconstruction and regenerative medicine.

### **7.2.7 Long-Term Degradation Studies**

An important facet of advancing the field of 3D-printed scaffolds, particularly in the context of regenerative medicine and tissue engineering, involves conducting thorough investigations into the long-term degradation behavior of these printed structures within various biological environments. This research aims to gain a comprehensive understanding of how these scaffolds change and deteriorate over extended periods. This knowledge is instrumental in assessing their durability and lifespan, critical factors in evaluating their efficacy for clinical applications.

Scaffold degradation over time is a multifaceted process influenced by several factors, including the choice of materials, the scaffold's porosity, and the specific biological environment it is placed within. Monitoring this degradation is essential as it helps researchers and medical practitioners anticipate how long the scaffold can effectively provide structural support, encourage tissue regeneration, and facilitate healing. It also aids in predicting when the scaffold may need to be replaced or if it can naturally integrate with the host tissue over time.

In practical terms, this research involves studying how the scaffold's physical and chemical properties change over time, whether it undergoes controlled degradation, and how these changes might influence its mechanical properties and its ability to promote tissue growth. An in-depth understanding of the long-term degradation behavior is pivotal for optimizing scaffold designs, ensuring their safety and effectiveness, and ultimately enhancing the success of regenerative treatments and tissue repair over extended periods of patient care.

### **7.2.8 Multi-Material Printing**

A valuable avenue of exploration in the realm of 3D-printed bone scaffolds is the assessment of the feasibility of multi-material printing techniques. These advanced techniques have the potential to create scaffolds with varying mechanical properties, enabling a more precise replication of the different regions found within natural bone.

Natural bone is a complex composite material that exhibits variations in mechanical properties throughout its structure. For instance, the outer cortical bone is denser and stiffer, providing robust support and protection, while the inner trabecular bone is more porous, allowing for flexibility and absorbing impact forces. To better emulate these distinct characteristics within 3D-printed bone scaffolds, the integration of multi-material printing becomes paramount.

Multi-material 3D printing allows for the strategic incorporation of different materials or material compositions into various regions of the scaffold. This opens up the possibility of achieving a seamless transition in mechanical properties from one part of the scaffold to another, much like the natural variations in bone. The ability to replicate these gradients in mechanical properties within the scaffold is particularly advantageous for areas such as bone-cartilage interfaces or the junctions between tendons and bone, where a gradual shift in stiffness is crucial.

By investigating the feasibility and refining the techniques for multi-material 3D printing, researchers aim to create more biomimetic and functional bone scaffolds. These scaffolds can offer an improved match to the diverse mechanical properties of natural bone, which in turn can enhance their performance in clinical applications, such as bone repair and regenerative medicine. The versatility of multi-material printing holds great potential for advancing the field of bone scaffold design, promoting better patient outcomes, and contributing to the development of more sophisticated and personalized regenerative treatments.

### **7.2.9 Clinical Translation**

A crucial step in the advancement of 3D-printed bone scaffolds is to establish collaborative partnerships with medical professionals. These partnerships aim to bridge the gap between laboratory research and the practical implementation of these scaffolds in clinical settings. This collaboration involves conducting preclinical trials and safety assessments, which serve as essential intermediary steps before the potential utilization of these innovative scaffolds in real patient scenarios.

In this collaborative approach, medical professionals, including clinicians and surgeons, provide valuable input and expertise to guide the research and development process. Their insights are instrumental in aligning the scaffold designs with the specific requirements and challenges encountered in clinical practice. By working closely with these experts, researchers can better tailor the scaffolds to address real-world medical needs and considerations.

Preclinical trials and safety assessments serve as a vital phase in this journey. These evaluations involve testing the scaffold's performance, biocompatibility, and safety in controlled settings that simulate aspects of human biology without directly involving patients. This step is critical for identifying any potential issues, refining the scaffold's design, and ensuring its safety and effectiveness before moving to clinical trials with human subjects.

By following this collaborative and methodical approach, researchers are not only better equipped to create scaffold designs that genuinely meet the needs of medical professionals and patients but also to facilitate a smoother transition from laboratory research to clinical application. This process ultimately contributes to the development of safer and more effective treatments, potentially transforming the landscape of bone repair, reconstruction, and regenerative medicine.

### **7.2.10 Incorporating Bioactive Factors**

One promising avenue of research in the development of 3D-printed bone scaffolds involves a deeper investigation into the incorporation of bioactive molecules. These molecules, which can include growth factors, signaling molecules, or other bioactive agents, are strategically integrated into the scaffold's design to enhance the processes of tissue regeneration and healing.

Bioactive molecules play a critical role in regulating various cellular activities, such as cell proliferation, differentiation, and tissue development. By embedding these molecules within the scaffold, researchers could aim to create a more conducive environment for these vital cellular processes. This, in turn, can significantly

accelerate the body's natural healing mechanisms and promote efficient tissue regeneration.

The incorporation of bioactive molecules into the scaffold design is especially relevant for bone regeneration, as it can help stimulate the formation of new bone tissue at an optimal rate. This approach can be tailored to address specific clinical scenarios, such as cases of bone defects or fractures where enhanced regrowth is desired.

In practical terms, the choice of bioactive molecules and the spatial distribution within the scaffold must be carefully considered. This requires a thorough understanding of the molecular signaling pathways involved in bone regeneration. Additionally, factors like the release kinetics of these molecules from the scaffold, their stability, and their compatibility with the scaffold materials need to be evaluated.

By exploring this avenue of research, scientists aim to develop advanced 3D-printed bone scaffolds that not only provide mechanical support but also actively participate in the healing process. This holds great potential for improving the outcomes of bone repair, reconstruction, and regenerative medicine by enhancing the body's own regenerative capabilities and potentially reducing the need for additional medical interventions.

Overall, the current study opens up a multitude of avenues for future investigations that can advance the field of BTE, refine scaffold design, and ultimately contribute to more effective and innovative bone repair and replacement strategies. The future steps for the study are to perform more work on the modelling of the scaffolds and perform accelerated aging simulations to evaluate the scaffold performance. In order to perform in-vitro biocompatibility tests using human and model animal cells, coatings of the scaffolds could be planned. For the proliferation and cytotoxicity, in-vitro and in-vivo biocompatibility tests will be performed. Sustainability of the scaffolds will need to be investigated.

# Bibliography

- [1] W. Wang and K. W. Yeung, “Bone grafts and biomaterials substitutes for bone defect repair: A review,” *Bioactive materials*, vol. 2, no. 4, pp. 224–247, 2017.
- [2] X. Zhou, Y. Feng, J. Zhang, Y. Shi, and L. Wang, “Recent advances in additive manufacturing technology for bone tissue engineering scaffolds,” *The International Journal of Advanced Manufacturing Technology*, vol. 108, pp. 3591–3606, 2020.
- [3] M. Ansari, “Bone tissue regeneration: biology, strategies and interface studies,” *Progress in biomaterials*, vol. 8, no. 4, pp. 223–237, 2019.
- [4] S. Verrier, M. Alini, E. Alsberg, S. Buchman, D. Kelly, M. Laschke, M. Menger, W. Murphy, J. Stegemann, M. Schütz, *et al.*, “Tissue engineering and regenerative approaches to improving the healing of large bone defects,” *Eur Cell Mater*, vol. 32, pp. 87–110, 2016.
- [5] Fortune Business Insights, “Bone graft substitutes market size, share covid-19 impact analysis, by type (allograft, demineralized bone matrix (dbm), synthetic, and xenograft), by application (spinal fusion, joint reconstruction, foot ankle, and others), by end-user (hospitals, specialty clinics, and others), and regional forecast, 2023-2030.” <https://www.fortunebusinessinsights.com/bone-graft-substitutes-market-103106>. Accessed: July 18, 2023.
- [6] T. Roberts, A. Rosenbaum, T. Roberts, *et al.*, “Bone grafts, bone substitutes and orthobiologics: Bone grafts, bone substitutes and orthobiologics the

- bridge between basic science and clinical advancements in fracture healing,” *Organogenesis*, vol. 8, pp. 114–124, 2012.
- [7] M. Rupp, L. Klute, S. Baertl, N. Walter, G.-K. Mannala, L. Frank, C. Pfeifer, V. Alt, and M. Kerschbaum, “The clinical use of bone graft substitutes in orthopedic surgery in germany—a 10-years survey from 2008 to 2018 of 1,090,167 surgical interventions,” *Journal of Biomedical Materials Research Part B: Applied Biomaterials*, vol. 110, no. 2, pp. 350–357, 2022.
- [8] L. Olivera and I. Antoniac, “Bone substitutes in orthopedic and trauma surgery,” *Bioceramics and Biocomposites: From Research to Clinical Practice*, pp. 341–366, 2019.
- [9] F. Donnalaja, E. Jacchetti, M. Soncini, and M. T. Raimondi, “Natural and synthetic polymers for bone scaffolds optimization,” *Polymers*, vol. 12, no. 4, p. 905, 2020.
- [10] C. Jiao, D. Xie, Z. He, H. Liang, L. Shen, Y. Yang, Z. Tian, G. Wu, and C. Wang, “Additive manufacturing of bio-inspired ceramic bone scaffolds: Structural design, mechanical properties and biocompatibility,” *Materials & design*, vol. 217, p. 110610, 2022.
- [11] B. Dhandayuthapani, Y. Yoshida, T. Maekawa, D. S. Kumar, *et al.*, “Polymeric scaffolds in tissue engineering application: a review,” *International journal of polymer science*, vol. 2011, 2011.
- [12] S. Amini, H. Salehi, M. Setayeshmehr, and M. Ghorbani, “Natural and synthetic polymeric scaffolds used in peripheral nerve tissue engineering: Advantages and disadvantages,” *Polymers for Advanced Technologies*, vol. 32, no. 6, pp. 2267–2289, 2021.
- [13] Y. Yang, G. Wang, H. Liang, C. Gao, S. Peng, L. Shen, and C. Shuai, “Additive manufacturing of bone scaffolds,” *International Journal of Bioprinting*, vol. 5, no. 1, 2019.

- [14] L. Suamte, A. Tirkey, J. Barman, and P. J. Babu, “Various manufacturing methods and ideal properties of scaffolds for tissue engineering applications,” *Smart Materials in Manufacturing*, vol. 1, p. 100011, 2023.
- [15] S. Mohanty, K. Sanger, A. Heiskanen, J. Trifol, P. Szabo, M. Dufva, J. Emnéus, and A. Wolff, “Fabrication of scalable tissue engineering scaffolds with dual-pore microarchitecture by combining 3d printing and particle leaching,” *Materials Science and Engineering: C*, vol. 61, pp. 180–189, 2016.
- [16] M. R. Rahman, J. L. C. Hui, and S. bin Hamdan, “Introduction and reinforcing potential of silica and various clay dispersed nanocomposites,” in *Silica and Clay Dispersed Polymer Nanocomposites*, pp. 1–24, Elsevier, 2018.
- [17] G. K. Sharma and N. R. James, “Electrospinning: The technique and applications,”
- [18] P. Chocholata, V. Kulda, and V. Babuska, “Fabrication of scaffolds for bone-tissue regeneration,” *Materials*, vol. 12, no. 4, p. 568, 2019.
- [19] S. Rasheed, W. A. Lughmani, M. A. Obeidi, D. Brabazon, and I. U. Ahad, “Additive manufacturing of bone scaffolds using polyjet and stereolithography techniques,” *Applied Sciences*, vol. 11, no. 16, p. 7336, 2021.
- [20] T. M. Koushik, C. M. Miller, and E. Antunes, “Bone tissue engineering scaffolds: Function of multi-material hierarchically structured scaffolds,” *Advanced Healthcare Materials*, p. 2202766, 2023.
- [21] H. C. Anderson, “Vesicles associated with calcification in the matrix of epiphyseal cartilage,” *The Journal of cell biology*, vol. 41, no. 1, pp. 59–72, 1969.
- [22] T. Hasegawa, T. Yamamoto, E. Tsuchiya, H. Hongo, K. Tsuboi, A. Kudo, M. Abe, T. Yoshida, T. Nagai, N. Khadiza, *et al.*, “Ultrastructural and biochemical aspects of matrix vesicle-mediated mineralization,” *Japanese Dental Science Review*, vol. 53, no. 2, pp. 34–45, 2017.

- [23] D. G. Walker, "Osteopetrosis cured by temporary parabiosis," *Science*, vol. 180, no. 4088, pp. 875–875, 1973.
- [24] A. M. Mohamed, "An overview of bone cells and their regulating factors of differentiation," *The Malaysian journal of medical sciences: MJMS*, vol. 15, no. 1, p. 4, 2008.
- [25] R. J. R. N. Van Blitterswijk, "Ca vascularization in tissue engineering," *Trends Biotechnol*, vol. 26, no. 8, pp. 434–441, 2008.
- [26] W. Risau, "Mechanisms of angiogenesis," *Nature*, vol. 386, no. 6626, pp. 671–674, 1997.
- [27] U. G. Wegst, H. Bai, E. Saiz, A. P. Tomsia, and R. O. Ritchie, "Bioinspired structural materials," *Nature materials*, vol. 14, no. 1, pp. 23–36, 2015.
- [28] S. K. Ramchand and E. Seeman, "The influence of cortical porosity on the strength of bone during growth and advancing age," *Current osteoporosis reports*, vol. 16, pp. 561–572, 2018.
- [29] J. Rho, L. Kuhn-Spearing, and P. Zioupos, "Med eng phys field full journal title," *Medical engineering & physics*, vol. 20, pp. 92–102, 1998.
- [30] C. Micheletti, A. Hurley, A. Gourrier, A. Palmquist, T. Tang, F. A. Shah, and K. Grandfield, "Bone mineral organization at the mesoscale: A review of mineral ellipsoids in bone and at bone interfaces," *Acta Biomaterialia*, vol. 142, pp. 1–13, 2022.
- [31] Y. Ha, X. Ma, S. Li, T. Li, Z. Li, Y. Qian, M. Shafiq, J. Wang, X. Zhou, and C. He, "Bone microenvironment-mimetic scaffolds with hierarchical microstructure for enhanced vascularization and bone regeneration," *Advanced Functional Materials*, vol. 32, no. 20, p. 2200011, 2022.
- [32] M. N. Collins, G. Ren, K. Young, S. Pina, R. L. Reis, and J. M. Oliveira, "Scaffold fabrication technologies and structure/function properties in bone tissue engineering," *Advanced functional materials*, vol. 31, no. 21, p. 2010609, 2021.

- [33] M. Maruyama, C. Rhee, T. Utsunomiya, N. Zhang, M. Ueno, Z. Yao, and S. B. Goodman, “Modulation of the inflammatory response and bone healing,” *Frontiers in endocrinology*, vol. 11, p. 386, 2020.
- [34] H. Zreiqat, C. R. Dunstan, and V. Rosen, *A tissue regeneration approach to bone and cartilage repair*. Springer, 2015.
- [35] M. N. Collins, G. Ren, K. Young, S. Pina, R. L. Reis, and J. M. Oliveira, “Scaffold fabrication technologies and structure/function properties in bone tissue engineering,” *Advanced functional materials*, vol. 31, no. 21, p. 2010609, 2021.
- [36] A. Shekaran and A. J. García, “Extracellular matrix-mimetic adhesive biomaterials for bone repair,” *Journal of biomedical materials research Part A*, vol. 96, no. 1, pp. 261–272, 2011.
- [37] G. Zhu, T. Zhang, M. Chen, K. Yao, X. Huang, B. Zhang, Y. Li, J. Liu, Y. Wang, and Z. Zhao, “Bone physiological microenvironment and healing mechanism: Basis for future bone-tissue engineering scaffolds,” *Bioactive materials*, vol. 6, no. 11, pp. 4110–4140, 2021.
- [38] B. Langdahl, S. Ferrari, and D. W. Dempster, “Bone modeling and remodeling: potential as therapeutic targets for the treatment of osteoporosis,” *Therapeutic advances in musculoskeletal disease*, vol. 8, no. 6, pp. 225–235, 2016.
- [39] M. Ansari, “Bone tissue regeneration: biology, strategies and interface studies,” *Progress in biomaterials*, vol. 8, no. 4, pp. 223–237, 2019.
- [40] P. Katsimbri, “The biology of normal bone remodelling,” *European journal of cancer care*, vol. 26, no. 6, p. e12740, 2017.
- [41] J.-M. Kim, C. Lin, Z. Stavre, M. B. Greenblatt, and J.-H. Shim, “Osteoblast-osteoclast communication and bone homeostasis,” *Cells*, vol. 9, no. 9, p. 2073, 2020.

- [42] X. Lin, S. Patil, Y.-G. Gao, and A. Qian, “The bone extracellular matrix in bone formation and regeneration,” *Frontiers in pharmacology*, vol. 11, p. 757, 2020.
- [43] M. Kerschnitzki, W. Wagermaier, P. Roschger, J. Seto, R. Shahar, G. N. Duda, S. Mundlos, and P. Fratzl, “The organization of the osteocyte network mirrors the extracellular matrix orientation in bone,” *Journal of structural biology*, vol. 173, no. 2, pp. 303–311, 2011.
- [44] J. Gluhak-Heinrich, L. Ye, L. F. Bonewald, J. Q. Feng, M. MacDougall, S. E. Harris, and D. Pavlin, “Mechanical loading stimulates dentin matrix protein 1 (dmp1) expression in osteocytes in vivo,” *Journal of Bone and Mineral Research*, vol. 18, no. 5, pp. 807–817, 2003.
- [45] S. Spiller, F. Clauder, K. Bellmann-Sickert, and A. G. Beck-Sickinger, “Improvement of wound healing by the development of ecm-inspired biomaterial coatings and controlled protein release,” *Biological Chemistry*, vol. 402, no. 11, pp. 1271–1288, 2021.
- [46] M. Rahmati, E. A. Silva, J. E. Reseland, C. A. Heyward, and H. J. Haugen, “Biological responses to physicochemical properties of biomaterial surface,” *Chemical Society Reviews*, vol. 49, no. 15, pp. 5178–5224, 2020.
- [47] T. M. Koushik, C. M. Miller, and E. Antunes, “Bone tissue engineering scaffolds: Function of multi-material hierarchically structured scaffolds,” *Advanced Healthcare Materials*, p. 2202766, 2023.
- [48] T. M. Koushik, C. M. Miller, and E. Antunes, “Bone tissue engineering scaffolds: Function of multi-material hierarchically structured scaffolds,” *Advanced Healthcare Materials*, p. 2202766, 2023.
- [49] M. Merola and S. Affatato, “Materials for hip prostheses: a review of wear and loading considerations,” *Materials*, vol. 12, no. 3, p. 495, 2019.
- [50] E. Erasmus, R. Sule, O. Johnson, J. Massera, and I. Sigalas, “In vitro evaluation of porous borosilicate, borophosphate and phosphate bioactive glasses

- scaffolds fabricated using foaming agent for bone regeneration,” *Scientific reports*, vol. 8, no. 1, p. 3699, 2018.
- [51] R. Ribas and V. Schatkoski, “Tl d. a. montanheiro, brc de menezes, c. steegemann, dmg leite, gp thim,” *Ceramics International*, vol. 45, p. 21051, 2019.
- [52] J. Lu, H. Yu, and C. Chen, “Biological properties of calcium phosphate biomaterials for bone repair: A review,” *RSC advances*, vol. 8, no. 4, pp. 2015–2033, 2018.
- [53] N. Kamboj, A. Ressler, and I. Hussainova, “Bioactive ceramic scaffolds for bone tissue engineering by powder bed selective laser processing: A review,” *Materials*, vol. 14, no. 18, p. 5338, 2021.
- [54] L. Guo, Z. Liang, L. Yang, W. Du, T. Yu, H. Tang, C. Li, and H. Qiu, “The role of natural polymers in bone tissue engineering,” *Journal of Controlled Release*, vol. 338, pp. 571–582, 2021.
- [55] Y. Li, Y. Liu, R. Li, H. Bai, Z. Zhu, L. Zhu, C. Zhu, Z. Che, H. Liu, J. Wang, *et al.*, “Collagen-based biomaterials for bone tissue engineering,” *Materials & Design*, vol. 210, p. 110049, 2021.
- [56] S. Sharma, P. Sudhakara, J. Singh, R. Ilyas, M. Asyraf, and M. Razman, “Critical review of biodegradable and bioactive polymer composites for bone tissue engineering and drug delivery applications,” *Polymers*, vol. 13, no. 16, p. 2623, 2021.
- [57] T. M. Koushik, C. M. Miller, and E. Antunes, “Bone tissue engineering scaffolds: Function of multi-material hierarchically structured scaffolds,” *Advanced Healthcare Materials*, p. 2202766, 2023.
- [58] F. Zhang and M. W. King, “Biodegradable polymers as the pivotal player in the design of tissue engineering scaffolds,” *Advanced healthcare materials*, vol. 9, no. 13, p. 1901358, 2020.

- [59] M. Zarei, M. Shabani Dargah, M. Hasanzadeh Azar, R. Alizadeh, F. S. Mahdavi, S. S. Sayedain, A. Kaviani, M. Asadollahi, M. Azami, and N. Beheshizadeh, “Enhanced bone tissue regeneration using a 3d-printed poly (lactic acid)/ti6al4v composite scaffold with plasma treatment modification,” *Scientific reports*, vol. 13, no. 1, p. 3139, 2023.
- [60] A. M. Sousa, A. M. Amaro, and A. P. Piedade, “3d printing of polymeric bioresorbable stents: A strategy to improve both cellular compatibility and mechanical properties,” *Polymers*, vol. 14, no. 6, p. 1099, 2022.
- [61] F. Ghorbani, M. Sahranavard, Z. Mousavi Nejad, D. Li, A. Zamanian, and B. Yu, “Surface functionalization of three dimensional-printed polycaprolactone-bioactive glass scaffolds by grafting gelma under uv irradiation,” *Frontiers in Materials*, vol. 7, p. 528590, 2020.
- [62] T. N. Vo, F. K. Kasper, and A. G. Mikos, “Strategies for controlled delivery of growth factors and cells for bone regeneration,” *Advanced drug delivery reviews*, vol. 64, no. 12, pp. 1292–1309, 2012.
- [63] E.-K. R. N. E. Chenab, K. J. A. R. F. Hashemi, and S. A. F. B. A. Mosafer, “J. mokhtarzadeh a. maleki a. hamblin mr j,” *Tissue Eng. Regener. Med.*, vol. 14, pp. 1687–1714, 2020.
- [64] B. Langdahl, S. Ferrari, and D. W. Dempster, “Bone modeling and remodeling: potential as therapeutic targets for the treatment of osteoporosis,” *Therapeutic advances in musculoskeletal disease*, vol. 8, no. 6, pp. 225–235, 2016.
- [65] M. Geetha, A. K. Singh, R. Asokamani, and A. K. Gogia, “Ti based biomaterials, the ultimate choice for orthopaedic implants—a review,” *Progress in materials science*, vol. 54, no. 3, pp. 397–425, 2009.
- [66] H. Zhao, Y. Han, C. Pan, D. Yang, H. Wang, T. Wang, X. Zeng, and P. Su, “Design and mechanical properties verification of gradient voronoi scaffold for bone tissue engineering,” *Micromachines*, vol. 12, no. 6, p. 664, 2021.

- [67] K. Hu, L. Zhang, Y. Zhang, B. Song, S. Wen, Q. Liu, and Y. Shi, “Electrochemical corrosion behavior and mechanical response of selective laser melted porous metallic biomaterials,” *Acta Metallurgica Sinica (English Letters)*, pp. 1–12, 2023.
- [68] W. Xu, X. Lu, M. D. Hayat, J. Tian, C. Huang, M. Chen, X. Qu, and C. Wen, “Fabrication and properties of newly developed ti35zr28nb scaffolds fabricated by powder metallurgy for bone-tissue engineering,” *Journal of Materials Research and Technology*, vol. 8, no. 5, pp. 3696–3704, 2019.
- [69] T. M. Koushik, C. M. Miller, and E. Antunes, “Bone tissue engineering scaffolds: Function of multi-material hierarchically structured scaffolds,” *Advanced Healthcare Materials*, p. 2202766, 2023.
- [70] I. Cockerill, Y. Su, S. Sinha, Y.-X. Qin, Y. Zheng, M. L. Young, and D. Zhu, “Porous zinc scaffolds for bone tissue engineering applications: A novel additive manufacturing and casting approach,” *Materials Science and Engineering: C*, vol. 110, p. 110738, 2020.
- [71] S. Kamrani and C. Fleck, “Biodegradable magnesium alloys as temporary orthopaedic implants: a review,” *Biometals*, vol. 32, pp. 185–193, 2019.
- [72] E. Dayaghi, H. Bakhsheshi-Rad, E. Hamzah, A. Akhavan-Farid, A. Ismail, M. Aziz, and E. Abdolahi, “Magnesium-zinc scaffold loaded with tetracycline for tissue engineering application: In vitro cell biology and antibacterial activity assessment,” *Materials Science and Engineering: C*, vol. 102, pp. 53–65, 2019.
- [73] D. N. Heo, W.-K. Ko, M. S. Bae, J. B. Lee, D.-W. Lee, W. Byun, C. H. Lee, E.-C. Kim, B.-Y. Jung, and I. K. Kwon, “Enhanced bone regeneration with a gold nanoparticle–hydrogel complex,” *Journal of Materials Chemistry B*, vol. 2, no. 11, pp. 1584–1593, 2014.
- [74] M. Rasoulianboroujeni, F. Fahimipour, P. Shah, K. Khoshroo, M. Tahriri, H. Eslami, A. Yadegari, E. Dashtimoghadam, and L. Tayebi, “Development

- of 3d-printed plga/tio2 nanocomposite scaffolds for bone tissue engineering applications,” *Materials Science and Engineering: C*, vol. 96, pp. 105–113, 2019.
- [75] J. Zhang, D. Huang, S. Liu, X. Dong, Y. Li, H. Zhang, Z. Yang, Q. Su, W. Huang, W. Zheng, *et al.*, “Zirconia toughened hydroxyapatite biocomposite formed by a dlp 3d printing process for potential bone tissue engineering,” *Materials Science and Engineering: C*, vol. 105, p. 110054, 2019.
- [76] D. Arcos and M. Vallet-Regí, “Substituted hydroxyapatite coatings of bone implants,” *Journal of Materials Chemistry B*, vol. 8, no. 9, pp. 1781–1800, 2020.
- [77] M. Rizwan, M. Hamdi, and W. Basirun, “Bioglass® 45s5-based composites for bone tissue engineering and functional applications,” *Journal of biomedical materials research Part A*, vol. 105, no. 11, pp. 3197–3223, 2017.
- [78] L. Gritsch, M. Maqbool, V. Mouriño, F. E. Ciraldo, M. Cresswell, P. R. Jackson, C. Lovell, and A. R. Boccaccini, “Chitosan/hydroxyapatite composite bone tissue engineering scaffolds with dual and decoupled therapeutic ion delivery: Copper and strontium,” *Journal of Materials Chemistry B*, vol. 7, no. 40, pp. 6109–6124, 2019.
- [79] G. Grass, C. Rensing, and M. Solioz, “Metallic copper as an antimicrobial surface,” *Applied and environmental microbiology*, vol. 77, no. 5, pp. 1541–1547, 2011.
- [80] C. Koski, B. Onuiké, A. Bandyopadhyay, and S. Bose, “Starch-hydroxyapatite composite bone scaffold fabrication utilizing a slurry extrusion-based solid freeform fabricator,” *Additive manufacturing*, vol. 24, pp. 47–59, 2018.
- [81] T. M. Koushik, C. M. Miller, and E. Antunes, “Bone tissue engineering scaffolds: Function of multi-material hierarchically structured scaffolds,” *Advanced Healthcare Materials*, p. 2202766, 2023.

- [82] S. Dutta, K. B. Devi, S. Mandal, A. Mahato, S. Gupta, B. Kundu, V. K. Balla, and M. Roy, “In vitro corrosion and cytocompatibility studies of hot press sintered magnesium-bioactive glass composite,” *Materialia*, vol. 5, p. 100245, 2019.
- [83] M. Khodaei, F. Nejatidanesh, M. J. Shirani, A. Valanezhad, I. Watanabe, and O. Savabi, “The effect of the nano-bioglass reinforcement on magnesium based composite,” *Journal of the Mechanical Behavior of Biomedical Materials*, vol. 100, p. 103396, 2019.
- [84] M. Bartoš, T. Suchý, and R. Foltán, “Note on the use of different approaches to determine the pore sizes of tissue engineering scaffolds: what do we measure?,” *Biomedical Engineering Online*, vol. 17, pp. 1–15, 2018.
- [85] T. M. Koushik, C. M. Miller, and E. Antunes, “Bone tissue engineering scaffolds: Function of multi-material hierarchically structured scaffolds,” *Advanced Healthcare Materials*, p. 2202766, 2023.
- [86] J. Krieghoff, A.-K. Picke, J. Salbach-Hirsch, S. Rother, C. Heinemann, R. Bernhardt, C. Kascholke, S. Möller, M. Rauner, M. Schnabelrauch, *et al.*, “Increased pore size of scaffolds improves coating efficiency with sulfated hyaluronan and mineralization capacity of osteoblasts,” *Biomaterials research*, vol. 23, pp. 1–13, 2019.
- [87] J. Chen, “Recent development of biomaterials combined with mesenchymal stem cells as a strategy in cartilage regeneration,” *International Journal of Translational Medicine*, vol. 2, no. 3, pp. 456–481, 2022.
- [88] T. Ghassemi, A. Shahroodi, M. H. Ebrahimzadeh, A. Mousavian, J. Movaffagh, and A. Moradi, “Current concepts in scaffolding for bone tissue engineering,” *Archives of bone and joint surgery*, vol. 6, no. 2, p. 90, 2018.
- [89] J. Zhou, S. Xiong, M. Liu, H. Yang, P. Wei, F. Yi, M. Ouyang, H. Xi, Z. Long, Y. Liu, *et al.*, “Study on the influence of scaffold morphology

- and structure on osteogenic performance,” *Frontiers in Bioengineering and Biotechnology*, vol. 11, p. 1127162, 2023.
- [90] M. Rahatuzzaman, M. Mahmud, S. Rahman, and M. E. Hoque, “Design, fabrication, and characterization of 3d-printed abs and pla scaffolds potentially for tissue engineering,” *Results in Engineering*, p. 101685, 2023.
- [91] M. Dziaduszevska and A. Zieliński, “Structural and material determinants influencing the behavior of porous ti and its alloys made by additive manufacturing techniques for biomedical applications,” *Materials*, vol. 14, no. 4, p. 712, 2021.
- [92] G. Lutzweiler, A. Ndreu Halili, and N. Engin Vrana, “The overview of porous, bioactive scaffolds as instructive biomaterials for tissue regeneration and their clinical translation,” *Pharmaceutics*, vol. 12, no. 7, p. 602, 2020.
- [93] M. Bahraminasab, “Challenges on optimization of 3d-printed bone scaffolds,” *BioMedical Engineering OnLine*, vol. 19, no. 1, pp. 1–33, 2020.
- [94] S. Kanwar, O. Al-Ketan, and S. Vijayavenkataraman, “A novel method to design biomimetic, 3d printable stochastic scaffolds with controlled porosity for bone tissue engineering,” *Materials & Design*, vol. 220, p. 110857, 2022.
- [95] S. Kechagias, K. Theodoridis, J. Broomfield, K. Malpartida-Cardenas, R. Reid, P. Georgiou, R. J. van Arkel, and J. R. Jeffers, “The effect of nodal connectivity and strut density within stochastic titanium scaffolds on osteogenesis,” *Frontiers in Bioengineering and Biotechnology*, vol. 11, 2023.
- [96] F. Paladini and M. Pollini, “Novel approaches and biomaterials for bone tissue engineering: a focus on silk fibroin,” *Materials*, vol. 15, no. 19, p. 6952, 2022.
- [97] L. Suamte, A. Tirkey, J. Barman, and P. J. Babu, “Various manufacturing methods and ideal properties of scaffolds for tissue engineering applications,” *Smart Materials in Manufacturing*, vol. 1, p. 100011, 2023.

- [98] A. G. Abdelaziz, H. Nageh, S. M. Abdo, M. S. Abdalla, A. A. Amer, A. Abdal-Hay, and A. Barhoum, “A review of 3d polymeric scaffolds for bone tissue engineering: Principles, fabrication techniques, immunomodulatory roles, and challenges,” *Bioengineering*, vol. 10, no. 2, p. 204, 2023.
- [99] M. P. Nikolova and M. S. Chavali, “Recent advances in biomaterials for 3d scaffolds: A review,” *Bioactive materials*, vol. 4, pp. 271–292, 2019.
- [100] S. S. Lee, X. Du, I. Kim, and S. J. Ferguson, “Scaffolds for bone-tissue engineering,” *Matter*, vol. 5, no. 9, pp. 2722–2759, 2022.
- [101] Z. Miri, H. J. Haugen, D. Loca, F. Rossi, G. Perale, A. Moghanian, and Q. Ma, “Review on the strategies to improve the mechanical strength of highly porous bone bioceramic scaffolds,” *Journal of the European Ceramic Society*, 2023.
- [102] G. Zhu, T. Zhang, M. Chen, K. Yao, X. Huang, B. Zhang, Y. Li, J. Liu, Y. Wang, and Z. Zhao, “Bone physiological microenvironment and healing mechanism: Basis for future bone-tissue engineering scaffolds,” *Bioactive materials*, vol. 6, no. 11, pp. 4110–4140, 2021.
- [103] R. Ambu and A. E. Morabito, “Modeling, assessment, and design of porous cells based on schwartz primitive surface for bone scaffolds,” *The Scientific World Journal*, vol. 2019, 2019.
- [104] S. Rajagopalan and R. A. Robb, “Schwarz meets schwann: design and fabrication of biomorphic and durataxic tissue engineering scaffolds,” *Medical image analysis*, vol. 10, no. 5, pp. 693–712, 2006.
- [105] L. Zhang, S. Feih, S. Daynes, S. Chang, M. Y. Wang, J. Wei, and W. F. Lu, “Energy absorption characteristics of metallic triply periodic minimal surface sheet structures under compressive loading,” *Additive Manufacturing*, vol. 23, pp. 505–515, 2018.

- [106] M. Tilton, A. Borjali, A. Isaacson, K. M. Varadarajan, and G. P. Manogharan, “On structure and mechanics of biomimetic meta-biomaterials fabricated via metal additive manufacturing,” *Materials & Design*, vol. 201, p. 109498, 2021.
- [107] X. Gao, M. Fraulob, and G. Haiat, “Biomechanical behaviours of the bone–implant interface: a review,” *Journal of The Royal Society Interface*, vol. 16, no. 156, p. 20190259, 2019.
- [108] G. G. Flores-Rojas, B. Gómez-Lazaro, F. López-Saucedo, R. Vera-Graziano, E. Bucio, and E. Mendizábal, “Electrospun scaffolds for tissue engineering: a review,” *Macromol*, vol. 3, no. 3, pp. 524–553, 2023.
- [109] M. Janmohammadi, M. S. Nourbakhsh, M. Bahraminasab, and L. Tayebi, “Enhancing bone tissue engineering with 3d-printed polycaprolactone scaffolds integrated with tragacanth gum/bioactive glass,” *Materials Today Bio*, vol. 23, p. 100872, 2023.
- [110] J. R. Porter, T. T. Ruckh, and K. C. Popat, “Bone tissue engineering: a review in bone biomimetics and drug delivery strategies,” *Biotechnology progress*, vol. 25, no. 6, pp. 1539–1560, 2009.
- [111] S. Yang, K.-F. Leong, Z. Du, and C.-K. Chua, “The design of scaffolds for use in tissue engineering. part i. traditional factors,” *Tissue engineering*, vol. 7, no. 6, pp. 679–689, 2001.
- [112] R. M. Grzeskowiak, J. Schumacher, M. S. Dhar, D. P. Harper, P.-Y. Mulon, and D. E. Anderson, “Bone and cartilage interfaces with orthopedic implants: a literature review,” *Frontiers in Surgery*, vol. 7, p. 601244, 2020.
- [113] A. Cheng, Z. Schwartz, A. Kahn, X. Li, Z. Shao, M. Sun, Y. Ao, B. D. Boyan, and H. Chen, “Advances in porous scaffold design for bone and cartilage tissue engineering and regeneration,” *Tissue Engineering Part B: Reviews*, vol. 25, no. 1, pp. 14–29, 2019.

- [114] M. Bohner, Y. Loosli, G. Baroud, and D. Lacroix, “Commentary: deciphering the link between architecture and biological response of a bone graft substitute,” *Acta biomaterialia*, vol. 7, no. 2, pp. 478–484, 2011.
- [115] T. Marew and G. Birhanu, “Three dimensional printed nanostructure biomaterials for bone tissue engineering,” *Regenerative Therapy*, vol. 18, pp. 102–111, 2021.
- [116] S. Bose and S. Tarafder, “Calcium phosphate ceramic systems in growth factor and drug delivery for bone tissue engineering: a review,” *Acta biomaterialia*, vol. 8, no. 4, pp. 1401–1421, 2012.
- [117] V. Karageorgiou and D. Kaplan, “Porosity of 3d biomaterial scaffolds and osteogenesis,” *Biomaterials*, vol. 26, no. 27, pp. 5474–5491, 2005.
- [118] C. Y. Lin, N. Kikuchi, and S. J. Hollister, “A novel method for biomaterial scaffold internal architecture design to match bone elastic properties with desired porosity,” *Journal of biomechanics*, vol. 37, no. 5, pp. 623–636, 2004.
- [119] S. R. Moore, G. M. Saidel, U. Knothe, and M. L. Knothe Tate, “Mechanistic, mathematical model to predict the dynamics of tissue genesis in bone defects via mechanical feedback and mediation of biochemical factors,” *PLoS computational biology*, vol. 10, no. 6, p. e1003604, 2014.
- [120] D. W. Hutmacher, “Scaffolds in tissue engineering bone and cartilage,” *Biomaterials*, vol. 21, no. 24, pp. 2529–2543, 2000.
- [121] B. Guo and P. X. Ma, “Synthetic biodegradable functional polymers for tissue engineering: a brief review,” *Science China Chemistry*, vol. 57, pp. 490–500, 2014.
- [122] S. Mohamed and B. H. Shamaz, “Bone tissue engineering and bony scaffolds,” *Int. J. Dent. Oral Health*, vol. 1, pp. 15–20, 2015.
- [123] S. Bhatia and S. Bhatia, “Natural polymers vs synthetic polymer,” *Natural polymer drug delivery systems: nanoparticles, plants, and algae*, pp. 95–118, 2016.

- [124] N. Salehi-Nik, M. R. Rad, P. Nazeman, and A. Khojasteh, "Polymers for oral and dental tissue engineering," in *Biomaterials for Oral and Dental Tissue Engineering*, pp. 25–46, Elsevier, 2017.
- [125] A. Sola, J. Bertacchini, D. D'Avella, L. Anselmi, T. Maraldi, S. Marmioli, and M. Messori, "Development of solvent-casting particulate leaching (scpl) polymer scaffolds as improved three-dimensional supports to mimic the bone marrow niche," *Materials Science and Engineering: C*, vol. 96, pp. 153–165, 2019.
- [126] I. M. Adel, M. F. ElMeligy, and N. A. Elkasabgy, "Conventional and recent trends of scaffolds fabrication: a superior mode for tissue engineering," *Pharmaceutics*, vol. 14, no. 2, p. 306, 2022.
- [127] F. V. Borbolla-Jiménez, S. I. Peña-Corona, S. J. Farah, M. T. Jiménez-Valdés, E. Pineda-Pérez, A. Romero-Montero, M. L. Del Prado-Audelo, S. A. Bernal-Chávez, J. J. Magaña, and G. Leyva-Gómez, "Films for wound healing fabricated using a solvent casting technique," *Pharmaceutics*, vol. 15, no. 7, p. 1914, 2023.
- [128] D. Puppi, A. Morelli, F. Bello, S. Valentini, and F. Chiellini, "Additive manufacturing of poly (methyl methacrylate) biomedical implants with dual-scale porosity," *Macromolecular Materials and Engineering*, vol. 303, no. 9, p. 1800247, 2018.
- [129] A. Haider, S. Haider, M. R. Kummara, T. Kamal, A.-A. A. Alghyamah, F. J. Iftikhar, B. Bano, N. Khan, M. A. Afridi, S. S. Han, *et al.*, "Advances in the scaffolds fabrication techniques using biocompatible polymers and their biomedical application: A technical and statistical review," *Journal of saudi chemical society*, vol. 24, no. 2, pp. 186–215, 2020.
- [130] C. Ji, N. Annabi, M. Hosseinkhani, S. Sivaloganathan, and F. Dehghani, "Fabrication of poly-dl-lactide/polyethylene glycol scaffolds using the gas foaming technique," *Acta biomaterialia*, vol. 8, no. 2, pp. 570–578, 2012.

- [131] H. Qu, “Additive manufacturing for bone tissue engineering scaffolds,” *Materials Today Communications*, vol. 24, p. 101024, 2020.
- [132] G. Turnbull, J. Clarke, F. Picard, P. Riches, L. Jia, F. Han, B. Li, and W. Shu, “3d bioactive composite scaffolds for bone tissue engineering,” *Bioactive materials*, vol. 3, no. 3, pp. 278–314, 2018.
- [133] R. Zeinali, L. J. Del Valle, J. Torras, and J. Puiggali, “Recent progress on biodegradable tissue engineering scaffolds prepared by thermally-induced phase separation (tips),” *International journal of molecular sciences*, vol. 22, no. 7, p. 3504, 2021.
- [134] Y. Wang, X. Shi, L. Ren, C. Wang, and D.-A. Wang, “Porous poly (lactico-glycolide) microsphere sintered scaffolds for tissue repair applications,” *Materials Science and Engineering: C*, vol. 29, no. 8, pp. 2502–2507, 2009.
- [135] V. Gupta, Y. Khan, C. J. Berkland, C. T. Laurencin, and M. S. Detamore, “Microsphere-based scaffolds in regenerative engineering,” *Annual review of biomedical engineering*, vol. 19, pp. 135–161, 2017.
- [136] P. Phutane, D. Telange, S. Agrawal, M. Gunde, K. Kotkar, and A. Pethe, “Biofunctionalization and applications of polymeric nanofibers in tissue engineering and regenerative medicine,” *Polymers*, vol. 15, no. 5, p. 1202, 2023.
- [137] J. R. Tumbleston, D. Shirvanyants, N. Ermoshkin, R. Januszewicz, A. R. Johnson, D. Kelly, K. Chen, R. Pinschmidt, J. P. Rolland, A. Ermoshkin, *et al.*, “Continuous liquid interface production of 3d objects,” *Science*, vol. 347, no. 6228, pp. 1349–1352, 2015.
- [138] J.-F. Xing, M.-L. Zheng, and X.-M. Duan, “Two-photon polymerization microfabrication of hydrogels: an advanced 3d printing technology for tissue engineering and drug delivery,” *Chemical Society Reviews*, vol. 44, no. 15, pp. 5031–5039, 2015.
- [139] Y. Tan, D. J. Richards, T. C. Trusk, R. P. Visconti, M. J. Yost, M. S. Kindy, C. J. Drake, W. S. Argraves, R. R. Markwald, and Y. Mei, “3d printing

- facilitated scaffold-free tissue unit fabrication,” *Biofabrication*, vol. 6, no. 2, p. 024111, 2014.
- [140] L. J. Pourchet, A. Thepot, M. Albouy, E. J. Courtial, A. Boher, L. J. Blum, and C. A. Marquette, “Human skin 3d bioprinting using scaffold-free approach,” *Advanced Healthcare Materials*, vol. 6, no. 4, p. 1601101, 2017.
- [141] P. Rider, Ž. P. Kačarević, S. Alkildani, S. Retnasingh, R. Schnettler, and M. Barbeck, “Additive manufacturing for guided bone regeneration: A perspective for alveolar ridge augmentation,” *International journal of molecular sciences*, vol. 19, no. 11, p. 3308, 2018.
- [142] G. Bugada Miguel Cervera and G. Lombera, “Numerical prediction of temperature and density distributions in selective laser sintering processes,” *Rapid Prototyping Journal*, vol. 5, no. 1, pp. 21–26, 1999.
- [143] H. Chen and D. Gu, “Effect of metallurgical defect and phase transition on geometric accuracy and wear resistance of iron-based parts fabricated by selective laser melting,” *Journal of Materials Research*, vol. 31, no. 10, pp. 1477–1490, 2016.
- [144] F. S. Senatov, K. V. Niaza, M. Y. Zadorozhnyy, A. Maksimkin, S. Kaloshkin, and Y. Estrin, “Mechanical properties and shape memory effect of 3d-printed pla-based porous scaffolds,” *Journal of the mechanical behavior of biomedical materials*, vol. 57, pp. 139–148, 2016.
- [145] A. Jezierski, K. Rennie, B. Zurakowski, M. Ribocco-Lutkiewicz, J. Haukenfrers, A. Ajji, A. Gruslin, M. Sikorska, and M. Bani-Yaghoub, “Neuroprotective effects of gdnf-expressing human amniotic fluid cells,” *Stem Cell Reviews and Reports*, vol. 10, pp. 251–268, 2014.
- [146] C. Shuai, Y. Li, P. Feng, W. Guo, W. Yang, and S. Peng, “Positive feedback effects of mg on the hydrolysis of poly-l-lactic acid (plla): Promoted degradation of plla scaffolds,” *Polymer Testing*, vol. 68, pp. 27–33, 2018.

- [147] L. Yang, J. Li, Y. Jin, M. Li, and Z. Gu, "In vitro enzymatic degradation of the cross-linked poly ( $\epsilon$ -caprolactone) implants," *Polymer Degradation and Stability*, vol. 112, pp. 10–19, 2015.
- [148] Y. Du, H. Liu, Q. Yang, S. Wang, J. Wang, J. Ma, I. Noh, A. G. Mikos, and S. Zhang, "Selective laser sintering scaffold with hierarchical architecture and gradient composition for osteochondral repair in rabbits," *Biomaterials*, vol. 137, pp. 37–48, 2017.
- [149] Y. Du, H. Liu, J. Shuang, J. Wang, J. Ma, and S. Zhang, "Microsphere-based selective laser sintering for building macroporous bone scaffolds with controlled microstructure and excellent biocompatibility," *Colloids and Surfaces B: Biointerfaces*, vol. 135, pp. 81–89, 2015.
- [150] T. Kumaresan, R. Gandhinathan, M. Ramu, M. Ananthasubramanian, and K. B. Pradheepa, "Design, analysis and fabrication of polyamide/hydroxyapatite porous structured scaffold using selective laser sintering method for bio-medical applications," *Journal of mechanical science and technology*, vol. 30, pp. 5305–5312, 2016.
- [151] C. Shuai, C. Gao, Y. Nie, H. Hu, Y. Zhou, and S. Peng, "Structure and properties of nano-hydroxyapatite scaffolds for bone tissue engineering with a selective laser sintering system," *Nanotechnology*, vol. 22, no. 28, p. 285703, 2011.
- [152] C. Shuai, P. Li, J. Liu, and S. Peng, "Optimization of tcp/hap ratio for better properties of calcium phosphate scaffold via selective laser sintering," *Materials Characterization*, vol. 77, pp. 23–31, 2013.
- [153] J. Liu, H. Hu, P. Li, C. Shuai, and S. Peng, "Fabrication and characterization of porous 45s5 glass scaffolds via direct selective laser sintering," *Materials and Manufacturing Processes*, vol. 28, no. 6, pp. 610–615, 2013.
- [154] S. L. Sing, W. Y. Yeong, F. E. Wiria, B. Y. Tay, Z. Zhao, L. Zhao, Z. Tian, and S. Yang, "Direct selective laser sintering and melting of ceramics: a review," *Rapid Prototyping Journal*, vol. 23, no. 3, pp. 611–623, 2017.

- [155] C. Gao, P. Feng, S. Peng, and C. Shuai, “Carbon nanotube, graphene and boron nitride nanotube reinforced bioactive ceramics for bone repair,” *Acta biomaterialia*, vol. 61, pp. 1–20, 2017.
- [156] A. Järvenpää, L. P. Karjalainen, and K. Mäntyjärvi, “Passive laser assisted bending of ultra-high strength steels,” *Advanced Materials Research*, vol. 418, pp. 1542–1547, 2012.
- [157] J. Liu, C. Gao, P. Feng, T. Xiao, C. Shuai, and S. Peng, “A bioactive glass nanocomposite scaffold toughed by multi-wall carbon nanotubes for tissue engineering,” *Journal of the Ceramic Society of Japan*, vol. 123, no. 1438, pp. 485–491, 2015.
- [158] C. Gao, T. Liu, C. Shuai, and S. Peng, “Enhancement mechanisms of graphene in nano-58s bioactive glass scaffold: mechanical and biological performance,” *Scientific reports*, vol. 4, no. 1, p. 4712, 2014.
- [159] S. Duan, P. Feng, C. Gao, T. Xiao, K. Yu, C. Shuai, and S. Peng, “Microstructure evolution and mechanical properties improvement in liquid-phase-sintered hydroxyapatite by laser sintering,” *Materials*, vol. 8, no. 3, pp. 1162–1175, 2015.
- [160] D. Liu, J. Zhuang, C. Shuai, and S. Peng, “Mechanical properties’ improvement of a tricalcium phosphate scaffold with poly-l-lactic acid in selective laser sintering,” *Biofabrication*, vol. 5, no. 2, p. 025005, 2013.
- [161] D. Gu, Y.-C. Hagedorn, W. Meiners, G. Meng, R. J. S. Batista, K. Wissenbach, and R. Poprawe, “Densification behavior, microstructure evolution, and wear performance of selective laser melting processed commercially pure titanium,” *Acta materialia*, vol. 60, no. 9, pp. 3849–3860, 2012.
- [162] L. Jiao, Z. Y. Chua, S. K. Moon, J. Song, G. Bi, and H. Zheng, “Femtosecond laser produced hydrophobic hierarchical structures on additive manufacturing parts,” *Nanomaterials*, vol. 8, no. 8, p. 601, 2018.

- [163] J. Čapek, M. Machová, M. Fousová, J. Kubásek, D. Vojtěch, J. Fojt, E. Jablonská, J. Lipov, and T. Ruml, “Highly porous, low elastic modulus 316l stainless steel scaffold prepared by selective laser melting,” *Materials Science and Engineering: C*, vol. 69, pp. 631–639, 2016.
- [164] V. Weißmann, R. Bader, H. Hansmann, and N. Laufer, “Influence of the structural orientation on the mechanical properties of selective laser melted ti6al4v open-porous scaffolds,” *Materials & Design*, vol. 95, pp. 188–197, 2016.
- [165] L. Wang, J. Kang, C. Sun, D. Li, Y. Cao, and Z. Jin, “Mapping porous microstructures to yield desired mechanical properties for application in 3d printed bone scaffolds and orthopaedic implants,” *Materials & Design*, vol. 133, pp. 62–68, 2017.
- [166] F. A. Shah, A. Snis, A. Matic, P. Thomsen, and A. Palmquist, “3d printed ti6al4v implant surface promotes bone maturation and retains a higher density of less aged osteocytes at the bone-implant interface,” *Acta biomaterialia*, vol. 30, pp. 357–367, 2016.
- [167] J. Mogan, W. Harun, K. Kadirgama, D. Ramasamy, F. Foudzi, A. Sulong, F. Tarlochan, and F. Ahmad, “Fused deposition modelling of polymer composite: A progress,” *Polymers*, vol. 15, no. 1, p. 28, 2022.
- [168] D. W. Hutmacher, “Scaffolds in tissue engineering bone and cartilage,” *Biomaterials*, vol. 21, no. 24, pp. 2529–2543, 2000.
- [169] C. Zhou, K. Yang, K. Wang, X. Pei, Z. Dong, Y. Hong, and X. Zhang, “Combination of fused deposition modeling and gas foaming technique to fabricated hierarchical macro/microporous polymer scaffolds,” *Materials & Design*, vol. 109, pp. 415–424, 2016.
- [170] B. Tellis, J. Szivek, C. Bliss, D. Margolis, R. Vaidyanathan, and P. Calvert, “Trabecular scaffolds created using micro ct guided fused deposition modeling,” *Materials Science and Engineering: C*, vol. 28, no. 1, pp. 171–178, 2008.

- [171] W. Kosorn, M. Sakulsumbat, P. Uppanan, P. Kaewkong, S. Chantawerod, J. Jitsaard, K. Sitthiseripratip, and W. Janvikul, "Pcl/phbv blended three dimensional scaffolds fabricated by fused deposition modeling and responses of chondrocytes to the scaffolds," *Journal of biomedical materials research Part B: Applied biomaterials*, vol. 105, no. 5, pp. 1141–1150, 2017.
- [172] R. De Santis, U. D'Amora, T. Russo, A. Ronca, A. Gloria, and L. Ambrosio, "3d fibre deposition and stereolithography techniques for the design of multifunctional nanocomposite magnetic scaffolds," *Journal of Materials Science: Materials in Medicine*, vol. 26, pp. 1–9, 2015.
- [173] M. Vaezi and S. Yang, "Extrusion-based additive manufacturing of peek for biomedical applications," *Virtual and Physical Prototyping*, vol. 10, no. 3, pp. 123–135, 2015.
- [174] M. Rinaldi, T. Ghidini, F. Cecchini, A. Brandao, and F. Nanni, "Additive layer manufacturing of poly (ether ether ketone) via fdm," *Composites Part B: Engineering*, vol. 145, pp. 162–172, 2018.
- [175] J.-H. Shim, J.-Y. Won, S.-J. Sung, D.-H. Lim, W.-S. Yun, Y.-C. Jeon, and J.-B. Huh, "Comparative efficacies of a 3d-printed pcl/plga/ $\beta$ -tcp membrane and a titanium membrane for guided bone regeneration in beagle dogs," *Polymers*, vol. 7, no. 10, pp. 2061–2077, 2015.
- [176] A. Youssef, S. J. Hollister, and P. D. Dalton, "Additive manufacturing of polymer melts for implantable medical devices and scaffolds," *Biofabrication*, vol. 9, no. 1, p. 012002, 2017.
- [177] N. Xu, X. Ye, D. Wei, J. Zhong, Y. Chen, G. Xu, and D. He, "3d artificial bones for bone repair prepared by computed tomography-guided fused deposition modeling for bone repair," *ACS applied materials & interfaces*, vol. 6, no. 17, pp. 14952–14963, 2014.
- [178] J. Kim, S. McBride, B. Tellis, P. Alvarez-Urena, Y.-H. Song, D. D. Dean, V. L. Sylvia, H. Elgendy, J. Ong, and J. O. Hollinger, "Rapid-prototyped

- plga/ $\beta$ -tcp/hydroxyapatite nanocomposite scaffolds in a rabbit femoral defect model,” *Biofabrication*, vol. 4, no. 2, p. 025003, 2012.
- [179] P. S. Poh, D. W. Hutmacher, B. M. Holzapfel, A. K. Solanki, M. M. Stevens, and M. A. Woodruff, “In vitro and in vivo bone formation potential of surface calcium phosphate-coated polycaprolactone and polycaprolactone/bioactive glass composite scaffolds,” *Acta biomaterialia*, vol. 30, pp. 319–333, 2016.
- [180] W. E. Frazier, “Metal additive manufacturing: a review,” *Journal of Materials Engineering and performance*, vol. 23, pp. 1917–1928, 2014.
- [181] M. K. Kolamroudi, M. Asmael, M. Ilkan, and N. Kordani, “Developments on electron beam melting (ebm) of ti-6al-4v: A review,” *Transactions of the Indian Institute of Metals*, vol. 74, pp. 783–790, 2021.
- [182] L. Hao and R. Harris, “Customised implants for bone replacement and growth,” in *Bio-materials and prototyping applications in medicine*, pp. 79–107, Springer, 2008.
- [183] Q. Feng, Y. Liu, J. Huang, K. Chen, J. Huang, and K. Xiao, “Uptake, distribution, clearance, and toxicity of iron oxide nanoparticles with different sizes and coatings,” *Scientific reports*, vol. 8, no. 1, pp. 1–13, 2018.
- [184] A. Ataei, Y. Li, D. Fraser, G. Song, and C. Wen, “Anisotropic ti-6al-4v gyroid scaffolds manufactured by electron beam melting (ebm) for bone implant applications,” *Materials & Design*, vol. 137, pp. 345–354, 2018.
- [185] M. A. Surmeneva, R. A. Surmenev, E. A. Chudinova, A. Koptioug, M. S. Tkachev, S. N. Gorodzha, and L.-E. Rännar, “Fabrication of multiple-layered gradient cellular metal scaffold via electron beam melting for segmental bone reconstruction,” *Materials & Design*, vol. 133, pp. 195–204, 2017.
- [186] S. Li, Q. Xu, Z. Wang, W. Hou, Y. Hao, R. Yang, and L. Murr, “Influence of cell shape on mechanical properties of ti-6al-4v meshes fabricated by electron beam melting method,” *Acta biomaterialia*, vol. 10, no. 10, pp. 4537–4547, 2014.

- [187] F. A. Shah, O. Omar, F. Suska, A. Snis, A. Matic, L. Emanuelsson, B. Norlindh, J. Lausmaa, P. Thomsen, and A. Palmquist, “Long-term osseointegration of 3d printed cocr constructs with an interconnected open-pore architecture prepared by electron beam melting,” *Acta biomaterialia*, vol. 36, pp. 296–309, 2016.
- [188] J. K. Algardh, T. Horn, H. West, R. Aman, A. Snis, H. Engqvist, J. Lausmaa, and O. Harrysson, “Thickness dependency of mechanical properties for thin-walled titanium parts manufactured by electron beam melting (ebm)®,” *Additive Manufacturing*, vol. 12, pp. 45–50, 2016.
- [189] I. Eldesouky, O. Harrysson, H. West, and H. Elhofy, “Electron beam melted scaffolds for orthopedic applications,” *Additive Manufacturing*, vol. 17, pp. 169–175, 2017.
- [190] N. B. Palaganas, J. D. Mangadlao, A. C. C. de Leon, J. O. Palaganas, K. D. Pangilinan, Y. J. Lee, and R. C. Advincula, “3d printing of photocurable cellulose nanocrystal composite for fabrication of complex architectures via stereolithography,” *ACS applied materials & interfaces*, vol. 9, no. 39, pp. 34314–34324, 2017.
- [191] Q. Wan, J. Tian, M. Liu, G. Zeng, Q. Huang, K. Wang, Q. Zhang, F. Deng, X. Zhang, and Y. Wei, “Surface modification of carbon nanotubes via combination of mussel inspired chemistry and chain transfer free radical polymerization,” *Applied Surface Science*, vol. 346, pp. 335–341, 2015.
- [192] B. Li, W. Hou, J. Sun, S. Jiang, L. Xu, G. Li, M. A. Memon, J. Cao, Y. Huang, C. W. Bielawski, *et al.*, “Tunable functionalization of graphene oxide sheets through surface-initiated cationic polymerization,” *Macromolecules*, vol. 48, no. 4, pp. 994–1001, 2015.
- [193] G. Suresh, M. H. Reddy, and N. Gurram, “Summarization of 3d-printing technology in processing & development of medical implants,” *J. Mech. Contin. Math. Sci*, vol. 14, 2019.

- [194] L. Elomaa, S. Teixeira, R. Hakala, H. Korhonen, D. W. Grijpma, and J. V. Seppälä, "Preparation of poly ( $\epsilon$ -caprolactone)-based tissue engineering scaffolds by stereolithography," *Acta biomaterialia*, vol. 7, no. 11, pp. 3850–3856, 2011.
- [195] L. Hockaday, K. Kang, N. Colangelo, P. Cheung, B. Duan, E. Malone, J. Wu, L. Girardi, L. Bonassar, H. Lipson, *et al.*, "Rapid 3d printing of anatomically accurate and mechanically heterogeneous aortic valve hydrogel scaffolds," *Biofabrication*, vol. 4, no. 3, p. 035005, 2012.
- [196] W. Meyer, S. Engelhardt, E. Novosel, B. Elling, M. Wegener, and H. Krüger, "Soft polymers for building up small and smallest blood supplying systems by stereolithography," *Journal of functional biomaterials*, vol. 3, no. 2, pp. 257–268, 2012.
- [197] O. Guillaume, M. Geven, C. Sprecher, V. Stadelmann, D. Grijpma, T. Tang, L. Qin, Y. Lai, M. Alini, J. De Bruijn, *et al.*, "Surface-enrichment with hydroxyapatite nanoparticles in stereolithography-fabricated composite polymer scaffolds promotes bone repair," *Acta biomaterialia*, vol. 54, pp. 386–398, 2017.
- [198] B. Thavornyutikarn, P. Tesavibul, K. Sitthiseripratip, N. Chatarapanich, B. Feltis, P. F. Wright, and T. W. Turney, "Porous 45s5 bioglass®-based scaffolds using stereolithography: Effect of partial pre-sintering on structural and mechanical properties of scaffolds," *Materials Science and Engineering: C*, vol. 75, pp. 1281–1288, 2017.
- [199] D. Du, T. Asaoka, T. Ushida, and K. S. Furukawa, "Fabrication and perfusion culture of anatomically shaped artificial bone using stereolithography," *Biofabrication*, vol. 6, no. 4, p. 045002, 2014.
- [200] R. A. Levy, T. Chu, J. W. Halloran, S. E. Feinberg, and S. Hollister, "Ct-generated porous hydroxyapatite orbital floor prosthesis as a prototype bioimplant.," *American Journal of Neuroradiology*, vol. 18, no. 8, pp. 1522–1525, 1997.

- [201] I. Sabree, J. E. Gough, and B. Derby, “Mechanical properties of porous ceramic scaffolds: influence of internal dimensions,” *Ceramics International*, vol. 41, no. 7, pp. 8425–8432, 2015.
- [202] J. Y. Kim, J. W. Lee, S.-J. Lee, E. K. Park, S.-Y. Kim, and D.-W. Cho, “Development of a bone scaffold using ha nanopowder and micro-stereolithography technology,” *Microelectronic Engineering*, vol. 84, no. 5-8, pp. 1762–1765, 2007.
- [203] F. P. Melchels, J. Feijen, and D. W. Grijpma, “A review on stereolithography and its applications in biomedical engineering,” *Biomaterials*, vol. 31, no. 24, pp. 6121–6130, 2010.
- [204] A. Ovsianikov, A. Deiwick, S. Van Vlierberghe, P. Dubruel, L. Moller, G. Drager, and B. Chichkov, “Laser fabrication of three-dimensional cad scaffolds from photosensitive gelatin for applications in tissue engineering,” *Biomacromolecules*, vol. 12, no. 4, pp. 851–858, 2011.
- [205] W. Song, L. Chen, J. Seta, D. C. Markel, X. Yu, and W. Ren, “Corona discharge: a novel approach to fabricate three-dimensional electrospun nanofibers for bone tissue engineering,” *ACS Biomaterials Science & Engineering*, vol. 3, no. 6, pp. 1146–1153, 2017.
- [206] S. J. Hollister, C. L. Flanagan, R. J. Morrison, J. J. Patel, M. B. Wheeler, S. P. Edwards, and G. E. Green, “Integrating image-based design and 3d biomaterial printing to create patient specific devices within a design control framework for clinical translation,” *ACS biomaterials science & engineering*, vol. 2, no. 10, pp. 1827–1836, 2016.
- [207] C. Shuai, W. Guo, C. Gao, Y. Yang, P. Wu, and P. Feng, “An nmgo containing scaffold: Antibacterial activity, degradation properties and cell responses,” *International journal of bioprinting*, vol. 4, no. 1, 2018.
- [208] J. He, F. Xu, R. Dong, B. Guo, and D. Li, “Electrohydrodynamic 3d printing of microscale poly ( $\epsilon$ -caprolactone) scaffolds with multi-walled carbon nanotubes,” *Biofabrication*, vol. 9, no. 1, p. 015007, 2017.

- [209] M. Guvendiren, J. Molde, R. M. Soares, and J. Kohn, “Designing biomaterials for 3d printing,” *ACS biomaterials science & engineering*, vol. 2, no. 10, pp. 1679–1693, 2016.
- [210] F. Calignano, “Design optimization of supports for overhanging structures in aluminum and titanium alloys by selective laser melting,” *Materials & Design*, vol. 64, pp. 203–213, 2014.
- [211] M. W. Naing, C. Chua, K. Leong, and Y. Wang, “Fabrication of customised scaffolds using computer-aided design and rapid prototyping techniques,” *Rapid Prototyping Journal*, vol. 11, no. 4, pp. 249–259, 2005.
- [212] A. Ovsianikov, A. Deiwick, S. Van Vlierberghe, P. Dubruel, L. Moller, G. Drager, and B. Chichkov, “Laser fabrication of three-dimensional cad scaffolds from photosensitive gelatin for applications in tissue engineering,” *Biomacromolecules*, vol. 12, no. 4, pp. 851–858, 2011.
- [213] W. Chiu, Y. Yeung, and K. M. Yu, “Toolpath generation for layer manufacturing of fractal objects,” *Rapid Prototyping Journal*, vol. 12, no. 4, pp. 214–221, 2006.
- [214] S. L. Sing, F. E. Wiria, and W. Y. Yeong, “Selective laser melting of lattice structures: A statistical approach to manufacturability and mechanical behavior,” *Robotics and Computer-Integrated Manufacturing*, vol. 49, pp. 170–180, 2018.
- [215] B. Duan, W. L. Cheung, and M. Wang, “Optimized fabrication of ca-p/phbv nanocomposite scaffolds via selective laser sintering for bone tissue engineering,” *Biofabrication*, vol. 3, no. 1, p. 015001, 2011.
- [216] F. P. Melchels, K. Bertoldi, R. Gabbrielli, A. H. Velders, J. Feijen, and D. W. Grijpma, “Mathematically defined tissue engineering scaffold architectures prepared by stereolithography,” *Biomaterials*, vol. 31, no. 27, pp. 6909–6916, 2010.

- [217] T. B. Sercombe, X. Xu, V. Challis, R. Green, S. Yue, Z. Zhang, and P. D. Lee, “Failure modes in high strength and stiffness to weight scaffolds produced by selective laser melting,” *Materials & Design*, vol. 67, pp. 501–508, 2015.
- [218] L. E. Murr, S. Gaytan, F. Medina, H. Lopez, E. Martinez, B. Machado, D. Hernandez, L. Martinez, M. Lopez, R. Wicker, *et al.*, “Next-generation biomedical implants using additive manufacturing of complex, cellular and functional mesh arrays,” *Philosophical Transactions of the Royal Society A: Mathematical, Physical and Engineering Sciences*, vol. 368, no. 1917, pp. 1999–2032, 2010.
- [219] C.-M. Cheah, C.-K. Chua, K.-F. Leong, C.-H. Cheong, and M.-W. Naing, “Automatic algorithm for generating complex polyhedral scaffold structures for tissue engineering,” *Tissue engineering*, vol. 10, no. 3-4, pp. 595–610, 2004.
- [220] G. Lu, S. Xu, Q. S. Yan, X. Xiong, and H. Yu, “Study on dimension change law from cad model to prototype of rapid investment casting based on selective laser sintering,” *Advanced Materials Research*, vol. 774, pp. 1046–1050, 2013.
- [221] G. Z. Yu, D.-T. Chou, D. Hong, A. Roy, and P. N. Kumta, “Biomimetic rotated lamellar plywood motifs by additive manufacturing of metal alloy scaffolds for bone tissue engineering,” *ACS biomaterials science & engineering*, vol. 3, no. 4, pp. 648–657, 2017.
- [222] S. J. Florczyk, M. Simon, D. Juba, P. S. Pine, S. Sarkar, D. Chen, P. J. Baker, S. Bodhak, A. Cardone, M. C. Brady, *et al.*, “A bioinformatics 3d cellular morphotyping strategy for assessing biomaterial scaffold niches,” *ACS Biomaterials Science & Engineering*, vol. 3, no. 10, pp. 2302–2313, 2017.
- [223] P. Kerativitayanan, M. Tatullo, M. Khariton, P. Joshi, B. Perniconi, and A. K. Gaharwar, “Nanoengineered osteoinductive and elastomeric scaffolds

- for bone tissue engineering,” *ACS Biomaterials Science & Engineering*, vol. 3, no. 4, pp. 590–600, 2017.
- [224] R. C. Thomas, P. Vu, S. P. Modi, P. E. Chung, R. C. Landis, Z. Z. Khaing, J. G. Hardy, and C. E. Schmidt, “Sacrificial crystal templated hyaluronic acid hydrogels as biomimetic 3d tissue scaffolds for nerve tissue regeneration,” *ACS Biomaterials Science & Engineering*, vol. 3, no. 7, pp. 1451–1459, 2017.
- [225] A. A. Al-Tamimi, P. R. A. Fernandes, C. Peach, G. Cooper, C. Diver, and P. J. Bartolo, “Metallic bone fixation implants: A novel design approach for reducing the stress shielding phenomenon,” *Virtual and Physical Prototyping*, vol. 12, no. 2, pp. 141–151, 2017.
- [226] M. Osanov and J. K. Guest, “Topology optimization for architected materials design,” *Annual Review of Materials Research*, vol. 46, pp. 211–233, 2016.
- [227] J. K. Guest and J. H. Prévost, “Design of maximum permeability material structures,” *Computer Methods in Applied Mechanics and Engineering*, vol. 196, no. 4-6, pp. 1006–1017, 2007.
- [228] J. K. Guest and J. H. Prévost, “Optimizing multifunctional materials: design of microstructures for maximized stiffness and fluid permeability,” *International Journal of Solids and Structures*, vol. 43, no. 22-23, pp. 7028–7047, 2006.
- [229] S. Sturm, S. Zhou, Y.-W. Mai, and Q. Li, “On stiffness of scaffolds for bone tissue engineering—a numerical study,” *Journal of biomechanics*, vol. 43, no. 9, pp. 1738–1744, 2010.
- [230] Y. Yang, G. Wang, H. Liang, C. Gao, S. Peng, L. Shen, and C. Shuai, “Additive manufacturing of bone scaffolds,” *International Journal of Bioprinting*, vol. 5, no. 1, 2019.

- [231] X. Huang, A. Radman, and Y. M. Xie, “Topological design of microstructures of cellular materials for maximum bulk or shear modulus,” *Computational Materials Science*, vol. 50, no. 6, pp. 1861–1870, 2011.
- [232] F. Losasso, R. Fedkiw, and S. Osher, “Spatially adaptive techniques for level set methods and incompressible flow,” *Computers & Fluids*, vol. 35, no. 10, pp. 995–1010, 2006.
- [233] S. Zhou and Q. Li, “A variational level set method for the topology optimization of steady-state navier–stokes flow,” *Journal of Computational Physics*, vol. 227, no. 24, pp. 10178–10195, 2008.
- [234] V. J. Challis and J. K. Guest, “Level set topology optimization of fluids in stokes flow,” *International journal for numerical methods in engineering*, vol. 79, no. 10, pp. 1284–1308, 2009.
- [235] A. Takezawa and M. Kobashi, “Design methodology for porous composites with tunable thermal expansion produced by multi-material topology optimization and additive manufacturing,” *Composites Part B: Engineering*, vol. 131, pp. 21–29, 2017.
- [236] S. J. Hollister, R. A. Levy, T.-M. Chu, J. W. Halloran, and S. E. Feinberg, “An image-based approach for designing and manufacturing craniofacial scaffolds,” *International Journal of Oral & Maxillofacial Surgery*, vol. 29, no. 1, pp. 67–71, 2000.
- [237] S. M. Giannitelli, D. Accoto, M. Trombetta, and A. Rainer, “Current trends in the design of scaffolds for computer-aided tissue engineering,” *Acta biomaterialia*, vol. 10, no. 2, pp. 580–594, 2014.
- [238] M. Stojkovic, J. Milovanovic, N. Vitkovic, M. Trajanovic, N. Grujovic, V. Milivojevic, S. Milisavljevic, and S. Mrvic, “Reverse modeling and solid free-form fabrication of sternum implant,” *Australasian Physical & Engineering Sciences in Medicine*, vol. 33, pp. 243–250, 2010.

- [239] W. Sun, B. Starly, J. Nam, and A. Darling, “Bio-cad modeling and its applications in computer-aided tissue engineering,” *Computer-aided design*, vol. 37, no. 11, pp. 1097–1114, 2005.
- [240] S. Hollister, T. Chu, R. Guldberg, P. Zysset, R. Levy, J. Halloran, and S. Feinberg, “Image based design and manufacture of scaffolds for bone reconstruction,” in *IUTAM Symposium on Synthesis in Bio Solid Mechanics: Proceedings of the IUTAM Symposium held in Copenhagen, Denmark, 24–27 May 1998*, pp. 163–174, Springer, 2002.
- [241] S. J. Hollister, “Porous scaffold design for tissue engineering,” *Nature materials*, vol. 4, no. 7, pp. 518–524, 2005.
- [242] L. Podshivalov, C. M. Gomes, A. Zocca, J. Guenster, P. Bar-Yoseph, and A. Fischer, “Design, analysis and additive manufacturing of porous structures for biocompatible micro-scale scaffolds,” *Procedia Cirp*, vol. 5, pp. 247–252, 2013.
- [243] H. U. Lemke, K. Inamura, K. Doi, M. W. Vannier, A. G. Farman, and J. H. Reiber, *CARS 2003: Computer Assisted Radiology and Surgery*. Elsevier Science, 2003.
- [244] D. K. Pattanayak, A. Fukuda, T. Matsushita, M. Takemoto, S. Fujibayashi, K. Sasaki, N. Nishida, T. Nakamura, and T. Kokubo, “Bioactive ti metal analogous to human cancellous bone: Fabrication by selective laser melting and chemical treatments,” *Acta biomaterialia*, vol. 7, no. 3, pp. 1398–1406, 2011.
- [245] N. Fujita and O. Terasaki, “Band structure of the p, d, and g surfaces,” *Physical Review B*, vol. 72, no. 8, p. 085459, 2005.
- [246] M. Lai, A. N. Kulak, D. Law, Z. Zhang, F. C. Meldrum, and D. J. Riley, “Profiting from nature: macroporous copper with superior mechanical properties,” *Chemical communications*, no. 34, pp. 3547–3549, 2007.

- [247] S. Rajagopalan and R. A. Robb, “Schwarz meets schwann: design and fabrication of biomorphic and durataxic tissue engineering scaffolds,” *Medical image analysis*, vol. 10, no. 5, pp. 693–712, 2006.
- [248] S. C. Kapfer, S. T. Hyde, K. Mecke, C. H. Arns, and G. E. Schröder-Turk, “Minimal surface scaffold designs for tissue engineering,” *Biomaterials*, vol. 32, no. 29, pp. 6875–6882, 2011.
- [249] F. P. Melchels, A. M. Barradas, C. A. Van Blitterswijk, J. De Boer, J. Feijen, and D. W. Grijpma, “Effects of the architecture of tissue engineering scaffolds on cell seeding and culturing,” *Acta biomaterialia*, vol. 6, no. 11, pp. 4208–4217, 2010.
- [250] J. Feng, J. Fu, C. Shang, Z. Lin, and B. Li, “Porous scaffold design by solid t-splines and triply periodic minimal surfaces,” *Computer Methods in Applied Mechanics and Engineering*, vol. 336, pp. 333–352, 2018.
- [251] N. Yang, Z. Quan, D. Zhang, and Y. Tian, “Multi-morphology transition hybridization cad design of minimal surface porous structures for use in tissue engineering,” *Computer-Aided Design*, vol. 56, pp. 11–21, 2014.
- [252] N. Yang, S. Wang, L. Gao, Y. Men, and C. Zhang, “Building implicit-surface-based composite porous architectures,” *Composite Structures*, vol. 173, pp. 35–43, 2017.
- [253] N. Yang and K. Zhou, “Effective method for multi-scale gradient porous scaffold design and fabrication,” *Materials Science and Engineering: C*, vol. 43, pp. 502–505, 2014.
- [254] N. Yang, Y. Tian, and D. Zhang, “Novel real function based method to construct heterogeneous porous scaffolds and additive manufacturing for use in medical engineering,” *Medical engineering & physics*, vol. 37, no. 11, pp. 1037–1046, 2015.

- [255] N. Yang, C.-f. Du, S. Wang, Y. Yang, and C. Zhang, “Mathematically defined gradient porous materials,” *Materials Letters*, vol. 173, pp. 136–140, 2016.
- [256] N. Yang, C.-f. Du, S. Wang, Y. Yang, and C. Zhang, “Mathematically defined gradient porous materials,” *Materials Letters*, vol. 173, pp. 136–140, 2016.
- [257] D.-J. Yoo, “Heterogeneous porous scaffold design using the continuous transformations of triply periodic minimal surface models,” *International Journal of Precision Engineering and Manufacturing*, vol. 14, pp. 1743–1753, 2013.
- [258] D.-J. Yoo and K.-H. Kim, “An advanced multi-morphology porous scaffold design method using volumetric distance field and beta growth function,” *International Journal of Precision Engineering and Manufacturing*, vol. 16, pp. 2021–2032, 2015.
- [259] N. Yang, L. Gao, and K. Zhou, “Simple method to generate and fabricate stochastic porous scaffolds,” *Materials Science and Engineering: C*, vol. 56, pp. 444–450, 2015.
- [260] A. P. Roberts and E. J. Garboczi, “Elastic moduli of model random three-dimensional closed-cell cellular solids,” *Acta materialia*, vol. 49, no. 2, pp. 189–197, 2001.
- [261] B. Boots, K. Sugihara, S. N. Chiu, and A. Okabe, “Spatial tessellations: concepts and applications of voronoi diagrams,” 2009.
- [262] X. Kou and S. Tan, “A simple and effective geometric representation for irregular porous structure modeling,” *Computer-Aided Design*, vol. 42, no. 10, pp. 930–941, 2010.
- [263] X. Kou and S. Tan, “Microstructural modelling of functionally graded materials using stochastic voronoi diagram and b-spline representations,” *International Journal of Computer Integrated Manufacturing*, vol. 25, no. 2, pp. 177–188, 2012.

- [264] H. Chow, S. Tan, and W. Sze, “Layered modeling of porous structures with voronoi diagrams,” *Computer-Aided Design and Applications*, vol. 4, no. 1-4, pp. 321–330, 2007.
- [265] M. Fantini, M. Curto, and F. De Crescenzo, “A method to design biomimetic scaffolds for bone tissue engineering based on voronoi lattices,” *Virtual and Physical Prototyping*, vol. 11, no. 2, pp. 77–90, 2016.
- [266] M. Fantini and M. Curto, “Interactive design and manufacturing of a voronoi-based biomimetic bone scaffold for morphological characterization,” *International Journal on Interactive Design and Manufacturing (IJIDeM)*, vol. 12, pp. 585–596, 2018.
- [267] S. Gómez, M. Vlad, J. López, and E. Fernández, “Design and properties of 3d scaffolds for bone tissue engineering,” *Acta biomaterialia*, vol. 42, pp. 341–350, 2016.
- [268] G. Wang, L. Shen, J. Zhao, H. Liang, D. Xie, Z. Tian, and C. Wang, “Design and compressive behavior of controllable irregular porous scaffolds: Based on voronoi-tessellation and for additive manufacturing,” *ACS biomaterials science & engineering*, vol. 4, no. 2, pp. 719–727, 2018.
- [269] I. Ochoa, J. A. Sanz-Herrera, J. M. García-Aznar, M. Doblaré, D. M. Yunos, and A. R. Boccaccini, “Permeability evaluation of 45s5 bioglass®-based scaffolds for bone tissue engineering,” *Journal of biomechanics*, vol. 42, no. 3, pp. 257–260, 2009.
- [270] S. Rasheed, W. A. Lughmani, M. A. Obeidi, D. Brabazon, and I. U. Ahad, “Additive manufacturing of bone scaffolds using polyjet and stereolithography techniques,” *Applied Sciences*, vol. 11, no. 16, p. 7336, 2021.
- [271] P. Heintl, L. Müller, C. Körner, R. F. Singer, and F. A. Müller, “Cellular ti-6al-4v structures with interconnected macro porosity for bone implants fabricated by selective electron beam melting,” *Acta biomaterialia*, vol. 4, no. 5, pp. 1536–1544, 2008.

- [272] I. Zein, D. W. Hutmacher, K. C. Tan, and S. H. Teoh, "Fused deposition modeling of novel scaffold architectures for tissue engineering applications," *Biomaterials*, vol. 23, no. 4, pp. 1169–1185, 2002.
- [273] P. H. Warnke, T. Douglas, P. Wollny, E. Sherry, M. Steiner, S. Galonska, S. T. Becker, I. N. Springer, J. Wiltfang, and S. Sivananthan, "Rapid prototyping: porous titanium alloy scaffolds produced by selective laser melting for bone tissue engineering," *Tissue engineering part c: Methods*, vol. 15, no. 2, pp. 115–124, 2009.
- [274] H. Seitz, W. Rieder, S. Irsen, B. Leukers, and C. Tille, "Three-dimensional printing of porous ceramic scaffolds for bone tissue engineering," *Journal of Biomedical Materials Research Part B: Applied Biomaterials: An Official Journal of The Society for Biomaterials, The Japanese Society for Biomaterials, and The Australian Society for Biomaterials and the Korean Society for Biomaterials*, vol. 74, no. 2, pp. 782–788, 2005.
- [275] Y. Liu, Y. Lu, X. Tian, G. Cui, Y. Zhao, Q. Yang, S. Yu, G. Xing, and B. Zhang, "Segmental bone regeneration using an rhbmp-2-loaded gelatin/nanohydroxyapatite/fibrin scaffold in a rabbit model," *Biomaterials*, vol. 30, no. 31, pp. 6276–6285, 2009.
- [276] R. S. Rosenson, A. McCormick, and E. F. Uretz, "Distribution of blood viscosity values and biochemical correlates in healthy adults," *Clinical chemistry*, vol. 42, no. 8, pp. 1189–1195, 1996.
- [277] M. Kinzl, U. Wolfram, and D. H. Pahr, "Identification of a crushable foam material model and application to strength and damage prediction of human femur and vertebral body," *Journal of the mechanical behavior of biomedical materials*, vol. 26, pp. 136–147, 2013.
- [278] M. Kinzl, U. Wolfram, and D. H. Pahr, "Identification of a crushable foam material model and application to strength and damage prediction of human femur and vertebral body," *Journal of the mechanical behavior of biomedical materials*, vol. 26, pp. 136–147, 2013.

- [279] N. Soltanihafshejani, T. Bitter, D. Janssen, and N. Verdonschot, “Development of a crushable foam model for human trabecular bone,” *Medical engineering & physics*, vol. 96, pp. 53–63, 2021.
- [280] L. G. Bracaglia, B. T. Smith, E. Watson, N. Arumugasaamy, A. G. Mikos, and J. P. Fisher, “3d printing for the design and fabrication of polymer-based gradient scaffolds,” *Acta biomaterialia*, vol. 56, pp. 3–13, 2017.
- [281] M. Castilho, G. Hochleitner, W. Wilson, B. Van Rietbergen, P. D. Dalton, J. Groll, J. Malda, and K. Ito, “Mechanical behavior of a soft hydrogel reinforced with three-dimensional printed microfibre scaffolds,” *Scientific reports*, vol. 8, no. 1, p. 1245, 2018.
- [282] W. Hendrikson, C. van Blitterswijk, J. Rouwkema, L. Moroni, *et al.*, “The use of finite element analyses to design and fabricate three-dimensional scaffolds for skeletal tissue engineering,” *Frontiers in bioengineering and biotechnology*, vol. 5, p. 30, 2017.